

**The Electrochemistry of Solid Oxide Fuel Cell Anodes:
Experiments, Modeling, and Simulations**

A dissertation submitted to the
SWISS FEDERAL INSTITUTE OF TECHNOLOGY
ZÜRICH

for the degree of
Doctor of Technical Sciences

presented by
Anja Bieberle
Dipl.-Ing. Univ.
born on October 18, 1971
Germany

accepted on the recommendation of
Prof. Dr. L.J. Gauckler, examiner
Prof. Dr. S. Virtanen, co-examiner
Dr. K. Honegger, co-examiner

Zürich, 2000

The important thing is not to stop questioning.

(Albert Einstein, 1879 - 1955)

Acknowledgement

I wish to express my deep gratitude to my advisor *Prof. Gauckler* for giving me the opportunity to realize this thesis in his laboratory. He encouraged and supported me with much kindness throughout this work. In particular, I appreciated his confidence in me and in the way I managed this project as well as the possibility he gave me to present my results to an international audience all over the world.

Prof. Virtanen is gratefully acknowledged for being co-examiner of the thesis.

Special thanks go further to *Kaspar Honegger* for not only being co-examiner of the thesis, but also for sputtering Ni layers and for representing the amicus curiae in the Swiss SOFC community.

I wish to express my high appreciation to *Mogens Mogensen* and *Søren Primdahl*, Risø National Laboratory, Roskilde, Denmark, for their constant interest in this work as well as for the many fruitful discussions concerning SOFC anodes.

Furthermore, I am deep in debt to many present and former colleagues at the chair of Nonmetallic Inorganic Materials, in particular, to

Martin Gödickemeier and *Andreas Mitterdorfer* who introduced me into the mysteries of SOFCs and of electrode kinetics.

Roger Stadler and *Michael Jörger* who suffered to my left.

Julia Will for her humor and frankness as well as for carefully reading the manuscript.

my students *Hartmut Rudmann*, *Sabine Kurz*, *Claudio Vanoni*, and *Kornelia Lips* for valuable contributions to this work.

all the other members of the SOFC dream team: *Christoph Kleinlogel*, *Dainius Perednis*, *Michel Prestat*, and *Robin Quartier* who supported me in this and that.

Lorenz Meier for explaining a material scientist some dark secrets of chemistry.

Nicholas Grundy for proof reading of the manuscript.

the permanent staff, i.e. *Irène Urbánek* for administrative work, *Peter Kocher* for technical support, and *Prof. Bayer* for all his advice with regard to ceramics.

I would like to thank *Hans Zogg* and *Joachim John*, Institute for Quantum Electron-

ics, ETH Zürich, for free access to their clean room facilities.

René Müller, Balzers Materials, Balzers, is appreciated for sputtering of Ni layers.

I also wish to thank *Prof. Kasemo* and his group, Chalmers University, Göteborg, for helpful discussions on reaction mechanisms.

Financial support from the Bundesamt für Energie in Bern (*Leo Dubal*) is gratefully acknowledged. *Beat Gut*, EMPA Dübendorf, and *Augustin McEvoy*, EPFL Lausanne, are thanked for the successful realization of our common project “Anodes for Intermediate Temperature Solid Oxide Fuel Cells”.

Finally, my highest appreciation is addressed to my family and to *Markus* who constantly listened carefully to all of my problems, who shared my sorrow, and who motivated me in all circumstances.

Table of Contents

Summary/ Zusammenfassung.....	1
Chapter 1 General Introduction	
1.1 SOFC Anodes	6
1.1.1 <i>Introduction</i>	6
1.1.2 <i>Materials</i>	10
1.1.3 <i>Microstructure</i>	11
1.1.4 <i>Kinetics</i>	12
1.2 Electrochemical Impedance Spectroscopy (EIS)	15
1.2.1 <i>Electrode Measurements</i>	15
1.2.2 <i>Characteristic Parameters</i>	18
1.3 Aim of the Study.....	19
1.4 References	20
Chapter 2 The State-Space Modeling Approach	
2.1 Introduction.....	28
2.2 The State-Space Modeling (SSM) Approach.....	28
2.2.1 <i>Surface Science Data</i>	29
2.2.2 <i>Modeling</i>	30
2.2.3 <i>Simulations</i>	31
2.2.4 <i>Experiments</i>	33
2.2.5 <i>The Kinetics of the System</i>	34
2.3 Application to SOFC Systems.....	35
2.3.1 <i>The Pt, O₂ YSZ System</i>	35
2.3.2 <i>The Ni, H₂-H₂O YSZ System</i>	36
2.4 Conclusions	37
2.5 References	37

Chapter 3 The Electrochemistry of Ni Pattern Anodes

3.1	Introduction.....	40
3.2	Experimental	44
3.2.1	<i>Preparation of SOFCs with Ni Pattern Anodes</i>	44
3.2.2	<i>Electrochemical Characterization</i>	47
3.3	Results	49
3.3.1	<i>Microstructure</i>	49
3.3.2	<i>Electrochemistry</i>	51
3.3.2.1	<i>Overpotential</i>	51
3.3.2.2	<i>Partial Pressure of Hydrogen</i>	59
3.3.2.3	<i>Partial Pressure of Water</i>	64
3.3.2.4	<i>Temperature</i>	68
3.3.2.5	<i>Pattern Geometry</i>	72
3.4	Discussion	78
3.5	Summary	86
3.6	References	86

Chapter 4 Ni-Based SOFC Anodes: Microstructure and Electrochemistry

4.1	Introduction.....	92
4.2	Experimental	93
4.2.1	<i>Preparation of Ni-Based Anodes</i>	93
4.2.2	<i>Electrochemical Characterization</i>	96
4.3	Results and Discussion	97
4.3.1	<i>Microstructure</i>	97
4.3.2	<i>Electrochemistry of Metallic Ni Anodes</i>	100
4.3.2.1	<i>Ni Pattern Anode</i>	100
4.3.2.2	<i>Ni Gauze Anode</i>	101
4.3.2.3	<i>Ni Paste Anode</i>	104
4.3.3	<i>Electrochemistry of Ni-YSZ Cermet Anodes</i>	107
4.3.3.1	<i>Screen-Printed Ni-YSZ Anode</i>	107

4.3.3.2	<i>Sputtered Ni-YSZ Anode</i>	110
4.3.3.3	<i>Electrostatically Sprayed Ni-YSZ Anode</i> ...	112
4.3.4	<i>Pt and Au Electrodes</i>	113
4.3.5	<i>Comparison of Ni-based Anodes</i>	116
4.3.5.1	<i>Polarization Resistance</i>	119
4.3.5.2	<i>Current Density</i>	120
4.3.5.3	<i>Temperature</i>	121
4.3.5.4	<i>Equivalent Circuit Fitting</i>	124
4.4	Conclusions	129
4.5	References	131

Chapter 5 Modeling and Simulations of the Ni, H₂-H₂O | YSZ System

5.1	Introduction.....	134
5.2	The State-Space Modeling Approach	136
5.3	Experimental	138
5.4	Modeling.....	138
5.4.1	<i>Electrochemical Model for the Ni, H₂-H₂O YSZ System</i>	138
5.4.2	<i>Assumptions</i>	141
5.4.3	<i>Estimation of Kinetic Parameters</i>	143
5.5	Implementation of the Electrochemical Model	148
5.6	Simulations	150
5.6.1	<i>Standard Conditions</i>	150
5.6.2	<i>Triple Phase Boundary</i>	155
5.6.3	<i>Partial Pressure of Hydrogen</i>	158
5.6.4	<i>Partial Pressure of Water</i>	160
5.6.5	<i>Overpotential</i>	163
5.7	Discussion	166
5.8	Summary	169
5.9	References	170

Chapter 6	General Conclusions	
6.1	Introduction.....	174
6.2	The State-Space Modeling Approach	174
6.3	The Kinetics of SOFC Anodes.....	176
6.4	References	178
Chapter 7	Outlook	
7.1	Introduction.....	180
7.2	Experiments.....	180
7.3	Modeling and Simulations	182
7.4	References	184
Appendix 1	Microstructure of Ni Pattern Anodes.....	187
Appendix 2	EIS Measurements: Single vs. Two Gas Chambers.....	193
Appendix 3	Equivalent Circuit Fitting: Constant Phase Element (CPE) and Relaxation Frequency	199
Appendix 4	Microstructural Characterization of Ni-YSZ Cermet	205
Abbreviations		211
Symbols		213
Curriculum Vitae and List of Publications		217

Summary

The electrochemically active component of a solid oxide fuel cell (SOFC) system is the fuel cell itself. It consists of three main parts: the anode, the electrolyte, and the cathode. At the anode the fuel is oxidized and electrons for the electrical current are extracted. Even though the anode is a central part of the SOFC, its electrochemistry is not yet well understood. This is mainly due to three reasons. First, the state-of-the-art cermet anode made of nickel and yttria stabilized zirconia, i.e. Ni-YSZ, has a complex microstructure with three interpenetrating networks of Ni, YSZ, and pores. Thus, it is difficult to characterize and to quantify the area where the electrochemistry takes place. Second, the results obtained from the main characterization method, i.e. electrochemical impedance spectroscopy (EIS), are difficult to interpret in a physical and in a chemical way. Third, fundamental surface science data under the particular operating conditions of SOFCs is not available from the literature. Despite these problems, it is the main goal of this thesis to investigate the anodic reaction mechanisms and to contribute to a better understanding of the electrochemistry of SOFC anodes.

In order to reach this goal, a new approach, the so-called state-space modeling (SSM) approach, is used. It combines experiments, modeling, and simulations. The experimental part focuses mainly on EIS measurements of SOFC anodes. Modeling implies that an electrochemical model is established which allows the calculation of impedance spectra directly from the chemical and the electrochemical equations. Hence, the experimentally measured and the simulated impedance data can be directly compared. Equivalent circuit fitting which is conventionally used for the interpretation of EIS data, is not necessary. The approach is described in a general way in chapter 2. Chapter 3 and 4 focus on the experiments of Ni pattern and Ni-YSZ cermet anodes, respectively. Chapter 5 considers the modeling and the simulations in more detail.

The electrochemistry of Ni pattern anodes is the subject of chapter 3. By means of this simplified anodic system, the electrochemistry is studied experimentally as a function of several important parameters, i.e. the triple phase boundary (TPB) length, the temperature, the partial pressures of hydrogen and of water, and the overpotential. It is found that Ni pattern anodes are dominated by one main electrode process which might be attributed to the adsorption / desorption of hydrogen or to the removal of oxygen from the electrolyte including charge transfer. A detailed mechanism for the catalytic effect of water on the anode ki-

netics is proposed. This simplified anode design emerged to be suitable for a detailed investigation of the electrochemistry of SOFC anodes.

Further insight into the electrochemistry of SOFC anodes from an experimental point of view is given in chapter 4: different anode designs are characterized concerning their microstructure and their electrochemistry. The impedance analyses agree with the findings and the interpretations of the Ni pattern anodes. Due to the more complex microstructures of the anodes in chapter 4, further effects and tendencies can be pointed out and the proposed reaction mechanism from chapter 3 is refined. Thus, all the experimental results of the thesis manifest that Ni-YSZ SOFC anodes are limited by two main processes, i.e. the adsorption / desorption of hydrogen including charge transfer and the desorption of water.

Modeling and simulations are finally merged in chapter 5 with respect to the simplified anodic SOFC system Ni, H₂ - H₂O | YSZ. An electrochemical model is established using literature data as far as available. The simulations are based on this electrochemical model. The comparison of the simulated and the experimental impedance spectra show a rather good coincidence of the data. The behavior of the simulated spectra under parameter variations similar to those carried out in the experiments on Ni pattern anodes confirm that the established electrochemical model is appropriate. However, on the basis of the impedance results and interpretations of the experimental work, modifications of the electrochemical model are recommended for the future.

Summarizing, it can be stated that the state-space modeling approach combining experiments, modeling, and simulations, has emerged as an extremely promising method to investigate the electrochemical behavior of SOFC anodes. The results obtained in this thesis contribute significantly to a better understanding of the electrochemistry of SOFC anodes.

Zusammenfassung

Der elektrochemisch aktive Teil eines Festelektrolyt-Brennstoffzellen (SOFC) Systems ist die Brennstoffzelle selbst. Sie besteht aus drei wichtigen Bestandteilen: der Anode, dem Elektrolyt und der Kathode. An der Anode wird der Brennstoff oxidiert und die Elektronen für den elektrischen Strom erzeugt. Obwohl die Anode eine zentrale Rolle spielt, ist die zugrundeliegende Elektrochemie bis heute nicht zufriedenstellend verstanden. Das ist hauptsächlich auf drei Gründe zurückzuführen. Erstens haben die heutzutage verwendeten Cermet-Anoden aus Nickel und Yttriumoxid stabilisiertem Zirkonoxid (Ni-YSZ) eine komplizierte Mikrostruktur, die aus drei ineinandergreifenden Netzwerken aus Ni, YSZ und Poren besteht. Es ist daher schwierig, den elektrochemisch aktiven Teil der Anode zu charakterisieren und zu quantifizieren. Zweitens können die Ergebnisse, die von der wichtigsten Charakterisierungsmethode der Anoden, der elektrochemischen Impedanzspektroskopie (EIS), erhalten werden, nur schwer in physikalischem und chemischem Sinne interpretiert werden. Drittens fehlen grundlegende Daten aus der Literatur der Oberflächenforschung, die das System unter SOFC Betriebsbedingungen charakterisieren. Trotz dieser Probleme ist es das Hauptziel dieser Arbeit, die Prozesse, die an der Anode ablaufen, zu erforschen und zu einem besseren Verständnis der Elektrochemie von SOFC Anoden beizutragen.

Um dieses Ziel zu erreichen, wurde ein neuer Lösungsansatz verfolgt, der auf einem sogenannten Zustandsraummodell (SSM) beruht. Er verknüpft Experimente, Modellierung und Simulationen. Von der experimentellen Seite her werden hauptsächlich EIS Messungen von SOFC Anoden durchgeführt. Bei der Modellierung wird ein elektrochemisches Modell aufgestellt, das es ermöglicht, Impedanzspektren direkt von den chemischen und elektrochemischen Gleichungen zu simulieren. Die experimentellen und die simulierten Impedanzspektren können direkt miteinander verglichen werden. Die konventionelle Methode EIS Daten zu interpretieren, nämlich das Fitten mit äquivalenten Schaltkreisen, ist nicht notwendig. Der neue Lösungsansatz ist allgemein in Kapitel 2 beschrieben. Die Kapitel 3 und 4 konzentrieren sich jeweils auf Experimente an mikrostrukturierten Ni und Ni-YSZ Cermet-Anoden. Das Kapitel 5 behandelt die Modellierung und die Simulationen.

Die Elektrochemie von mikrostrukturierten Ni Anoden steht im Fokus von Kapitel 3. Anhand dieses vereinfachten anodischen Systems wurde die Elektro-

chemie experimentell als Funktion von den folgenden Parametern untersucht: der Länge der Dreiphasengrenze (TPB), der Temperatur, dem Partialdruck von Wasserstoff und Wasser und der Überspannung. Man fand, dass mikrostrukturierte Ni Anoden hauptsächlich von einem Elektrodenprozess bestimmt werden. Dieser Prozess kann entweder der Adsorption / Desorption von Wasserstoff oder dem Ausbau von Sauerstoff aus dem Elektrolyten mit gleichzeitigem Ladungstransfer zugeschrieben werden. Für den katalytischen Effekt von Wasser auf die Kinetik wird ein ausführlicher Mechanismus vorgeschlagen. Die Untersuchungen an dem vereinfachten Anodendesign haben sich demnach als geeignet für die Erforschung der Elektrochemie von SOFC Anoden herausgestellt.

Weitere Einblicke von experimenteller Seite werden im Kapitel 4 gewährt. Verschiedene Anodendesigns wurden bezüglich ihrer Mikrostruktur und der Elektrochemie charakterisiert. Die Analyse der Impedanzdaten stimmt mit den Ergebnissen und den Interpretationen der mikrostrukturierten Ni Anoden überein. Aufgrund der komplexeren Mikrostrukturen der Anoden in Kapitel 4 konnten weitere Effekte und Tendenzen verdeutlicht und der vorgeschlagene Reaktionsmechanismus von Kapitel 3 verfeinert werden. Alle experimentellen Ergebnisse der Arbeit verdeutlichen nun, dass Ni-YSZ SOFC Anoden durch zwei Prozesse limitiert werden: die Adsorption / Desorption von Wasserstoff mit gleichzeitigem Ladungstransfer und die Desorption von Wasser.

Die Modellierung und die Simulationen werden schliesslich in Kapitel 5 anhand des vereinfachten anodischen Systems Ni, H₂ - H₂O | YSZ behandelt. Ein elektrochemisches Modell wurde mit Hilfe der Literatur aufgestellt. Die Simulationen stützen sich direkt auf dieses Modell. Ein Vergleich der simulierten und der experimentellen Impedanzspektren zeigte eine ziemlich gute Übereinstimmung der Daten. Das Verhalten der Spektren, die unter den gleichen Bedingungen simuliert wurden wie die Experimente an den mikrostrukturierten Ni Anoden durchgeführt wurden, bestätigte, dass das aufgestellte elektrochemische Modell die experimentellen Daten ziemlich gut darstellt. Jedoch wird aufgrund der EIS Daten und der Interpretationen der experimentellen Arbeit empfohlen, in der Zukunft Modifikationen des elektrochemischen Modells vorzunehmen.

Zusammenfassend kann man festgehalten, dass der Ansatz der Zustandsraummodellierung, welcher Experimente, Modellierung und Simulationen vereinigt, eine sehr vielversprechende Methode ist, um die Elektrochemie von SOFC Anoden zu erforschen. Die Ergebnisse dieser Arbeit tragen eindeutig zu einem besseren Verständnis der Elektrochemie von SOFC Anoden bei.

Chapter 1

General Introduction

Abstract

This chapter gives an introduction to SOFC anodes as well as to the main measurement technique used throughout this thesis, i.e. electrochemical impedance spectroscopy (EIS). In particular, the main literature with regard to SOFC anodes is listed and material, microstructural, as well as kinetic aspects are discussed. Concerning EIS, the main attention is focused on the manner of how to perform electrode measurements and on the characteristic parameters which are used for the analyses of the impedance data in chapters 3-5. All this information and all these discussions cumulate then in a summary of the aim of this thesis.

1.1 SOFC Anodes

1.1.1 Introduction

Fuel cells are electrochemical devices which convert chemical energy from the reaction of a fuel (H_2 , CH_4 , natural gas) with an oxidant (O_2 , air) directly into electrical energy. The SOFC (Solid Oxide Fuel Cell) is one of the five different types of fuel cells which are currently being worked on [1,2]. The different types of fuel cells are named according to their electrolyte material.

Besides the electrolyte, the cathode, the anode, and the interconnector are the main components of a single fuel cell. In the case of SOFCs which are operated at temperatures between 600°C and 1000°C , the electrolyte is in most systems the load bearing part of the single cell. However, the development tends towards anode supported cells [3-5] where an anode substrate becomes the load bearing part. A thinner electrolyte allows then a higher performance due to a reduction of the ohmic losses.

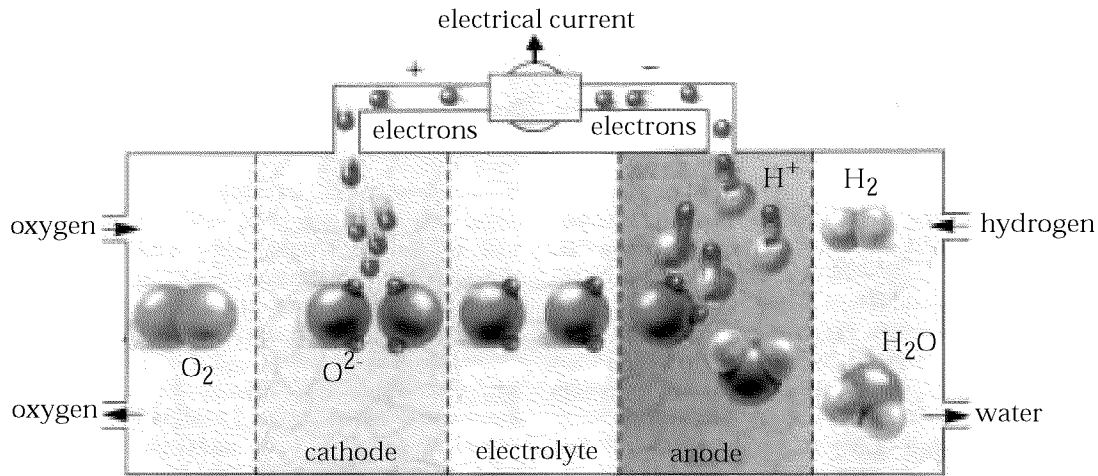


Fig. 1.1: Schematic representation of the operating principle of a SOFC [6].

The cathode, made, for instance, of a Sr doped LaMnO_3 , is the electrode where the oxidant is reduced. Oxygen ions are formed and can pass through the electrolyte which consists in the state-of-the-art systems of yttria stabilized zirconia (YSZ). The driving force for the drift of the oxygen ions through the electrolyte is the low partial pressure of oxygen at the anode side of the fuel cell where the hydrogen is oxidized. The anode is usually made of a Ni-YSZ cermet. At the

anode, oxygen and hydrogen are combined to form water and electrons. The electrons which represent the electrical current, are drawn from the fuel cell by the electrically conducting interconnector. A schematic representation of the overall operating principle is illustrated in Fig. 1.1.

The anode as the part of the SOFC where the electrons are released, is obviously crucial for a high performance of the fuel cell. In particular, the following specific properties are required for the anode [7]:

- (1) *catalytic activity*: the anode must have a high catalytic activity for the oxidation of the fuel gas.
- (2) *stability*: the anode must be chemically, morphologically, and dimensionally stable at operating temperature in the fuel gas environment; it must also be tolerant towards contaminants.
- (3) *conductivity*: a maximum electrical conductivity under a large variety of operating conditions is desired to minimize the ohmic losses.
- (4) *compatibility*: the anode must be chemically, thermally, and mechanically compatible with the other fuel cell components during fabrication as well as under operation.
- (5) *porosity*: the porosity of the anode must be tailored with regard to mass transport considerations as well as mechanical strength.

Many studies in the last years focused on these requirements in order to develop an anode with high performance. The results of these studies are summarized in form of a table which contains the research groups with their main interests as well as their important papers in the field of SOFC anodes (Tab. 1.1). In the following subsections, materials, microstructural, and kinetic aspects of SOFC anodes will be discussed in some more detail, since these aspects are of major significance with regard to this thesis.

Tab. 1.1: Research groups and their main interests with regard to SOFC anodes.

Research group	Main researchers	Interests	Material	exp./sim. ^{*)}	Ref.
Riso National Laboratory, DK	M. Mogensen, S. Primdahl	kinetics, microstructure/performance relation, alternative materials	Ni-YSZ, CDG	exp.	[8-16]
University of Twente, Enschede, NL	B. de Boer, H.J.M. Bouwmeester	model anodes, kinetics	Ni, Ni-YSZ	exp.	[17-18]
SINTEF / NTNU Trondheim, NO	R.J. Aaberg, S. Sunde	microstructure/electrochemistry, model anodes, Monte Carlo simulations	Ni, Pt, Ni-YSZ	exp./sim.	[19-23]
Imperial College, London, UK	B.C.H. Steele, P.H. Middleton	alternative materials	Nb-ceria, chromite	exp.	[24-26]
University of St. Andrews, UK	J. Irvine	alternative materials	Ti-YSZ, Nb-TiO ₂	exp.	[27-30]
Keele University, UK	C.M. Finnerty, R.H. Cunningham, R.M. Ormerod	catalysis, fuel reforming	Ni-YSZ	exp.	[31-32]
Research Center Jülich, D	P. Holtappels, J. Divisek, W. Lehnert, L.G.J. deHaart, I.C. Vinke	structural properties, kinetics, degradation, gas transport	Ni-YSZ	exp./sim.	[33-50]
University of Karlsruhe, D	A. Müller, H. Schichlein, E. Ivers-Tiffée	simulations (system identification), multi-layer anode	Ni-YSZ	exp./sim.	[51-53]
ETHZ, Zürich, CH	P. Ekanayake, A. Bieberle, L.J. Gauckler	microstructure, kinetics, model anode, state-space modeling	Ni, Ni-YSZ	exp./sim.	[54-58]
EPFL, Lausanne, CH	J. Van herle, A.J. McEvoy	catalysis, alternative materials	Ni-YSZ, ceria, chromite	exp.	[59-60]
University of Genova, I	P. Costamagna	partial oxidation, electrochemical reactor, active anode thickness	Ni-YSZ	sim.	[61-62]

(Tab. 1.1 continued).

Research group	Main researchers	Interests	Material	exp./sim. ^{*)}	Ref.
Tsukuba Research Center, J	T. Kawada, M. Dokiya	electrochemical characterization	Ni-YSZ, ceria	exp.	[63-66]
Yokohama National University, J	J. Mizusaki, H. Tagawa	kinetics, model anodes, H ₂ -H ₂ O and CH ₄ -H ₂ O systems	Ni, Pt	exp.	[67-74]
Yamanashi University, Kofu, J	H. Uchida, M. Watanabe	microstructure, catalysis, internal reforming	SDC, Ni-YSZ, Pt, Ru	exp.	[75-81]
Gunma University, J	N. Nakagawa, K. Kato	triple phase boundary, kinetics	Ni, Ni-YSZ	exp.	[82-84]
Kyushu University, J	K. Eguchi, H. Arai	electrochemical characterization, interface analysis	Ni-YSZ, Ni/Pt-SDC	exp.	[85-89]
Japan Fine Ceramics Center, Nagoya, J	S. Ohara, K. Mukai, T. Fukui	high performance, long term stability	Ni-YSZ, Ni-SDC	exp.	[90-93]
Tokyo University, J	A. Abudula, K. Yamada	kinetics, reforming	Ni-YSZ	exp.	[94-98]
Northwestern University, Illinois, USA	T. Tsai, S.A. Barnett	low temperature, reforming, interfacial layers	Ni-YSZ, ceria	exp.	[99-101]
University of Pennsylvania, USA	S. Park, R.J. Gorte, W.L. Worrell	processing, direct oxidation	SDC, Rh-SDC	exp.	[102-104]
CSIRO, Victoria, AU	S.P. Jiang, S.P.S. Badwahl	kinetics, $p(\text{H}_2\text{O})$, model anode	Ni, Pt, Ni-YSZ	exp.	[105-107]

^{*)} exp. = experimental study, sim. = simulations

1.1.2 Materials

Nickel - yttria stabilized zirconia (Ni-YSZ) cermet (cermet = mixture of ceramic and metal) is currently the state-of-the-art material for SOFC anodes. It is used as anode in the systems of Sulzer HEXIS (Heat EXchanger Integrated Stack) [3,4,108], of Siemens-Westinghouse [109], of Ceramic Fuel Cells Limited [110], as well as of Electric Power Development Co. [111]. It is also the material of choice for Acumentrics Corporation [112] and Global Thermoelectric Inc. [113].

Ni is used for several reasons: it withstands high temperatures and reducing atmospheres; it has excellent catalytic properties [85], it does not react heavily with other SOFC components, and it is available at reasonable cost. However, Ni expands by more than 30 vol.% under re-oxidation [11] which might lead to fragmentation and detachment of the anode in the case of an emergency shut-down of the SOFC system. In addition, volatile $\text{Ni}(\text{OH})_2$ species can be formed at elevated temperatures under high partial pressures of water [11] which results in an insufficient long term stability. Finally, Ni-based anodes are not suitable for operation under natural gas due to the strong tendency of carbon formation. Gas channels might become blocked and the catalytic activity will be reduced.

While Ni plays the role of the catalytically active as well as electronically conducting phase, the YSZ is added in order to support the Ni particles, to inhibit coarsening of the Ni, and to provide a thermal expansion coefficient which is similar to that of the zirconia based electrolyte. The functional properties of the YSZ in the anode are a matter of discussion: it is so far not clear whether the YSZ phase itself influences the anode kinetics or not. According to [17], the YSZ plays an active role by forming conductive paths for the oxygen and thereby enlarging the active area available for the electrode reaction.

Besides Ni-YSZ, many other materials have been investigated and are currently under consideration as alternative materials for SOFC anodes. The main goals for these studies are to increase the performance of the state-of-the-art anode as well as to fabricate an anode which is more resistant with regard to operation under natural gas. There exist mainly two approaches:

The first is to replace the Ni as the catalytic material by other electrochemically active elements, such as Co or Ru: Cobalt has a higher sulfur tolerance (sulfur is a critical contaminant in natural gas) and a higher oxidation potential, but

it is rather expensive [7]. Ruthenium is less susceptible towards coarsening due to the higher melting point compared to Ni ($T_m(\text{Ni}) = 1453^\circ\text{C}$, $T_m(\text{Ru}) = 2310^\circ\text{C}$), has a high catalytic activity for steam reforming, and shows no carbon deposition under reforming conditions [7]. Disadvantages are costs as well as the evaporation of ruthenium oxide [17].

Another approach is to use a completely different compound instead of Ni-YSZ. Ceria [15,16,75,76,100,104], titanates [29,30,114], chromites [115,116], or perovskite type materials, such as $(\text{LaSr})(\text{CoFe})\text{O}_3$ [117], are currently under investigation in different laboratories. The most promising results have so far been obtained with ceria anodes. As ceria exhibits both ionic as well as electronic conduction under reducing atmosphere, it is not necessary to prepare a cermet. A higher performance is achieved due to the mixed ionic electronic conduction (MIEC) of ceria which can even be enhanced by the addition of dopants, such as Gd [15,16]. Ceria anodes are much more stable concerning carbon deposition [16]. However, ceria exhibits a volume change when redox cycles are undertaken due to the valence change of Ce [15,16]. The other alternative anode materials mentioned above are less investigated so far. They all have very advantageous properties, such as, for instance, the similar thermal expansion coefficient of TiO_2 and YSZ. However, most of these alternative materials suffer from a rather low performance.

1.1.3 Microstructure

The performance of a SOFC anode is strongly dependent on the microstructure which is determined by the fabrication method. However, irrespective of the processing route, each of the three phases of the cermet, Ni, YSZ, and gas should form a percolating network. This is mandatory for the electrons, the oxygen ions, as well as the fuel gas to reach the electrochemically active area. The electrochemically active area is the location where the three phases meet and where the chemical and the electrochemical reactions are supposed to take place. It is usually called the triple phase boundary (TPB). In the case of model anodes, it has been demonstrated that the anode conductivity which determines the performance of the anode, correlates with the TPB length [17,67,68]. In the case of Ni-YSZ cermet anodes, it is very difficult to determine the exact TPB due to the three dimensionally connected microstructure. So far, only one study in the literature focused on the determination of the TPB length of a Ni-YSZ cermet anode

[43].

Although the exact length of the TPB of a Ni-YSZ cermet anode is not known, more and more studies focus on the increase of the TPB length. One approach currently under consideration concerns the introduction of an intermediate layer between the anode and the electrolyte. This intermediate layer can on the one hand increase the electrochemically active reaction zone due to MIEC behavior and can on the other hand reduce the thermal expansion coefficient mismatch between the anode and the electrolyte [66,99]. Another approach is to enlarge the TPB length geometrically. However, since SOFC anodes are usually fabricated homogeneously over the entire thickness of the anode and since a longer TPB would most easily be realized by a finer microstructure, the porosity of the anode would become too small so that the fuel gas will not reach the electrochemically active zone anymore. Hence, it is advisable to design a graded microstructure in the future. This is in particular necessary when anode supported fuel cell designs come on the market. One attempt for the development of a graded anode microstructure is described in [53].

State-of-the-art Ni-YSZ anodes used in an electrolyte supported SOFC design are typically 100 μm thick [109,110]. In the case of an anode supported design, the active anode layer is only about 10 μm thick [4]. The anode must consist of at least 30 vol% of Ni in the reduced state in order to guarantee a sufficient electronic conductivity under SOFC operation [7,13,43]. For a sufficient gas supply, the porosity should be adjusted between 30% - 50% [7,13,14,43,84]. This results in pore radii of 100 nm - 1000 nm [40,43]. The YSZ is preferentially added to the cermet with two different particle sizes. Coarse YSZ (particle size around 1 μm) adjusts the thermal expansion coefficient of the anode to that of the YSZ electrolyte and prevents the anode layer from significant shrinkage during fabrication and on reduction of the NiO (particle size around 0.1 μm). Fine YSZ (particle size around 0.1 μm) prevents Ni from coarsening by trapping the Ni grains [54,77].

1.1.4 Kinetics

The materials as well as the microstructure have already been discussed as important factors for a high performance of SOFC anodes. The kinetics is a further aspect, since it underlies the entire fuel cell process. It includes the kind of the chemical and of the electrochemical reactions as well as their reaction rates, the surface species, and the electrochemical parameters, such as reaction rate

constants, surface coverages, and sticking coefficients. Detailed knowledge on each of these aspects allows, in principle, to determine the limitations of the fuel cell processes with regard to the electrochemistry. This is of particular interest, since materials and microstructural properties have in recent years been optimized to a considerably high level, while only little information is available concerning the electrochemistry of SOFC anodes (cf. Tab. 1.1).

For several years, it has been criticized in the literature that “the details of the determining mechanisms for H₂ oxidation on Ni-YSZ cermets at SOFC conditions are still not understood” [10]. Many similar quotations are found in recent literature [7,10,23,99,120,121]. The reasons for this are mainly due to the fact that the kinetics of SOFC systems under the specific operating conditions, i.e. $T > 973$ K and a total gas pressure around 1 atm, are not studied by surface science and catalysis groups. Hence, the fundamental literature on these systems is missing. On the other hand, it is rather difficult to obtain the missing data from SOFC measurements.

Despite this considerable lack of information, but due to the significant need of exploring SOFC anode kinetics in order to improve the performance of the anodes specifically, several studies focused in the last few years on this topic (Tab. 1.1). It was soon realized that the SOFC anode kinetics cannot straight-forwardly be understood due to the complicated, three dimensionally interconnected microstructure of the anode as well as due to the manifold chemical and electrochemical reactions taking place under SOFC operating conditions. In order to simplify the systems, the microstructure of the anode was simplified to a two dimensional Ni-YSZ contact, such as a Ni pattern [17,67,68], a Ni point [19,122-124], or a porous Ni [11,17,82,105-107] electrode. The interface was analyzed using DC and AC techniques and the results were interpreted by means of equivalent circuit fitting. However, the method of equivalent circuit fitting does not allow a clear physical and chemical interpretation of the system.

Nevertheless, detailed electrochemical measurements allowed to predict the electrochemical models in Fig. 1.2 with regard to the kinetics of SOFC anodes. The schematic representations clarify the specific reaction steps assumed to take place at the interface Ni, YSZ, and gas phase.

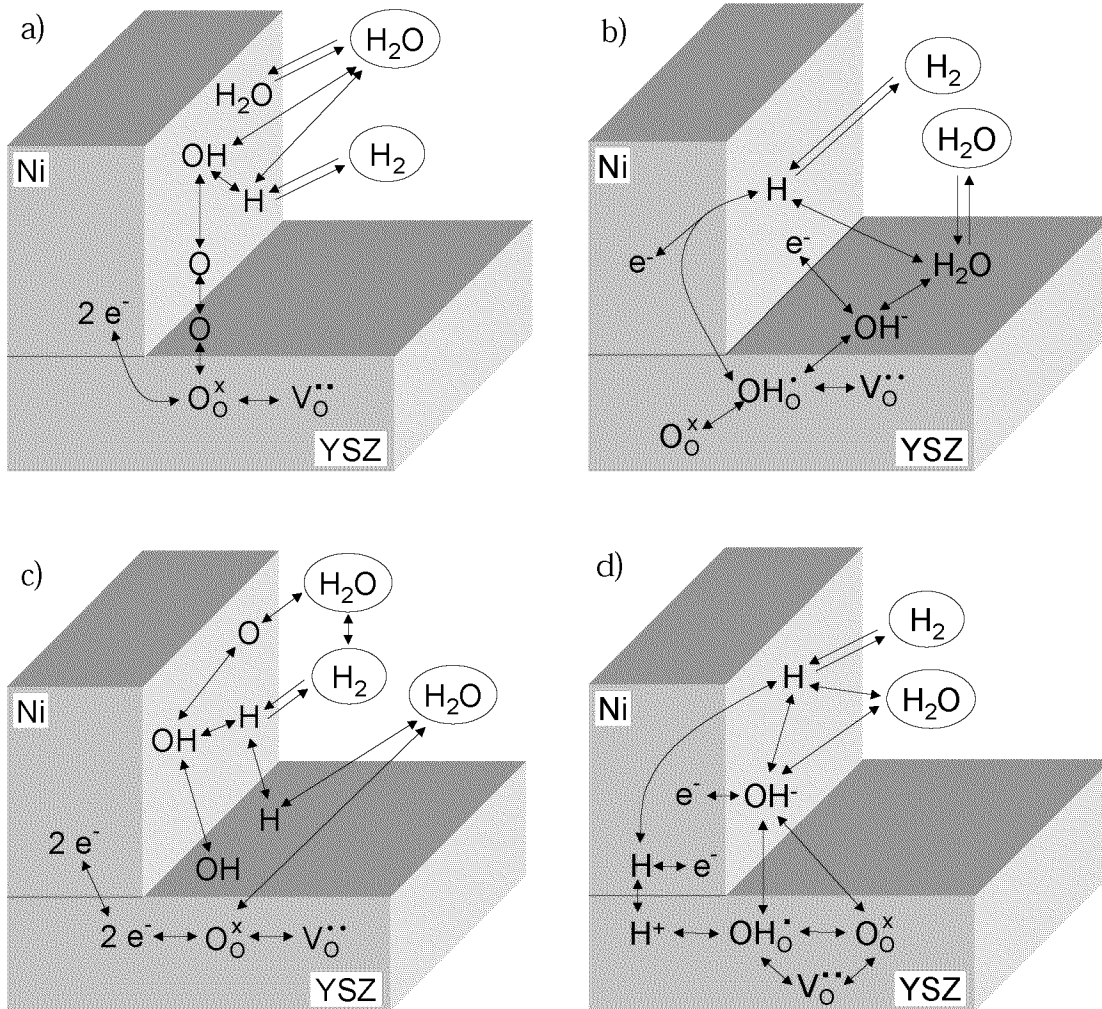


Fig. 1.2: Electrochemical models predicted for the kinetics of SOFC anodes: a) Mizusaki *et al.* [68,71], b) de Boer *et al.* [17], c) Jiang *et al.* [105], d) Holtappels *et al.* [34].

The different electrochemical models in Fig. 1.2 mainly agree with regard to the adsorption and to the desorption behavior of hydrogen as well as to the formation of hydroxyl. Major diversity is found concerning the location where the chemical and the electrochemical reactions take place (either merely on the Ni surface or equally on the Ni and on the YSZ surface, respectively) as well as concerning the reactions related to the interstitial oxygen in the YSZ, the adsorption and the desorption behavior of water, and the charge transfer step. While Mizusaki *et al.* [68,71] (Fig. 1.2a) consider exclusively the Ni surface to be electrochemically active and while Jiang *et al.* [105] (Fig. 1.2c) include surface reactions

on the YSZ surface into the model, de Boer *et al.* [17] (Fig. 1.2b) as well as Holtapels *et al.* [34] (Fig. 1.2d) even suggest that interstitial hydrogen and hydroxyl are formed. The removal of oxygen from the YSZ is assumed to proceed rather differently: the oxygen becomes either adsorbed onto the YSZ surface (Fig. 1.2a), or it forms a hydroxyl interstitial (Fig. 1.2b), or a negatively charged hydroxyl on the Ni surface (Fig. 1.2c), or water is immediately formed without any intermediate step (Fig. 1.2d).

In summary, it should be noted that a large number of reaction steps are supposed to take place at the interface of Ni, YSZ, and gas phase. All these models are predicted from AC and DC electrochemical measurements with special focus on particular parameters.

1.2 Electrochemical Impedance Spectroscopy

The experimental method of electrochemical impedance spectroscopy (EIS) originates from liquid electrochemistry but it is, in recent years, equally used for solid state electrochemistry. The method of EIS is discussed in detail in [125-130]. In this chapter, we will merely focus on some specific aspects which are of particular importance for the understanding of the EIS analyses in chapter 3-5 of this thesis.

1.2.1 Electrode Measurements

Electrode measurements are usually carried out with respect to a reference electrode. This kind of experimental set-up is referred to as three point mode (Fig. 1.3). The three points are the working, the reference, and the counter electrode. If one uses two different wires for the current and for the voltage at the working electrode, one refers to a four lead configuration. A schematic diagram of the wire connections for a three point, four lead configuration for impedance measurements of SOFC electrodes is illustrated in Fig. 1.3. Additional information is given in [131]. In the case of an anode measurement, the terms working and counter electrode refer to the anode and to the cathode, respectively. The reference electrode is in this study always associated with the working electrode: it is composed of the same material and it is situated in the same gas atmosphere as the working electrode.

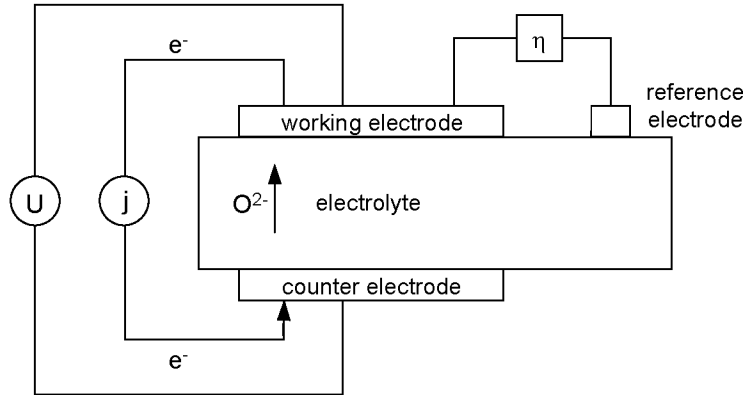


Fig. 1.3: Schematic diagram of the wire connections for a three point, four lead configuration for impedance measurements of SOFC electrodes.

Under equilibrium conditions, the working and the reference electrode are set at the same potential, i.e. $\eta = 0$ mV (Fig. 1.3). In order to study the polarization characteristic of the working electrode, a certain potential, the so-called overpotential, η ($\eta \neq 0$ mV), is applied between the working and the reference electrode. A positive potential signifies an anodic overpotential, whereas a negative potential signifies a cathodic overpotential. In this thesis, mainly anodic overpotentials were applied. The working electrode is polarized with respect to the reference electrode and due to the electrical driving force, oxygen ions are forced through the electrolyte. In consequence, a current, j , flows. A typical current - voltage characteristic obtained from the polarization of a SOFC is illustrated in Fig. 1.4. The different contributions of the anode (A), of the cathode (C), and of the electrolyte (el) to the total fuel cell losses are plotted separately.

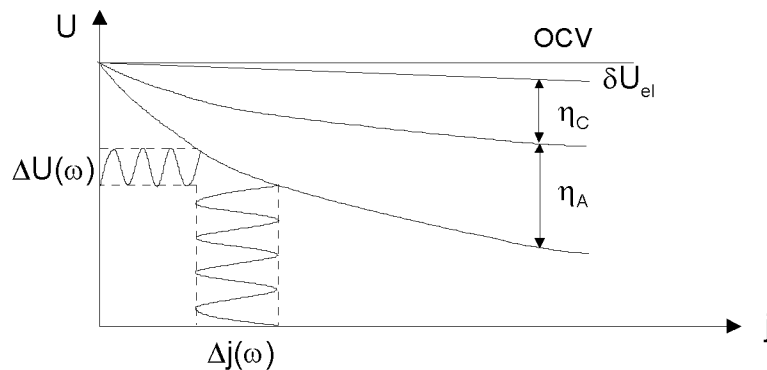


Fig. 1.4: Typical current - voltage characteristic of a SOFC.

EIS measurements as a function of the overpotential are carried out at different points of the current - voltage curve in Fig. 1.4, i.e. a certain overpotential η is applied between the working and the reference electrode. An alternating voltage, $\Delta U(\omega)$, is then superimposed under constant polarization of the electrode and the answer is measured in terms of an alternating current, $\Delta j(\omega)$:

$$\Delta U(\omega, t) = U_m \cdot e^{-i\omega t} \quad (1.1)$$

$$\Delta j(\omega, t) = I_m \cdot e^{-i(\omega t + \phi)} \quad (1.2)$$

where t is the time, U_m and I_m the amplitudes, ω the angular frequency, ϕ the phase difference between the voltage and the current. The impedance, Z , is then defined as

$$Z(\omega) = \frac{\Delta U(\omega, t)}{\Delta j(\omega, t)} = \frac{U_m}{I_m} \cdot e^{i\phi} \quad (1.3)$$

Using the Euler relation

$$e^{i\phi} = \cos\phi + i \sin\phi \quad (1.4)$$

the impedance becomes

$$Z(\omega) = Z'(\omega) + i Z''(\omega) \quad (1.5)$$

where

$$Z'(\omega) = \text{real}(Z) = |Z| \cdot \cos\phi \quad (1.6)$$

$$Z''(\omega) = \text{imag}(Z) = |Z| \cdot \sin\phi \quad (1.7)$$

$$|Z| = \frac{U_m}{I_m} = \sqrt{Z'^2 + Z''^2} \quad (1.8)$$

$$\tan\phi = \frac{Z''(\omega)}{Z'(\omega)} \quad (1.9)$$

1.2.2 Characteristic Parameters

Impedance spectra can be plotted in two ways: in the Nyquist representation where the negative imaginary part of the impedance, Z'' , is plotted vs. the real part of the impedance, Z' (Fig. 1.5a) or in the Bode representation where the absolute impedance, $|Z|$, as well as the phase shift, ϕ , are plotted vs. the angular frequency, ω (Fig. 1.5b). Both representations contain, in principle, the same information and can be transformed into each other. However, depending on the data, one or the other representation is preferred because specific details can be resolved more precisely. Hence, in impedance analyses, both representations have always to be considered. The following characteristic parameters are obtained from the impedance data:

- the *polarization resistance*, R_p , which is the purely ohmic part of the electrode resistance. It can be determined from both the Nyquist as well as from the Bode plot (Fig. 1.5).
- the so-called *electrolyte resistance*, R_e , which is caused by a certain contribution of the electrolyte. It can be determined from the high frequency part of the Nyquist plot at the intersection of the impedance data with the real axis (Fig. 1.5a).
- the *relaxation frequency*, ω^* , which is defined as the frequency at the maximum imaginary impedance value. In the case of several relaxation processes, there exist several relaxation frequencies which can be identified as local maxima in the Nyquist plot (Fig. 1.5a).

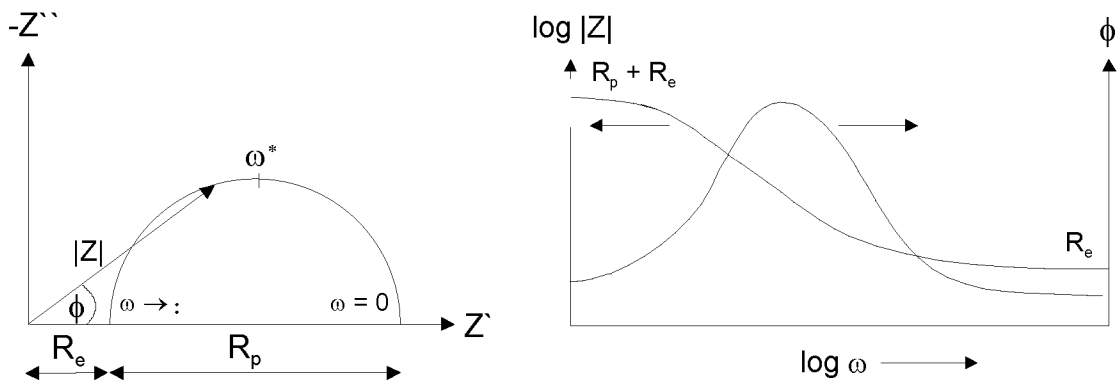


Fig. 1.5: Schematic representation of a) Nyquist plot, b) Bode plot.

Electrochemical impedance spectra are usually analyzed by fitting the data to an equivalent circuit consisting of resistances, capacitances, and inductances. The main difficulty with this method is related to the physical and the chemical interpretation of the equivalent circuit elements. Therefore, a different approach is followed in this thesis. It is based on a state-space model and is explained in a general way in chapter 2. For some cases, however, as well as for a comparison with the literature, equivalent circuit fitting is once in a while used in this thesis. For detailed information, the reader is referred to [125-127]. Two special terms, the constant phase element (CPE) and the relaxation frequency, are discussed in appendix 3, since both of these terms are frequently used with regard to equivalent circuit fitting in this thesis.

1.3 Aim of the Study

The discussions above clearly indicate that research on SOFC anodes is still a major as well as a challenging area in the field of solid oxide fuel cells. In particular, the kinetics of the anodic processes demand special attention, since kinetic aspects are controversially discussed in the literature and are not clearly understood so far. This is mainly due to the complicated anode microstructure which is used for many studies in the literature. In addition, the results of the analyses of the main characterization method, i.e. electrochemical impedance spectroscopy (EIS), cannot be interpreted satisfyingly in a chemical or physical way. Hence, alternative interpretation methods are urgently required.

Both of these two main demands for further work on SOFC anodes will be considered in this study. The main goal of the present work focuses on the understanding of the electrochemistry of SOFC anodes. In particular, the following sub-goals will be accomplished:

- (1) A simplified SOFC anode should be investigated which allows to study directly the interface of Ni, YSZ, and gas phase. Ni pattern anodes should be fabricated and electrochemically characterized as a function of the TPB length, of the fuel gas atmosphere, of the temperature, and of the overpotential applied between the working and the reference anode. The results should give detailed information about the main limitations of Ni pattern anodes (chapter 3).
- (2) Several Ni-based SOFC anodes differing in the processing route

and their microstructure should be compared and analyzed in terms of their electrochemical behavior (chapter 4). The analyses should allow the derivation of a feasible reaction mechanism taking place at Ni-YSZ anodes. The rate limiting reaction steps should be identified.

- (3) A new approach for the identification of reaction mechanisms at SOFC electrodes should be investigated for the Ni, H₂ - H₂O | YSZ system. An electrochemical model should be established which should allow to simulate impedance spectra directly from the chemical and the electrochemical equations. The simulated results should be compared to the experimental data so that a correlation of the electrochemistry and of the impedance data is possible (chapter 5).

1.4 References

- [1] K. Kordesch, G. Simader, "Fuel Cells and Their Applications", VCH Verlagsgesellschaft, Weinheim, Germany (1996).
- [2] L. Blomen (Ed.), Proc. of the Intern. Conference "Fuel Cell 2000", European Fuel Cell Forum (Publ.), Lucerne, Switzerland (2000).
- [3] K. Honegger, J. Krumeich, R. Diethelm, Proc. of the 4th Europ. Fuel Cell Forum, Lucerne, Switzerland, Ed.: A.J. McEvoy (2000) 29.
- [4] G.M. Christie, P. Nammensma, J.P.P. Huijsmans, Proc. of the 4th Europ. Fuel Cell Forum, Lucerne, Switzerland, Ed.: A.J. McEvoy (2000) 3.
- [5] S. Linderoth, Proc. of the 4th Europ. Fuel Cell Forum, Lucerne, Switzerland, Ed.: A.J. McEvoy (2000) 19.
- [6] W. Gajewski, *Spektrum der Wissenschaft* **Juli 1995** (1995) 88.
- [7] N.Q. Minh, T. Takahashi, "Science and Technology of Ceramic Fuel Cells", Elsevier, Amsterdam, The Netherlands (1995) 147.
- [8] S. Primdahl, M. Mogensen, *J. Electrochem. Soc.* **144** (1997) 3409.
- [9] M. Mogensen, S. Skaarup, *Solid State Ionics* **86-88** (1996) 1151.
- [10] M. Mogensen, S. Sunde, S. Primdahl, Proc. of the 17th Risø Intern. Symp. on Mat. Sci.: High Temperature Electrochemistry: Ceramics and Metals, Eds.: F.W. Poulsen, N. Bonanos, S. Linderoth, M. Mogensen, B. Zachau-Christiansen, Risø National Laboratory, Roskilde, Denmark (1996) 77.
- [11] S. Primdahl, PhD Thesis, University of Twente, Twente, The Netherlands (1999).
- [12] S. Primdahl, M. Mogensen, *J. Electrochem. Soc.* **145** (1998) 2431.
- [13] S. Primdahl, M. Mogensen, *J. Electrochem. Soc.* **146** (1999) 2827.

-
- [14] M. Brown, S. Primdahl, M. Mogensen, *J. Electrochem. Soc.* **147** (2000) 475.
- [15] M. Mogensen, T. Lindegaard, U.R. Hansen, G. Mogensen, *J. Electrochem. Soc.* **141** (1994) 2122.
- [16] O.A. Marina, C. Bagger, S. Primdahl, M. Mogensen, *Solid State Ionics* **123** (1999) 199.
- [17] B. de Boer, PhD Thesis, University of Twente, Twente, The Netherlands (1998).
- [18] B. de Boer, M. Gonzalez, H.J.M. Bouwmeester, H. Verweij, *Solid State Ionics* **127** (2000) 269.
- [19] R.J. Aaberg, PhD Thesis, NTNU Trondheim, Trondheim, Norway (1998).
- [20] R.J. Aaberg, R. Tunold, M. Mogensen, R.W. Berg, R. Ødegård, *J. Electrochem. Soc.* **145** (1998) 2244.
- [21] S. Sunde, *J. Electrochem. Soc.* **143** (1996) 1123.
- [22] S. Sunde, *J. Electrochem. Soc.* **143** (1996) 1930.
- [23] S. Sunde, *Electrochim. Acta.* **42** (1997) 2637.
- [24] B.C.H. Steele, P.H. Middleton, R.A. Rudkin, *Solid State Ionics* **40/41** (1990) 388.
- [25] R.T. Baker, I.S. Metcalfe, P.H. Middleton, B.C.H. Steele, *Solid State Ionics* **72** (1994) 328.
- [26] I.S. Metcalfe, P.H. Middleton, P. Petrolekas, B.C.H. Steele, *Solid State Ionics* **57** (1992) 257.
- [27] J.T.S Irvine, D.P. Fagg, J. Labrincha, F.M.B. Marques, *Catal. Today* **38** (1997) 467.
- [28] P.R. Slater, D.P. Fagg, J.T.S. Irvine, *J. Mater. Chem.* **7** (1997) 2495.
- [29] D.M. Flot, J.T.S. Irvine, *Ionics* **4** (1998) 175.
- [30] A. Kaiser, A.J. Feighery, D.P. Fagg, J.T.S. Irvine, *Ionics* **4** (1998) 215.
- [31] C.M. Finnerty, R.H. Cunningham, K. Kendall, R.M. Ormerod, *Chem. Comm.* (1998) 915.
- [32] C.M. Finnerty, N.J. Coe, R.H. Cunningham, R.M. Ormerod, *Catal. Today* **46** (1998) 137.
- [33] P. Holtappels, L.G.J. de Haart, U. Stimming, *J. Electrochem. Soc.* **146** (1999) 1620.
- [34] P. Holtappels, L.G.J. de Haart, U. Stimming, *J. Electrochem. Soc.* **146** (1999) 2976.
- [35] J. Divisek, A. Kornyshev, W. Lehnert, U. Stimming, I.C. Vinke, K. Wippermann, Proc. of the 5th Intern. Symp. on Solid Oxide Fuel Cells (SOFC-V), Aachen, Germany, Eds.: U. Stimming, S.C. Singhal, H. Tagawa, W. Lehnert (1997) 606.
- [36] J. Divisek, L.G.J. de Haart, P. Holtappels, T. Lennartz, W. Mallener, U. Stimming, K. Wippermann, *J. Power Sources* **49** (1994) 257.
- [37] J. Divisek, L.G.J. de Haart, P. Holtappels, U. Stimming, I.C. Vinke, Proc. of the 17th Risø Intern. Symp. on Mat. Sci.: High Temperature Electrochemistry: Ceramics and Metals, Eds.: F.W. Poulsen, N. Bonanos, S. Linderoth, M. Mogensen, B. Zachau-Christiansen, Risø National Laboratory, Roskilde, Denmark (1996) 235.
- [38] K. Wippermann, Materials and Mechanisms: 12th SOFC Workshop, Wadahl, Norway, Ed.: K. Nisanciogly (1999) 31.
- [39] I. Drescher, W. Lehnert, J. Meusinger, *Electrochim. Acta* **43** (1998) 3059.
- [40] D. Simwonis, A. Naoumidis, F.J. Dias, J. Linke, A. Moropoulou, *J. Mater. Res.* **12** (1997) 1508.
- [41] L.G.J. de Haart, K. Mayer, U. Stimming, I.C. Vinke, *J. Power Sources* **71** (1998) 302.

- [42] P. Holtappels, L.G.J. de Haart, U. Stimming, I.C. Vinke, M. Mogensen, *J. Appl. Electrochem.* **29** (1999) 561.
- [43] J. Divisek, R. Wilkenhöfner, Y. Volfkovich, *J. Appl. Electrochem.* **29** (1999) 153.
- [44] J. Divisek, R. Jung, I.C. Vinke, *J. Appl. Electrochem.* **29** (1999) 165.
- [45] J. Abel, A.A. Kornyshev, W. Lehnert, *J. Electrochem. Soc.* **144** (1997) 4253.
- [46] A. Isoelevich, A.A. Kornyshev, W. Lehnert, *Solid State Ionics* **124** (1999) 221.
- [47] A. Isoelevich, A.A. Kornyshev, W. Lehnert, *J. Electrochem. Soc.* **144** (1997) 3010.
- [48] A. Naoumidis, Patentschrift DE 43 40 486 C1 (1995).
- [49] W. Lehnert, J. Meusinger, F. Thom, *J. Power Sources* **87** (2000) 57.
- [50] F. Tietz, F.J. Dias, D. Simwonis, D. Stöver, *J. Europ. Ceram. Soc.* **20** (2000) 1023.
- [51] A. Müller, H. Schichlein, M. Feuerstein, A. Weber, A. Krügel, E. Ivers-Tiffée, Proc. of the 6th Intern. Symp. on Solid Oxide Fuel Cells (SOFC-VI), Honolulu, Hawaii, USA, Eds.: S.C. Singhal, M. Dokiya (1999) 925.
- [52] H. Schichlein, M. Feuerstein, A. Müller, A. Weber, A. Krügel, E. Ivers-Tiffée, Proc. of the 6th Intern. Symp. on Solid Oxide Fuel Cells (SOFC-VI), Honolulu, Hawaii, USA, Eds.: S.C. Singhal, M. Dokiya (1999) 1069.
- [53] A. Müller, D. Herbstritt, A. Weber, E. Ivers-Tiffée, Proc. of the 4th Europ. Fuel Cell Forum, Lucerne, Switzerland, Ed.: A.J. McEvoy (2000) 579.
- [54] P. Ekanayake, M. Gödickemeier, L.J. Gauckler, Proc. of the 5th Asian Conf. on Solid State Ionics: New Developments, Eds.: B.V.R. Chowdari, M.A.K.L. Dissanayake, M.A. Careem, World Scientific Publishing, Singapore (1996) 535.
- [55] P. Ekanayake, M. Gödickemeier, L.J. Gauckler, Proc. of the 5th Asian Conf. on Solid State Ionics: New Developments, Eds.: B.V.R. Chowdari, M.A.K.L. Dissanayake, M.A. Careem, World Scientific Publishing, Singapore (1996) 417.
- [56] A. Bieberle, L.J. Gauckler, *Solid State Ionics* **135** (2000) 337.
- [57] A. Bieberle, L.J. Gauckler, Proc. of the 6th Intern. Symp. on Solid Oxide Fuel Cells (SOFC-VI), Honolulu, Hawaii, USA, Eds.: S.C. Singhal, M. Dokiya (1999) 549.
- [58] A. Bieberle, L.J. Gauckler, Proc. of the 4th Europ. Fuel Cell Forum, Lucerne, Switzerland, Ed.: A.J. McEvoy (2000) 305.
- [59] K. R. Thampi, A.J. McEvoy, J. Van herle, *J. Electrochem. Soc.* **142** (1995) 504.
- [60] J. Van herle, R. Ihringer, A.J. McEvoy, Proc. of the 5th Intern. Symp. on Solid Oxide Fuel Cells (SOFC-V), Aachen, Germany, Eds.: U. Stimming, S.C. Singhal, H. Tagawa, Lehnert (1997) 565.
- [61] P. Costamagna, E. Arato, P.L. Antonucci, V. Antonucci, *Chem. Eng. Sci.* **51** (1996) 3013.
- [62] P. Costamagna, P. Costa, E. Arato, *Electrochim. Acta* **43** (1998) 967.
- [63] T. Kawada, N. Sakai, H. Yokokawa, M. Dokiya, M. Mori, T. Iwata, *Solid State Ionics* **40/41** (1990) 402.
- [64] T. Kawada, N. Sakai, H. Yokokawa, M. Dokiya, M. Mori, T. Iwata, *J. Electrochem. Soc.* **137** (1990) 3042.

-
- [65] T. Kawada, B.A. van Hassel, T. Horita, N. Sakai, H. Yokokawa, M. Dokiya, *Solid State Ionics* **70/71** (1994) 65.
- [66] T. Horita, N. Sakai, H. Yokokawa, M. Dokiya, T. Kawada, *Solid State Ionics* **86-88** (1996) 1259.
- [67] J. Mizusaki, H. Tagawa, K. Isobe, M. Tajika, I. Koshiro, H. Maruyama, K. Hirano, *J. Electrochem. Soc.* **141** (1994) 1674.
- [68] J. Mizusaki, H. Tagawa, T. Saito, T. Yamamura, K. Kamitani, K. Hirano, S. Ehara, T. Takagi, T. Hikita, M. Ippomatsu, S. Nakagawa, K. Hashimoto, *Solid State Ionics* **70/71** (1994) 52.
- [69] J. Mizusaki, H. Tagawa, Y. Miyaki, S. Yamauchi, K. Fueki, I. Koshiro, K. Hirano, *Solid State Ionics* **53-56** (1992) 126.
- [70] J. Mizusaki, H. Tagawa, T. Saito, K. Kamitani, T. Yamamura, K. Hirano, S. Ehara, T. Takagi, T. Hikita, M. Ippomatsu, S. Nakagawa, K. Hashimoto, *J. Electrochem. Soc.* **141** (1994) 2129.
- [71] J. Mizusaki, T. Yamamura, N. Mori, H. Tagawa, K. Hirano, S. Ehara, T. Takagi, M. Hishinuma, H. Sasaki, T. Sogi, Y. Nakamura, K. Hashimoto, Proc. of the 17th Risø Intern. Symp. on Mat. Sci.: High Temperature Electrochemistry: Ceramics and Metals, Eds.: F.W. Poulsen, N. Bonanos, S. Linderoth, M. Mogensen, B. Zachau-Christiansen, Risø National Laboratory, Roskilde, Denmark (1996) 363.
- [72] T. Yamamura, H. Tagawa, T. Saito, J. Mizusaki, K. Kamitani, K. Hirano, S. Ehara, T. Takagi, Y. Hishinuma, H. Sasaki, T. Sodi, Y. Nakamura, K. Hashimoto, Proc. of the 4th Intern. Symp. on Solid Oxide Fuel Cells (SOFC-IV), Yokohama, Japan, Eds.: M. Dokiya, O. Yamamoto, H. Tagawa, S.C. Singhal (1995) 741.
- [73] S. Onuma, A. Kaimai, K. Kawamura, Y. Nigara, T. Kawada, J. Mizusaki, H. Inaba, H. Tagawa, *J. Electrochem. Soc.* **145** (1998) 920.
- [74] S. Onuma, A. Kaimai, K. Kawamura, Y. Nigara, T. Kawada, J. Mizusaki, H. Inaba, H. Tagawa, *J. Electrochem. Soc.* **145** (1998) 3117.
- [75] H. Uchida, H. Suzuki, M. Watanabe, *J. Electrochem. Soc.* **145** (1998) 615.
- [76] H. Uchida, T. Osuga, M. Watanabe, *J. Electrochem. Soc.* **146** (1999) 1677.
- [77] H. Itho, T. Yamamoto, M. Mori, T. Watanabe, T. Abe, *Denki Kagaku* **64** (1996) 549.
- [78] H. Uchida, M. Yoshida, M. Watanabe, *J. Phys. Chem.* **99** (1995) 3282.
- [79] M. Watanabe, H. Uchida, M. Yoshida, *J. Electrochem. Soc.* **144** (1997) 1739.
- [80] M. Watanabe, H. Uchida, M. Shibata, N. Mochizuki, K. Amikuta, *J. Electrochem. Soc.* **141** (1994) 342.
- [81] M.J. Saeki, H. Uchida, M. Watanabe, *Catal. Lett.* **26** (1994) 149.
- [82] N. Nakagawa, H. Sakurai, K. Kondo, T. Morimoto, K. Hatanaka, K. Kato, *J. Electrochem. Soc.* **142** (1995) 3474.
- [83] N. Nakagawa, K. Kato, *Solid State Ionics* **98** (1997) 209.
- [84] N. Nakagawa, K. Nakajima, M. Sato, K. Kato, *J. Electrochem. Soc.* **146** (1999) 1290.
- [85] T. Setoguchi, K. Okamoto, K. Eguchi, H. Arai, *J. Electrochem. Soc.* **139** (1992) 2875.
- [86] K. Eguchi, Y. Kunisa, K. Adachi, H. Arai, *J. Electrochem. Soc.* **143** (1996) 3699.

- [87] K. Eguchi, Y. Kunisa, K. Adachi, M. Kayano, K. Sekizawa, H. Arai, *Chem. Lett.* **9** (1995) 963.
- [88] K. Eguchi, *J. Alloys and Comp.* **250** (1997) 486.
- [89] H. Mitsuyasu, Y. Nonaka, K. Eguchi, H. Arai, *J. Solid State Chem.* **129** (1997) 74.
- [90] T. Fukui, S. Ohara, K. Mukai, *Electrochem. Solid State Lett.* **1** (1998) 120.
- [91] R. Maric, S. Ohara, T. Fukui, T. Inagaki, J. Fujita, *Electrochem. Solid State Lett.* **1** (1998) 201.
- [92] S. Ohara, R. Maric, X. Zhang, K. Mukai, T. Fukui, H. Yoshida, T. Inagaki, K. Miura, *J. Power Sources* **86** (2000) 455.
- [93] X. Zhang, S. Ohara, R. Maric, K. Mukai, T. Fukui, H. Yoshida, M. Nishimura, T. Inagaki, K. Miura, *J. Power Sources* **83** (1999) 170.
- [94] C. Wen, R. Kato, H. Fukunaga, H. Ishitani, K. Yamada, *J. Electrochem. Soc.* **147** (2000) 2076.
- [95] M. Ihara, C. Yokoyama, A. Abudula, R. Kato, H. Komiyama, K. Yamada, *J. Electrochem. Soc.* **146** (1999) 2481.
- [96] A. Abudula, M. Ihara, R. Kato, K. Sakai, H. Komiyama, K. Yamada, *Denki Kagaku* **65** (1997) 852.
- [97] A. Abudula, T. Aida, H. Komiyama, K. Yamada, *Denki Kagaku.* **63** (1995) 852.
- [98] A. Abudula, M. Ihara, H. Komiyama, K. Yamada, *Solid State Ionics* **86-88** (1996) 1203.
- [99] T. Tsai, S.A. Barnett, *J. Electrochem. Soc.* **145** (1998) 1696.
- [100] E. Perry Murray, T. Tsai, S.A. Barnett, *Nature* **400** (1999) 649.
- [101] T. Tsai, S.A. Barnett, *Solid State Ionics* **98** (1997) 191.
- [102] R. Craciun, S. Park, R.J. Gorte, J.M. Vohs, C. Wang, W.L. Worrell, *J. Electrochem. Soc.* **146** (1999) 4019.
- [103] S. Park, R. Craciun, J.M. Vohs, R.J. Gorte, *J. Electrochem. Soc.* **146** (1999) 3603.
- [104] E.S. Putna, J. Stubenrauch, J.M. Vohs, R.J. Gorte, *Langmuir* **11** (1995) 4832.
- [105] S.P. Jiang, S.P.S. Badwal, *J. Electrochem. Soc.* **144** (1997) 3777.
- [106] S.P. Jiang, S.P.S. Badwal, *Solid State Ionics* **123** (1999) 209.
- [107] S.P. Jiang, S.P.S. Badwal, *Solid State Ionics* **122** (1999) 211.
- [108] R. Diethelm, M. Schmidt, K. Honegger, E. Batawi, Proc. of the 6th Intern. Symp. on Solid Oxide Fuel Cells (SOFC-VI), Honolulu, Hawaii, USA, Eds.: S.C. Singhal, M. Dokiya, The Electrochemical Society, Inc., Pennington, NJ, USA(1999) 60.
- [109] S.C. Singhal, Proc. of the 6th Intern. Symposium on Solid Oxide Fuel Cells (SOFC-VI), Honolulu, Hawaii, USA, Eds.: S.C. Singhal, M. Dokiya, The Electrochemical Society, Inc., Pennington, NJ, USA(1999) 39.
- [110] R. Bolden, K. Föger, T. Pham, Proc. of the 6th Intern. Symp. on Solid Oxide Fuel Cells (SOFC-VI), Honolulu, Hawaii, USA, Eds.: S.C. Singhal, M. Dokiya, The Electrochemical Society, Inc., Pennington, NJ, USA(1999) 80.
- [111] H. Mori, H. Omura, N. Hisatome, K. Ikeda, K. Tomidal, Proc. of the 6th Intern. Symp. on Solid Oxide Fuel Cells (SOFC-VI), Honolulu, Hawaii, USA, Eds.: S.C. Singhal, M. Dokiya, The Electrochemical Society, Inc., Pennington, NJ, USA (1999) 52.

-
- [112] G.A. Tompsett, M.S. Brown, C. Finnerty, N.M. Sammes, K. Kendall, Proc. of the 4th Europ. Fuel Cell Forum, Lucerne, Switzerland, Ed.: A.J. McEvoy (2000) 13.
- [113] D. Ghosh, G. Wang, R. Brule, E. Tang, P. Huang, Proc. of the 6th Intern. Symp. on Solid Oxide Fuel Cells (SOFC-VI), Honolulu, Hawaii, USA, Eds.: S.C. Singhal, M. Dokiya, The Electrochemical Society, Inc., Pennington, NJ, USA (1999) 822.
- [114] M.T. Colomer, J.R. Jurado, *J. Europ. Ceram. Soc.* **19** (1999) 143.
- [115] J. Sfeir, J. Van herle, A.J. McEvoy, Proc. of the 3rd Europ. Fuel Cell Forum, Nantes, France, Ed.: P. Stevens (1998) 267.
- [116] A.-L. Sauvet, J. Guindet, J. Fouletier, *Ionics* **5** (1999) 150.
- [117] S. Wang, Y. Jiang, Y. Zhang, W. Li, J. Yan, Z. Lu, *Solid State Ionics* **120** (1999) 75.
- [118] T. Iwata, *J. Electrochem. Soc.* **143** (1996) 1521.
- [119] H. Itoh, T. Yamamoto, M. Mori, T. Watanabe, *Denki Kagaku* **64** (1996) 549.
- [120] M. Suzuki, H. Sasaki, S. Otsoshi, A. Kajimura, M. Ippommatsu, *Solid State Ionics* **62** (1993) 125.
- [121] S. Skaarup, B. Zachau-Christiansen, T. Jacobsen, Proc. of the 17th Risø Intern. Symp. on Mat. Sci.: High Temperature Electrochemistry: Ceramics and Metals, Eds.: F.W. Poulsen, N. Bonanos, S. Linderoth, M. Mogensen, B. Zachau-Christiansen, Risø National Laboratory, Roskilde, Denmark (1996) 423.
- [122] T. Norby, O.J. Velle, H. Leth-Olsen, R. Tundold, Proc. of the 3rd Intern. Symp. on Solid Oxide Fuel Cells (SOFC-III), Honolulu, Hawaii, USA, Eds.: S.C. Singhal, H. Iwahara, The Electrochemical Society, Inc., Pennington, NJ, USA (1993) 473.
- [123] T. Norby, P. Kofstad, Proc. of the 17th Risø Intern. Symp. on Mat. Sci.: High Temperature Electrochemistry: Ceramics and Metals, Eds.: F.W. Poulsen, N. Bonanos, S. Linderoth, M. Mogensen, B. Zachau-Christiansen, Risø National Laboratory, Roskilde, Denmark (1996) 381.
- [124] F.Z. Mohamedi-Boulenouar, J. Guindet, A. Hammou, Proc. of the 5th Intern. Symp. on Solid Oxide Fuel Cells (SOFC-V), Aachen, Germany, Eds.: U. Stimming, S.C. Singhal, H. Tagawa, W. Lehnert, The Electrochemical Society, Inc., Pennington, NJ, USA (1997) 441.
- [125] J.R. Macdonald, "Impedance Spectroscopy", John Wiley & Sons, Inc., New York, NY, USA (1987).
- [126] M. Sluyters-Rehbach, J.H. Sluyters, in: Comprehensive Treatise of Electrochemistry, Vol. 9, Eds.: E. Yeager, J. O'M. Bockris, B.E. Conway, S. Saranagapani, Plenum Press, New York, NY, USA (1984) 177.
- [127] M. Sluyters-Rehbach, J.H. Sluyters, in: Electroanalytical Chemistry, A Series of Advances, Vol. 4, Eds.: A.J. Bard, Marcel Dekker, New York, NY, USA (1970) 1.
- [128] K.J. Vetter, "Elektrochemische Kinetik", Springer Verlag, Berlin, Germany (1961).
- [129] J. Maier, "Festkörper - Fehler und Funktion", Teubner Studienbücher, Stuttgart, Germany (2000) 457.
- [130] C.H. Hamann, W. Vielstich, "Elektrochemie", Wiley-VCH, Weinheim, Germany (1998) 271.
- [131] "ZAHNER[®] Messtechnik - Owner's Manual", Version: Thales IM6, ZAHNER[®] Elektrik, Kronach, Germany (2000).

Chapter 2 ^{*)}

The State-Space Modeling Approach

Abstract

The kinetics of SOFC electrodes are in great demand today, since a better understanding of the electrochemistry is vital for an improvement of the performance of SOFC electrodes. In this chapter, a new approach focusing on the identification of the reaction mechanisms at electrochemical interfaces is described. It is based on state-space modeling (SSM) which is an approach used in control theory for the simulation of coupled differential equations. Here, the state-space modeling approach consists of a combination of modeling, simulations, and experiments. It is explained in a general way in this chapter. Subsequent chapters of the thesis (chapters 3 - 5) consider different parts of the approach in terms of the anodic SOFC system from the experimental as well as from the simulation side. In the end of this chapter, we focus shortly on applications to SOFC systems.

^{*)} revised version of the Proceeding of the 12th SOFC Workshop: Materials and Mechanisms, IEA Program of R&D on Advanced Fuel Cells, Ed.: K. Nisancioglu, Wadahl, Norway (1999) 39.

2.1 Introduction

Many studies in the field of solid oxide fuel cells (SOFC) are concerned with the selection of electrode materials with high performance. It is found that $\text{La}_{(1-x)}\text{Sr}_x\text{MnO}_3$ (LSM) and Ni-YSZ cermet are the most suitable cathode and anode materials on zirconia electrolytes today. However, the losses at the electrodes are still a considerable part of the total losses in SOFCs. Hence, further improvement of the electrodes is desirable and demands a thorough understanding of the electrode kinetics down to an atomistic level. A useful method to gain insight into the limitations of the electrode kinetics is electrochemical impedance spectroscopy (EIS). Even though EIS is a common method for the investigation of the electrochemistry, it is so far not possible to interpret the experimental data, i.e. the impedance spectra, unambiguously. The spectra are usually fitted to equivalent circuits where a net of resistances, capacitances, and inductances is assumed [1-3]. However, it is difficult to relate the equivalent circuit elements to the electrochemistry of the system. The physical and the chemical meaning of the single elements is not clear.

In order to obtain a better understanding of the electrochemical behavior of SOFC electrodes, we developed a new approach with the aim to correlate directly the experimental EIS data with the chemical and the electrochemical equations characterizing the system. Due to the geometrical complexity of the state-of-the-art electrodes (LSM, Ni-YSZ), simplified model electrode systems, i.e. metal, gas | YSZ systems, are studied at first. The simulations are based on a state-space model (SSM), a denotation which is well-known from control theory. The entire approach which consists of experiments, modeling, and simulations, is called state-space modeling approach. The approach will be described in general in this chapter. Some details concerning the application to SOFC systems will be addressed in the last subsection. For more detailed information on the mathematics, the interested reader is referred to the fundamental literature [4-7].

2.2 The State-Space Modeling Approach

The state-space modeling approach for the identification of the reaction mechanisms at SOFC electrodes is based on a combination of experiments, modeling, and simulations. The approach is not specific for a certain materials system, but can, in principle, be adopted to all electrochemical interfaces. Hence, the ap-

proach is described in a general way in the following subsections. The scheme of the approach is summarized in Fig. 2.1.

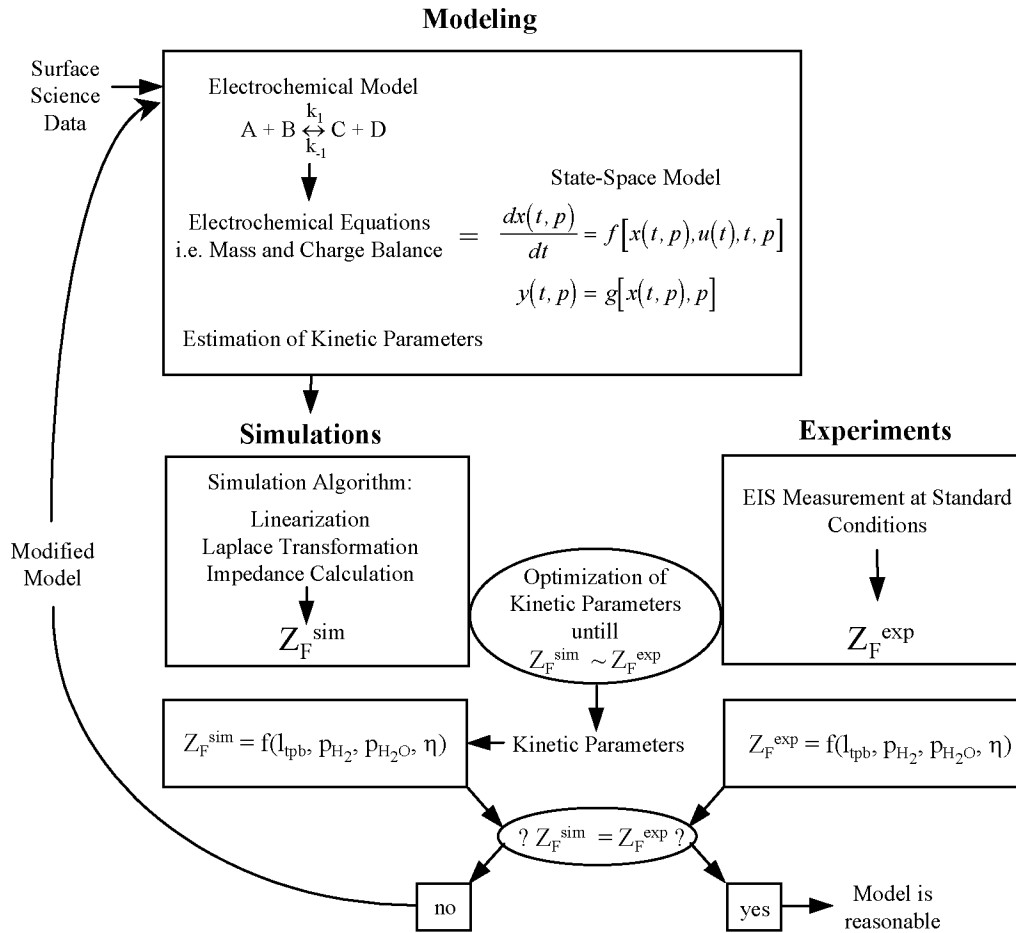


Fig. 2.1: State-Space Modeling (SSM) approach for the investigation of the reaction mechanisms at SOFC electrodes.

2.2.1 Surface Science Data

From surface science literature, data is extracted which allows the prediction of the main reaction steps that might take place at the electrochemically active interface. In SOFC literature, this electrochemically active interface is called the triple phase boundary (TPB), since the three phases, the electrode, the electrolyte, and the pores, are connected here. The main task of this part of the work is to find surface chemistry data which is relevant for the conditions that exist at the electrode: atmospheric pressure and high temperature (873 K - 1273 K). However, most data on the systems of interest, especially in the case of Ni, H_2 - H_2O , is

available only at low temperature (300 K) [8-10]. This impedes the establishment of an electrochemical model.

Besides the main reaction steps, the surface science literature is also a source of kinetic data, such as the reaction rate constants and the surface coverages of the adsorbed species, as well as sticking, adsorption, desorption, and surface diffusion coefficients.

2.2.2 Modeling

The electrochemical model consists of a set of possible chemical and electrochemical reactions that are derived from the relevant surface science literature. These reactions are of the following form



where A , B , C , and D are gas phase species, surface species, adsorption sites, or electrons; k_1 and k_{-1} are the reaction rate constants for the forward and the backward reaction, respectively. In order to establish an electrochemical model which describes the entire system, several assumptions have to be taken into consideration. For instance, the number and the kind of surface species, their diffusion and their reaction behavior have to be estimated. As many of the kinetic constants are not known from the literature, it is necessary to estimate the unknown kinetic constants. Detailed information is given in [4] for the cathodic system Pt, O₂ | YSZ, and in chapter 5 for the anodic system Ni, H₂ - H₂O | YSZ, respectively.

The chemical and the electrochemical equations of the electrochemical model can be formulated as mass and charge balance [11,12]. The mass balance concerning the time-dependent surface species C in Eq. 2.1 is given as

$$[\dot{C}] = \frac{d[C]}{dt} = k_1 \cdot [A] \cdot [B] - k_{-1} \cdot [C] \cdot [D]. \quad (2.2)$$

In the case of several parallel and consecutive reactions as well as several surface species, a whole system of coupled differential equations results. The system becomes very complex and cannot be solved analytically anymore. For a numerical solution, the electrochemical model must be written in a form that can be

used for computer analysis. Here, Eq. 2.2 is suggestive of the well-known state-space model used in control theory [13,14]. The state-space model is believed to be the most reliable linear time-dependent model used for computer analysis. The general state-space representation is formulated as

$$\dot{\mathbf{x}}(t, \mathbf{p}) = \frac{d\mathbf{x}(t, \mathbf{p})}{dt} = \mathbf{f}[\mathbf{x}(t, \mathbf{p}), \mathbf{u}(t), t, \mathbf{p}] \quad (2.3)$$

where $\mathbf{x}(t, \mathbf{p})$ represents the vector of the state-variables depending on the time, t , and on the vector of the unknown parameters, \mathbf{p} . The vector $\mathbf{u}(t)$ signifies the input variables that can be varied in the experiment and in the simulations.

In addition to the differential equations (Eq. 2.3), the state-space description contains the observation function $\mathbf{y}(t, \mathbf{p})$ which denotes the observed quantities and is referred to as the model output

$$\mathbf{y}(t, \mathbf{p}) = \mathbf{g}[\mathbf{x}(t, \mathbf{p}), \mathbf{p}] \quad (2.4)$$

The variables in the general state-space model can be directly interpreted in terms of the kinetic variables used in the electrochemical model: The vector of state-variables, $\mathbf{x}(t, \mathbf{p})$, represents the surface concentrations of the different adsorbed species. The concentration of the adsorbed species is a function of the time, t , and the vector of unknown parameters, \mathbf{p} , i.e. the reaction rate constants and the surface coverage values. The vector $\mathbf{u}(t)$ signifies the overpotential, η , and the model output, $\mathbf{y}(t, \mathbf{p})$, can be interpreted as the Faraday current, I_F .

2.2.3 Simulations

Having established an electrochemical model for the system, it is now required to implement the system into the computer. An impedance spectrum, Z_F^{sim} , can then be simulated and can be compared to the experimental EIS data, Z_F^{exp} . The simulations are carried out using the computer program MATLAB[®] with the graphical programming extension SIMULINK[™] which is used in control theory for simulations of dynamic systems.

SIMULINK[™] is designed as a unit construction system. The mathematical equations are built from construction blocks given in the program. An illustrative example is shown in Fig. 2.2 where the computer implementation for the calcula-

tion of the surface concentration C according to Eq. 2.2 is illustrated. The concentrations A , B , and D are assumed to be constant and are illustrated as boxes in Fig. 2.2. The triangles containing k_1 and k_{-1} represent multiplications, whereas the program element $1/s$ stands for the integration of a Laplace transformed variable. The output is shown in the display box and represents, in this example, the concentration of the surface species C .

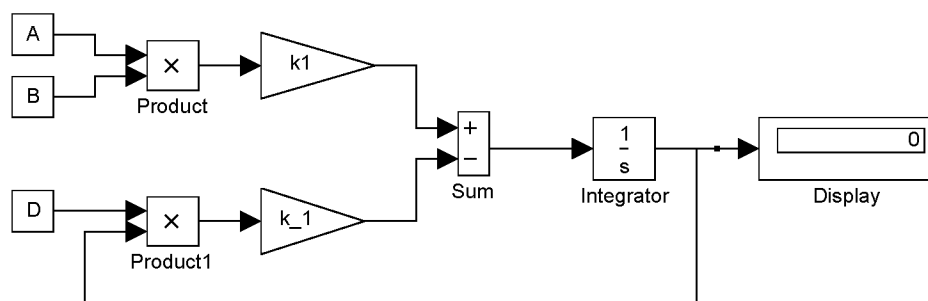


Fig. 2.2: SIMULINK™ implementation of Eq. 2.2 concerning C as time-dependent surface concentration before Laplace transformation:

$$C(t) = \int (k_1 \cdot [A] \cdot [B] - k_{-1} \cdot [C] \cdot [D]) dt .$$

Since, a real electrode system consists of several chemical and electrochemical reactions which occur simultaneously and consecutively at different locations of the anode, the SIMULINK™ diagrams become more complex than the one shown in Fig. 2.2. For this reason, single SIMULINK™ systems, such as the one in Fig. 2.2, can be grouped into subsystems which are then connected among each other. When surface diffusion effects are additionally implemented, the electrochemically active area of the electrode near the triple phase boundary is structured in different compartments meaning that a finite element analysis (FEM) is superimposed on the simulation procedure. The differential equations are solved for each compartment using the proper boundary conditions.

The SIMULINK™ diagrams are not only used for the calculation of surface concentrations; they represent a general graphical formulation of the differential equations of the kinetics of the system. The diagrams are called in MATLAB® each time when a command refers to the differential equations. The commands for the calculation of the impedance Z_F^{sim} are programmed in MATLAB®. In a first step, the electrochemical model is linearized. Afterwards, a Laplace transformation takes place in order to transfer the system into the frequency domain. A

special command in MATLAB[®] allows then directly the calculation of the impedance. An illustrative example for the implementation of an electrochemical model and the calculation of the impedance including the SIMULINK[™] diagrams and the MATLAB[®] commands is given in [7].

2.2.4 Experiments

Impedance measurements of SOFC electrodes are carried out under usual operating conditions of a fuel cell, i.e. atmospheric pressure and high temperature. The two electrodes, the anode and the cathode, are measured separately so that unique information on the two electrodes is obtained. General information on electrode measurements and the characteristic parameters which are analyzed in this study, is given in chapter 1 (subsection 1.2). The experimental conditions and the set-up for EIS measurements of SOFC anodes are described in detail in chapter 3 (subsection 3.2.2) as well as in appendix 2.

The experimental impedance data is measured under standard conditions and as a function of specific parameters, such as the TPB length, the gas composition, the overpotential, and the temperature. Standard conditions signify the usual operating conditions in the experiments, i.e. $p(\text{H}_2) = 2.5 \cdot 10^4 \text{ Pa}$, $p(\text{H}_2\text{O}) = 4 \cdot 10^1 \text{ Pa}$, $T = 973 \text{ K}$, $\eta = 0 \text{ mV}$, and $10^{-3} \text{ Hz} < \omega < 10^3 \text{ Hz}$ for the Ni, $\text{H}_2 - \text{H}_2\text{O} \mid \text{YSZ}$ system.

It should be noted that the measured impedance, Z^{exp} , does not give directly an answer to the mass and charge balances such as described in Eq. 2.2. As elaborated in detail by Berthier [15], the electrochemically relevant impedance of the electrode, the Faraday impedance, $Z_{\text{F}}^{\text{exp}}$, is obscured by contributions from the electrolyte and from the interface of the electrode and the electrolyte. The contribution from the electrolyte is purely ohmic and can be described in equivalent circuit notation by a resistance, i.e. the electrolyte resistance, R_{e} . The interface between the electrode and the electrolyte can best be illustrated by a capacitance, the so-called double layer capacitance, C_{dl} . The interrelation of the different contributions is shown in form of an equivalent circuit model in Fig. 2.3. In order to compare the experimental to the simulated data, the experimentally determined impedance data, Z^{exp} , must be corrected for R_{e} and C_{dl} .

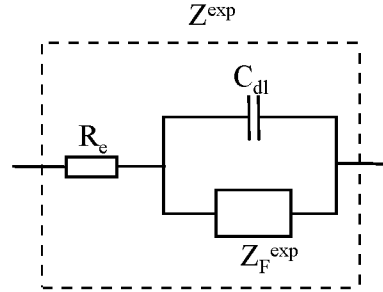


Fig. 2.3: Equivalent circuit model of a metal, gas | electrolyte system [15].

2.2.5 The Kinetics of the System

The kinetics of the electrochemical system are investigated by a combination of the simulations described in subsection 2.2.3 and the experiments described in subsection 2.2.4. According to Fig. 2.1, the kinetic parameters, i.e. the reaction rate constants, k , and the fractions of surface coverage, θ , are determined by an optimization procedure of the electrochemical model and an experimental impedance spectrum, Z_F^{exp} , under standard experimental conditions. The optimization procedure is terminated when $Z_F^{sim} = Z_F^{exp}$. This includes that the number and the characteristic frequencies of the relaxation processes correspond, the polarization resistance, i.e. the low frequency intercept of the impedance data in the Nyquist plot, as well as the distribution of the discrete data points are as similar as possible. A combination of the three impedance plots, i.e. $-Z'$ vs. Z' , $|Z|$ vs. ω , and Φ vs. ω , gives the best evidence for a suitable fit. This part of the work is one of the most important and time consuming tasks, since the quality of the kinetic parameters strongly affects the further simulations.

After the optimization procedure, the kinetic parameters, i.e. the reaction rate constants and the surface coverages are closely examined. Only if reasonable values are found, the fit is considered as good and the optimization procedure is terminated. Impedance spectra are then simulated as a function of the TPB length, the fuel gas composition, the overpotential, and the temperature. The results are compared with the experimental data under the same conditions. If the simulated and the experimental impedance spectra behave in the same way, it is assumed that the electrochemical model might describe the kinetics of the system correctly. If major differences are identified, either the kinetic parameters or the electrochemical model have to be modified.

2.3 Application to SOFC Systems

The main difficulty with transferring the general SSM approach into practice is the electrochemistry which is not well understood for SOFC electrodes. As the electrochemical mechanisms are very complicated and not well-known so far, simplified electrode systems are considered to start with. The systems consist of metal electrodes, i.e. Pt as cathode or Ni as anode, in contact with a YSZ single crystalline electrolyte and the corresponding gas atmosphere, i.e. O_2 for the cathode and $H_2 - H_2O$ for the anode.

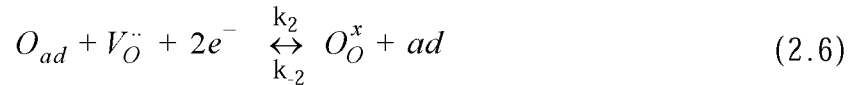
2.3.1 The Pt, O_2 | YSZ System

This system is rather well described in the literature and has been investigated experimentally as well as theoretically [16-18]. The SSM approach was first used for this system [4-7]. The following reaction mechanism is considered:

dissociative adsorption/desorption of oxygen:



incorporation/removal of oxygen from the electrolyte:



surface diffusion:

$$J = -D(\theta) \cdot \nabla c \quad (2.7)$$

Five unknown kinetic parameters have been estimated from EIS measurements by numerical optimization. It is found that the sensitivity of the Faraday impedance with respect to the unknown parameters is high and that the estimated parameters are in excellent agreement with the data from the literature. The rates for the adsorption and for the desorption of oxygen on Pt depend strongly on the surface coverage of oxygen on Pt.

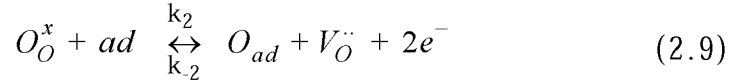
2.3.2 The Ni, H₂ - H₂O | YSZ System

The anodic SOFC system is much more complicated than the cathodic system because of many parallel reactions and several time-dependent surface species. The literature does not provide sufficient information about the system at high temperature and atmospheric pressure. From low pressure systems and from other material systems, such as Pt, H₂ - H₂O, the following electrochemical model is assumed [19]

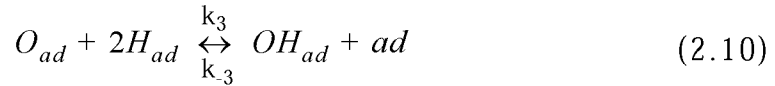
dissociative adsorption of hydrogen:



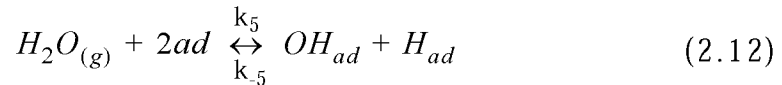
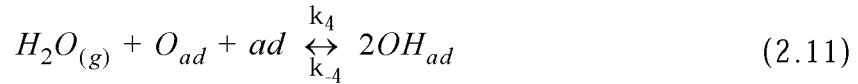
removal of oxygen from the electrolyte:



formation of hydroxyl:



dissociative adsorption of water/recombination of hydroxyl:



where *ad* signifies free adsorption sites. Hydrogen, oxygen, water, and hydroxyl are considered as time-dependent surface species in the dynamic system. They may have a specific charge which is not considered here. It is assumed that the removal of oxygen from the YSZ electrolyte is the only charge transfer reaction. No diffusion effects are included in the model, since no experimental evidence for diffusion effects exists in the Ni, H₂ - H₂O | YSZ system.

According to the four time-dependent surface species (H_{ad}, OH_{ad}, H₂O_{ad}, O_{ad}), the entire system consists of four differential equations that have to be fitted to the experimentally determined Faraday impedance. From the 10 rate constants

of the five chemical and electrochemical equations only two, i.e. the adsorption and the desorption coefficients of hydrogen, are known exactly at 973 K and atmospheric pressure. The rate constants k_2 and k_{-2} are related to one another [7]. Hence, only one of the two constants is unknown. Nevertheless, there remain 7 unknown rate constants which can only roughly be estimated from the literature. In addition, surface coverage values as well as sticking coefficients are not exactly known.

2.4 Conclusions

The state-space modeling approach for the identification of reaction mechanisms of SOFC electrodes is described in a general way in this paper. The approach consists of a combination of modeling, simulations, and experiments and can be adopted to each kind of electrochemical system. Due to the direct relation of the simulated and the experimental data, this approach is superior compared to other methods concerned with the identification of the electrode kinetics. The main difficulties are related to the kinetic parameters (reaction rate constants and surface coverages) which are in most cases not straight-forwardly available from the literature. Hence, they have to be estimated by an optimization procedure. The application of the SSM approach to SOFC systems is illustrated by means of the cathodic Pt, O₂ | YSZ system and the anodic Ni, H₂ - H₂O | YSZ system.

2.5 References

- [1] S. Primdahl, M. Mogensen, *J. Electrochem. Soc.* **144** (1997) 3409.
- [2] N. Nakagawa, K. Kato, *Solid State Ionics* **98** (1997) 209.
- [3] B. de Boer, PhD Thesis, University of Twente, Twente (1998).
- [4] A. Mitterdorfer, L. J. Gauckler, *Solid State Ionics* **117** (1999) 187.
- [5] A. Mitterdorfer, L. J. Gauckler, *Solid State Ionics* **117** (1999) 203.
- [6] A. Mitterdorfer, L. J. Gauckler, *Solid State Ionics* **120** (1999) 211.
- [7] A. Mitterdorfer, PhD Thesis, ETH Zürich, Switzerland (1997).
- [8] T. N. Truong, G. Hancock, D. G. Truhlar, *Surf. Sci.* **214** (1989) 523.
- [9] R. H. Stulen, P. A. Thiel, *Surf. Sci.* **157** (1985) 99.
- [10] H. Yang, J. L. Whitten, *Surf. Sci.* **223** (1989) 131.
- [11] G. Wedler, "Lehrbuch der Physikalischen Chemie", VCH Verlagsgesellschaft, Weinheim,

- Germany (1987) 182.
- [12] M. Quack, "Molekulare Thermodynamik und Kinetik, Teil 1: Chemische Reaktionskinetik", Verlag der Fachvereine an den Schweizerischen Hochschulen und Techniken, Zürich, Switzerland (1986) 12.
- [13] T. Kailath, "Linear Systems", Prentice Hall, New York, NY, USA (1980).
- [14] G.F. Franklin, J.D. Powell, A.E. Naeini, "Feedback Control of Dynamic Systems", Addison-Wesley, Reading, MA, USA (1994).
- [15] F. Berthier, J.-P. Diard, B. Le Gorrec, C. Montella, *Corr. Sci.* **51** (1995) 105.
- [16] J. L. Gland, B. A. Sexton, G.B. Fisher, *Surf. Sci.* **95** (1980) 587.
- [17] R. Lewis, R. Gomer, *Surf. Sci.* **12** (1968) 157.
- [18] A. N. Artsyukhovich, V. A. Ukrainsev, I. Harrison, *Surf. Sci.* **347** (1996) 303.
- [19] A. Bieberle, A. Mitterdorfer, L. J. Gauckler, Proc. of the 3rd Europ. Solid Oxide Fuel Cell Forum, Nantes, France, Ed.: P. Stevens, (1998) 19.

Chapter 3 ^{*)}

The Electrochemistry of Ni Pattern Anodes

Abstract

In order to study the reaction mechanisms at solid oxide fuel cell (SOFC) anodes, Ni pattern electrodes with well-defined triple phase boundary lengths were prepared. The anode microstructures were stable during thermal treatment and electrochemical measurements. Electrochemical impedance spectroscopy (EIS) was used in order to study the influence of the overpotential, of the gas atmosphere, of the temperature, and of the pattern geometry on the electrochemistry of the anodes. According to the impedance data, the reaction kinetics are dominated by one main process under a large range of experimental conditions. This process is thermally activated with an activation energy of $E_A = 0.88 \pm 0.04$ eV. At overpotentials higher than 300 mV, a second process becomes relevant. Variations of the concentration of hydrogen in the fuel gas atmosphere have no significant influence on the electrode behavior. Only with a diffusion barrier in combination with an applied overpotential, small diffusion effects can be observed. A catalytic effect of the partial pressure of water in the fuel gas atmosphere is observed and discussed by means of a detailed model. The direct proportionality between the relaxation frequency and the TPB length suggests a TPB limitation of the reaction mechanisms.

^{*)} This chapter has been submitted in a shorter version as A. Bieberle, L.P. Meier, L.J. Gauckler, "The Electrochemistry of Ni Pattern Anodes as Solid Oxide Fuel Cell Model Electrodes", J. Electrochem. Soc. (2000).

3.1 Introduction

Ni-YSZ cermet is the most widely used anode material in solid oxide fuel cell (SOFC) systems [1-4]. In recent years, many studies focused in detail on the improvement of the performance and of the long term stability of these anodes by optimizing their microstructure [5-7], by modifying their chemical composition [8-10], and by introducing catalytically active intermediate layers [11,12]. Thus, the anode is not the bottle neck in SOFC systems anymore. However, it is still desirable to lower the losses at the anode and to improve the long-term stability, as most anodes still suffer from long-term degradation, redox instability, sulfur poisoning, and carbon deposition. At the moment, improving the state-of-the-art Ni-YSZ anode and finding alternative anode materials is done empirically as the basic kinetics of the anodic processes are not known in detail. This is mainly due to the very complicated microstructure of Ni-YSZ with the three interpenetrating networks of Ni, YSZ, and pores. The microstructural features range from the μm to the nm dimensions and are, thus, difficult to resolve qualitatively in three dimensions. Lacking this information, it is difficult to localize the anodic reactions and to identify the rate limiting reaction steps.

Nevertheless, the kinetics of SOFC anodes are mainly studied using the before mentioned Ni-YSZ cermet material [13-26]. Significant operating parameters, such as the partial pressure of hydrogen and of water as well as the temperature, are specifically modified in order to identify the kinetics. For example, Primdahl *et al.* [16,25,26] separated the electrode mechanisms at Ni-YSZ cermet anodes into three main contributions: first, a gas conversion process at a relaxation frequency of about 1 Hz which is due to the experimental set-up when the working and the reference electrodes are placed in separate gas atmospheres [26]; second, a gas diffusion process at a relaxation frequency of about 100 Hz which is due to a stagnant gas layer of about 1 mm outside the anode structure [27]; third, a TPB related process at about 10 kHz [25]. The analysis of the different relaxation processes is strongly related to the measurement set-up and to the microstructure of the electrodes. The nature of the TPB related process which is representative for all Ni-YSZ anodes, is not discussed in detail.

An alternative approach to investigate the kinetics of SOFC anodes is to avoid the complex microstructure of Ni-YSZ cermets. The system is usually simplified by omitting the granular YSZ in the anode and by reducing the microstructure to a two dimensional one. The electrochemically active area, i.e. the so-called triple

phase boundary (TPB), is then well-defined and microstructural effects can be eliminated. Possible electrode designs are Ni pattern anodes [28-31], Ni point anodes [14,32-34], and porous Ni anodes [25,31,35-38]. Each of these anode designs is briefly discussed in the following. The characteristic data related to the electrochemistry is summarized in Tab. 3.1.

Ni pattern anodes are microstructured Ni layers on top of the electrolyte material. For this anode design, one rate determining reaction step was identified [28-31]. According to Mizusaki *et al.* [28-30,39], the nature of the rate determining step is either an adsorption or a diffusion process which is supposed to take place on the Ni surface. A charge transfer process was, in contrast, proposed by de Boer [31]. The YSZ is attributed an active role in the electrode process [31] and it is proposed that adsorbed intermediates play an important role in the electrode kinetics. Both groups found a linear relationship between the total electrode conductivity and the TPB length. However, the absolute data scattered considerably in both studies and significant differences in the absolute data were observed as well.

Ni point anodes are usually made of a Ni wire which is pressed onto the electrolyte. Several rate controlling steps were found by electrochemical impedance spectroscopy in [33]. In general, however, the total impedance is dominated by one process which is assumed to be a chemical process, such as an adsorption or a desorption reaction. The charge transfer reaction is found to become more dominant under polarization of the electrode implying that the chemical processes at the surface are more enhanced by polarization than the charge transfer reaction [33]. The electrocatalytic effect of water on the kinetics of a Ni point anode is studied in [34]. The same reaction mechanism was found for dry and for wet fuel gas (4% - 20% H₂O). It is claimed that the reaction mechanism is not only charge transfer limited even though the data is analyzed with Tafel plots. The Ni point electrodes in [14,32] consisted of several Ni points realized by Ni wires wound around an alumina tube and pressed against an electrolyte. Comparing these multi-point electrodes to microstructured Ni anodes, it is concluded that the kinetics of Ni-YSZ anodes is limited by a too small and a too inactive surface.

Tab.3.1: Electrochemical data on simplified Ni anodes (l_{TPB} : TPB length, ω^* : relaxation frequency, E_A : activation energy, T : temperature, hf/lf: high/low frequency).

Electrode design	l_{TPB} [m/cm ²]	# EIS arcs	ω^* [Hz]	Equivalent circuit model ^{†††}	E_A [eV]	T [K]	Limitations of anode kinetics	Reference
Ni pattern	0.02-6	1	0.215	-	0.7	773-973	adsorption of H ₂ or surface diffusion of H _{ad}	[28, 29, 39]
Ni pattern	1-10	3	-	$(L_W R_e (R_1 Q_1) (R_2 Q_2) (R_3 Q_3))$	1.6	873-1123	charge transfer	[31]
Ni point	- [†]	-	1-10	$(R_{e,hf} C_{i,hf}) (R_{e,lf} (C_{dl} (R_{ct} (C_1 (R_2 L_2) R_3))))$	-	1273	adsorption/desorption	[33]
Ni point	-	1	1-1 k	$R_e (R_p Q)$	1.6	973-1273	not only charge transfer	[34]
Ni point	0.003-0.015 ^{††}	-	-	$LR_e (R_{ct} Q_{dl})$	R_{hf} 0.6 R_{lf} 1.8	823-1173	too small and inactive surface	[14, 32, 40]
Ni micro-structured	121 ^{††}	-	-	$LR_e (R_{ct} Q_{dl}) (RQ)$	0.3	973-1223	too small and inactive surface	[14, 32, 40]
Ni porous	-	2	8 k, 18 k	$R_e (R_1 Q_1) (R_2 Q_2)$	1.6	1073-1273	dry: diffusion of H _{ad} wet: adsorption/desorption	[35 ,36]
Ni porous	45-60	2-4	-	$(L_W R_e (R_1 Q_1) (R_2 Q_2))$	1.6	873-1123	$OH'_o + ad_{YSZ} \rightarrow OH^- + V''_o$	[31]
Ni porous	-	2	1, 10 k	$LR_e (R_1 Q_1) (R_2 C_2)$	1.0±0.1	973-1273	-	[25]
Ni covered with ceramic	-	1-2	10-100	$R_e (((R_1 Z_W) Z_d) C)$	0.49	973-1323	adsorption/desorption, surface diffusion	[38, 41, 42]

[†] no data available

^{††} in units of m (area unknown)

^{†††} notation according to Boukamp [43]

Porous Ni electrodes which are usually prepared from a Ni paste painted on top of the electrolyte, were investigated in detail by Jiang *et al.* [35,36]. In a dry gas atmosphere ($\sim 0.07\%$ H_2O), the anodic reactions were supposed to be limited by the diffusion of hydrogen. Adsorption and desorption processes are assumed to be fast at SOFC operating temperature (1073 K - 1273 K) and the initial sticking coefficient for hydrogen on a clean metal surface as well as the initial surface coverage of hydrogen are expected to be very small. In a wet gas atmosphere ($< 2\%$ H_2O), the overall reaction rate is increased due to a much faster surface diffusion via a spillover mechanism which furthermore frees up metal sites for dissociative adsorption of hydrogen. Two relaxation processes were distinguished in the impedance spectra: the low frequency impedance arc is associated with dissociative adsorption and diffusion, whereas the high frequency arc is supposed to be due to a charge transfer process. It is suggested that hydrogen can easily diffuse on the electrolyte surface and can react with the O^{2-} from the electrolyte. The rate of charge transfer should be enhanced, if electrons can be picked up by an electronic conductor near the reaction sites and move back towards the TPB after the reaction. In contrast to these results, the rate determining process for a porous Ni anode was attributed to the removal of hydroxide from the electrolyte in [31].

Ni electrodes covered with a ceramic layer studied by Nakagawa *et al.* [38,41,42] showed the same rate determining processes as the pattern electrodes in [28,29,30]. The electrode processes are predicted to take place within $0.8\ \mu\text{m}$ from the electrode/electrolyte interface. The electrode impedance allows to distinguish between an activated process around the TPB and a diffusion process related with the diffusion of water from the outside to the inside of the porous ceramic layer.

According to the literature, adsorption/desorption, surface diffusion, and charge transfer reactions are feasible rate determining reaction steps at simplified SOFC anodes. However, the results published in the literature are not consistent and sometimes contradictory. Furthermore, the impedance data depends strongly on the electrode design, on the measurement conditions, and on the measurement set-up. Thus, it is difficult to compare the data from different research groups which is necessary as each group focuses mainly on one or two parameters, such as the electrode polarization or the partial pressures of water or hydrogen. A clear understanding of the anode kinetics does not exist so far [1,8,12,17,19].

In the following, we will present a detailed electrochemical characterization of

the simplified anodic system Ni, H₂ - H₂O | YSZ as a starting point for further studies on Ni-YSZ cermet anodes. Flat Ni pattern anodes are used for the investigations, since this design allows to tailor the TPB length due to the well-defined edges. The overpotential, the fuel gas atmosphere, the temperature, and the pattern geometry of the anode are regarded as key parameters to identify the reaction mechanism of these simplified anodes.

3.2 Experimental

3.2.1 Preparation of SOFCs with Ni Pattern Anodes

The Ni anodes were prepared on single crystalline electrolytes of 9.5 mol% Y₂O₃ - stabilized ZrO₂ (25 mm in diameter, 0.5 mm thick, (001) orientation, polished on both sides) (Zirmat Corp., Westford, MA, USA). A dense, 1 μm thick, metallic Ni layer was first deposited onto the entire surface of the YSZ substrate by DC magnetron sputtering (Sulzer, Winterthur, CH). A specially designed Ni target was used which accounts for the magnetic properties of Ni. The sputter parameters are listed in Tab. 3.2. After deposition, the Ni anodes were structured in two steps using photolithography and wet chemical etching. First, the working electrode (1 cm²) and the reference electrode (4 mm²) were etched. In a second step, the line pattern of the working electrode was etched within a square of 0.8 cm · 0.8 cm. For all structures, the photoresist (S1813, Shipley, Kempraten-Rapperswil, CH) was spin-coated for 45 s with a rotation speed of 4000 rotations/s (thickness about 1.3 μm) and was exposed using a halogen lamp for 15 s. The photoresist was developed for about 15 s and the pattern were etched for 45 s - 60 s in diluted nitric acid (1:19 = 65 % nitric acid : deionized water). A schematic representation of a typical anode design is illustrated in Fig. 3.1.

A summary of the anode designs prepared in this thesis is listed in Tab. 3.3. Note that all anodes cover a surface area of 1 cm². Anodes 1 to 4 consist of equidistant lines of Ni and of YSZ. The TPB length increases from 0.04 m/cm² to 12.85 m/cm², while the Ni coverage of the electrolyte remains nearly constant. A cross-section of the anodes with equidistant lines of Ni and of YSZ is shown in Fig. 3.2a. In contrast to this design, Anodes 5 to 8 have different Ni coverages due to different Ni and YSZ line widths, respectively (Fig. 3.2b). The TPB lengths are almost constant (l_{TPB} around 0.2 m/cm²).

Tab. 3.2: Sputter parameters for the deposition of Ni layers.

Parameter	Value	Unit
DC bias	-50	V
Sputtergas	Ar	-
Basis pressure in the chamber	$6 \cdot 10^{-6}$	mbar
Pressure during sputtering	$3 \cdot 10^{-3}$	mbar
Size of the target	10 * 30	cm ²
Power at the target	650	W
Rate of sputtering	1	μm/h

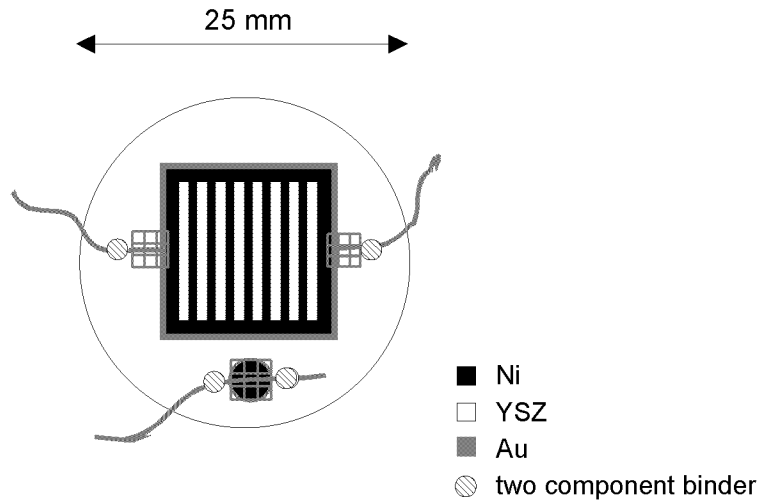


Fig. 3.1: Schematic top view of the anode design and the wire connection: Ni pattern anode of 1 μm thickness on a single crystalline YSZ electrolyte of 0.5 mm thickness connected with Au wires, gauze, and sputtered area for the electrical contact.

Tab. 3.3: Anode designs for electrochemical impedance spectroscopy (EIS) measurements.

Sample	Ni Line width [μm]	YSZ Line width [μm]	Ni coverage [cm^2]	l_{TPB} [m/cm^2]
Anode 1	10000	0	1	0.040
Anode 2	20	20	0.68	3.65
Anode 3	10	10	0.68	6.45
Anode 4	5	5	0.68	12.85
Anode 5	100	710	0.43	0.216
Anode 6	333	500	0.60	0.210
Anode 7	787	100	0.92	0.202
Anode 8	878	10	0.99	0.200

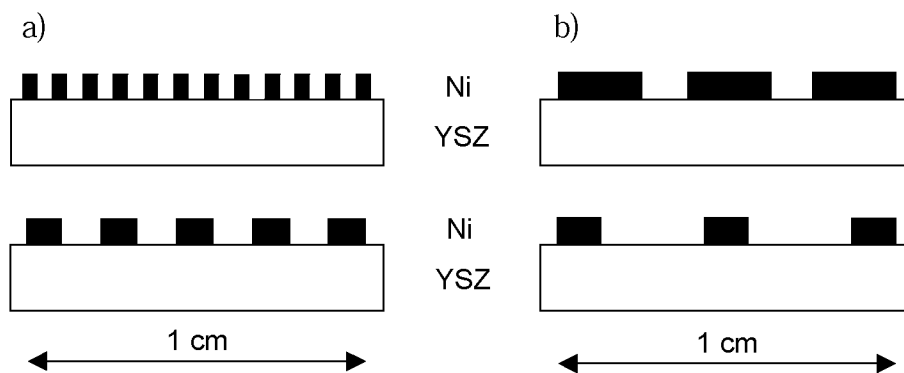


Fig. 3.2: Schematic cross-sections of the two different anode designs: a) Anodes 1 - 4 with equidistant lines of Ni and of YSZ and varying TPB length, b) Anodes 5 - 8 with varying line widths of Ni and of YSZ and a constant TPB length.

The cathodes were prepared by DC-sputtering (model SCD 040, Baltec, Balzers, FL) of a 30 nm thick Pt layer on the YSZ single crystal. They were placed symmetrically to the anode on the opposite side of the single crystal and were not patterned.

The anodes and reference anodes were connected with Au wire (99.99 %, 0.3 mm in diameter), Au gauze (52 mesh, woven from 0.102 mm Au wire), and Au paste (type C5754B, Heraeus GmbH, Hanau, D) as shown in Fig. 3.1. The cathodes were connected with a Pt wire (0.35 mm in diameter), Pt gauze (52 mesh, woven from 0.1 mm Pt wire), and Pt paste (type C3605P, Heraeus GmbH, Hanau, D) on the entire 1 cm² surface area of the cathode. All precious metals were obtained from Johnson Matthey & Brandenberger AG, Zürich, CH. The wires and gauzes were fixed onto the electrolyte with a ceramic two-component binder (type 1500, Firag, Ebmatingen, CH) (Fig. 3.1).

The anode microstructures were investigated using a light microscope (Polyvar Met, Reichert-Jung, D) and a scanning electron microscope (SEM) (JSM 6400, Jeol, Eching, D) before and after photolithography as well as before and after the electrochemical measurements.

3.2.2 *Electrochemical Characterization*

The electrochemical measurements were carried out in a single gas chamber measurement set-up (Fig. 3.3). A discussion concerning EIS measurements in a single gas chamber and in two gas chambers is given in appendix 2. For general information about the analyses of EIS data, the reader is referred to chapter 1 and to [48].

In the single gas chamber measurement set-up, the SOFC was fixed with the connecting wires in the middle of a horizontal split-furnace (length = 65 cm) inside of an alumina tube. The temperature was varied between 673 K and 973 K. The fuel gas (total gas pressure = 1 atm) consisted of a mixture of H₂ and N₂ (purity of the gases > 99.5 %). The gas flow was adjusted with manual mass flow controls in the range of 10 ml/min - 100 ml/min (Vögtlin Instruments AG, Aesch, CH). The partial pressures of hydrogen, $p(\text{H}_2)$, discussed in the text refer to the adjusted mass flows at the flow controls. They were varied between $2 \cdot 10^3$ Pa and $8.8 \cdot 10^4$ Pa.

For the impedance measurements as a function of the partial pressure of water, $p(\text{H}_2\text{O})$, the fuel gas was wetted using a water bubbler system (Fig. 3.4). The tem-

perature of the oil bath was varied between 289 K and 361 K corresponding to theoretical water vapor pressures of $3 \cdot 10^3$ Pa and $7 \cdot 10^4$ Pa, respectively [43]. The partial pressure of water inside the furnace was determined by means of an YSZ oxygen sensor installed near the SOFC in the fuel gas atmosphere.

The impedance measurements as well as the equivalent circuit fits were carried out with an IM6 ZAHNER[®] Impedance Analyzer, Kronach, D, in a three electrode, four lead configuration (cf. chapter 1, subsection 1.2). The frequency, f , was varied between 100 mHz and 100 kHz and the excitation voltage was fixed at 10 mV. The impedance was measured at anodic overpotentials, η , between 0 mV and 400 mV.

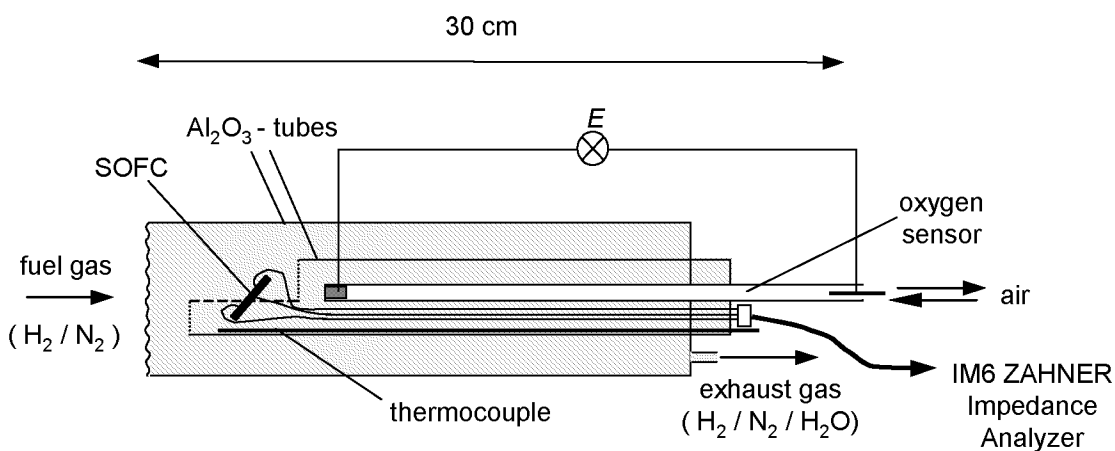


Fig. 3.3: Single gas chamber measurement set-up for the electrochemical characterization of SOFC anodes.

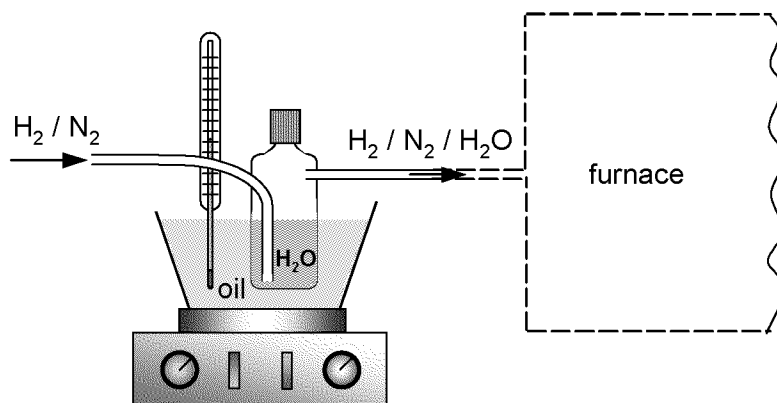


Fig. 3.4: Gas bubbler system for the wetting of the fuel gas atmosphere.

3.3 Results

3.3.1 Microstructure

A photograph of a Ni pattern anode on top of a YSZ single crystal electrolyte is shown in Fig. 3.5. This anode is very coarsely patterned with 500 μm thick equidistant lines of Ni and YSZ. The single crystal is totally translucent and the Ni stripes (dark regions) are continuous. A Ni pattern with smaller line width (20 μm) photographed at a higher magnification indicates that the edges of the Ni stripes are frayed out due to the wet chemical etching process (Fig. 3.6). However, thermal treatment levels out this fractal impression, so that the real TPB length is estimated to be only about 15 % larger than the theoretical one (Fig. 3.7).

It is well known from Ni-YSZ literature that Ni coagulates during thermal treatment so that the Ni network might not be continuous in a Ni-YSZ cermet after thermal treatment [1]. However, no detrimental coagulation was found for the Ni pattern anodes in this study. The line width of the Ni stripes decreased negligibly during the electrochemical experiments so that small coagulated Ni grains appeared at the edges of the Ni stripes (Fig. 3.7b). As these distinct Ni grains had no contact to the Ni stripes, they should not largely influence the anodic processes. More detailed information about the microstructure of Ni pattern anodes is given in appendix 1.

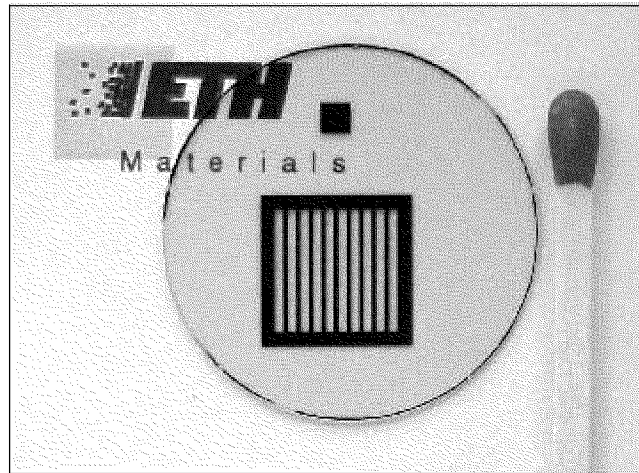


Fig. 3.5: Photograph of a Ni pattern anode with equidistant lines of 500 μm width on top of a single crystalline YSZ electrolyte of 0.5 mm thickness. The visibility of the ETH logo demonstrates the translucency of the YSZ single crystal.

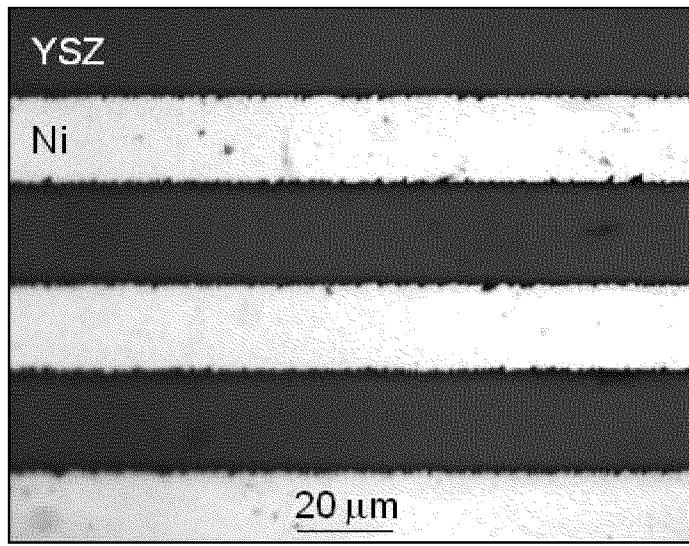


Fig. 3.6: Light micrograph of a Ni pattern anode with equidistant lines of 20 μm width and an ideal TPB length of 3.65 m/cm² (Anode 2, Tab. 3.3).

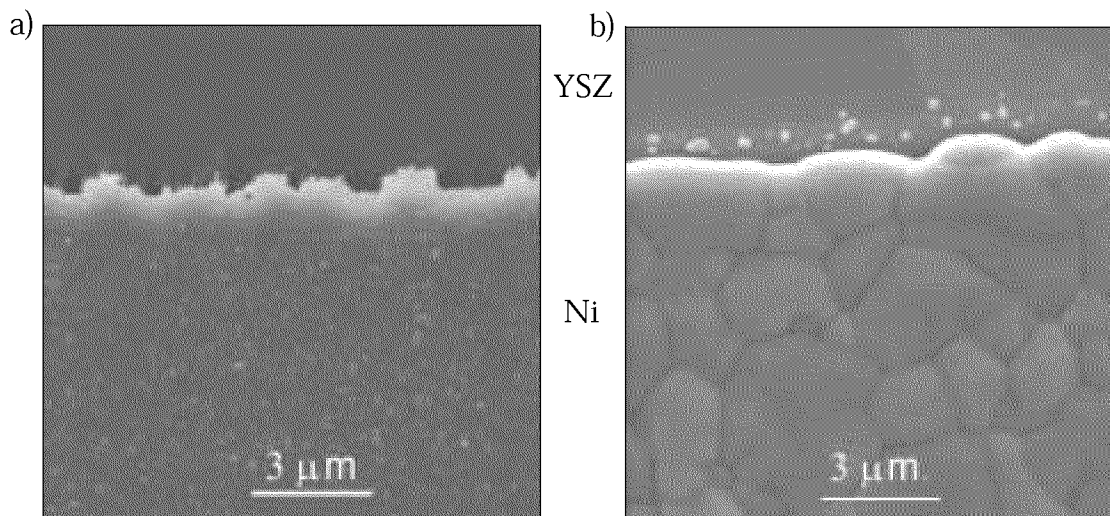


Fig. 3.7: Scanning electron micrographs of the TPB line of a Ni pattern anode a) before thermal treatment and b) after thermal treatment in reducing atmosphere at 973 K for 48 h.

3.3.2 Electrochemistry

3.3.2.1 Overpotential

The overpotential applied between the working and the reference anode is the electrical driving force for the anodic processes. It is used to adjust the fuel cell to a specific operating condition on the current - voltage curve (cf. chapter 1, Fig. 1.4). In Fig. 3.8, the overpotential is plotted as a function of the current density, j , in order to illustrate the performance of Ni pattern anodes. At an overpotential of $\eta = 200$ mV, the current density amounts to 1.5 mA/cm^2 . Current densities of 0.06 mA/cm^2 and 20 mA/cm^2 were obtained in [28] and [31], respectively. One should note that the data is not corrected for the small voltage drop in the electrolyte. The current is neither in this study nor in the other studies limited at high overpotentials. This indicates that a Ni pattern anode is most probably not limited by diffusion, in particular up to overpotentials of $\eta = 400$ mV.

Tafel analysis, where the current density is logarithmically plotted vs. the electrode potential, allows to determine the charge transfer coefficient, β ($\beta = \text{slope} \cdot \frac{RT}{F}$). At overpotentials between 50 mV and 400 mV, a charge transfer coefficient of 1.1 was found. For similar pattern anodes ($i_{\text{TPB}} \approx 3 \text{ m/cm}^2$), Tafel slopes of 2.3 [28] and 1.5 to 2.5 [31] were determined. These α values are all very high and suggest therefore that Tafel analysis is not suitable here, in particular, as it is only valid for single-step single-electron-exchange reactions [46,47]. Such a behavior has not been proven for this system yet.

Electrochemical impedance spectra were recorded at each point of the current - voltage curve in Fig. 3.8. The experimental conditions are summarized in Tab. 3.4. It should be noted that always anodic overpotentials were applied. The influence of the applied overpotential on the impedance response is shown in the Nyquist and in the Bode plot in Fig. 3.9. One arc is observed for overpotentials up to 300 mV (Fig. 3.9a). The almost 90° tangent to the Nyquist data at high frequencies indicates that Warburg diffusion [45] is not relevant under these experimental conditions. At $\eta = 400$ mV, at least one more semicircle develops and a 45° tangent fits to the data at high frequencies (inset in Fig. 3.9a). Hence, the anode kinetics might be limited by diffusion at high overpotentials. The impedance spectra were found to be reversible after polarization, i.e. almost the same impedance was obtained for $\eta = 0$ mV before and after polarization. The degradation as a function of time can also be neglected here.

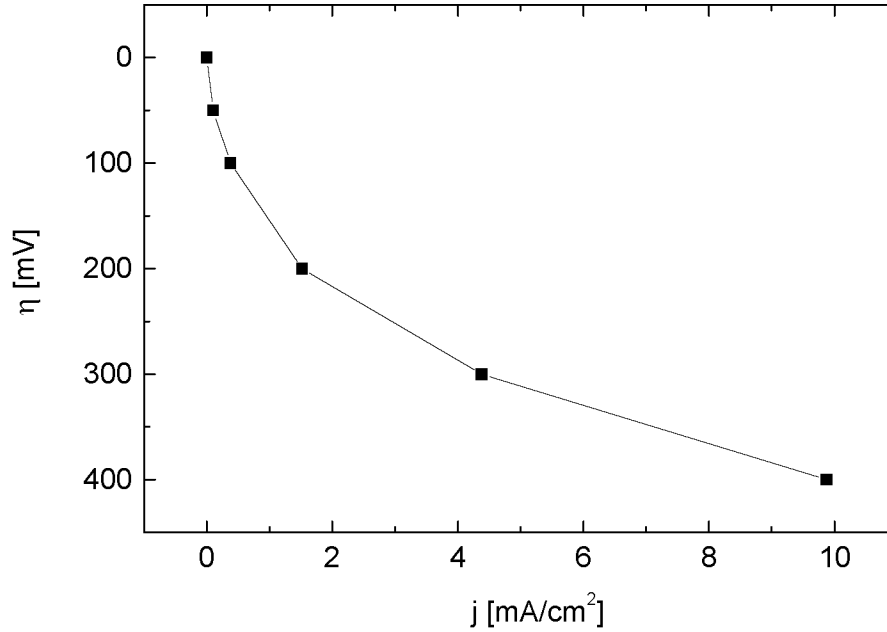


Fig. 3.8: Anodic overpotential, η , as a function of the current density, j , of a Ni pattern anode (line width Ni and YSZ = 20 μm , $I_{\text{TPB}} = 3.65 \text{ m/cm}^2$ (Anode 2, Tab. 3.3)). Experimental conditions: $T = 973 \text{ K}$, total gas flow ($\text{H}_2 + \text{N}_2$) = 40 ml/min, $p(\text{H}_2) = 2.5 \cdot 10^4 \text{ Pa}$. The data is not corrected for the small voltage drop in the electrolyte. The lines are drawn to guide the eye.

Tab. 3.4: Standard experimental conditions for EIS measurements (standard anode: Anode 2, $I_{\text{TPB}} = 3.65 \text{ m/cm}^2$).

Quantity	Symbol	Value	Unit
Temperature	T	973	K
Total gas flow ($\text{H}_2 + \text{N}_2$)	F	40	ml/min
Partial pressure of hydrogen	$p(\text{H}_2)$	$1.5 \cdot 10^4$	Pa
Partial pressure of water	$p(\text{H}_2\text{O})$	$5 \cdot 10^1$	Pa
Overpotential	η	0	mV
Frequency	f	$10^{-3} - 10^3$	Hz
Excitation voltage	V_{exc}	10	mV

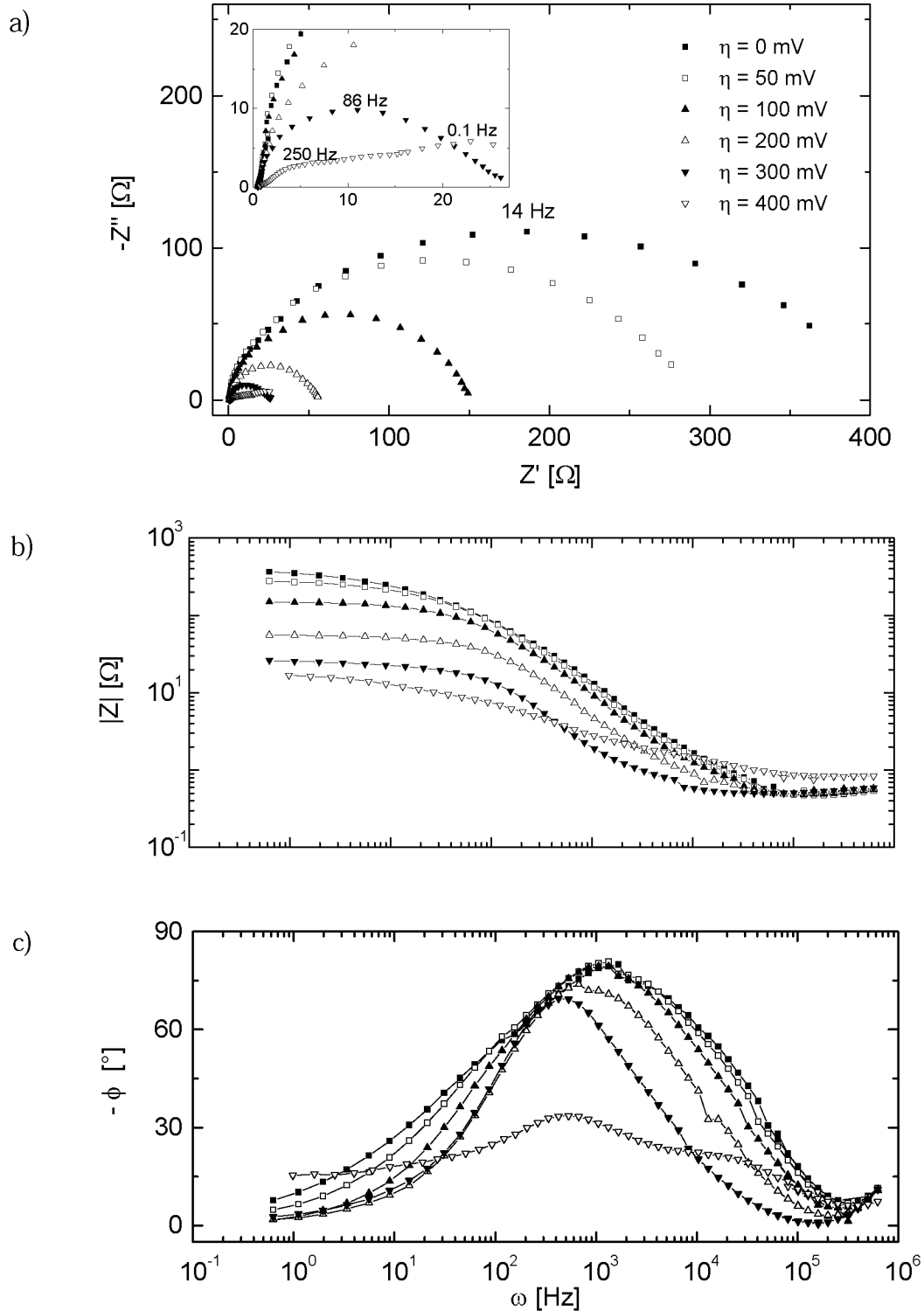


Fig. 3.9: Electrochemical impedance data of a Ni pattern anode as a function of an anodic overpotential, η : a) Nyquist, b) and c) Bode plots (for the experimental conditions see Tab. 3.4). The data is not corrected for the electrolyte resistance R_e (R_e is very low and nearly constant).

The absolute impedance $|Z|$ in the Bode representation (Fig. 3.9b) shows an average slope of -0.957 ± 0.027 for overpotentials up to 300 mV at frequencies around 10^3 Hz. A slope of -1 in combination with a phase angle of 90° would correspond to a first order reaction mechanism [45]. In the literature, a first order reaction mechanism was proposed for several Ni electrodes [28-35,36]. However, as the negative slopes in Fig. 3.9b are slightly smaller than 1 and as the phase angle distribution is neither a symmetrical bell-curve nor does it reach 90° (Fig. 3.9c), another effect comes in. This can either be a second process or a distortion due to a distribution of relaxation frequencies [48]. At very high overpotential ($\eta = 400$ mV), a second maximum arises in the Nyquist as well as in the Bode representation (Fig. 3.9a and Fig. 3.9b, respectively). The slope in Fig. 3.9b decreases to -0.3 and the phase shift is only 30° (Fig. 3.9c).

It should be noted that the characteristic frequencies in Fig. 3.9c are not the relaxation frequencies of the process. The relaxation frequency, ω^* , is rather the frequency belonging to the maximum impedance in the Nyquist plot (cf. chapter 1). It can best be determined from the maximum in the Z' vs. ω plot. For the main electrode process, ω^* increases linearly with η at small overpotentials ($0 \text{ mV} < \eta < 200 \text{ mV}$) (Fig. 3.10). A considerable deviation from the linear behavior is found for $\eta > 200 \text{ mV}$. Note that the relaxation frequency at $\eta = 400 \text{ mV}$ can hardly be determined.

The relaxation frequencies reach values between 10 Hz and 250 Hz corresponding to relaxation times, τ^* , between 0.1 s and 4 ms ($\tau^* = 1/\omega^*$). This signifies that the main anode process accelerates under an electrical driving force by almost two orders of magnitude. In the literature, a broad range of relaxation frequencies between 0.1 Hz and 1 kHz is reported (Tab. 3.1). The most similar conditions compared to this study are described in [29] and [31]: the relaxation frequency in [29] reaches values of around 0.2 Hz at $\eta = 0 \text{ mV}$ (this study: $\omega^*_{0 \text{ mV}} = 14 \text{ Hz}$); no frequency values are mentioned in [31].

The second electrode process which arises at $\eta = 400 \text{ mV}$, is a very slow process. It appears at a frequency of about 0.1 Hz which is equal to a relaxation time of 10 s (Fig. 3.9a, not shown in Fig. 3.10).

Fig. 3.11 illustrates the exponential decrease of the polarization resistance, R_p , determined from the low frequency intercept of the impedance data in the Nyquist plot (Fig. 3.9a) as a function of the overpotential. It indicates that Ni pattern anodes react strongly to an applied overpotential. A much less intense response is known from Ni-YSZ cermet anodes.

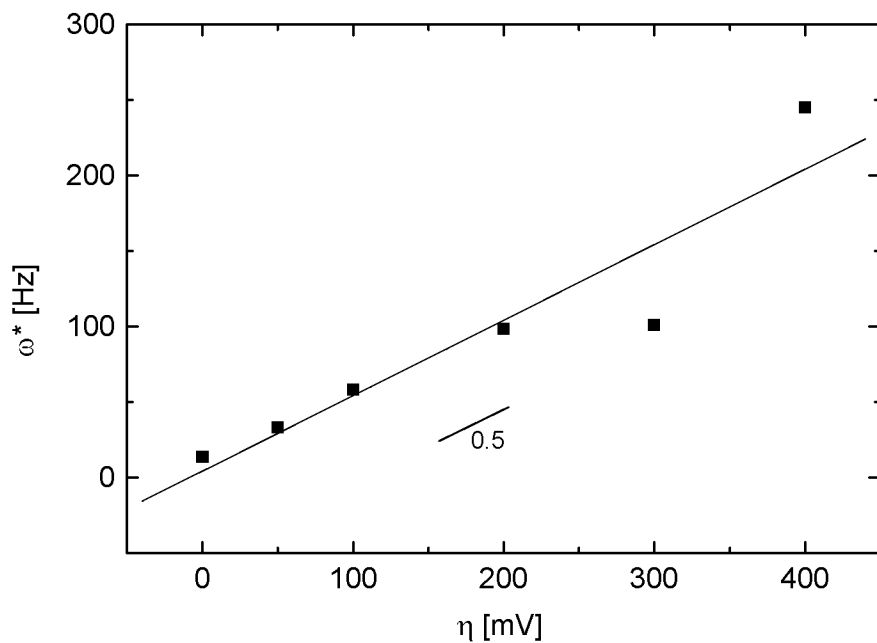


Fig. 3.10: Relaxation frequency, ω^* , as a function of an anodic overpotential, η , applied between the working and the reference anode (for the experimental conditions see Tab. 3.4).

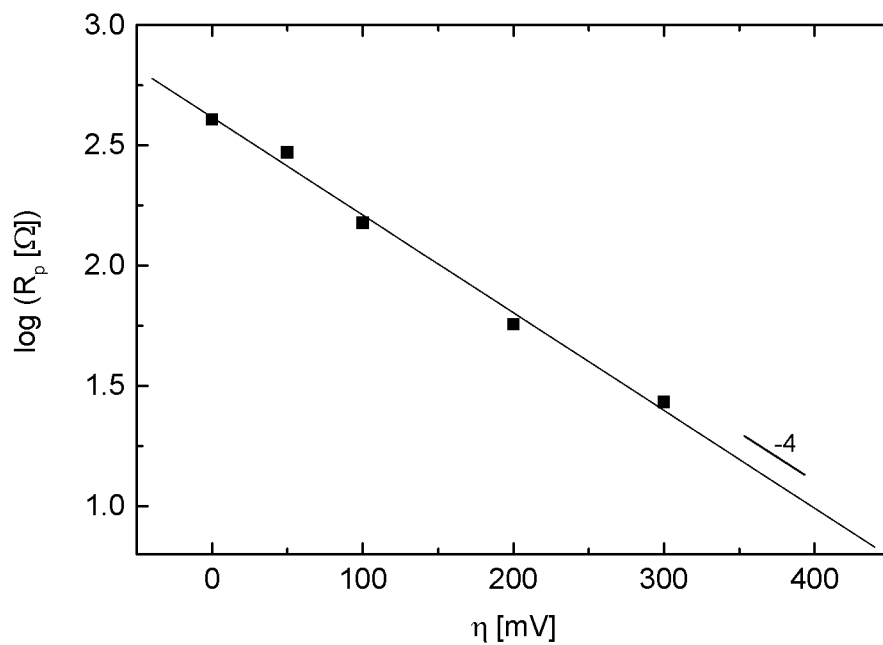


Fig. 3.11: Polarization resistance, R_p , as a function of an anodic overpotential, η , applied between the working and the reference anode (for the experimental conditions see Tab. 3.4).

For further interpretation of the electrochemical data, the impedance spectra were fitted to an equivalent circuit (Fig. 3.12). The following equivalent circuit model was chosen for the data up to 300 mV: $R_e(C_{dl}(R_t(R_1Q_1)))$ where R_i represent resistances, C_i capacitances, and Q_i constant phase elements (CPE). The code for the description of the equivalent circuit has been adopted from [44]. The impedance of a CPE is given by $Z_{CPE} = 1/Q(i\omega)^n$, where i denotes the imaginary unit, ω the angular frequency, and n the deviation of the impedance of a CPE from an ideal capacitive behavior ($n = 1$ for the impedance of an ideal capacitor and $n = 0$ for the impedance of an ideal resistor). A CPE was used for the fitting of the impedance data, as due to the broadening of the bell-shaped curve of the phase angle a distribution of relaxation times is expected. Such a behavior can best be fitted by a CPE [48]. Additional information in terms of the impedance of a CPE is given in appendix 3.

In the equivalent circuit model, the electrolyte resistance R_e is required because some contribution from the electrolyte is measured in case of three point impedance measurements. C_{dl} signifies the double layer capacitance that arises due to the interface electrode/electrolyte. R_t is a purely ohmic resistance which is often attributed to a charge transfer reaction in equivalent circuit models of SOFC electrodes. Hence, even without a priori knowledge about this resistance, it is called charge transfer resistance here. R_1Q_1 represents an electrode process which is responsible for a semicircle in the Nyquist plot. The impedance at 400 mV could be fitted quite well to an equivalent circuit with two RQ elements in series instead of only one. However, due to the different equivalent circuit model, the fitting data at $\eta = 400$ mV is not compared to the low overpotential data ($\eta < 300$ mV) in the following.

According to Fig. 3.12a, the electrolyte resistance, R_e , is very low (about 0.6Ω) meaning that the electrolyte contribution is mediocre in this system. The charge transfer resistance, R_t , is also rather small ($< 2 \Omega$ at $\eta = 0$ mV) and decreases with increasing overpotential. The resistance R_1 is more than 2 orders of magnitude larger than R_t . Both resistances, R_1 and R_t , decrease with almost the same slope (about -4) as the total polarization resistance R_p determined directly from the experimental data (Fig. 3.11). Due to the high resistance of R_1 , this element seems to limit the anode process. The capacitance Q_1 has no significant influence on the electrode performance (Fig. 3.12b).

The double layer capacitance, C_{dl} , increases by one order of magnitude with increasing overpotential (Fig. 3.12b). The reason for this behavior is not clear,

since the surface coverage of Ni should stay constant and since the impedance spectra are mainly reversible after polarization. Thus, the variations of C_{dl} cannot be due to a change of the microstructure or of the electrode/electrolyte contact. Straight-forward from the general equation of a plate condenser

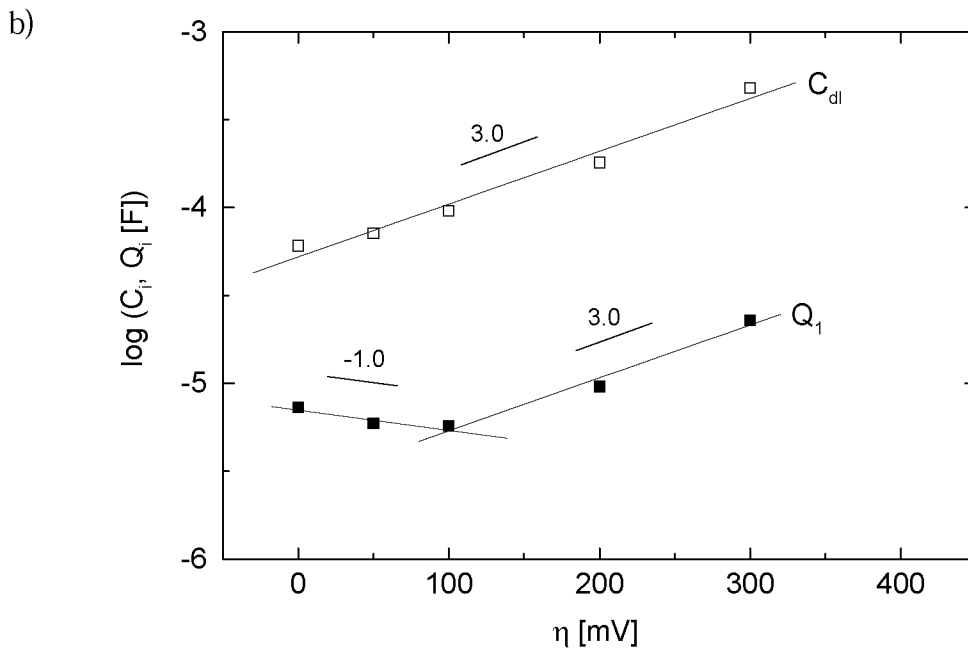
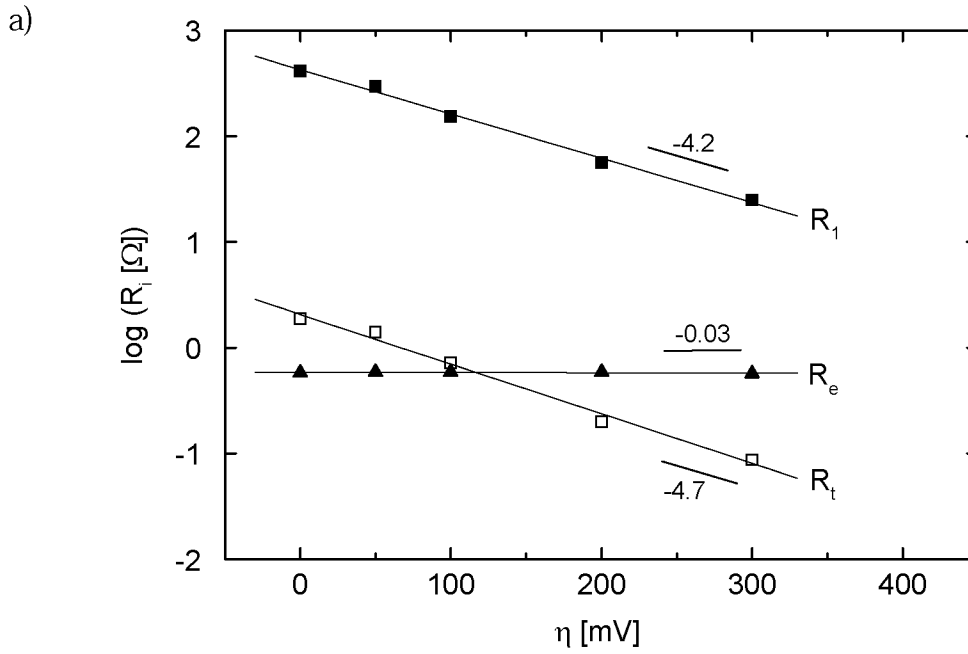
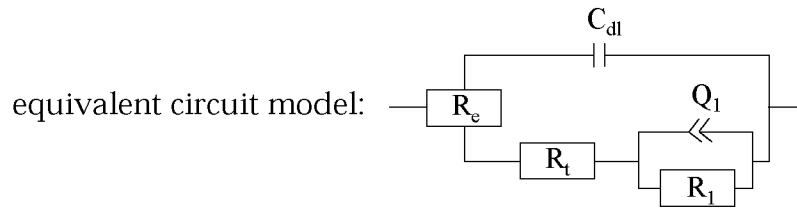
$$C_{dl} = \varepsilon \frac{A}{d} \quad (3.1)$$

where ε is the dielectric constant, A the area, and d the thickness of the plate condenser, it follows that the increase of C_{dl} must be either related to a decrease of d or to an increase of A with increasing overpotential (ε is assumed to be constant). An increase of the electrode area, A , could originate from an extension of the effective electrode area onto the YSZ surface near the electrode. It is probable that the YSZ electrolyte is electrochemically active and that a charged layer develops on the YSZ near the electrode. Hence, an additional capacitance would show up and would yield in an effective increase of C_{dl} . A decrease of d would signify that the plates of the condenser move towards each other. Hence, the double layer would be compressed when applying an anodic overpotential.

The relaxation frequency for a process which is described by an RQ element was derived in appendix 3 as

$$\omega^* = \sqrt[n_1]{\frac{1}{R_1 \cdot Q_1 \cdot \omega_o^{1-n_1}}} \quad (3.2)$$

where $\omega_o = 2\pi \cdot 1000$ Hz and R_1 , Q_1 , n_1 are the equivalent circuit elements of the R_1Q_1 unit. It is found that the relaxation frequencies scatter considerably (Fig. 3.12c). The absolute values for ω^* as well as the slope are considerably higher compared to the data obtained directly from the measurements (Fig. 3.10). Thus, the equivalent circuit model does most probably not describe the system perfectly.



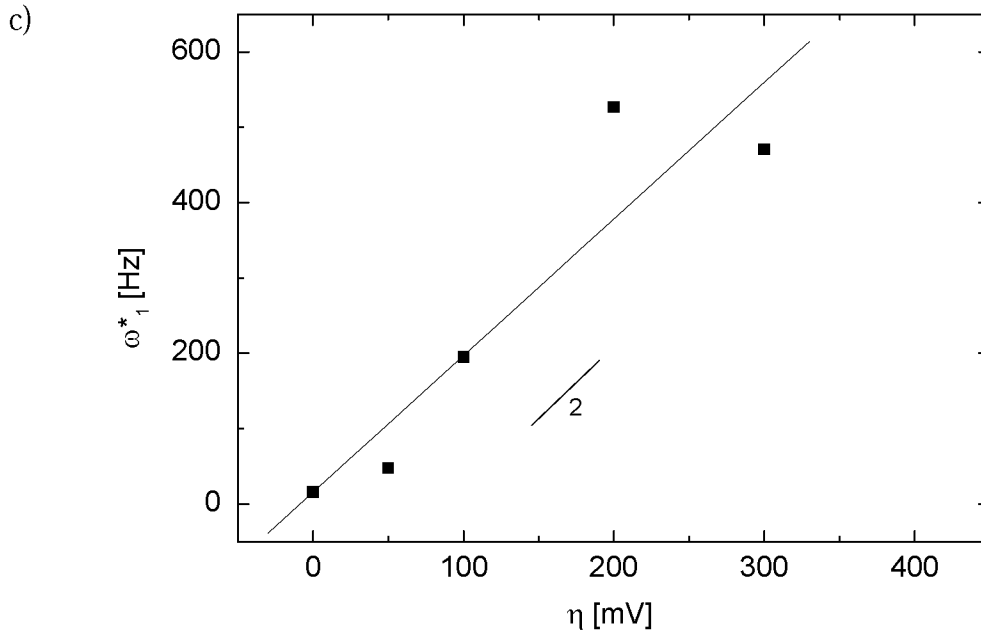


Fig. 3.12: Fitting results of the impedance data in Fig. 3.9 with the equivalent circuit $R_e(C_{dl}(R_t(R_1Q_1)))$: a) resistive elements, b) capacitive elements, c) relaxation frequencies ($n_1 = 0.492$) (for the experimental conditions see Tab. 3.4).

3.3.2.2 Partial Pressure of Hydrogen

The fuel gas atmosphere consists of a mixture of hydrogen, H_2 , and nitrogen, N_2 . The H_2 is the catalytically active fuel gas component, whereas the N_2 is used as dilutant. Other dilutants, such as Ar or He, did not evoke a specific influence on the electrochemical behavior of Ni pattern anodes. Variations in the total gas flow (10 ml/min - 100 ml/min) and in the fuel gas composition ($2.5 \cdot 10^4 \text{ Pa} < p(H_2) < 8.8 \cdot 10^4 \text{ Pa}$) did not influence the electrode behavior significantly. Fig. 3.13 demonstrates the small influence of the partial pressure of hydrogen on the polarization resistance of a Ni pattern anode. It is found that the higher the overpotential the more distinct the influence of the $p(H_2)$ becomes (steeper negative slope).

These observations were related to the partial pressure of oxygen $p(O_2)$ in the gas atmosphere measured with an oxygen sensor near the SOFC inside the furnace. The $p(O_2)$ decreases significantly with increasing $p(H_2)$, whereas no influ-

ence of the overpotential is found (Fig. 3.14). The contrary behavior of R_p and $p(\text{O}_2)$ with respect to the partial pressure of hydrogen and to the overpotential indicates that the water which is produced during the operation of the fuel cell does not change the partial pressures in the fuel gas chamber significantly. However, by changing the $p(\text{H}_2)$ at the flow controls, the $p(\text{O}_2)$ is shifted considerably. The polarization resistance is not largely influenced by changes in the $p(\text{O}_2)$ of one order of magnitude, but it is directly coupled to the overpotential.

Considerable differences in the reaction orders for $p(\text{H}_2)$ are found in the literature [37]. The differences are due to the measurement technique (electrochemical impedance spectroscopy or galvanostatic current interruption), the design, and the microstructure of the anodes. For Ni pattern anodes, a considerable influence of the $p(\text{H}_2)$ on the polarization resistance (slope + 0.5) was found at a very low partial pressure of hydrogen ($p(\text{H}_2) < 0.1$ atm) and at a high temperature ($T = 1123$ K) [29,31]. At $p(\text{H}_2) > 10^4$ Pa and at $T < 973$ K, no significant influence was observed comparable to Fig. 3.13.

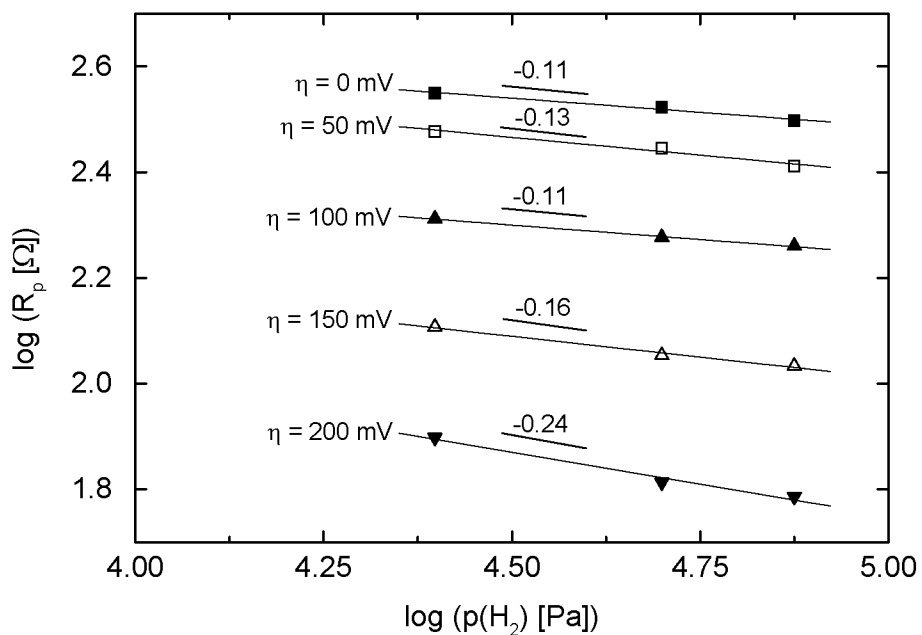


Fig. 3.13: Influence of the partial pressure of hydrogen, $p(\text{H}_2)$, (adjusted with the flow controls) on the polarization resistance, R_p , at different overpotentials, η (for the experimental conditions see Tab. 3.4).

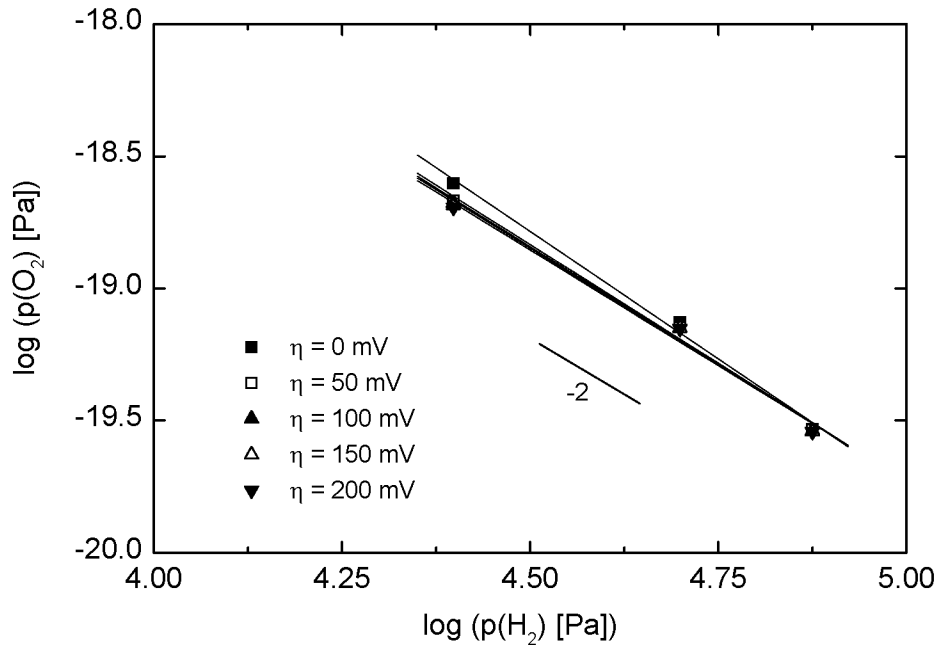


Fig. 3.14: Influence of the partial pressure of hydrogen, $p(\text{H}_2)$, (adjusted with the flow controls) on the partial pressure of oxygen, $p(\text{O}_2)$, (measured with an oxygen sensor in the gas chamber).

The results above indicate that a small total gas flow and a rather low concentration of hydrogen, e.g. total gas flow = 40 ml/min and $p(\text{H}_2) = 2.5 \cdot 10^4$ Pa, such as in the standard operating conditions in this study, are sufficient to assure that the electrode process is not limited by the gas supply. However, in order to drive the system into diffusion limitations, a special set-up for the anode was designed: the Ni pattern anode was covered with a Ni net and a piece of YSZ single crystal as a barrier for the fuel gas.

Under equilibrium conditions ($\eta = 0$ mV), no effects of the diffusion barrier were detected and the data is comparable with those of an uncovered anode. However, at $\eta = 200$ mV, a significantly lower negative Bode slope of about -0.35 was found for the covered electrode compared to the uncovered electrode having a Bode slope of -0.62. Also, the angle of the high frequency tangent to the impedance data in the Nyquist plot was smaller for the covered electrode compared to the uncovered electrode (compare the square symbols in the inset in Fig. 3.15). This points to a diffusion effect due to the coverage of the electrode.

According to equivalent circuit fitting, no significant changes in the resistive elements were found between the uncovered and the covered electrode at $p(\text{H}_2)$

$= 2.5 \cdot 10^4$ Pa, as shown in Fig. 3.16 (note that only the data at $p(\text{H}_2) = 2.5 \cdot 10^4$ Pa is compared for a moment). However, the capacitive elements increase notably due to the coverage of the electrode. The electrode process becomes about one order of magnitude slower in case of the diffusion barrier (covered electrode).

Now, considering only the covered electrode, it is found that the Warburg effect in the Nyquist plot decreases the lower the $p(\text{H}_2)$ (Fig. 3.15, (closed symbols)). This signifies that diffusion is not relevant at a very low hydrogen partial pressure. Variations in the partial pressure of hydrogen from $1.3 \cdot 10^4$ Pa to $2.5 \cdot 10^4$ Pa have no significant influence on the electrode performance according to equivalent circuit fitting (Fig. 3.16). Even up to $p(\text{H}_2) = 8.8 \cdot 10^4$ Pa, the equivalent circuit elements are constant in first approximation (not shown in Fig. 3.16). However, at $p(\text{H}_2) < 1.3 \cdot 10^4$ Pa, the resistive elements increase and the capacitive elements decrease for lower $p(\text{H}_2)$ (Fig. 3.16). Hence, a critical value is exceeded.

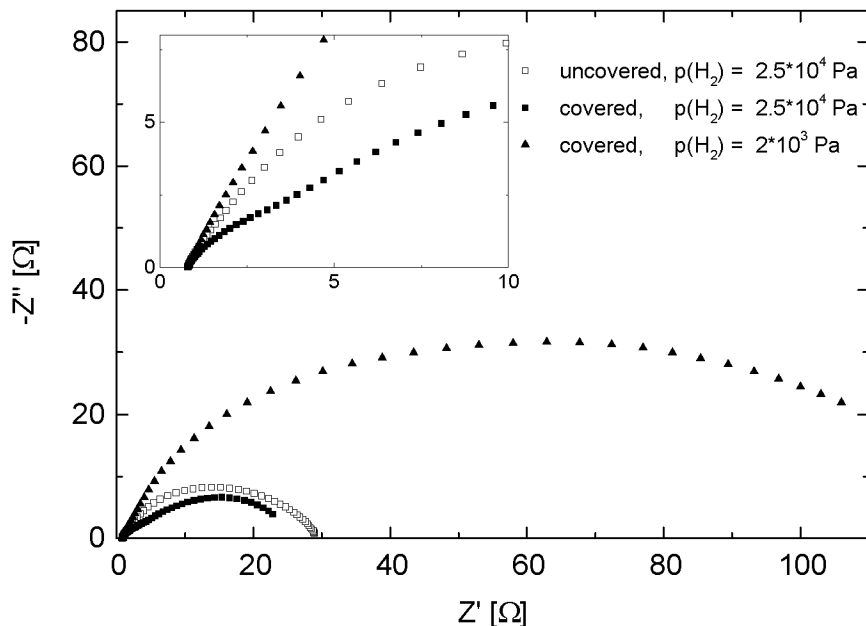


Fig. 3.15: Nyquist diagram of uncovered and covered electrode at different partial pressures of hydrogen, $p(\text{H}_2)$, at $\eta = 200$ mV (for the experimental conditions see Tab. 3.4).

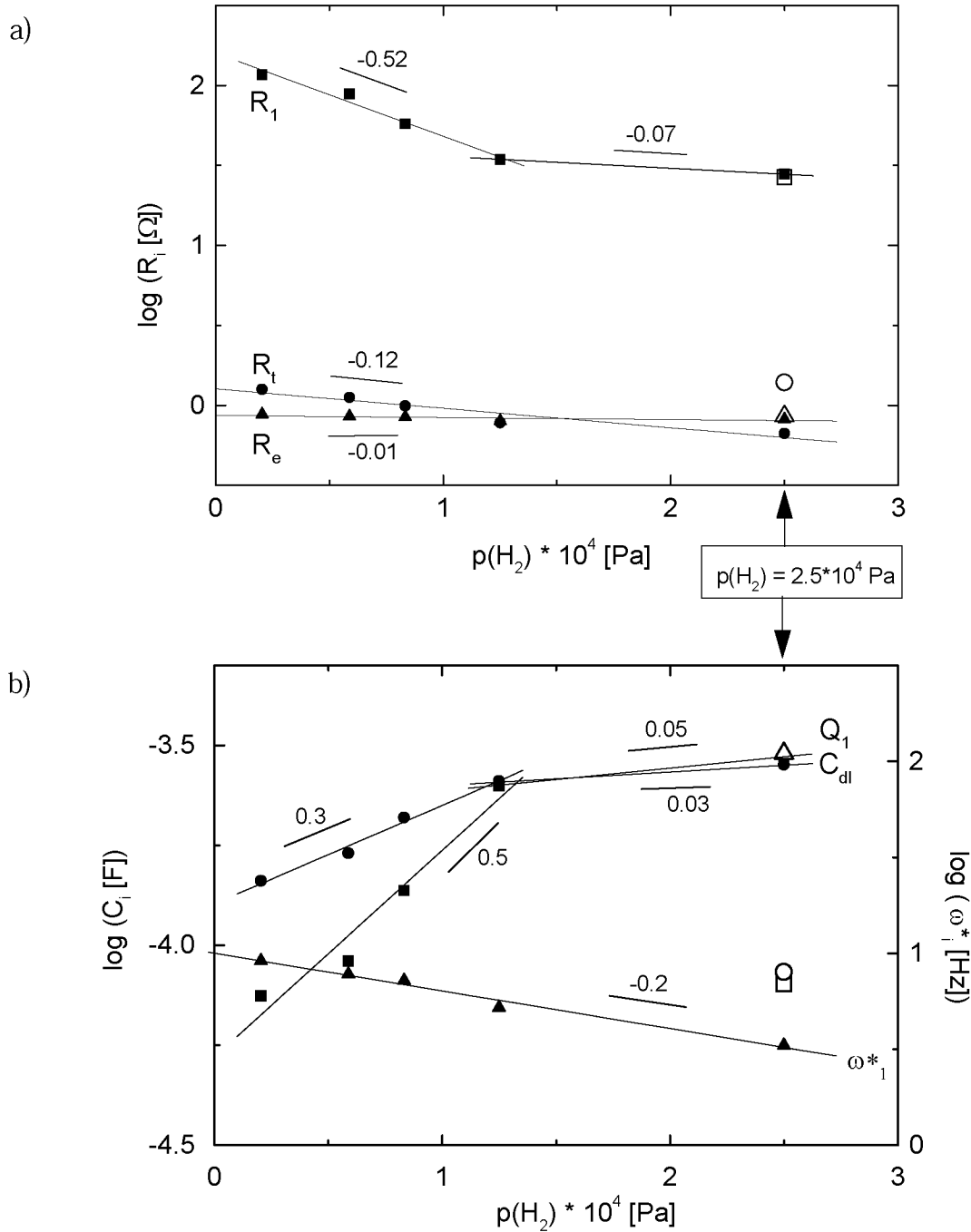


Fig. 3.16: Equivalent circuit ($R_e(C_{dl}(R_t(R_1Q_1)))$) fitting results as a function of the partial pressure of hydrogen, $p(\text{H}_2)$, adjusted with the flow controls ($\eta = 200$ mV) (for the experimental conditions see Tab. 3.4): a) resistive elements, b) capacitive elements and relaxation frequency ($n_1 = 0.6$). Open symbols: uncovered electrode; closed symbols: electrode covered with a Ni net and a piece of YSZ.

3.3.2.3 Partial Pressure of Water

The partial pressure of water, $p(\text{H}_2\text{O})$, in the fuel gas atmosphere is known to have a catalytic effect on the anodic kinetics of SOFCs [29,31,35]. Here, the partial pressure of water is adjusted with a water bubbler which is installed outside the furnace. The actual water vapor pressure in the fuel gas atmosphere is determined by means of an oxygen sensor near the SOFC inside the furnace. It is found that the most distinct changes in the $p(\text{H}_2\text{O})$ are observed between the dry fuel gas coming directly out of the high pressure gas cylinders ($p(\text{H}_2\text{O}) = 4 \cdot 10^1$ Pa) and the wet fuel gas coming from the water bubbler. Even though the temperature of the water bubbler was varied from 298 K to 361 K, only small changes of the partial pressure of water inside the furnace were recorded ($p(\text{H}_2\text{O})$ around 10^3 Pa).

The impedance data as a function of the partial pressure of water is shown in Fig. 3.17: the absolute impedance decreases (Fig. 3.17a) and the bell-shaped curve of the phase angle becomes more symmetrical when the amount of water in the fuel gas is increased (Fig. 3.17b). No significant changes in the shape of the impedance curves are observed as a function of the partial pressure of water.

The polarization resistance, R_p , is illustrated as a function of the partial pressure of water, $p(\text{H}_2\text{O})$, at different overpotentials in Fig. 3.18. It is found that the polarization resistance decreases both with an increase of the partial pressure of water as well as with an increase of the overpotential. The most intense effect of the $p(\text{H}_2\text{O})$ is found at $\eta = 0$ mV. With increasing overpotential, the influence of the partial pressure of water in the fuel gas decreases (smaller negative slope in Fig. 3.18). This observation might be due to the following: the application of an overpotential results in a stronger drift of oxygen through the electrolyte and, thus, to a higher production of water at the anode side of the fuel cell. If the presence of water in the gas atmosphere and thereby at the interface decreases the polarization resistance, then the overpotential which is also responsible for the production of water reduces the catalytic effect of the additional water in the fuel gas. This would mean that a higher partial pressure of water near the TPB would favor the anodic reaction mechanism. This might also explain why Ni-YSZ cermet anodes have a much better performance than Ni pattern anodes not only due to a longer TPB length: water can be stored in the porous, three dimensional microstructure of the anode and, thus, increases the $p(\text{H}_2\text{O})$ near the TPB. The water then catalyses the anode kinetics.

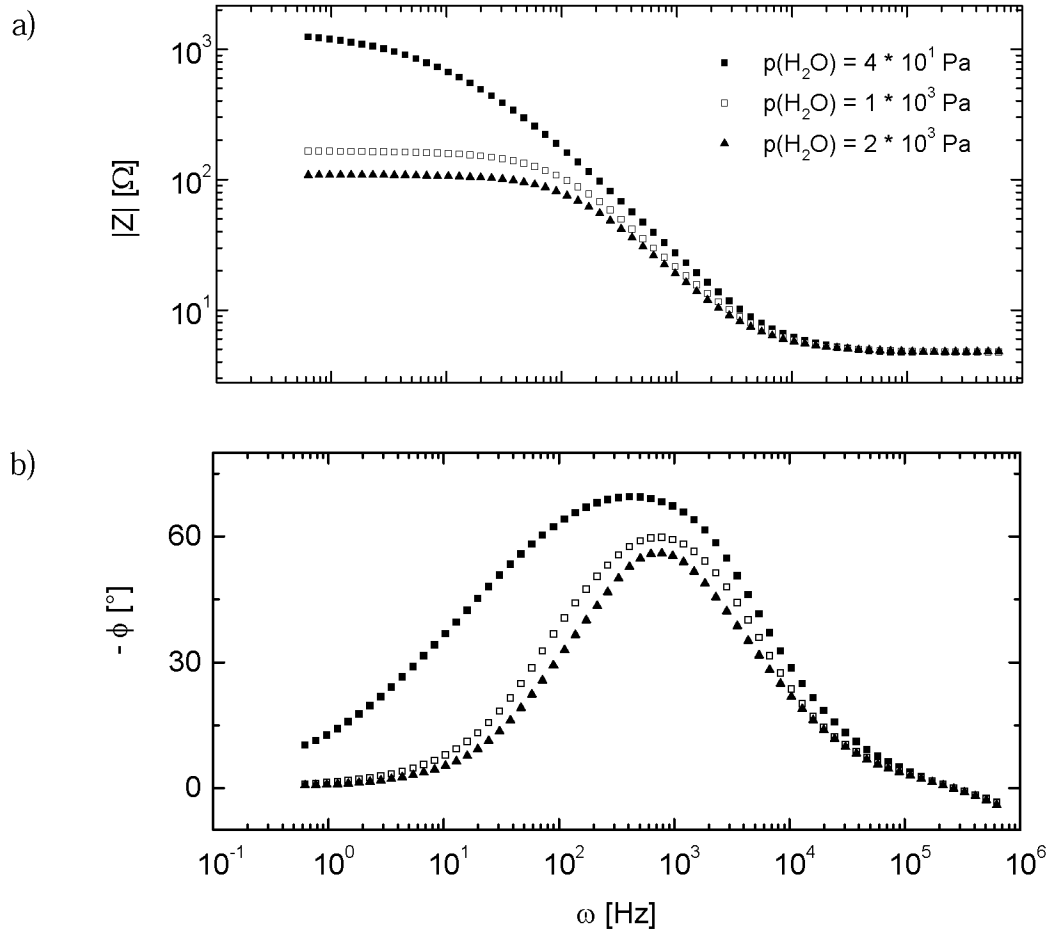


Fig. 3.17: Electrochemical impedance data as a function of the partial pressure of water, $p(\text{H}_2\text{O})$, in the fuel gas atmosphere (for the experimental conditions see Tab. 3.4). Note that the data is not corrected for R_e .

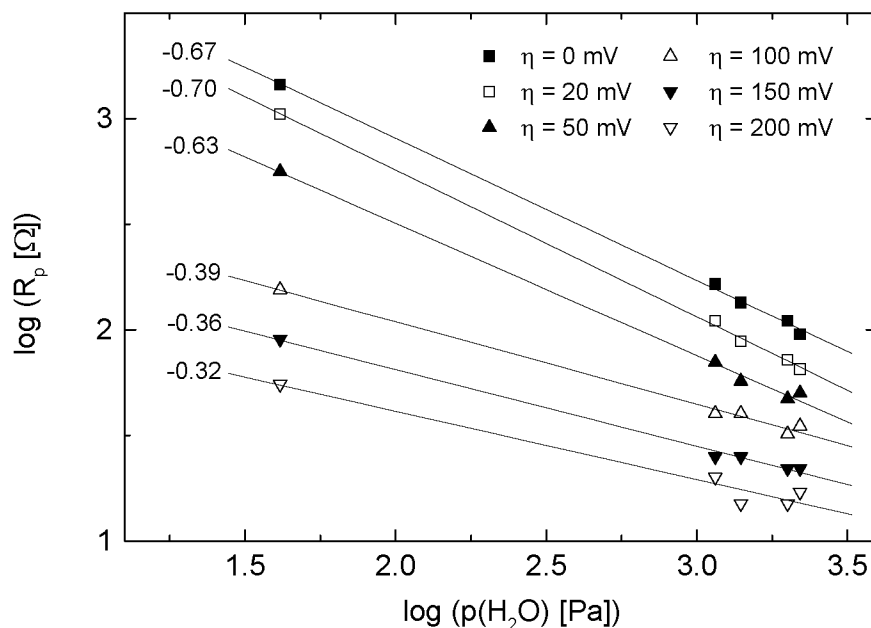


Fig. 3.18: Polarization resistance, R_p , as a function of the partial pressure of water, $p(\text{H}_2\text{O})$, at different overpotentials, η (for the experimental conditions see Tab. 3.4). The numbers at the lines indicate the slopes of the curves.

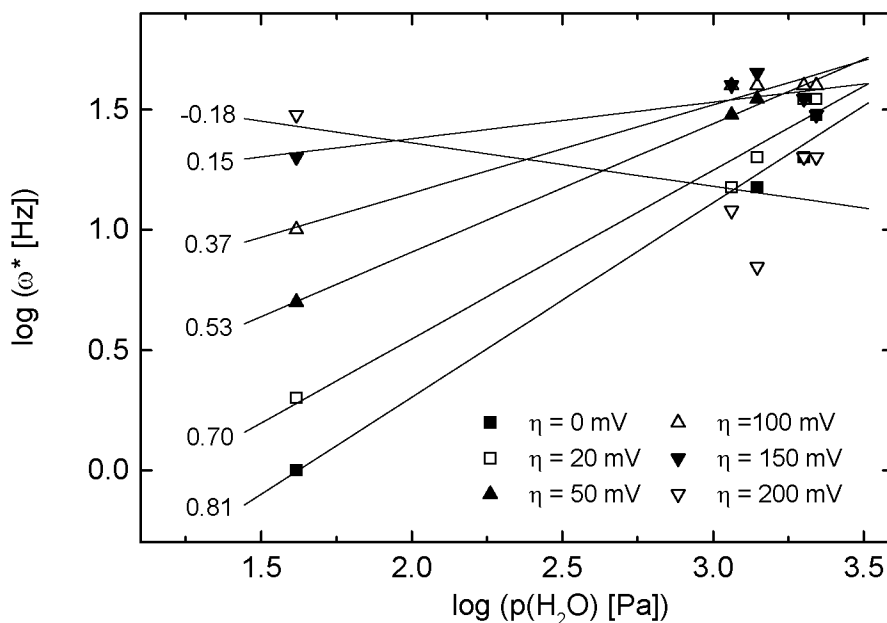
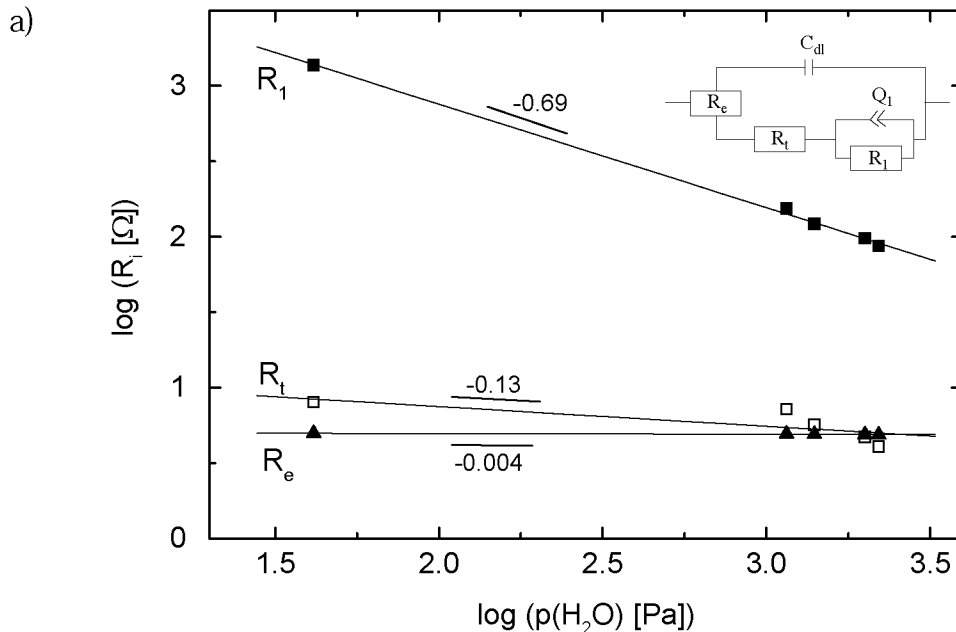


Fig. 3.19: Relaxation frequency, ω^* , as a function of the partial pressure of water, $p(\text{H}_2\text{O})$, at different overpotentials, η (for the experimental conditions see Tab. 3.4). The numbers at the lines indicate the slopes of the curves.

The relaxation frequency, ω^* , is found to increase with increasing partial pressure of water according to a power law (Fig. 3.19). It should be noted that the effect of the overpotential on the relaxation frequency is linear according to Fig. 3.10. This signifies that the main anode processes is much more accelerated with an increase of the amount of water than with an increase of the applied overpotential.

Equivalent circuit fitting of the impedance data as a function of the partial pressure of water was carried out with a model of the form $R_e(C_{dl}(R_t(R_1Q_1)))$ (Fig. 3.20). The impedance response is dominated by the resistance, R_1 , which behaves in the same way as the polarization resistance, R_p , in Fig. 3.18. The electrolyte resistance, R_e , as well as the charge transfer resistance, R_t , are very small and do not depend on the partial pressure of water. The same accounts for the double layer capacitance, C_{dl} . The capacitance, Q_1 , increases with a slope of 0.3 so that the relaxation frequency, ω_1 , increases with the same slope as ω^* determined in the experiments (Fig. 3.19). This indicates that the equivalent circuit model seems to represent the anode kinetics quite well and that the reaction mechanisms can be accurately described by one RQ equivalent circuit element.



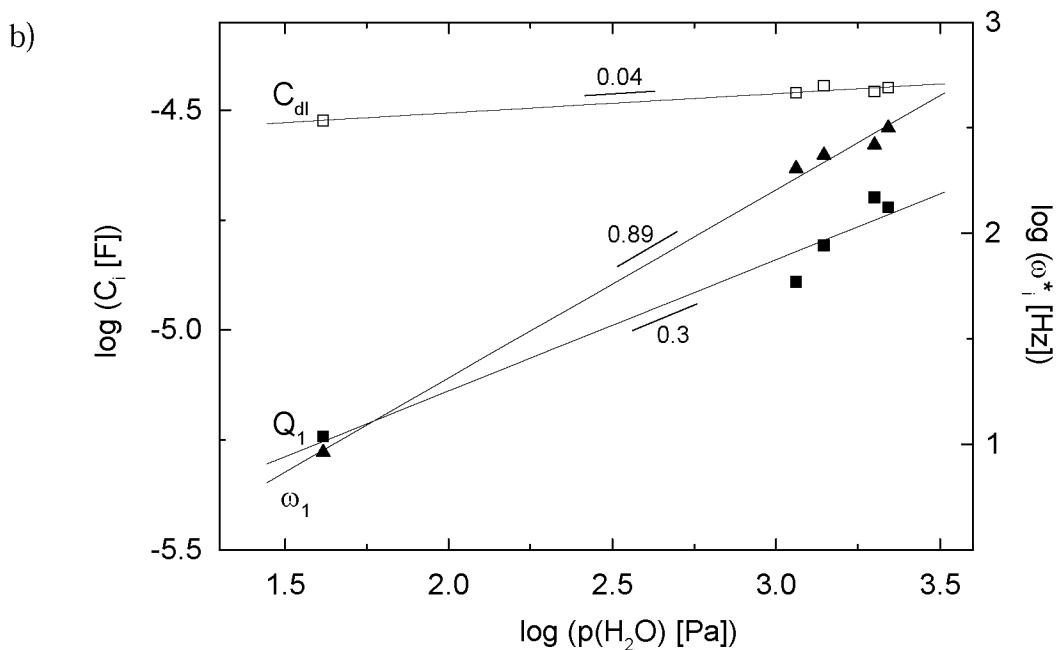


Fig. 3.20: Equivalent circuit ($R_e(C_{dl}(R_t(R_1Q_1)))$) fitting results as a function of the partial pressure of water, $p(\text{H}_2\text{O})$, at $\eta = 0$ mV: a) resistive elements, b) capacitive elements and relaxation frequencies ($n_1 = 0.75$) (for the experimental conditions see Tab. 3.4).

3.3.2.4 Temperature

The temperature dependence of the impedance data of a Ni pattern anode is shown in Fig. 3.21. Qualitatively the same anodic behavior is found for the entire temperature range from 673 K to 973 K. One single process is identified. No Warburg diffusion is found at any temperature. The increase of the Bode slope in Fig. 3.21a from about -1 to -0.8 is due to the increase of the electrolyte resistance with decreasing temperature (Note that the impedance data in Fig. 3.21 is not corrected for R_e). The shift of the phase angle in Fig. 3.21b indicates a shift of the relaxation frequency of the main electrode process as a function of the temperature.

As shown in Fig. 3.22, both the polarization resistance R_p as well as the electrolyte resistance, R_e , decrease exponentially with increasing temperature. The activation energy of R_p determined from the low frequency intercept of the Nyquist plot minus the high frequency intercept (corrected R_p) is found to be

0.88 ± 0.04 eV (averaged value for the different overpotentials). This value is similar to the activation energy of 0.7 eV determined in [39], but much lower than the activation energy of 1.6 eV determined in [31]. Both of these activation energies were determined for Ni pattern anodes measured under similar conditions as in this study. The activation energy of R_e is determined from the high frequency intercept of the Nyquist data; it is 1.02 eV (Fig. 3.22).

The relaxation frequencies, ω^* , as a function of the temperature indicate also a thermal activation of the main electrode process (Fig. 3.23). The activation energy, E_A , is 0.73 eV. The main electrode process becomes slower at low temperatures.

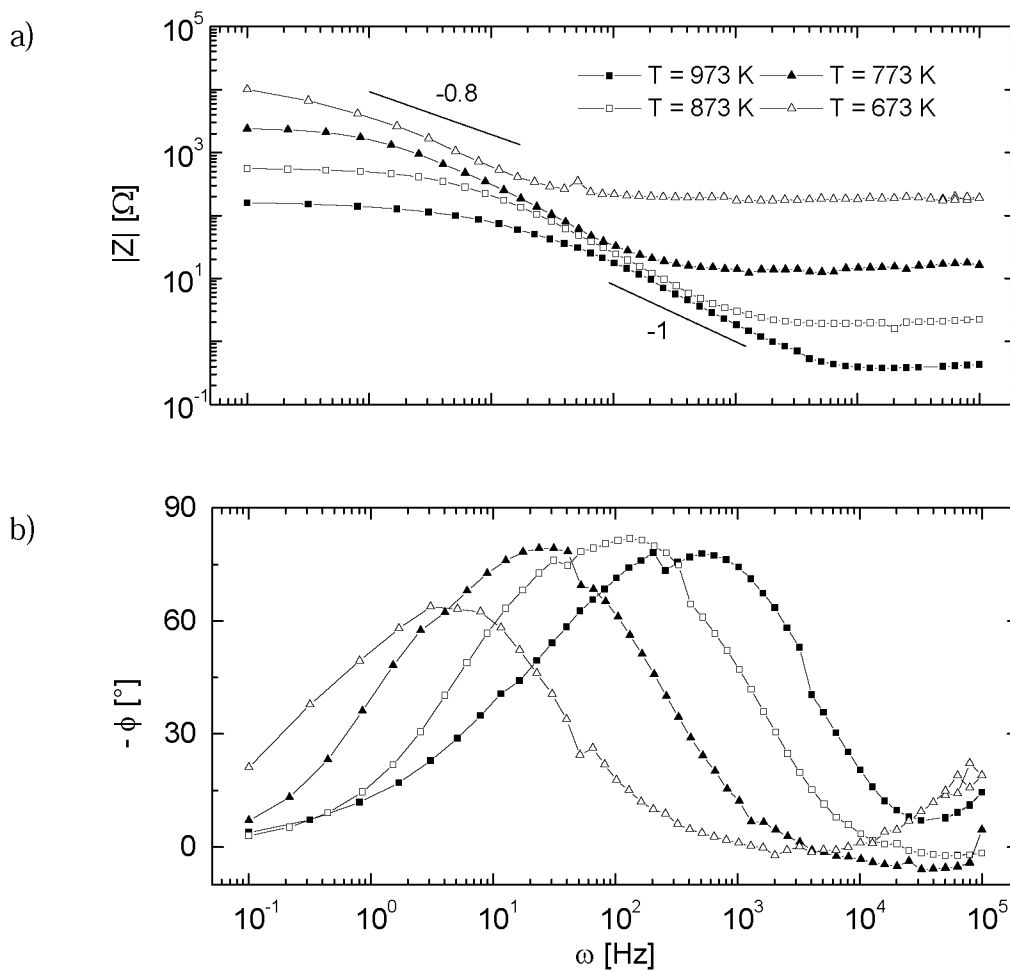


Fig. 3.21: Electrochemical impedance data as a function of the temperature (for the experimental conditions see Tab. 3.4). Note that the data is not corrected for R_e . The lines are drawn to guide the eye.

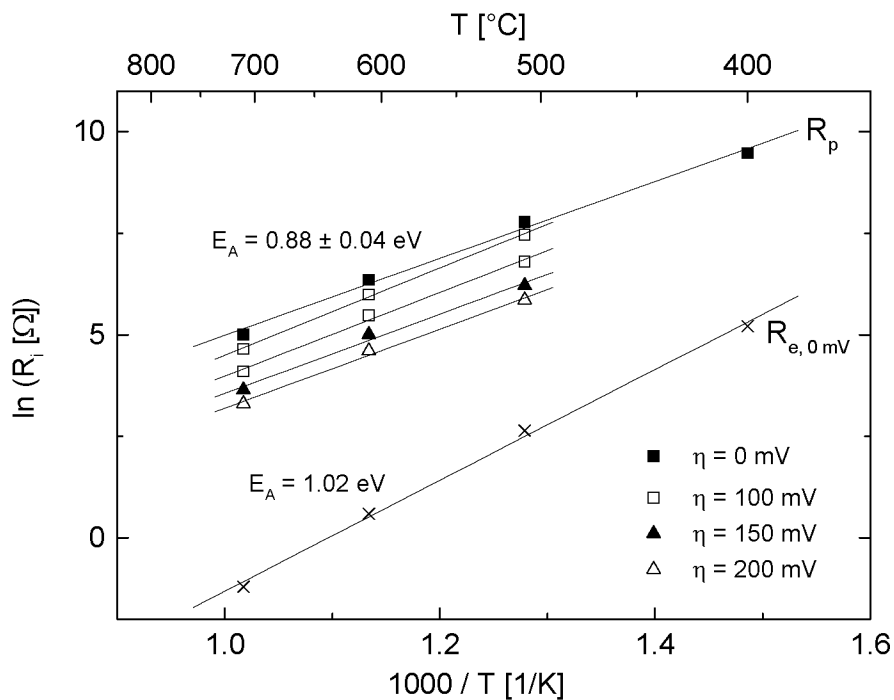


Fig. 3.22: Polarization resistance, R_p , and electrolyte resistance, R_e , as a function of the temperature, T (for the experimental conditions see Tab. 3.4). Note that R_p is corrected for R_e .

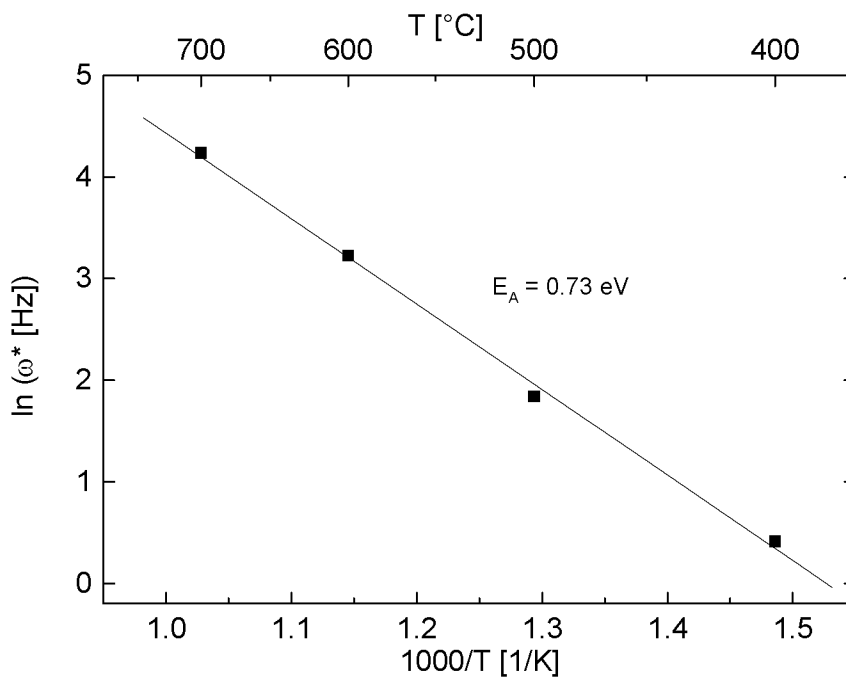


Fig. 3.23: Relaxation frequency, ω^* , as a function of the temperature, T , at $\eta = 0$ mV (for the experimental conditions see Tab. 3.4).

The impedance data was fitted to an equivalent circuit model of the form $R_e(C_{dl}(R_t(R_1Q_1)))$. The activation energies for the different equivalent circuit elements are listed in Tab. 3.5. The resistance R_1 and the relaxation frequency ω_1 have the same activation energies as R_p (Fig. 3.22) and ω^* (Fig. 3.23) determined directly from the experiments. The activation energy for the charge transfer resistance R_t is also similar to R_1 and to R_p . The activation energy of R_e determined from equivalent circuit fitting is very similar to the R_e determined from impedance measurements as well as to the R_e determined by four point in-plane conductivity measurements of the YSZ single crystal containing 9.5 mol% Y_2O_3 . All these three values for the activation energy of R_e correspond quite well to the values found in the literature where an activation energy of 1.0 eV - 1.08 eV is reported for 9 mol% yttria stabilized zirconia [49,50]. The capacitive elements, C_{dl} and Q_1 , are not significantly thermally activated.

Tab. 3.5: Activation energies of the equivalent circuit elements $R_e(C_{dl}(R_t(R_1Q_1)))$ compared to the experimentally determined activation energies from the impedance parameters R_e , R_p , and ω^ at $673 K < T < 973 K$.*

Method	Characteristic parameter	E_A [eV]
equivalent circuit fitting	R_e	1.15
“	C_{dl}	0.09
“	R_t	0.73
“	R_1	0.87
“	Q_1	0.23
“	ω_1	0.5-0.7
EIS measurement	R_p	0.88
“	ω^*	0.73
“	R_e	1.02
4 point conductivity measurement	“	1.18
literature [49,50]	“	1.0-1.08

3.3.2.5 Pattern Geometry

Triple Phase Boundary (TPB) Length

The TPB of Ni, YSZ, and pores is the site where the electrochemistry at the anode is assumed to take place. In order to study the influence of the TPB on the characteristic impedance parameters, i.e. R_p , ω , η , j , the TPB length was varied between 0.04 m/cm^2 and 13 m/cm^2 (Anodes 1 - 4, Tab. 3.3). It is found that an increase in the TPB length results in a decrease of the polarization resistance (Fig. 3.24). In the entire range of TPB lengths measured here, R_p decreased with a slope of about -0.7 independently of the applied overpotential. Assuming that the electrochemical reactions are localized at the TPB line, a slope of -1 is expected meaning that the electrode conductivity which is $1/R_p$ is directly proportional to the TPB length. A close view on the data yields a slope of around -1 only for high TPB lengths (Fig. 3.24). The R_p at a small TPB length ($l_{\text{TPB}} = 0.04 \text{ m/cm}^2$) deviates considerably from this behavior and R_p seems to be underestimated. This is probably due to the fact that the dense sputtered Ni layer contains considerably more defects, such as scratches or holes, than it is predicted from the microstructural characterization. The electrochemistry can, thus, take place at a larger number of sites than assumed and the polarization resistance is, in consequence, smaller than expected.

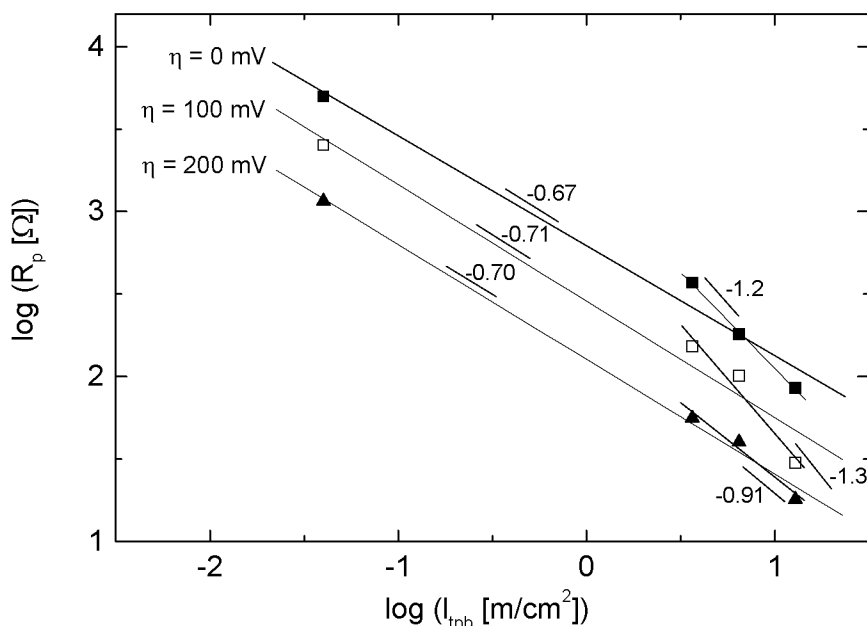


Fig. 3.24: Polarization resistance, R_p , as a function of the TPB length, l_{TPB} , (Anode 1 - 4, Tab. 3.3) at different overpotentials, η (for the experimental conditions see Tab. 3.4).

The electrode conductivity, σ , which is $1/R_p$, is shown in a linear plot versus the TPB length (Fig. 3.25). Here, the deviation of the polarization resistance at small TPB length does not affect the data due to the linear representation. A perfect, linear relation between the electrode conductivity, σ , and the length of the TPB, I_{TPB} , is found under equilibrium conditions ($\eta = 0$ mV) as well as under polarization ($\eta = 100$ mV and $\eta = 200$ mV).

The absolute values for the electrode conductivity in this study are very similar to those in [31], whereas the electrode conductivities in [29] are considerably lower (Fig. 3.26). We were able to measure the Ni pattern anodes in a larger range of I_{TPB} : 0.04 m/cm² - 13 m/cm² compared to 0 m/cm² - 6 m/cm² in [29] and 2 m/cm² - 11 m/cm² in [31]. Also, the quality of the pattern anodes seems to be better in this study. The data scattered much less compared to both references, in particular for long TPB lengths, i.e. 6 m/cm² in [29] and 11 m/cm² in [31]. Note that only the fitted lines are shown for the literature data.

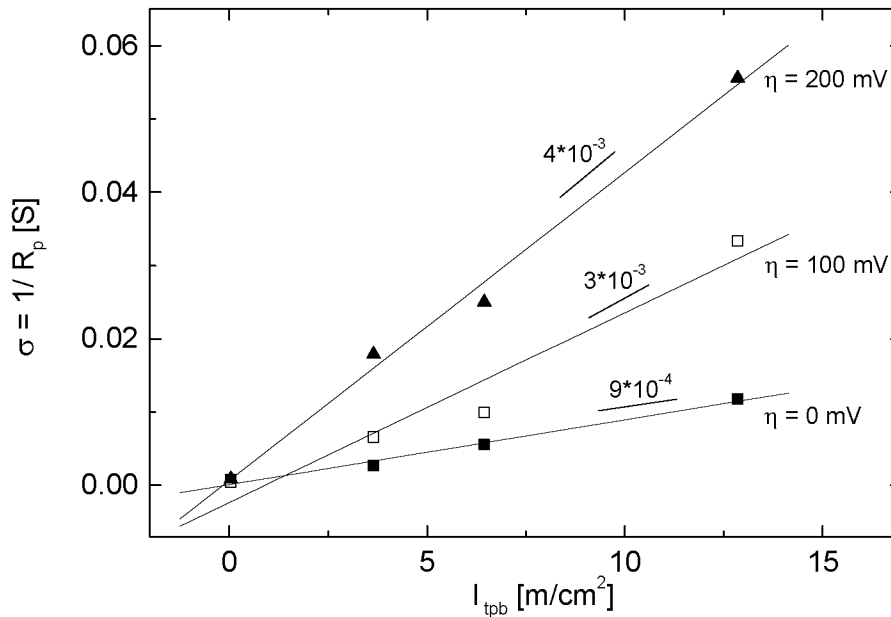


Fig. 3.25: Electrode conductivity, $\sigma = 1/R_p$, as a function of the TPB length, I_{TPB} , at different overpotentials, η (for the experimental conditions see Tab. 3.4).

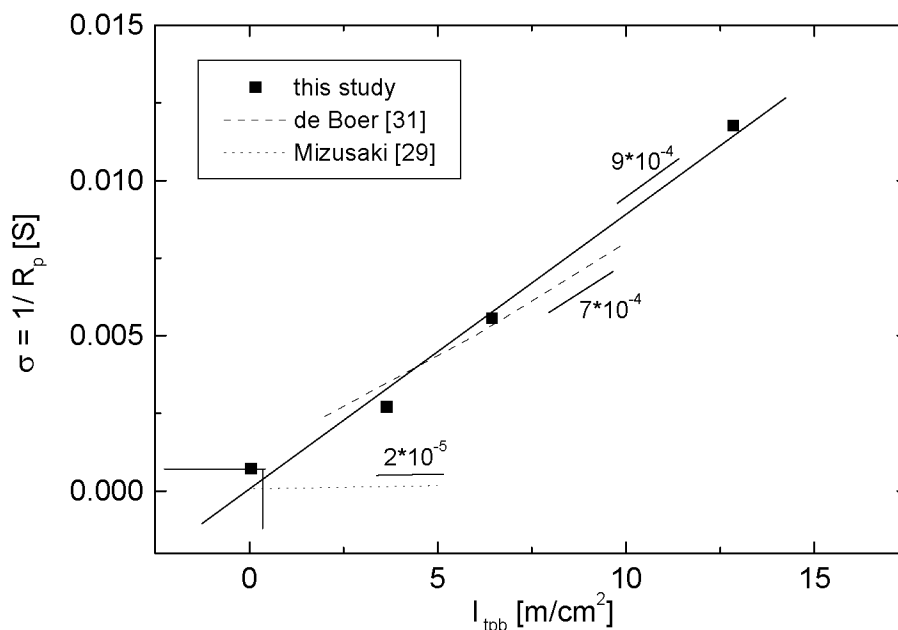


Fig. 3.26: Comparison of the electrode conductivities, σ , at $\eta = 0$ mV obtained in this study with those in the literature for similar systems (for the experimental conditions see Tab. 3.4). Only the fitted lines are shown for the literature data.

The current density, j , measured in addition to the impedance data is shown as a function of the TPB length in Fig. 3.27. A linear behavior between j and I_{TPB} is expected, if the geometrical TPB is the only region where the anodic reactions can take place. Indeed, a linear relation is found for small TPB lengths ($I_{TPB} < 6.5$ m/cm²), whereas a considerable deviation from the linear behavior is found for $I_{TPB} = 13$ m/cm². A linear continuation of the low TPB data at $\eta = 200$ mV would result in a TPB length around 20 m/cm² for a current density of about 7 mA/cm². An error of about 50 % in the determination of the TPB length would result. However, due to considerably smaller average errors in the determination of the TPB length (cf. subsection 3.3.1), the deviation from the linear behavior in Fig. 3.27 should not alone be due to the TPB length.

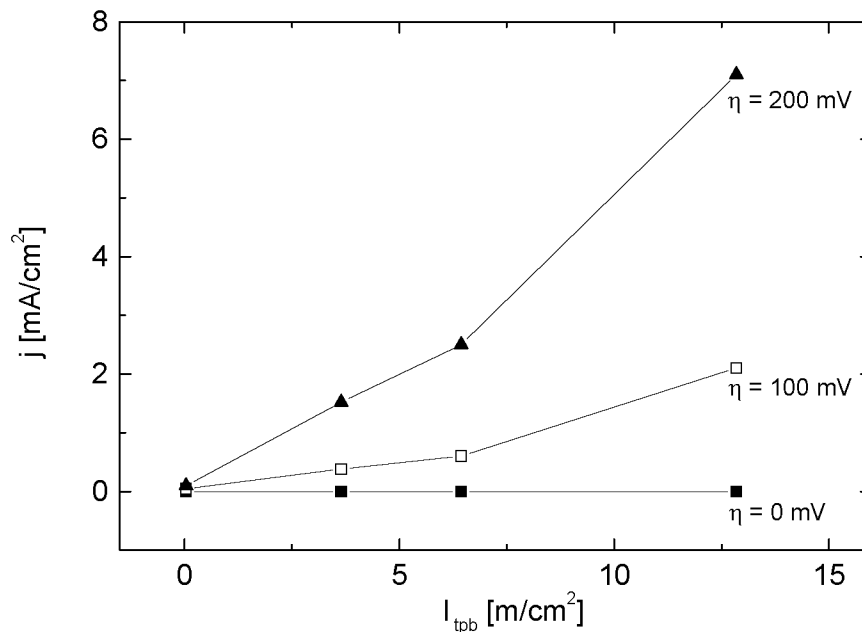


Fig. 3.27: Current density, j , as a function of the TPB length, I_{TPB} , at different overpotentials, η (for the experimental conditions see Tab. 3.4). The lines are drawn to guide the eye.

The same nonlinearity which was noticed in the current density plot (Fig. 3.27) shows up also in the relaxation frequency data as a function of the TPB length (Fig. 3.28). The low TPB region shows a linear relation between the relaxation frequency and the TPB length, whereas a considerable deviation can be noticed at long TPB. It can also be extracted from Fig. 3.28 that ω^* tends towards 0 Hz at very low TPB lengths ($I_{TPB} = 0.04$ m/cm²). This indicates that the predominant electrode process which is detected in the impedance spectra is connected to the existence of the TPB line. Hence, the main electrode process is directly coupled to the TPB.

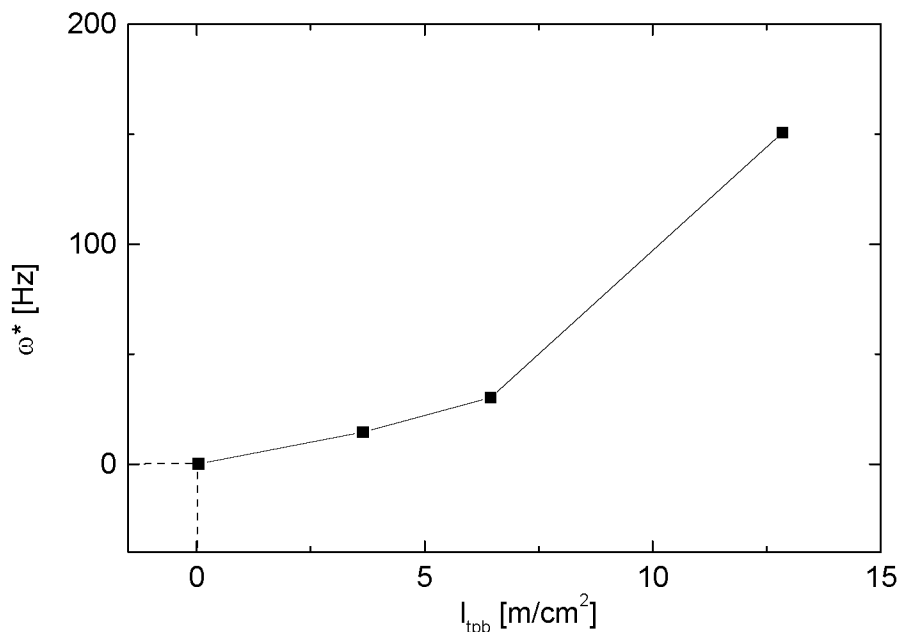


Fig. 3.28: Relaxation frequency, ω^* , as a function of the TPB length, l_{TPB} , at $\eta = 0$ mV (for the experimental conditions see Tab. 3.4). The lines are drawn to guide the eye.

The impedance data is fitted to the ordinary equivalent circuit with one RQ element: $R_e(C_{dl}(R_t(R_1Q_1)))$ (Fig. 3.29). It was not possible to obtain perfect equivalent circuit fits of the impedance data neither with this equivalent circuit nor with more complex ones. The errors were, in particular, high for the charge transfer resistance, R_t , which seems to be negligible due to very low fitting values of $< 10^{-2} \Omega$. The contribution of the electrolyte resistance, R_e , is very low with values around 0.5Ω . The double layer capacitance, C_{dl} , obtained values between 10^{-4} F and 10^{-6} F, when increasing the TPB length from 0.04 m/cm² to 13 m/cm². The fitting results for the R_1Q_1 element are shown in Fig. 3.29. The inverse resistance R_1 (Fig. 3.29a) behaves in the same way as the total electrode conductivity shown in Fig. 3.25. Also, the relaxation frequency of the R_1Q_1 element, ω^*_{1} (Fig. 3.29b), shows a very similar behavior as the relaxation frequency determined in Fig. 3.28. However, it must be noted that it was not possible to fit all anodes with the same exponent, n , of the CPE. The n values varied between 0.5 and 1.

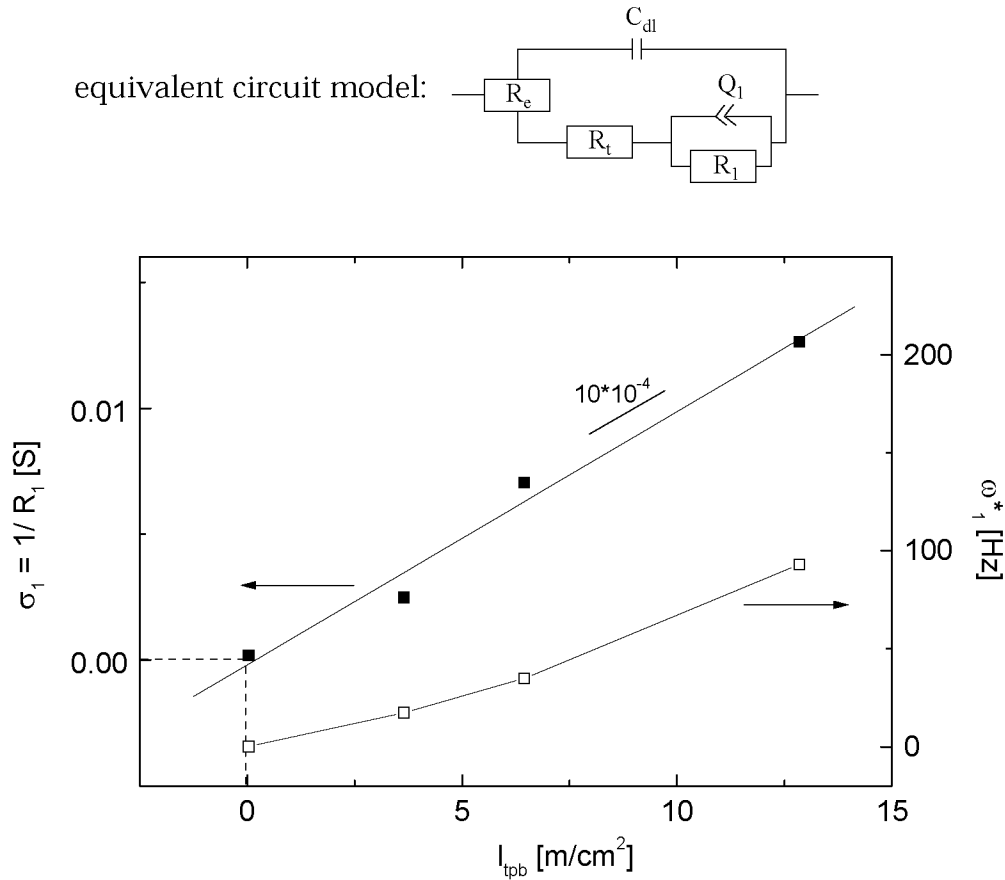


Fig. 3.29: Equivalent circuit ($R_e(C_{dl}(R_t(R_1Q_1)))$) fitting results as a function of the TPB length, I_{TPB} , at $\eta = 0$ mV: resistive element, R_1 , and relaxation frequency, ω^*_1 (for the experimental conditions see Tab. 3.4). The lines for ω^*_1 are drawn to guide the eye.

Line Width of Ni Stripes

The influence of the Ni surface coverage on the electrochemistry of Ni pattern anodes was studied by varying the line width of the Ni and of the YSZ stripes, respectively. The TPB length (I_{TPB} around 0.2 m/cm²) as well as the total anode area (1 cm²) were kept constant. The anode design is explained in Fig. 3.2 and the different anodes (Anodes 5 - 8) are listed in Tab. 3.3. It is found that the polarization resistance increased slightly with increasing line width of the Ni stripes. However, as the data scatters and as the data is overlaid by errors due to the determination of the TPB length, this small increase is negligible. Thus, the imped-

ance measurements prove rather that only the length of the TPB and neither the design of the pattern nor the Ni coverage determines the anode performance.

The current characteristics in Fig. 3.30 shows a small decrease of the current with increasing Ni line width. The decrease of the current density is most evident at high overpotentials ($\eta = 200$ mV). As an increase in the Ni line width signifies an increase in the Ni coverage of the YSZ electrolyte, the current density behavior in Fig. 3.30 might indicate that the YSZ surface plays an active role in the anode kinetics.

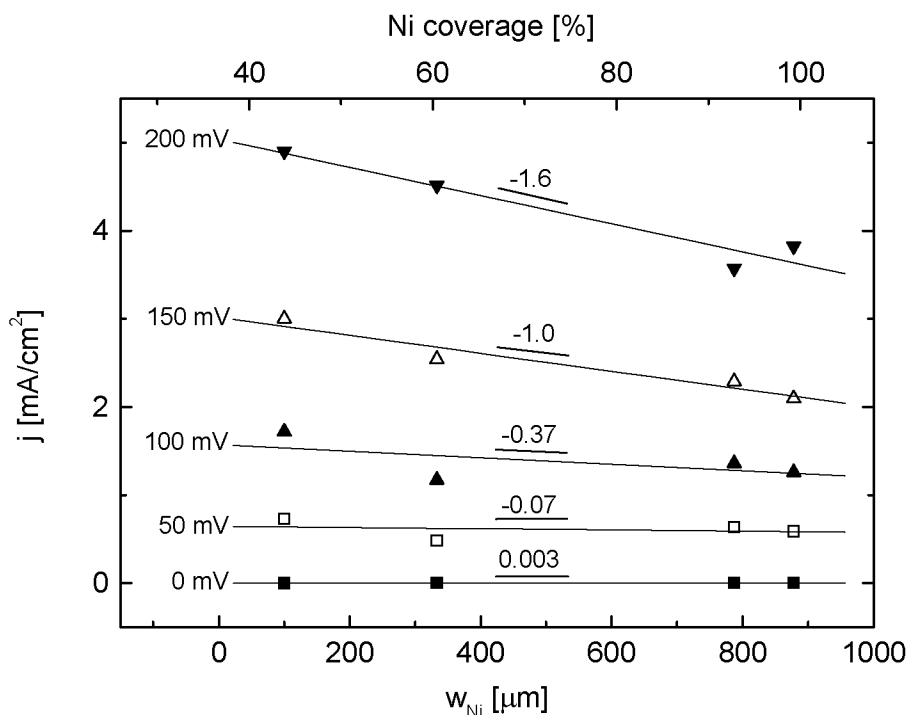


Fig. 3.30: Current density, j , as a function of the Ni line width, w_{Ni} (Anodes 5 - 8, Tab. 3.3) (for the experimental conditions see Tab. 3.4).

3.4 Discussion

The study is based on the investigation of simplified SOFC anodes, so-called Ni pattern anodes. The various results indicate that these model anodes give a lot of information about the electrochemistry of the anodic SOFC system which is so far not understood in detail.

In terms of the microstructure, it was found that Ni pattern anodes can be pre-

pared stably and reproducibly on YSZ single crystal electrolytes using reactive magnetron sputtering and wet chemical etching. Unfortunately, the method of wet chemical etching is restricted to line widths of at least 5 μm corresponding to a maximum TPB length of 13 m/cm^2 .

The miscellaneous data on the electrochemistry of Ni pattern anodes clearly indicate that Ni pattern anodes are dominated in a very broad range of experimental conditions by one main electrode process ($673\text{ K} < T < 973\text{ K}$, $10^4\text{ Pa} < p(\text{H}_2) < 8.8 \cdot 10^4\text{ Pa}$, $40\text{ Pa} < p(\text{H}_2\text{O}) < 2 \cdot 10^3\text{ Pa}$, $10\text{ ml}/\text{min} < \text{total gas flow} < 100\text{ ml}/\text{min}$, $0\text{ mV} < \eta < 300\text{ mV}$, $0.04\text{ m}/\text{cm}^2 < I_{\text{TPB}} < 13\text{ m}/\text{cm}^2$). However, the arcs in the Nyquist plot are no perfect semicircles and the bell curves of the phase angle vs. the frequency are broadened for low overpotential and for low partial pressure of water. Hence, a second effect may contribute to the response of the anode. In equivalent circuit fitting, an additional RQ element cannot ameliorate the fitting results and the double layer capacitance can also not fully compensate for this effect. Thus, a frequency shift might also be responsible for the broadening of the phase angle vs. the frequency according to [48]. At very high overpotential ($\eta = 400\text{ mV}$), two processes are clearly separated (Fig. 3.9).

The main electrode process is found to be directly correlated to the TPB length: the electrode conductivity which is one over the polarization resistance depends linearly on the TPB length (Fig. 3.25). This means that exactly this process, which is responsible for the limitation of the anode kinetics at the TPB, is represented by the main impedance arc. The polarization resistance is found not to be a suitable parameter as a function of the TPB length: in a double logarithmic plot, failures in the anode microstructure are more dominant at anodes with a short TPB length compared to anodes with a longer TPB length (Fig. 3.24). In the linear plot of the electrode conductivity, this effect does not distort the relation between the electrode performance and the TPB length (Fig. 3.25). Since both the electrode conductivity (Fig. 3.26) as well as the relaxation frequency (Fig. 3.28) pass the origin of the plots, no other effect disturbs the impedance results than the TPB process. Thus, the impedance arc is no artifact which is due to the measurement set-up or due to the sample geometry. This is important to notice, as many electrochemical data on Ni-YSZ cermet anodes are suffering from these problems so that the basic electrode effect is hidden.

All experimental data were fitted to an equivalent circuit model. This method of interpreting EIS data is rather controversial, as the physical and the chemical interpretation of the single equivalent circuit elements is ambiguous and not

straight-forward [33,56,57]. It is often possible to build different equivalent circuit models which allow to fit a set of data appropriately. In this study, the equivalent circuit model $R_e(C_{dl}(R_t(R_1Q_1)))$ was found to fit the data under all operating conditions rather well. The R_1Q_1 element always dominates the impedance response, whereas R_e and R_t are almost negligible.

The electrode response is mainly influenced by four parameters: the overpotential, the temperature, the partial pressure of water, and the TPB length. An increase of all of these parameters decreases the polarization resistance as well as the relaxation time of the main electrode process. Although similar in their final effect, the impact of the four parameters on the electrode behavior is very different in nature: applying an overpotential results in a higher amount of oxygen, most probably in form of O^{2-} , at the anode side of the SOFC. An increase of the temperature facilitates the chemical and the electrochemical reactions which are thermally activated. A higher partial pressure of water in the fuel gas increases the partial pressure of oxygen at the anode side of the fuel cell. A longer TPB length simply offers a larger number of reaction sites at the anode and could, thus, decrease the total electrode impedance.

Now, the question arises which chemical or electrochemical process might be responsible for the main arc in the impedance spectra. Diffusion is frequently proposed as the rate limiting reaction step in anode kinetics not only for Ni-YSZ cermet electrodes [28-30,35,36,38,41,42]. Diffusion effects can be identified in a Nyquist plot by a 45° tangent to the high frequency data [45] or in the current-voltage characteristic by a constant current density despite increasing overpotential. For the Ni pattern anodes in this study, no diffusion limitations were observed in the spectra for a large range of experimental conditions, i.e. $673\text{ K} < T < 973\text{ K}$, $10^4\text{ Pa} < p(\text{H}_2) < 8.8 \cdot 10^4\text{ Pa}$, $40\text{ Pa} < p(\text{H}_2\text{O}) < 2 \cdot 10^3\text{ Pa}$, $10\text{ ml/min} < \text{total gas flow} < 100\text{ ml/min}$, $0\text{ mV} < \eta < 300\text{ mV}$, $0.04\text{ m/cm}^2 < I_{\text{TPB}} < 13\text{ m/cm}^2$. Moreover, the activation energy of the main impedance arc of $E_A = 0.88\text{ eV}$ seems to be much too high for a diffusion limited process.

Only at high overpotentials (Fig. 3.9) as well as with a coverage of the electrode in combination with an overpotential (Fig. 3.15), the system can be driven into diffusion limitation. High overpotentials signify that a lot of oxygen is pushed through the electrolyte and is available at the anode. On the other side, the coverage of the anode pattern with a Ni net and a YSZ single crystal plate signifies a barrier for the fuel gas to reach the TPB and for the exhaust gas (water vapor) to

be removed from the reaction zone. These two examples where diffusion seems to limit the anode kinetics are, in principle, not so different: in both cases, the diffusion effect might be either due to gas phase diffusion of H_2 and/or H_2O to the catalytic Ni surface or due to surface diffusion of adsorbed surface species. Since an increase of the partial pressure of hydrogen in the gas phase did not decrease the diffusion effect at the anode with diffusion barrier, the amount of hydrogen in the gas phase, i.e. gas phase diffusion of H_2 , can be ruled out as being responsible for the diffusion limitation. The diffusion of water away from the TPB region is a very feasible kind of diffusion, in particular, as the diffusion effects are more distinct at high overpotential where a lot of water is produced (Fig. 3.9, Fig. 3.15). This would also explain why diffusion effects can more often be observed in the case of Ni-YSZ cermet anodes: the three dimensional, porous microstructure might trap water which is then hindered to desorb into the gas phase. In the case of Ni pattern anodes, the very open, two dimensional microstructure is, thus, considerably less susceptible to diffusion effects.

Surface diffusion is another possible kind of diffusion process which was already suggested as a feasible limitation of the anode kinetics in the literature [28-30,35,36,38,41,42]. Due to the high diffusion coefficient of hydrogen on Ni ($(D(H))_{T=973\text{ K}} = 4 \cdot 10^{-8} \text{ m}^2/\text{s}$ [53,54]) and due to the low activation energy for the diffusion of hydrogen ($E_A = 0.16 \text{ eV}$ [54]), hydrogen should be the diffusing species in this system and, hence, surface diffusion should not be responsible for the small diffusion effect at the anode with a diffusion barrier.

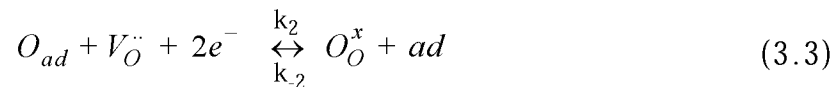
Besides surface and gas phase diffusion, the bulk diffusion of oxygen ions through the electrolyte has to be considered. According to the literature, the activation energy for oxygen conduction in 9 mol% YSZ reaches values between 1.0 eV and 1.08 eV [49]. In the impedance measurements in this study, the activation energy for the electrolyte resistance, R_e , was 1.02 eV (Tab. 3.5). However, the main impedance arc in the EIS measurements has a more than 10 % smaller activation energy of 0.88 eV (Fig. 3.23, Tab. 3.5). Hence, bulk diffusion of oxygen should most probably not contribute to the limitations of the anode kinetics.

Summarizing the discussion about diffusion, it is found that diffusion is not dominating the reaction mechanism of Ni pattern anodes. Only under specific operating conditions, a diffusion effect can be observed which can most probably be attributed to the diffusion of water away from the TPB region.

Apart from diffusion, charge transfer is another feasible limiting process at

SOFC anodes. According to the results from equivalent circuit fitting, the single charge transfer resistance, R_t , does not limit the electrode process under any experimental conditions (Fig. 3.12, Fig. 3.16, Fig.). The charge transfer resistance determined from equivalent circuit fitting is always very low ($R_t < 2 \Omega$) and also several orders of magnitude smaller than the resistance from the R_1Q_1 element. A separate arc in the high frequency region due to R_t in combination with C_{dl} cannot be observed. The R_1Q_1 element itself can also be related to a charge transfer reaction, most probably to a charge transfer process related to ions due to the low frequency region where the process appears in the Nyquist diagram. The activation energy of $E_A = 0.88$ eV found for the main impedance arc does not exclude charge transfer as limiting process (Fig. 3.22, Fig. 3.23, Tab. 3.5). Hence, it can be concluded that the so-called charge transfer resistance in the equivalent circuit fitting, R_t , is not limiting the electrode reaction and is not of significant importance here. The main impedance arc which is characterized by R_1Q_1 , might, however, include a charge transfer reaction. In [31], a charge transfer limitation of the electrode process was suggested due to the linear relationship that was found between the electrode conductivity and the TPB length. The data is fitted with three RQ elements where one of those represented the charge transfer reaction. Hence, in summary, it should be noticed that a charge transfer reaction in combination with a mass transfer could limit the kinetics of Ni pattern anodes.

Besides diffusion and charge transfer, the removal of O^{2-} from the electrolyte has to be considered for the identification of the rate limiting process at Ni pattern anodes. So far, no reliable model exists in the literature which describes and explains the removal of oxygen at the anode side of the SOFC. In [28,30], it is suggested that the interstitial oxygen in the YSZ releases two electrons to the Ni and adsorbs as oxygen atom at the TPB. In [31] and in [21], the interstitial oxygen in the YSZ receives a hydrogen, so that a hydroxyl group (OH_o^-) forms in the YSZ and adsorbs afterwards on the YSZ surface or on the Ni surface, respectively, including a charge transfer step. Finally, the immediate formation and desorption of water is proposed in [35]. Hence, it follows that the removal of O^{2-} from the electrolyte at the anode side of the SOFC is so far not clearly understood. For the cathode side, i.e. the Pt, O_2 | YSZ system, the following reaction mechanism is predicted



An activation energy of 1.3 eV to 1.4 eV was determined for this process in [57]. This activation energy is considerably higher than the activation energy which was determined for the main impedance arc in this study ($E_A = 0.88$ eV (Fig. 3.22, Tab. 3.5)). Hence, the same mechanism is not expected to take place at the anode side. However, due to the considerable differences of the two systems, a definite prediction concerning the rate limiting process cannot be drawn and the removal of O^{2-} from the electrolyte is still a feasible reaction which could be responsible for the main impedance arc found in this study.

Finally, adsorption and desorption reactions have to be discussed as possible limitations of the anodic reaction mechanisms. Possible processes are the adsorption of hydrogen and the adsorption / desorption of water (The desorption of hydrogen is considered as a minor reaction step and is therefore not discussed here.). An increase of the overpotential as well as a longer TPB length both result in a larger amount of O^{2-} on the surface of the anode (Note that we refer to the absolute concentrations here). Due to the high affinity of hydrogen to oxygen, an enhanced adsorption of hydrogen could then result in a lower polarization resistance as found in Fig. 3.9 and Fig. 3.24. In addition, an increase in the partial pressure of water should increase the number of hydroxyl species on the YSZ surface which should facilitate the adsorption of hydrogen as well. With regard to the temperature dependence, a very similar activation energy was found for the main electrode process in this study ($E_A = 0.88$ eV, Fig. 3.22, Fig. 3.23, Tab. 3.5) and the activation energy for the adsorption / desorption of hydrogen in the literature ($E_A = 1.0$ eV [55]). The observation that the partial pressure of hydrogen has no significant influence on the main impedance arc (Fig. 3.13), does not exclude the adsorption of hydrogen as the rate limiting step, because only very little hydrogen is needed for the maintenance of the overall fuel cell process at Ni pattern anodes. Hence, the main impedance arc in the EIS plots could be related to the adsorption of hydrogen.

Concerning the adsorption and the desorption of water, one has to distinguish between the water which is added to the fuel gas atmosphere and which adsorbs onto the Ni and onto the YSZ surface, and the water which is produced during the operation of the fuel cell and which desorbs into the fuel gas atmosphere. It is expected that both sources of water result in a decrease of the total electrode resistance. In the first case, it is assumed that the water can adsorb on both the Ni surface as well as on the YSZ surface. For the adsorption of water on a clean Ni surface, an activation energy of 0.4 eV is quoted in the literature, whereas an ac-

tivation energy of 0.7 eV is recorded for the adsorption on an oxygen modified Ni surface [58]. The model of an oxygen modified surface seems to be more appropriate for the Ni, H₂-H₂O | YSZ system discussed in this study. The adsorption of water on YSZ is studied in detail in [59]. Two activation energies are found by thermo-gravimetry: $E_{A,1} = 0.94$ eV and $E_{A,2} = 0.70$ eV [59]. Comparing these activation energies with the experimentally found activation energy for the main impedance arc, i.e. $E_A = 0.88$ eV (Fig. 3.22, Fig. 3.23, Tab. 3.5), an adsorption / desorption process of water either on Ni or on YSZ could both limit the electrode process. However, the observation that a higher overpotential decreases the impedance cannot be explained by a limitation due to the adsorption / desorption of water. A higher overpotential should increase the impedance, if it is related to the desorption of water, since more water is produced. The adsorption of water should also rather impede the electrode process, as the additional oxygen from the gas phase occupies surface sites which are designated for the removal of O²⁻ from the electrolyte. The adsorption and the desorption of water should therefore not be represented by the main impedance arc.

The catalytic effect of the partial pressure of water on the anode performance illustrated, for instance, in Fig. 3.18 must be discussed in more detail. In the literature, it is suggested that small amounts of water added to the fuel gas increase the concentration of adsorbed oxygen sites or lead to the formation of sub-surface oxide sites on the Ni surface [35,36]. This is assumed to enhance the hydrogen adsorption / dissociation and diffusion by the so-called spillover mechanism [35,36,54]. Spillover denotes the possibility of a molecule to adsorb or to react in a multiphase system (usually a metal-oxide composite) on one of the constituents before diffusing over onto the second phase where it reacts with a different adsorbed species and might desorb afterwards [54]. The multiphase system consists here of the metallic Ni and the YSZ electrolyte. The hydrogen is assumed to dissociate on the Ni surface and to diffuse to the TPB where it reacts with the oxygen to form hydroxyl and water. The addition of water in the fuel gas is assumed to enhance the spillover effect, since more adsorbed oxygen or sub-surface oxygen species are provided on the Ni surface [35,36]. This explanation for the catalytic effect of water is not completely satisfying, since the additional oxygen species due to the wet fuel gas atmosphere are described as being very closely related to the Ni surface. Moreover, the status of the electrolyte surface is only very roughly described and a detailed model concerning the charge distribution and transfer

is not given (for instance, the charge balance in [35] (Eq. 11) is questionable).

Including the electrolyte surface and referring to the model of spillover, we propose the following hypothesis for the catalytic effect of water: in a dry fuel gas atmosphere, the YSZ surface is assumed to be primarily covered with oxygen. The electrochemically active sites are restricted to the vicinity of the TPB. In contrast to this, the YSZ surface will most probably be hydroxylated in a wet fuel gas atmosphere (Fig. 3.31a). The existence of hydroxyl groups on a zirconia surface at high temperatures is discussed in [59]. The catalytic effect of water might be explained by the mechanism illustrated in Fig. 3.31a to Fig. 3.31d. A summary is shown in the center of Fig. 3.31.

At first, H_2 adsorbs onto the Ni surface and O^{2-} diffuses to the YSZ surface (Fig. 3.31a). Then, the hydrogen atoms are oxidized to H^+ on the Ni surface and the O^{2-} is removed from the YSZ bulk (Fig. 3.31b). Due to the strong basicity of the O^{2-} , an adjacent hydroxyl group on the YSZ is deprotonated (Fig. 3.31b). Note that the small arrows indicate the shift of the electronic bond. In Fig. 3.31c, the following cascade of protonation and deprotonation reactions of the hydroxyl groups on the YSZ surface is shown. The driving force for these steps is the neutralization reaction due to acidity of the H^+ and the basicity of the negative oxygen centers on the YSZ surface. The protonation and the deprotonation reactions represent an effective proton migration from the Ni to the basic center. In Fig. 3.31d, a second H^+ migrates towards this basic center. Water is formed and desorbs from the YSZ surface. Hence, the situation illustrated in Fig. 3.31a is reached again and the process can be iterated.

The peculiarity of this mechanism is due to the fact that the O^{2-} which is removed from the electrolyte far away from the TPB, is included into the anode kinetics. This mechanism seems to be unique for a wet fuel gas atmosphere where the electrochemically active region is enlarged due to a hydroxylated YSZ surface. Hence, the anode kinetics is facilitated and the performance of the anode is better compared to a dry fuel gas atmosphere, where the YSZ surface is not hydroxylated so that the electrochemistry can only take place directly at the TPB.

Finally, the second process which appears at a very high overpotential will only shortly be discussed, since it was merely observed under one experimental condition, i.e. $\eta = 400$ mV, Fig. 3.9. It was found that this process has a very small relaxation frequency, thus, signifying a very slow process. At equilibrium and at low overpotential, this process cannot be separated from the main impedance arc.

The total electrode impedance increases in the case that the second arc appears. Due to these characteristics and following the discussion above, this process can most probably be attributed to the desorption of water which might limit the electrode process in the case when a lot of water is produced at the TPB.

3.5 Summary

The kinetics of simplified SOFC anodes were studied using Ni pattern anodes with TPB lengths between 0.04 m/cm^2 and 13 m/cm^2 . Microstructural as well as electrochemical characterization methods validated the benefit of these investigations compared to studies of the complex state-of-the-art Ni-YSZ cermet anodes. In a wide range of experimental conditions, Ni pattern electrodes were found to be limited by one main electrode process. This process is attributed to either the adsorption / desorption of hydrogen or to the removal of oxygen from the electrolyte. Both processes might be combined with a charge transfer reaction. The desorption of water as well as diffusion effects seem not to limit the kinetics of Ni pattern anodes under most experimental conditions. The partial pressure of water in the fuel gas atmosphere is found to have a catalytic effect on the anode kinetics. A detailed mechanism for the catalytic effect is proposed. It considers a hydroxylated YSZ surface which allows the migration of H^+ on the YSZ. Hence, O^{2-} which is removed far away from the TPB, is incorporated into the anodic reaction mechanism. The electrochemically active region for the anode kinetics is enlarged so that the performance of the anode increases.

3.6 References

- [1] N.Q. Minh, T. Takahashi, "Science and Technology of Ceramic Fuel Cells", Elsevier, Amsterdam, The Netherlands (1995).
- [2] S.C. Singhal, Proc. of the 6th Intern. Symp. on Solid Oxide Fuel Cells (SOFC-VI), Honolulu, Hawaii, USA, Eds.: S.C. Singhal, M. Dokiya (1999) 39.
- [3] H. Mori, H. Omura, N. Hisatome, K. Ikeda, K. Tomida, Proc. of the 6th Intern. Symposium on Solid Oxide Fuel Cells (SOFC-VI), Honolulu, Hawaii, USA, Eds.: S.C. Singhal, M. Dokiya (1999) 52.
- [4] R. Bolden, K. Föger, T. Pham, Proc. of the 6th Intern. Symp. on Solid Oxide Fuel Cells (SOFC-VI), Honolulu, Hawaii, USA, Eds.: S.C. Singhal, M. Dokiya (1999) 80.

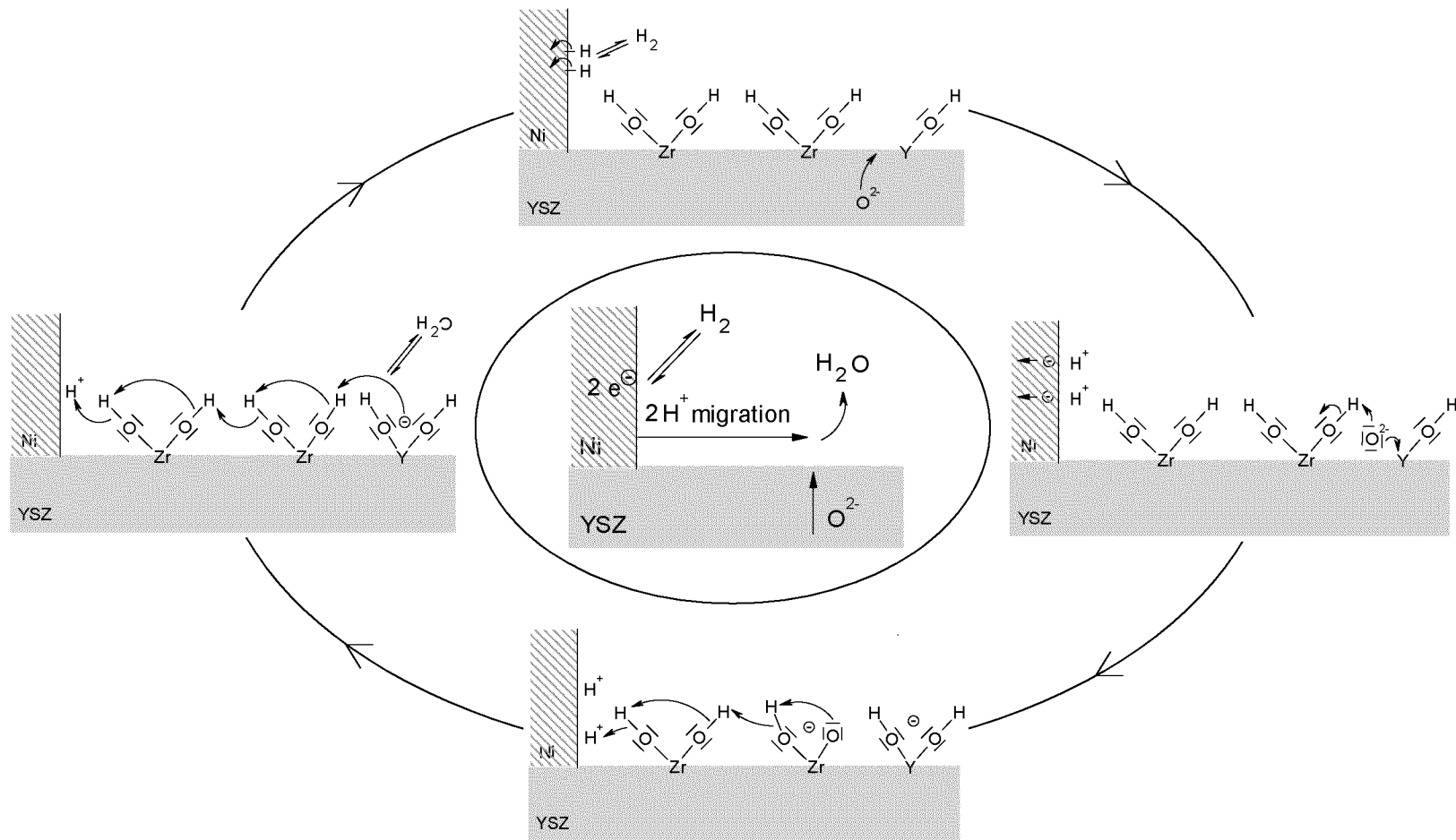


Fig. 3.31: Model for the catalytic effect of the addition of water in the fuel gas atmosphere on the performance of SOFC anodes. The small arrows indicate the migration of the electrons. For detailed information refer to the text.

-
- [5] P. Ekanayake, M. Gödickemeier, L.J. Gauckler, Proc. of the 5th Asian Conf. on Solid State Ionics: New Developments, Eds.: B.V.R. Chowdari, M.A.K.L. Dissanayake, M.A. Careem, World Scientific Publishing, Singapore (1996) 535.
- [6] H. Itho, T. Yamamoto, M. Mori, T. Watanabe, T. Abe, *Denki Kagaku* **64** (1996) 549.
- [7] H. Itho, T. Yamamoto, M. Mori, T. Horita, N. Sakai, H. Yokokawa, M. Dokiya, *J. Electrochem. Soc.* **144** (1997) 641.
- [8] M. Suzuki, H. Sasaki, S. Otsoshi, A. Kajimura, M. Ippommatsu, *Solid State Ionics* **62** (1993) 125.
- [9] H. Uchida, H. Suzuki, M. Watanabe, *J. Electrochem. Soc.* **145** (1998) 615.
- [10] H. Uchida, T. Osuga, M. Watanabe, *J. Electrochem. Soc.* **146** (1999) 1677.
- [11] T. Horita, N. Sakai, H. Yokokawa, M. Dokiya, T. Kawada, *Solid State Ionics* **86-88** (1996) 1259.
- [12] T. Tsai, S.A. Barnett, *J. Electrochem. Soc.* **145** (1998) 1696.
- [13] T. Kawada, N. Sakai, H. Yokokawa, M. Dokiya, M. Mori, T. Iwata, *Solid State Ionics* **40/41**(1990) 402.
- [14] T. Norby, P. Kofstad, Proc. of the 17th Risø Intern. Symp. on Mat. Sci.: High Temperature Electrochemistry: Ceramics and Metals, Eds.: F.W. Poulsen, N. Bonanos, S. Linderorth, M. Mogensen, B. Zachau-Christiansen, Risø National Laboratory, Roskilde, Denmark (1996) 381.
- [15] J. Geyer, H. Kohlmüller, H. Landes, R. Stübner, Proc. of the 5th Intern. Symp. on Solid Oxide Fuel Cells (SOFC-V), Aachen, Germany, Eds.: U. Stimming, S.C. Singhal, H. Tagawa, W. Lehnert (1997) 585.
- [16] S. Primdahl, M. Mogensen, *J. Electrochem. Soc.* **144** (1997) 3409.
- [17] M. Mogensen, S. Skaarup, *Solid State Ionics* **86-88** (1996) 1151.
- [18] M. Mogensen, S. Sunde, S. Primdahl, Proc. of the 17th Risø Intern. Symp. on Mat. Sci.: High Temperature Electrochemistry: Ceramics and Metals, Eds.: F.W. Poulsen, N. Bonanos, S. Linderorth, M. Mogensen, B. Zachau-Christiansen, Risø National Laboratory, Roskilde, Denmark (1996) 77.
- [19] S. Sunde, *Electrochim. Acta* **42** (1997) 2637.
- [20] P. Holtappels, L.G.J. de Haart, U. Stimming, *J. Electrochem. Soc.* **146** (1999) 1620.
- [21] P. Holtappels, L.G.J. de Haart, U. Stimming, *J. Electrochem. Soc.* **146** (1999) 2976.
- [22] J. Divisek, A. Kornyshev, W. Lehnert, U. Stimming, I.C. Vinke, K. Wippermann, Proc. of the 5th Intern. Symp. on Solid Oxide Fuel Cells (SOFC-V), Aachen, Germany, Eds.: U. Stimming, S.C. Singhal, H. Tagawa, W. Lehnert (1997) 606.
- [23] J. Divisek, L.G.J. de Haart, P. Holtappels, T. Lennartz, W. Mallener, U. Stimming, K. Wippermann, *J. Power Sources* **49** (1994) 257.
- [24] J. Divisek, L.G.J. de Haart, P. Holtappels, U. Stimming, I.C. Vinke, Proc. of the 17th Risø Intern. Symp. on Mat. Sci.: High Temperature Electrochemistry: Ceramics and Metals, Eds.: F.W. Poulsen, N. Bonanos, S. Linderorth, M. Mogensen, B. Zachau-Christiansen, Risø National Laboratory, Roskilde, Denmark (1996) 235.

-
- [25] S. Primdahl, PhD Thesis, University of Twente, Twente, The Netherlands (1999).
- [26] S. Primdahl, M. Mogensen, *J. Electrochem. Soc.* **145** (1998) 2431.
- [27] S. Primdahl, M. Mogensen, *J. Electrochem. Soc.* **146** (1999) 2827.
- [28] J. Mizusaki, H. Tagawa, T. Saito, T. Yamamura, K. Kamitani, K. Hirano, S. Ehara, T. Takagi, T. Hikita, M. Ippomatsu, S. Nakagawa, K. Hashimoto, *Solid State Ionics* **70/71** (1994) 52.
- [29] J. Mizusaki, H. Tagawa, T. Saito, K. Kamitani, T. Yamamura, K. Hirano, S. Ehara, T. Takagi, T. Hikita, M. Ippomatsu, S. Nakagawa, K. Hashimoto, *J. Electrochem. Soc.* **141** (1994) 2129.
- [30] J. Mizusaki, T. Yamamura, N. Mori, H. Tagawa, K. Hirano, S. Ehara, T. Takagi, M. Hishinuma, H. Sasaki, T. Sogi, Y. Nakamura, K. Hashimoto, Proc. of the 17th Risø Intern. Symp. on Mat. Sci.: High Temperature Electrochemistry: Ceramics and Metals, Eds.: F.W. Poulsen, N. Bonanos, S. Linderoth, M. Mogensen, B. Zachau-Christiansen, Risø National Laboratory, Roskilde, Denmark (1996) 363.
- [31] B. de Boer, PhD Thesis, University of Twente, Twente, The Netherlands (1998).
- [32] T. Norby, O.J. Velle, H. Leth-Olsen, R. Tundold, Proc. of the 3rd Intern. Symp. on Solid Oxide Fuel Cells (SOFC-III), Honolulu, Hawaii, USA, Eds.: S.C. Singhal, H. Iwahara (1993) 473.
- [33] R.J. Aaberg, PhD Thesis, NTNU Trondheim, Trondheim, Norway (1998).
- [34] F.Z. Mohamedi-Boulenouar, J. Guindet, A. Hammou, Proc. of the 5th Intern. Symp. on Solid Oxide Fuel Cells (SOFC-V), Aachen, Germany, Eds.: U. Stimming, S.C. Singhal, H. Tagawa, W. Lehnert (1997) 441.
- [35] S.P. Jiang, S.P.S. Badwal, *J. Electrochem. Soc.* **144** (1997) 3777.
- [36] S.P. Jiang, S.P.S. Badwal, *Solid State Ionics* **123** (1999) 209.
- [37] S.P. Jiang, S.P.S. Badwal, *Solid State Ionics* **122** (1999) 211.
- [38] N. Nakagawa, H. Sakurai, K. Kondo, T. Morimoto, K. Hatanaka, K. Kato, *J. Electrochem. Soc.* **142** (1995) 3474.
- [39] T. Yamamura, H. Tagawa, T. Saito, J. Mizusaki, K. Kamitani, K. Hirano, S. Ehara, T. Takagi, Y. Hishinuma, H. Sasaki, T. Sodi, Y. Nakamura, K. Hashimoto, Proc. of the 4th Intern. Symp. on Solid Oxide Fuel Cells (SOFC-IV), Yokohama, Japan, Eds.: M. Dokiya, O. Yamamoto, H. Tagawa, S.C. Singhal (1995) 741.
- [40] T. Norby, Proc. of the 2nd Europ. Solid Oxide Fuel Cell Forum, Oslo, Norway, Ed.: B. Thorstensen (1996) 607.
- [41] N. Nakagawa, K. Kato, *Solid State Ionics* **98** (1997) 209.
- [42] N. Nakagawa, K. Nakajima, M. Sato, K. Kato, *J. Electrochem. Soc.* **146** (1999) 1290.
- [43] DMK/DPK, "Formeln und Tafeln", Orell Füssli Verlag Zürich, Zürich, Switzerland (1984) 174.
- [44] B.A. Boukamp, *Solid State Ionics* **20** (1986) 31.
- [45] C. Gabrielli, in: Use and Application of Electrochemical Impedance Techniques, Technical Report 24, Solartron Instruments, Hampshire, UK (1990) 2.34.
- [46] P.J. Gellings, H.J.M. Boumeester, "The CRC Handbook of Solid State Electrochemistry", CRC Press, Inc., New York, NY, USA (1997) 43.

-
- [47] J.O'M. Bockris, A.K.N. Reddy, "Modern Electrochemistry", Vol. 2, Plenum Publishing Corporation, New York, NY, USA (1977) 883.
- [48] J.R. Macdonald, "Impedance Spectroscopy", John Wiley & Sons, Inc., New York, NY, USA (1987).
- [49] M. Levy, J. Fouletier, M. Kleitz, *J. Electrochem. Soc.* **135** (1988) 1584.
- [50] J.-H. Park, R.N. Blumenthal, *J. Electrochem. Soc.* **136** (1989) 2867.
- [51] S. Skaarup, B. Zachau-Christiansen, T. Jacobsen, Proc. of the 17th Risø Intern. Symp. on Mat. Sci.: High Temperature Electrochemistry: Ceramics and Metals, Eds.: F.W. Poulsen, N. Bonanos, S. Linderth, M. Mogensen, B. Zachau-Christiansen, Risø National Laboratory, Roskilde, Denmark (1996) 423.
- [52] R. Lewis, R. Gomer, *Surf. Sci.* **12** (1968) 157.
- [53] K. Christmann, *Surf. Sci. Rep.* **9** (1988) 1.
- [54] G.A. Somorjai, "Introduction to Surface Chemistry and Catalysis", John Wiley & Sons, Inc., New York, USA (1994) 347.
- [55] P.A. Thiel, T.E. Madey, *Surf. Sci. Rep.* **7** (1987) 211.
- [56] H. Schichlein, M. Feuerstein, A. Müller, A. Weber, A. Krügel, E. Ivers-Tiffée, Proc. of the 6th Intern. Symp. on Solid Oxide Fuel Cells (SOFC-VI), Honolulu, Hawaii, USA, Eds.: S.C. Singhal, M. Dokiya, The Electrochemical Society, Inc., Pennington, NJ, USA (1999) 1069.
- [57] A. Mitterdorfer, PhD Thesis No. 12380, ETH Zürich, Zürich, Switzerland (1997).
- [58] V.I. Avdeev, I.I. Zakharov, *J. Struct. Chem.* **33** (1992) 185.
- [59] S. Raz, K. Sasaki, J. Maier, I. Riess, *Solid State Ionics* (2000) submitted.

Chapter 4

Ni-Based SOFC Anodes: Microstructure and Electrochemistry

Abstract

Different types of Ni-based SOFC anodes, metallic Ni anodes and Ni-YSZ cermet anodes, were studied in terms of their microstructure and of their electrochemical behavior. The metallic Ni anodes consisted either of a Ni pattern, a Ni gauze, or a Ni paste. The Ni-YSZ cermet anodes were deposited by screen-printing, by sputtering, or by electrostatic spraying. According to electrochemical impedance spectroscopy (EIS) measurements, the anodes were dominated by two main impedance arcs signifying two main relaxation processes. The high frequency impedance arc was found to decrease exponentially with an applied overpotential and to be thermally activated with an activation energy of around 1 eV. With regard to the results obtained in chapter 3, this process is attributed to the adsorption of hydrogen including charge transfer. The low frequency impedance arc arises only under a high overpotential applied between the working and the reference anode. The impedance increases the higher the overpotential and is thermally activated with an activation energy of 0.5 eV. The process is assigned to the desorption of water.

4.1 Introduction

The performance of SOFC (solid oxide fuel cell) anodes is found to be strongly dependent on the material (composition, powder characteristics, etc.) as well as on the preparation and on the deposition techniques of the anode on the electrolyte. It is well known that a high electrical conductivity and a microstructure with three well interconnected phases of Ni catalyst, of YSZ electrolyte, and of pores are advantageous for a high performance [1-6]. However, unfortunately, little information is available on the kinetics of the anodic reactions [1,4,7-10]. The reaction mechanisms at SOFC anodes are not clearly understood and the limiting processes at the anode are not known. Hence, it is rather challenging at the moment to improve the performance of SOFC anodes.

In the literature, many measurements concerning the performance or the electrochemistry of SOFC anodes were carried out in recent years. The performance varies considerably from research group to research group [8,11-14]. In terms of the electrochemical characterization, the results from different research groups are inconsistent concerning the number of the impedance arcs, the activation energies of the main electrode process, as well as the rate limiting reaction steps [8,11-17]. The disagreement is obvious, since the results are based on rather different experimental conditions (anode design including anode deposition, electrical contact, location of the reference electrode, measurement set-up, etc.).

Facing these difficulties, Primdahl *et al.* measured four different anodes under the same experimental conditions and compared them in terms of the microstructure, the electrochemical impedance spectra (EIS), the thermal activation energies, as well as the composition of the fuel gas [11,18]. One main impedance arc was found for a range of electrode structures. Concerning the thermal activation of the main electrode process, a distinct tendency towards lower activation energies was observed for fine cermets and Ni anodes covering a high percentage of the electrolyte surface, whereas higher activation energies were observed for coarse cermets and Ni anodes covering a lower percentage of the electrolyte surface [11]. It is proposed that n-type conductivity in the electrolyte surface is the limiting process with high activation energy at 1273 K. The measurements were merely carried out under equilibrium conditions, i.e. without any polarization of the anode. Due to the rather different measurement conditions and set-up compared to our studies, it is difficult to compare the results with the findings in chapter 3.

De Boer *et al.* also studied the influence of the microstructure of SOFC anodes on the electrochemical behavior [14,19]. Detailed studies on specifically modified SOFC anodes manifested an active role of the YSZ in the Ni-YSZ cermet anodes [19]. The dominant impedance arc is attributed to a charge transfer process which is not specified further [14].

In chapter 3 of this thesis, the kinetics of simplified Ni anodes, so-called Ni pattern anodes, were investigated in detail. One main impedance arc was found for these model anodes. It is attributed to either the adsorption of hydrogen including charge transfer or to the electronation of oxygen at the interface of the anode and of the electrolyte. These results are the basis for the investigation of the kinetics of the more complex Ni-YSZ cermet anodes in this chapter. If more information is available concerning the kinetics of these anodes, it might be possible to modify the state-of-the-art anodes specifically and, thus, to improve the performance considerably.

Hence, it is the aim of this chapter to study different types of Ni-based anodes with regard to their kinetic behavior. The anodes differ in terms of the materials selection (metallic Ni anodes and Ni-YSZ cermet anodes) and in terms of the preparation technique (sputtering, painting, screen-printing, electrostatic spraying). The anodes were all measured under the same experimental conditions. The overpotential applied between the anode and the reference anode as well as the temperature were the main experimental parameters. In continuation to chapter 3, the main focus was attributed to the understanding of the rate limiting reaction steps. It was studied whether similar effects can be observed for the different anodes so that general tendencies for the reaction mechanisms at SOFC anodes can be drawn from the results.

4.2 Experimental

4.2.1 Preparation of Ni-Based Anodes

Six different types of Ni-based anodes were prepared in this study. The anodes differed in their composition (metallic Ni anode and Ni-YSZ cermet anode) and in their preparation technique. The metallic Ni anodes are denominated as Ni pattern anode, Ni gauze anode, and porous Ni anode. The Ni-YSZ cermet anodes can be distinguished by the deposition technique: screen-printing, sputtering,

and electrostatic spraying. These three methods are either already used or are very promising to use for the deposition of electrodes in SOFC systems.

All anodes prepared in this study have an area of 1 cm^2 and were prepared on an electrolyte of 9.5 mol% Y_2O_3 -stabilized ZrO_2 single crystal (25 mm in diameter, 0.5 mm thick, (001) orientation, polished on both sides) (Zirmat Corp., Westford, MA, USA). The reference anodes covering an area of 4 mm^2 were prepared in parallel to the working anodes, i.e. they consisted of the same material and were deposited in the same way as the working anode. The reference anodes were placed at a distance of 4 mm from the working anode. The geometrical design is illustrated in chapter 3 (Fig. 3.1) of this thesis. In the following, the experimental conditions for the deposition of the different anodes designs considered in this chapter are described shortly.

The Ni pattern anode was prepared from a dense, $1 \text{ }\mu\text{m}$ thick, metallic Ni film which was deposited on the entire surface of the YSZ electrolyte by DC magnetron sputtering (Sulzer, Winterthur, CH). A specially designed Ni target was used which accounts for the magnetic properties of Ni. The following sputter parameters were used: DC bias = -50 V, Ar flow = 18 sccm, pressure during deposition = $3 \cdot 10^{-3}$ mbar, power at the target = 650 W, deposition time = 60 min. After deposition, the Ni layer was structured in two steps using the photolithography technique and wet chemical etching. The photoresist (S1813, Shipley, Kempraten-Rapperswil, CH) was spin-coated with a rotation speed of 4000 rotations/s for 45 s (thickness about $1.3 \text{ }\mu\text{m}$) and was exposed using a halogen lamp for 15 s. The photoresist was developed for about 15 s and the pattern was etched for 45 s - 60 s in diluted nitric acid (1:19 = 65 % nitric acid : deionized water). First, a 1 cm^2 square electrode was etched. In a second step, the line pattern with equidistant lines of Ni and of YSZ with a line width of $20 \text{ }\mu\text{m}$ was etched within a square of $0.8 \text{ cm} \cdot 0.8 \text{ cm}$. The Ni pattern anode prepared in this study had a theoretical triple phase boundary (TPB) length of 3.7 m/cm^2 . More detailed information about the preparation and about the design of Ni pattern anodes is given in chapter 3 (subsection 3.2.1). The anode and the reference anode were connected with Au wire (99.99 %, 0.3 mm in diameter), Au gauze (52 mesh, woven from 0.102 mm Au wire), and Au paste (type C5754B, Heraeus GmbH, Hanau, D) at the edges of the Ni pattern (cf. Fig. 3.1 in chapter 3). All precious metals were obtained from Johnson Matthey & Brandenberger AG, Zürich, CH.

The Ni gauze anode consists of a 1 cm^2 Ni gauze (150 mesh, woven from 0.1 mm Ni wire, Paul GmbH, Metallgewebe und Filterfabrik, Steinau, D) which

was fixed with a two component binder (type 1500, Firag, Ebmatingen, CH) between two pieces of single crystalline YSZ. The electrical contact was realized by spot-welding of Pt wires onto the Ni gauze. No paste was used for further contact.

The Ni paste anode is assigned to the metallic Ni anodes, even though it contains small amounts of YSZ (10 wt.%). The Ni paste was obtained from S. Primdahl, Risø National Laboratory, Risø, Denmark. The preparation of the Ni paste is described in detail in [11]. It was applied with a brush on top of the single crystalline YSZ electrolyte. The electrical contact was realized with a Pt gauze (52 mesh, woven from 0.1 mm Pt wire) pressed onto the wet Ni paste over the entire surface of the anode.

The screen-printed Ni-YSZ anode was prepared as described in [6]. The screen-printing recipes for the inorganics and for the organics are listed in Tab. 4.1. After the preparation of the green paste, the anode was screen-printed using a non-automated screen-printing machine from Dickfilm System AG, Bergdietikon, CH. A screen-printing mask for a theoretical green film thickness of 50 μm was used. The anode was contacted with a Pt gauze and diluted Ni-YSZ paste over the entire surface of the anode. It was sintered at a maximum temperature of 1623 K (sintering program: heating rate 1 K/min up to 873 K, 2 h dwell time, heating rate 3 K/min up to 1623 K, 2 h dwell time, cooling rate 5 K/min).

The sputtered Ni-YSZ anode was prepared by reactive magnetron sputtering from a NiZrYO_x target (Sulzer Innotec, Winterthur, CH). The following parameters were used: DC bias = -50 V, Ar flow = 18 sccm, pressure during deposition = $7 \cdot 10^{-4}$ mbar, deposition time = 75 min. After deposition, the anode was electrically contacted with a Pt gauze (52 mesh, woven from 0.1 mm Pt wire) and Pt paste (type C3605P, Heraeus GmbH, Hanau, D) covering the entire surface of the anode.

The electrostatically sprayed Ni-YSZ anode was prepared from a solution (0.05 mol/l) of NiNO₃, ZrO(NO₃)₂, and Y(NO₃)₃ and ethanol mixed with diethylene-glycol-monobutyl-ether (3:1). The ratio of NiO : 8YSZ was 70 : 30. The following spray parameters were chosen: $T_{\text{heating plate}} = 723$ K, $T_{\text{substrate}} = 593$ K, $V = 20$ kV, pumpage = 5.8 ml/min, $\text{distance}_{\text{substrate-nozzle}} = 120$ mm. The electrical contact of the anode was realized with an Au gauze (52 mesh, woven from 0.102 mm Au wire) and Au paste (type C5754B, Heraeus GmbH, Hanau, D) covering the entire anode.

Tab. 4.1: Recipes for the Ni-YSZ cermet paste used for screen-printing.

Inorganics	Grain size [μm]	Quantity [wt%]	Supplier	Lotnumber
NiO	0.1	26.6	Baker, Deventer, The Netherlands	649150
NiO + 8 YSZ	0.2 + 1.0	66.8	SSC, Woodinville, Washington, USA	03-P1268BM
8 YSZ	0.06	6.60	Tosoh, Japan	Z800846P

Organics	Quantity [g]	Function	Supplier	Productnumber Lotnumber
Diethylenglycol-monobutyletheracetate	28.0	solvent	Fluka Chemie, Buchs, CH	32260 401899/150600
Ethylcellulose	5.76	binder	Fluka Chemie, Buchs, CH	46070 327568/21295
Beycostat	1.50	dispersant	CECA, Paris, F	C213 73226

In order to study the influence of the contacting materials, i.e. Pt and Au, on the electrochemical behavior, Pt and Au anodes were prepared separately. The electrodes were prepared by sputtering a thin layer of the corresponding metal on the single crystalline electrolyte and by contacting the layer using the corresponding gauze and paste.

The cathodes which were the same for all SOFCs were prepared by DC-sputtering (model SCD 040, Baltec, Balzers, FL) of a 30 nm thick Pt layer on the single crystalline YSZ electrolyte. The cathodes were placed symmetrically to the anode on the opposite side of the single crystal. They were connected with a Pt wire (0.35 mm in diameter), Pt gauze (52 mesh, woven from 0.1 mm Pt wire), and Pt paste (type C3605P, Heraeus GmbH, Hanau, D) on the entire 1 cm² surface area of the cathode. The precious metals were obtained from Johnson Matthey & Brandenberger AG, Zürich, CH. The wires and gauzes were fixed on the electrolyte with a ceramic two-component binder (type 1500, Firag, Ebmatingen, CH).

4.2.2 Electrochemical Characterization

The electrochemical measurements were carried out in a single gas chamber measurement set-up which is described in detail in chapter 3 (subsection 3.2.2).

A discussion concerning impedance measurements in a single gas chamber and in two gas chambers is given in appendix 2.

The impedance measurements were carried out with an IM6 ZAHNER[®] Impedance Analyzer, Kronach, D, in a three electrode, four lead configuration. The electrical connections are described in chapter 1 and the standard conditions are summarized in Tab. 4.2. The impedances of the different anodes were not only measured under standard conditions, but also at overpotentials, η , between 0 mV and 400 mV and at temperatures between 673 K and 1173 K. The fuel gas consisted of a mixture of H₂ and N₂ equal to 1:3 (total gas pressure = 1 atm, purity of the gases > 99.5 %). The gas flow was adjusted with manual mass flow controls (Vögtlin Instruments AG, Aesch, CH).

Tab. 4.2: Standard experimental conditions for the EIS measurements of the different anode designs.

Quantity	Symbol	Value	Unit
Temperature	T	973	K
Total gas flow	F	40	ml/min
Partial pressure of hydrogen	$p(\text{H}_2)$	$1.5 \cdot 10^4$	Pa
Partial pressure of water	$p(\text{H}_2\text{O})$	$5 \cdot 10^1$	Pa
Overpotential	η	0 mV	mV
Frequency	f	$10^{-3} - 10^3$	Hz
Excitation voltage	V_{exc}	10	mV

4.3 Results and Discussion

4.3.1 Microstructure

Due to the different anode designs and due to the different electrode preparation techniques, the anodes considered in this study consist of rather different microstructures. Whereas the Ni pattern and the Ni gauze anode have a well-defined, two dimensional region for the chemical and the electrochemical reactions to take place, the other anodes have a three dimensional microstructure where Ni and YSZ are interconnected in a complicated manner. The TPB (triple

phase boundary), i.e. the region where the catalyst Ni, the electrolyte YSZ, and the pores are interconnected, is not exactly known in the case of Ni-YSZ cermet anodes. However, it is much longer compared to Ni pattern and Ni gauze anodes. Scanning Electron Micrograph (SEM) images of the six anodes are shown in Fig. 4.1 and are discussed in the following paragraphs.

The Ni pattern anode consists of lines of Ni and YSZ with a width of 20 μm and a height of 1 μm (Fig. 4.1a). According to the anode design, this line width results in a TPB length of 3.7 m/cm^2 for the entire anode. The microstructure allows a direct contact of the fuel gas with the area where the chemical and the electrochemical reactions take place. It is found that the anode microstructure is not destroyed by thermal treatment or by electrochemical measurements. More detailed information about the microstructure of Ni pattern anodes is given in chapter 3 and appendix 1 as well as in [20].

The microstructure of the Ni gauze anode is determined by the mesh size of the Ni gauze (Fig. 4.1b). Due to the woven structure of the gauze, the anode touches the electrolyte only at the cross points of two wires. Hence, the Ni gauze anode is, in effect, a point electrode made of several, single contacts. It does not degrade under the experimental conditions used in this study.

A cross section image of the Ni paste anode is illustrated in Fig. 4.1c. The anode is 40 μm - 60 μm thick and has a porous microstructure. The Ni paste anode is well adhered to the electrolyte even after thermal treatment and electrochemical measurement. The inset illustrates that the paste anode mainly consists of Ni with small amounts of zirconia which is located on top of the large Ni grains (Energy Dispersive X-ray (EDX) analyses).

The screen-printed Ni-YSZ anode has a cross-section which looks rather similar to that of the Ni paste anode (Fig. 4.1d). The average thickness of the anode layer is 10 μm to 30 μm . The interface between the anode and the electrolyte indicates that the screen-printed anode is well adhered to the YSZ electrolyte. Using EDX analyses, it is possible to distinguish between Ni and Zr in general. However, it is not possible to see the difference between Ni and Zr in the SEM picture directly which is due to the three dimensional structure. No degradation effects due to thermal treatment and due to electrochemical measurements were found for the screen-printed Ni-YSZ cermet anode according to SEM analyses.

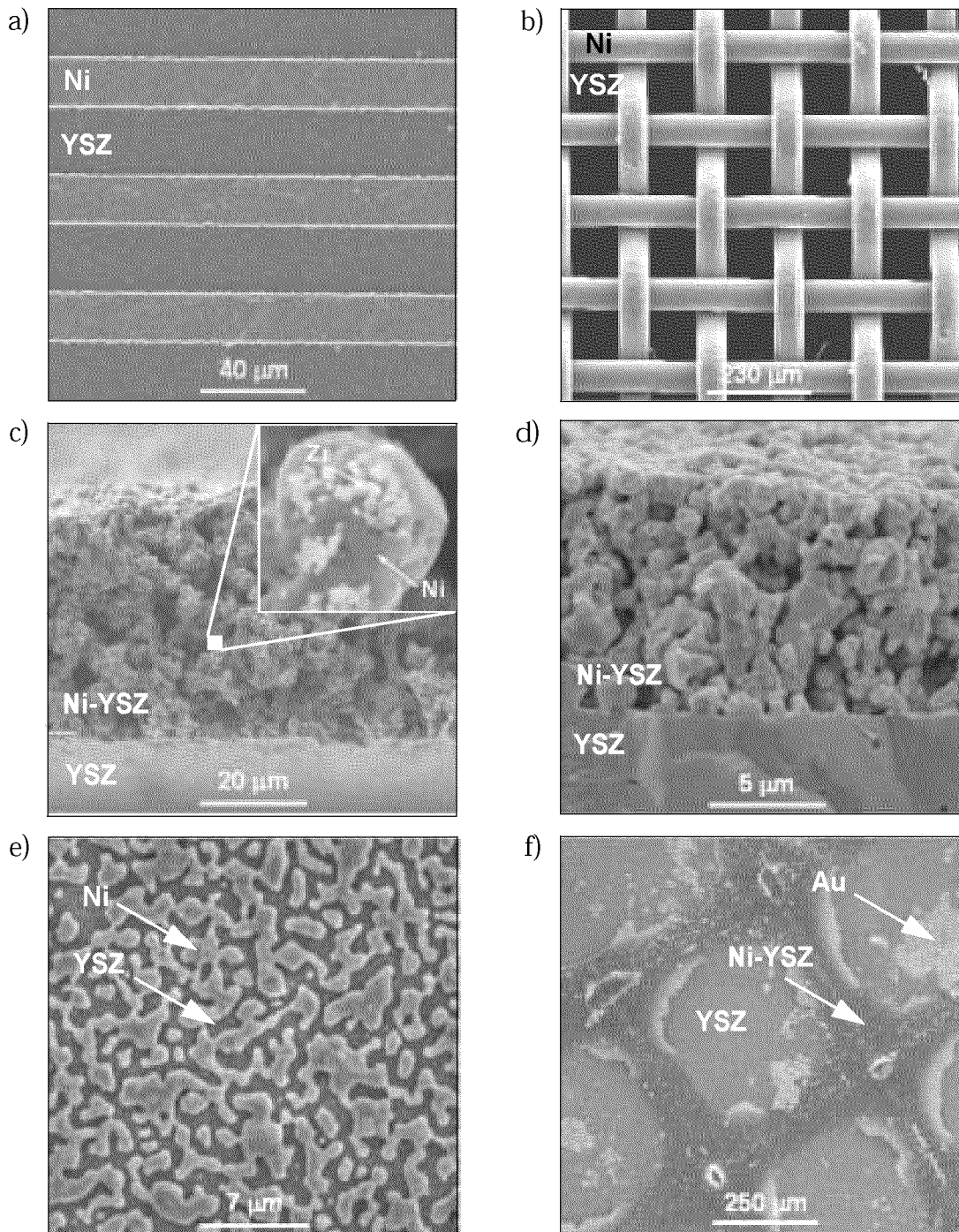


Fig. 4.1: Scanning electron micrographs of Ni-based anodes: a) Ni pattern anode (top view), b) Ni gauze anode (top view), c) Ni paste anode (cross section), d) screen-printed Ni-YSZ anode (cross section), e) sputtered Ni-YSZ anode (top view, after electrochemical measurement), f) electrostatically sprayed Ni-YSZ anode (top view, after electrochemical measurement).

The sputtered Ni-YSZ anode is 1 μm thick in the as-prepared state. During thermal treatment under reducing atmosphere, it degrades considerably so that distinct islands of Ni are formed. Fig. 4.1e illustrates the surface of the sputtered Ni-YSZ anode after the electrochemical characterization and after detaching the Pt gauze. The microstructure has no finely dispersed Ni-YSZ cermet structure and the coagulated Ni areas are not interconnected throughout the entire surface. Hence, the electrical contact is only realized by the Pt gauze and the Pt paste which are used for contacting. No close contact between the Pt gauze and the Pt paste on the one side and the Ni islands on the other side was found. The Pt gauze could be easily detached with the Pt paste from the Ni anode. According to EDX analysis, the Pt paste created no residue on the anode surface. A small sample which was thermocycled, but not electrochemically measured, had mainly the same microstructure as the one shown in Fig. 4.1e. Hence, the contacting as well as the electrochemical measurements have not deteriorated the microstructure of the anode.

The electrostatically sprayed Ni-YSZ anode is about 1 μm thick in the as-prepared state and forms a dense layer according to SEM images. After the electrochemical characterization, however, the anode layer is highly deteriorated so that the anode is not continuously attached to the electrolyte anymore (Fig. 4.1f). EDX analyses revealed that the spray deposited layer is accumulated in the vicinity of the Au mesh, while it is completely eliminated in the holes of the Au mesh. The bright regions in Fig. 4.1f originate from the Au paste which was used to ensure a good electrical contact.

4.3.2 Electrochemistry of Metallic Ni Anodes

4.3.2.1 Ni Pattern Anode

The electrochemistry of Ni pattern anodes is described in detail in chapter 3. In this chapter, the most important features are repeated and the main focus is addressed towards the comparison with other anode designs.

Ni pattern anodes are dominated by one main impedance arc under a large range of experimental conditions (Fig. 4.2). The anodes are not limited by diffusion which could be identified by a 45° so-called Warburg tangent to the high frequency impedance data [21]. No inductive loops neither in the low nor in the high frequency part of the Nyquist plot are observed. However, Ni pattern anodes react extremely sensitively to an overpotential applied between the anode and the

reference anode: the impedance decreases strongly with increasing overpotential. At a very high overpotential ($\eta = 400$ mV), a second impedance arc arises at low frequencies. In consequence, the total anode impedance increases (inset in Fig. 4.2). Fig. 4.3 illustrates the linear dependence of the relaxation frequency of the main impedance arc as a function of the overpotential. The relaxation frequency of the second impedance arc at $\eta = 400$ mV is around 0.1 Hz (not shown in Fig. 4.3).

As a function of the temperature (Fig. 4.4), the total anode impedance decreases and the relaxation frequency increases with increasing temperature. No remarkable changes in the shape of the impedance spectra are found. Diffusion effects are absent at all temperatures under consideration. A detailed discussion in terms of the activation energy is given in subsection 4.3.5.3.

4.3.2.2 Ni Gauze Anode

For the discussion of the Ni gauze anode, it should be noted that the Ni gauze is not strongly attached to the electrolyte, such as in the case of other anode designs. The Ni gauze anode is fixed at the four corners of the gauze using a two component binder. In addition, a piece of YSZ single crystal is used as cover. This cover might be a barrier for the fuel gas to reach the electrochemically active region. The impedance analysis indicates that the electrochemical response of the Ni gauze anode is determined by two characteristic relaxation times (Fig. 4.5): the high frequency relaxation process does not form a well-defined semicircle, even though it can be clearly separated from the low frequency relaxation process. The low frequency arc is not a closed semicircle and the maximum of the semicircle is not reached up to an angular frequency of 0.6 Hz. Thus, the characteristic relaxation frequencies cannot be analyzed for this anode design.

The inset in Fig. 4.5 shows that the applied overpotential has the most influence on the low frequency impedance data, whereas the high frequency impedance is namely the same for all overpotentials. The inset also predicts a rather high value for the electrolyte resistance (around 14 Ω) which is characterized by the high frequency intercept of the impedance data with the real axis. It is assumed that this high value for the electrolyte resistance is due to the bad contact of the Ni gauze anode to the electrolyte. The rather flat increase of the impedance in the high frequency region should finally be noted. A 45° tangent fits well to the data indicating that the Ni gauze anode might be limited by diffusion.

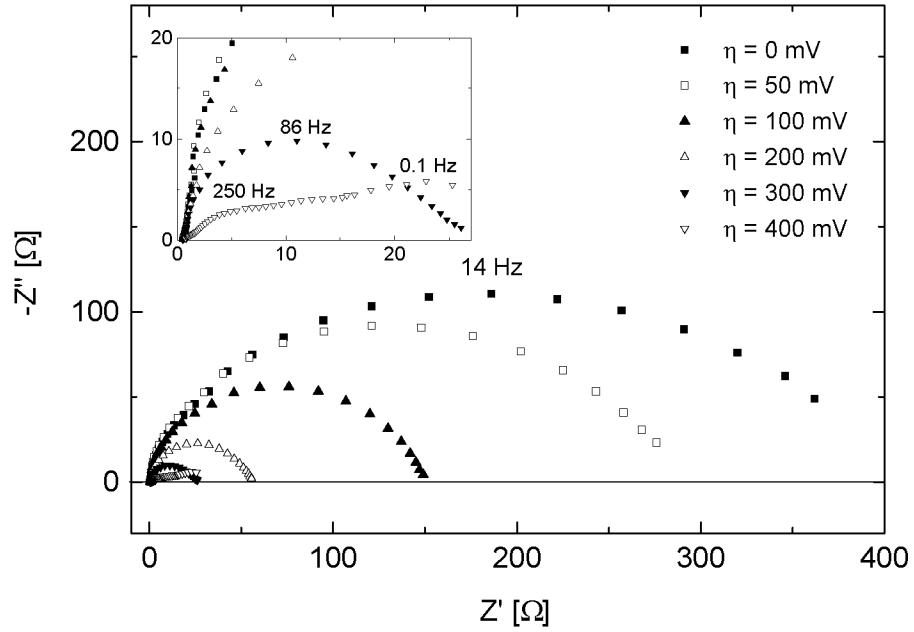


Fig. 4.2: Electrochemical impedance data of a Ni pattern anode (line width of Ni and of YSZ = 20 μm , $I_{TPB} = 3.648 \text{ m/cm}^2$) as a function of the overpotential, η , between the working and the reference anode (for the experimental conditions see Tab. 4.2).

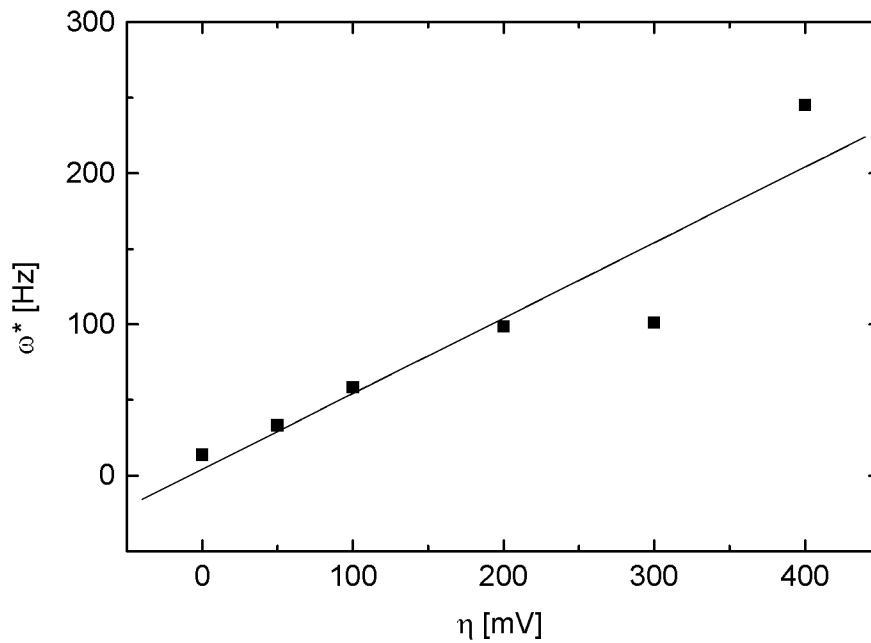


Fig. 4.3: Relaxation frequency of a Ni pattern anode, ω^* , as a function of the overpotential, η (for the experimental conditions see Tab. 4.2).

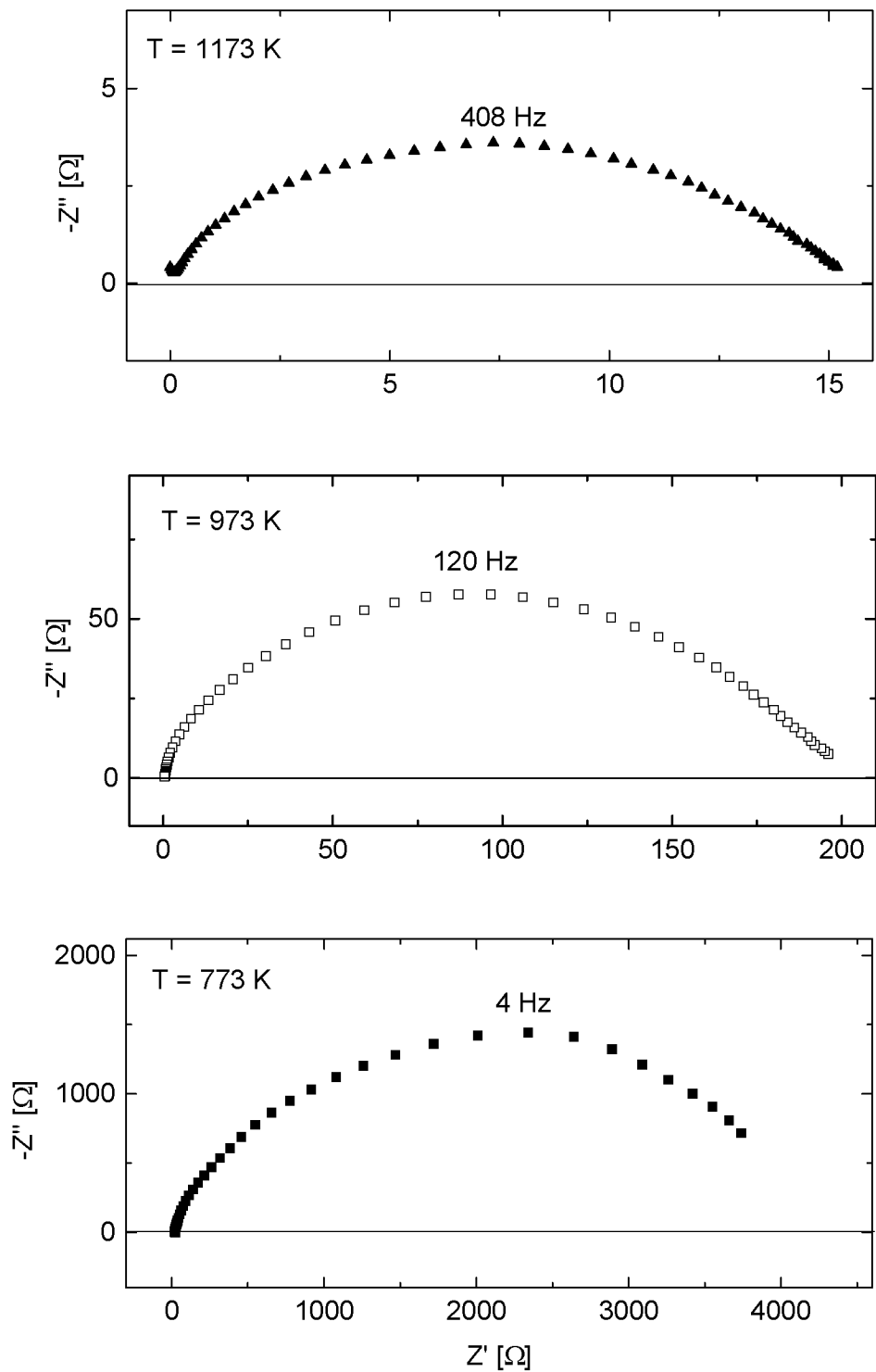


Fig. 4.4: Temperature dependence of the EIS data of a Ni pattern anode at equilibrium ($\eta = 0$ mV) (for the experimental conditions see Tab. 4.2).

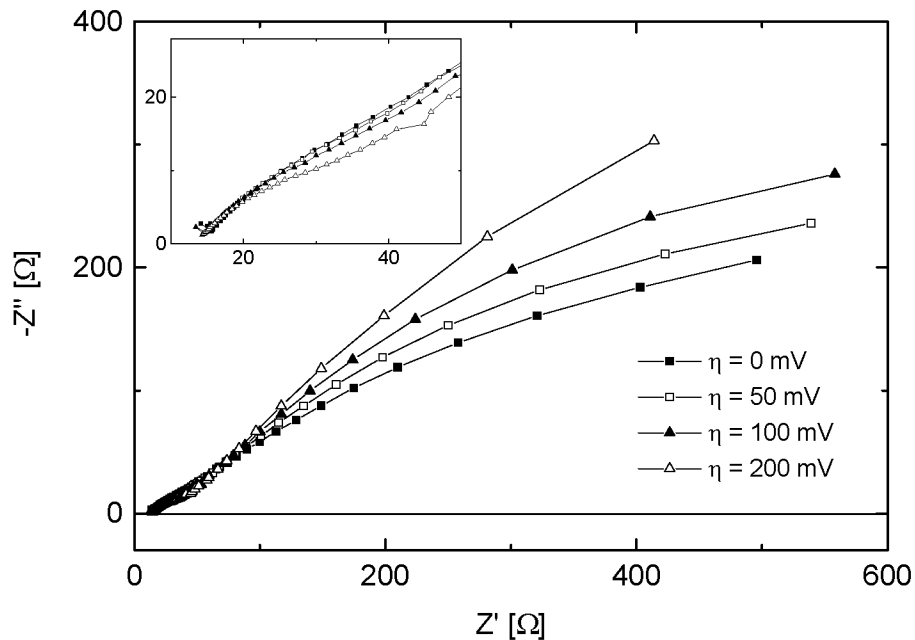


Fig. 4.5: Electrochemical impedance data of a Ni gauze anode as a function of the overpotential, η , between the working and the reference anode (for the experimental conditions see Tab. 4.2). The lines are drawn to guide the eye.

4.3.2.3 Ni Paste Anode

The Ni paste anode with the porous microstructure and the small amounts of YSZ is found to attain the lowest anode impedance of all of the metallic Ni anodes which were analyzed in this study (Fig. 4.6). Under equilibrium conditions, the impedance spectrum is dominated by a large inductive behavior at low frequencies. As a function of an overpotential applied between the working and the reference anode, the inductive behavior decreases strongly and merges in a second semicircle which is clearly separated at an overpotential of $\eta = 200$ mV. The second semicircle at low frequencies is found to increase with increasing overpotential. The high frequency impedance data suggests a diffusion limitation of the Ni paste anode. In particular under polarization of the Ni paste anode, the high frequency impedance data follows a 45° line.

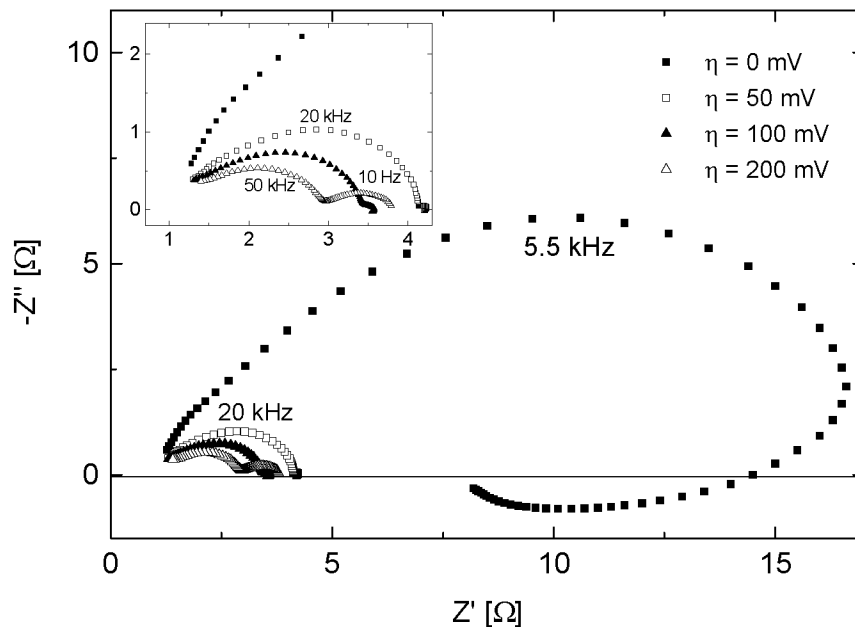


Fig. 4.6: Electrochemical impedance data of a Ni paste anode as a function of the overpotential, η (for the experimental conditions see Tab. 4.2).

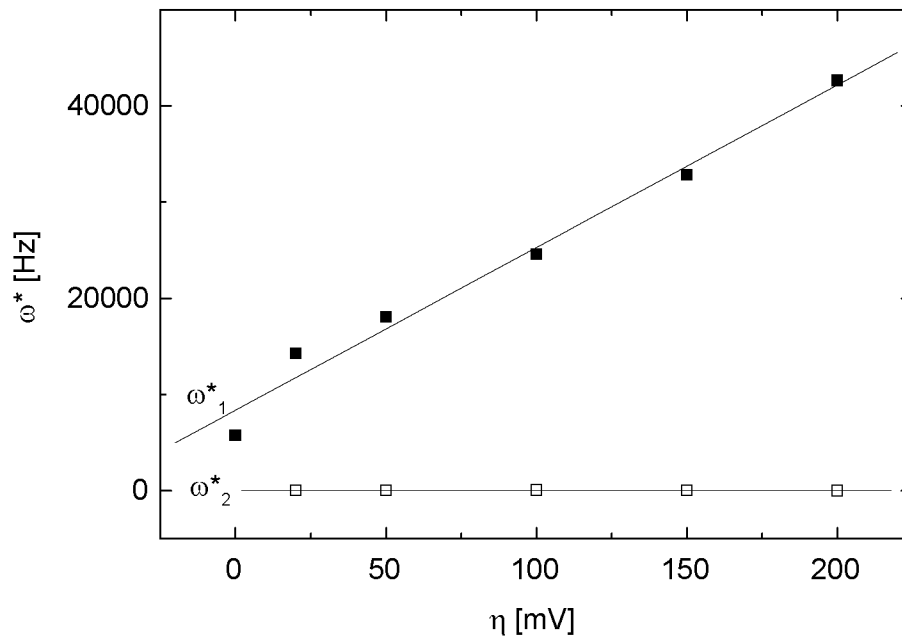


Fig. 4.7: Relaxation frequency of a Ni paste anode, ω^* , as a function of the overpotential, η (for the experimental conditions see Tab. 4.2).

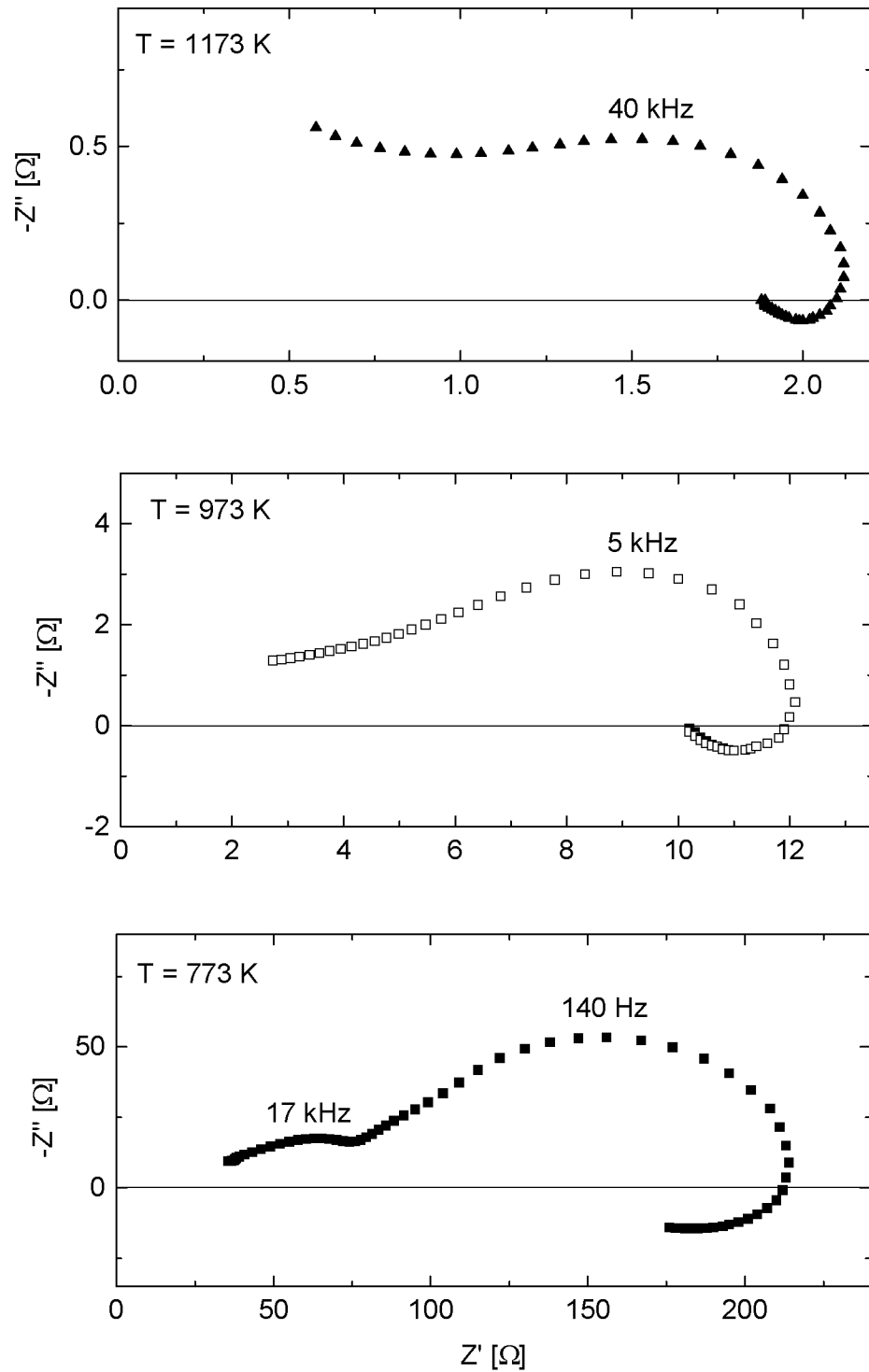


Fig. 4.8: Temperature dependence of the EIS data of a Ni paste anode at equilibrium ($\eta = 0$ mV) (for the experimental conditions see Tab. 4.2).

The relaxation frequencies as a function of the overpotential are illustrated in Fig. 4.7. The two lines belong to the two semicircles observed in Fig. 4.6. It is found that both relaxation processes are linearly dependent on the overpotential. The high frequency data increases strongly with increasing overpotential, whereas the low frequency data is almost independent of the applied overpotential.

As a function of the temperature, significant changes concerning the shape of the impedance spectra are found (Fig. 4.8): whereas two, clearly separated arcs are found under equilibrium conditions at low temperatures ($T = 773$ K), only one arc is observed at higher temperatures. At $T = 1173$ K, the high frequency data even seems to increase to infinity. The large inductive behavior which was observed under equilibrium conditions is found to decrease due to thermal treatment at 1173 K as well as after long term operation of the fuel cell. Inductive loops in the low frequency region were also found in the literature. This topic is discussed in more detail in subsection 4.3.5.

4.3.3 Electrochemistry of Ni-YSZ Cermet Anodes

4.3.3.1 Screen-Printed Ni-YSZ Anode

The electrochemical behavior of the screen-printed Ni-YSZ cermet anode is illustrated in Fig. 4.9. The total anode impedance is in the same range as for the Ni paste anode, i.e. around 10Ω . It is rather difficult to compare this anode performance to the results of other groups, as most studies are carried out at higher temperatures, i.e. $T = 1273$ K. Comparable data is only given in [8] and [13]: a total anode impedance of $0.6 \Omega\text{cm}^2$ at 1023 K and of $5 \Omega\text{cm}^2$ at 998 K was measured.

The impedance spectra in this study are dominated by one main impedance arc at $T = 973$ K (Fig. 4.9). The shape of the curves does not change significantly when an overpotential is applied. Since the high frequency data does not reach the real axis and since the high frequency tangent to the impedance data is slightly higher than 45° , no definite predictions concerning diffusion limitations can be drawn. In the low frequency region, a small inductive loop is observed. The relaxation frequency of the main impedance arc increases linearly with increasing overpotential (Fig. 4.10).

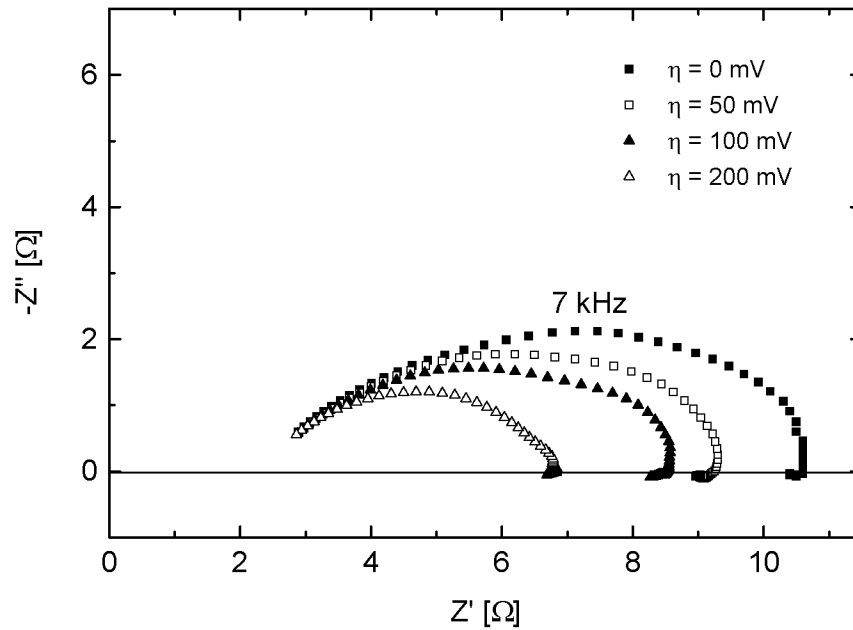


Fig. 4.9: Electrochemical impedance data of a screen-printed Ni-YSZ cermet anode as a function of the overpotential, η (for the experimental conditions see Tab. 4.2).

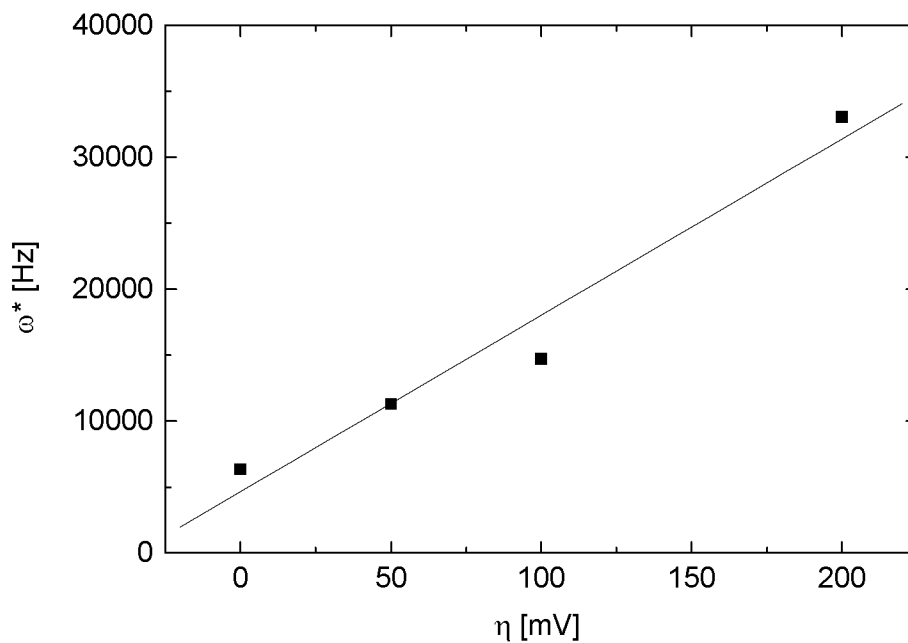


Fig. 4.10: Relaxation frequency of a screen-printed Ni-YSZ cermet anode, ω^* , as a function of the overpotential, η (for the experimental conditions see Tab. 4.2).

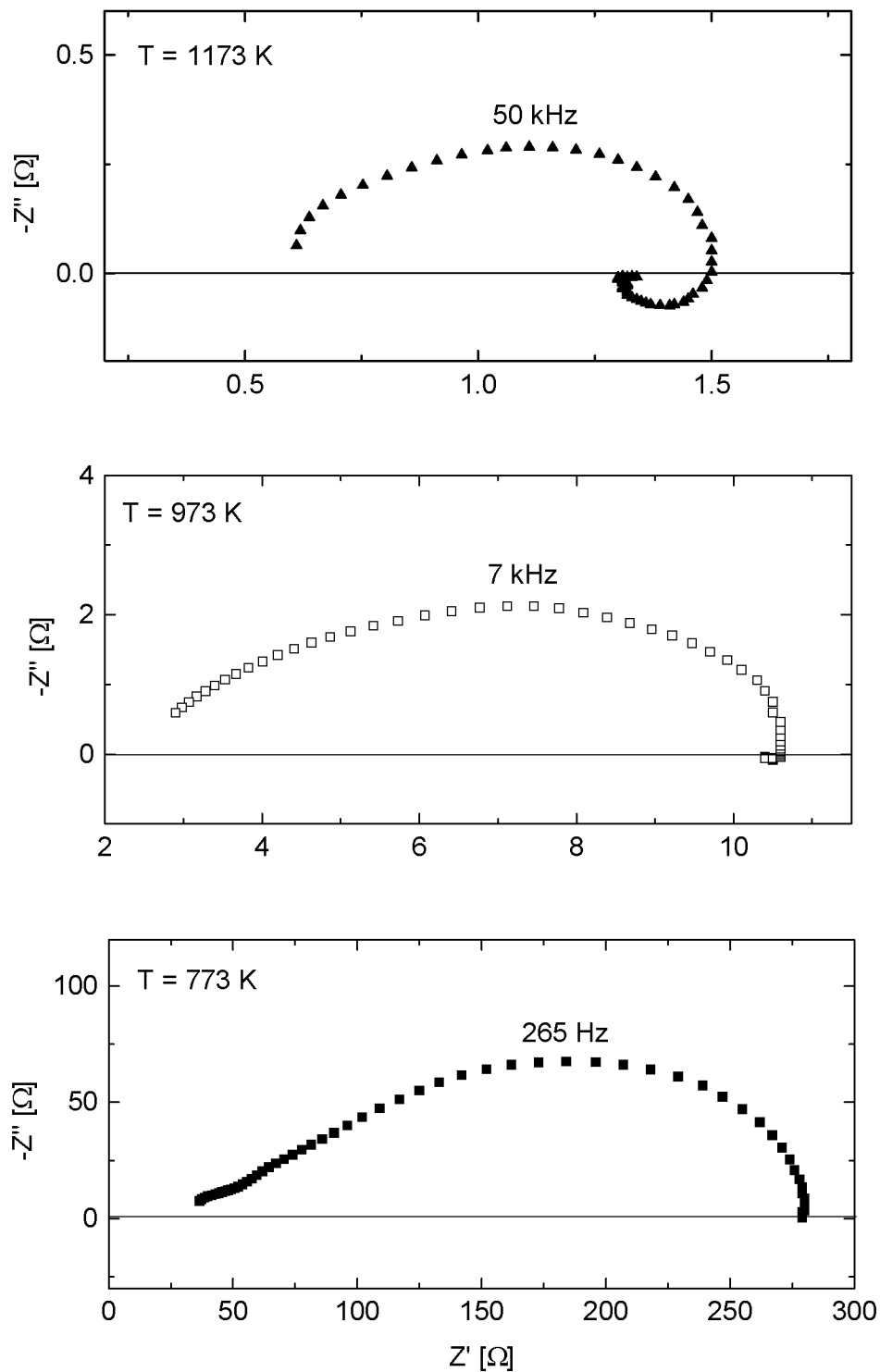


Fig. 4.11: Temperature dependence of the EIS data of a screen-printed Ni-YSZ cermet anode at equilibrium ($\eta = 0$ mV) (for the experimental conditions see Tab. 4.2).

As a function of the temperature, considerable modifications of the shape of the impedance spectra are found (Fig. 4.11): at low temperature ($T = 773$ K), the total anode impedance is not only the highest, but it is also possible to distinguish between at least two single relaxation processes. The anodic reaction mechanisms seem to be limited by diffusion. At higher temperatures ($T > 773$ K), the diffusion effect vanishes as well as the clearly separated high frequency impedance arc. Instead, an inductive loop shows up at low frequencies. For a discussion on the activation energy of the main process one should refer to subsection 4.3.5.3.

4.3.3.2 Sputtered Ni-YSZ Anode

The impedance data of the sputtered Ni-YSZ anode shows the most diversified data compared to the other data discussed before (Fig. 4.12): starting from an impedance spectrum with a clearly separated low frequency semicircle at equilibrium ($\eta = 0$ mV), this semicircle decreases with increasing overpotential until it is almost invisible at an overpotential of $\eta = 200$ mV. At an overpotential of $\eta = 100$ mV, the low frequency arc is most pronounced. For the interpretation of the impedance data, one has to keep in mind the microstructure of the sputtered Ni-YSZ anode after the electrochemical measurements (Fig. 4.1e): the Ni does not form an interconnected network. Microstructural changes during the impedance measurements might be responsible for the obscure data. Diffusion effects were not found to be relevant at sputtered Ni-YSZ cermet anodes.

The two relaxation processes show both a linear relation of the relaxation frequency as a function of the overpotential (Fig. 4.13). The high frequency process increases strongly with increasing overpotential, whereas the low frequency process is almost independent of the applied overpotential.

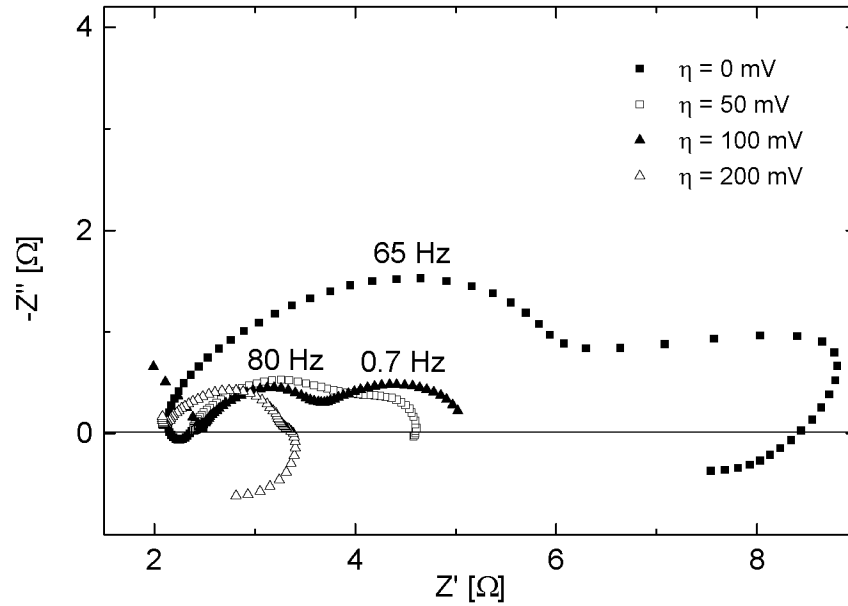


Fig. 4.12: Electrochemical impedance data of a sputtered Ni-YSZ cermet anode as a function of the overpotential η between the working and the reference anode (for the experimental conditions see Tab. 4.2).

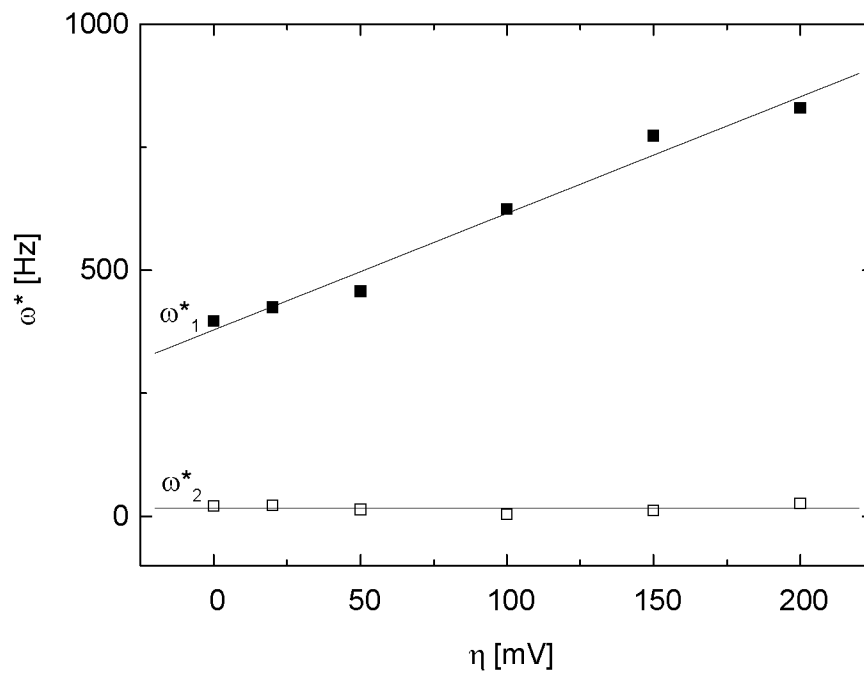


Fig. 4.13: Relaxation frequency of a sputtered Ni-YSZ cermet anode, ω^* , as a function of the overpotential, η , between the working and the reference anode (for the experimental conditions see Tab. 4.2).

4.3.3.3 Electrostatically Sprayed Ni-YSZ Anode

The electrostatically sprayed Ni-YSZ cermet anode has a rather high total electrode impedance of almost 70Ω (Fig. 4.14). The other Ni-YSZ cermet anodes have a total anode impedance of around 10Ω (Fig. 4.9, Fig. 4.12). The shape of the impedance curves in Fig. 4.14 shows a considerable dependence on the overpotential applied between the working and the reference anode: at equilibrium ($\eta = 0 \text{ mV}$), one main impedance arc exists which is located in the high frequency part of the spectrum. A second arc can be identified at low frequencies. This low frequency impedance arc becomes more important at high overpotential. Whether the absolute value of this semicircle increases as a function of the overpotential, cannot be decided from the Nyquist plot in Fig. 4.14. The high frequency semicircle obviously decreases as a function of the overpotential. Diffusion effects cannot be observed under the experimental conditions used here. The relaxation frequency analysis shows again one process which is strongly dependent on the overpotential and one which is almost independent of the overpotential. Compared to all the other anode measurements, the high frequency relaxation frequency is not linearly dependent of the overpotential in the entire region of applied overpotentials.

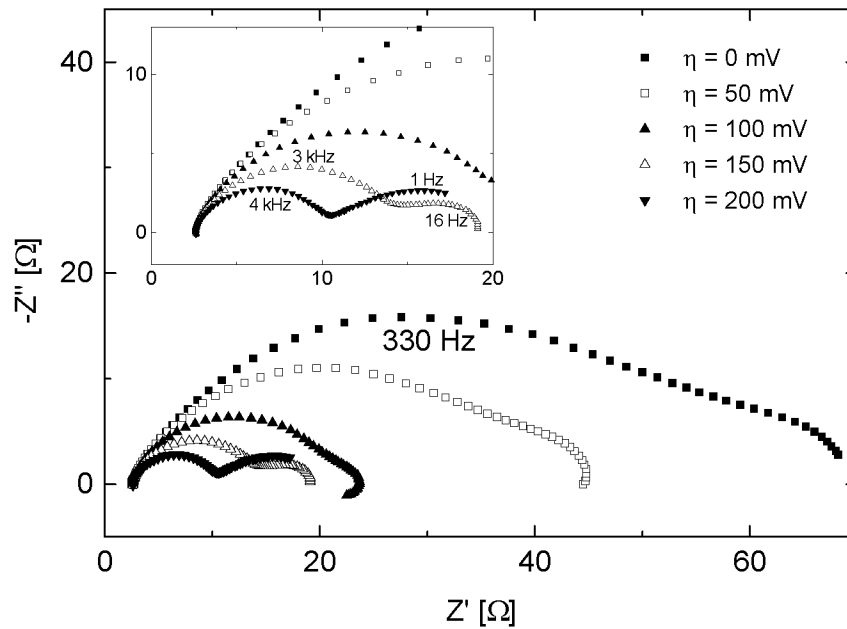


Fig. 4.14: Electrochemical impedance data of a electrostatically sprayed Ni-YSZ cermet anode as a function of the overpotential, η , between the working and the reference anode (for the experimental conditions see Tab. 4.2).

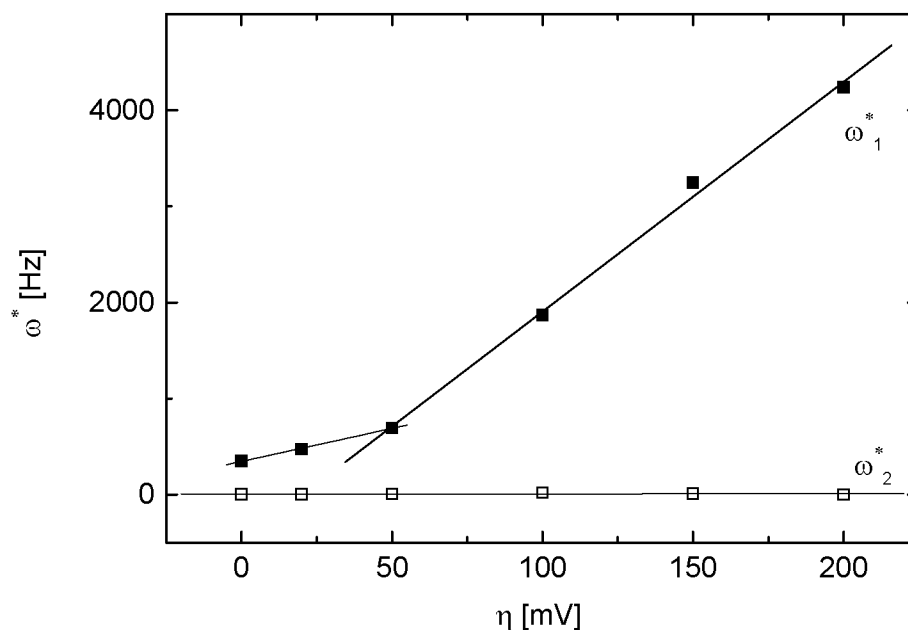


Fig. 4.15: Relaxation frequency of an electrostatically sprayed Ni-YSZ cermet anode, ω^* , as a function of the overpotential, η , between the working and the reference anode (for the experimental conditions see Tab. 4.2).

4.3.4 Pt and Au Electrodes

One should remember that the sputtered and the electrostatically sprayed Ni-YSZ anodes were contacted over the entire surface with Pt and Au paste, respectively. While Au should not be electrochemically active, it is well known that Pt is active for the oxidation of hydrogen. Hence, it has to be checked, whether the results obtained for the sputtered anode can be uniquely ascribed to the sputtered layer or whether the Pt affects the electrochemical results. For this purpose, Pt electrodes which were similarly prepared as the Pt contact layer on the sputtered surface, were studied. For the sake of completeness, separate studies on Au electrodes were carried out.

It was found that the Pt electrode behaves rather similarly to the Ni pattern anode, if one compares the shape of the impedance spectra (Fig. 4.16) as well as the polarization resistance as a function of the overpotential (Fig. 4.17) and as a function of the temperature (Fig. 4.18). The polarization resistance of the Pt electrode

is always higher than the one determined for the Ni pattern electrode. This indicates that Pt is less electrochemically active than Ni, in particular, since the TPB length of the porous Pt electrode should be larger than the TPB length of the Ni pattern electrode. As the total electrode impedance of the sputtered Ni-YSZ anode (Fig. 4.12) is more than a factor of 10 smaller than the electrode impedance of the pure Pt electrode (Fig. 4.16), the sputtered Ni-YSZ layer indeed dominates the impedance data in Fig. 4.12. This finding is not in contradiction to the results in [22] where different current collectors were studied. It was found that a Pt paste current collector does influence the electrochemical behavior of a Ni-YSZ anode. However, since the total impedance of the sputtered Ni-YSZ anode is much lower than the impedance of the pure Pt electrode here, the Pt paste seems to have no major influence.

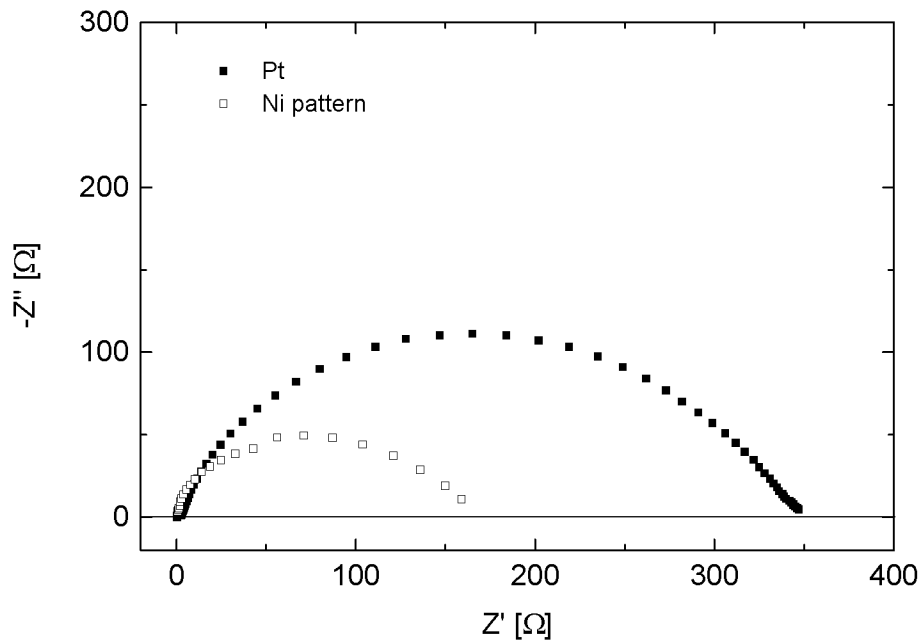


Fig. 4.16: Nyquist plots of a Pt electrode and a Ni pattern electrode at $\eta = 0$ mV (for the experimental conditions see Tab. 4.2).

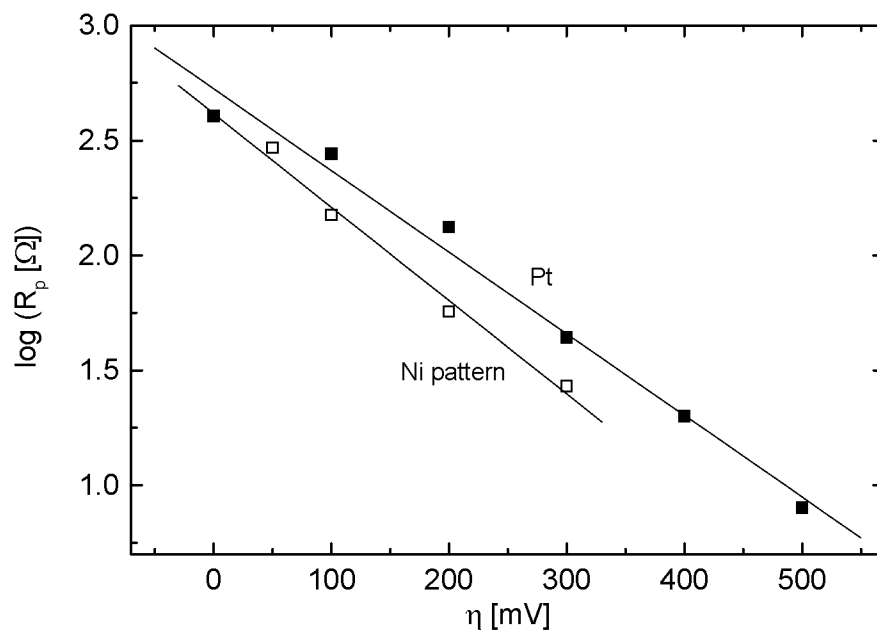


Fig. 4.17: Polarization resistance, R_p , as a function of the overpotential, η , for a Pt and a Ni pattern electrode (for the experimental conditions see Tab. 4.2).

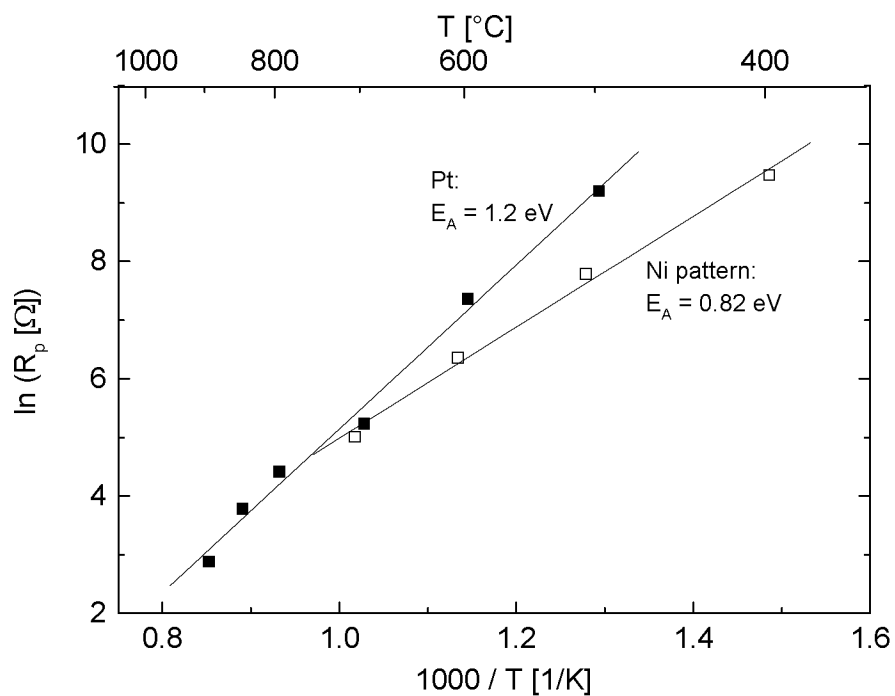


Fig. 4.18: Polarization resistance, R_p , as a function of the temperature, T , for a Pt and a Ni pattern electrode (for the experimental conditions see Tab. 4.2).

For an Au electrode deposited directly onto a YSZ single crystal electrolyte, no electrochemical activity for the oxidation of hydrogen was found. As a function of the overpotential, the impedance did not decrease. In contrast, a slight increase of the impedance could be observed. This was also observed in [22] where Ni-YSZ anodes were electrically connected with a Au paste current collector. It was found that the Au can diffuse to the interface of the anode and the electrolyte and that a Ni-Au alloy is formed at high temperatures. The performance deteriorates, in particular during long-term operation. This suggests that the high impedance of the electrostatically sprayed anode might not necessarily be due to a bad microstructure of the anode layer, but that the impedance might also be impeded by the Au current collector.

In summary, it is found that the sputtered and the electrostatically sprayed anode can properly be compared to the other Ni-based anodes even though they were covered with Pt and Au paste, respectively. However, for the future, it should be considered whether both Pt as well as Au paste current collectors could be avoided, in particular, since the electrochemical behavior of Ni-YSZ cermets was found to be very sensitive to the physical and to the chemical nature of the current collector [22]. It is suggested that Ni-YSZ electrodes should be electrically connected by means of a Ni mesh. For a continuous contact of the current collector over the entire surface of the anode, we advice to use some Ni-YSZ or Ni paste.

4.3.5 Comparison of Ni-Based Anodes

A summary of the main results obtained for the Ni-based anodes is given in Tab. 4.3. The anodes considered in this study are all dominated by one main impedance arc. A second arc develops merely at high overpotentials in the low frequency domain. This low frequency impedance arc increases the higher the overpotential which is applied between the working and the reference anode. The high frequency arc, in contrast, decreases strongly the higher the overpotential.

The absolute values for the total anode impedance seem to be directly coupled to the TPB length of the anode. Ni pattern and Ni gauze anodes have a very high polarization resistances, R_p . Hence, their TPB length should be rather short. The Ni paste and the screen-printed Ni-YSZ anode have a porous microstructure with

many free sites for the chemical and the electrochemical reactions to take place; thus, the electrode impedance is low. In the case of the sputtered Ni-YSZ anode, the low electrode impedance is most probably attributed to the large number of Ni islands which are all electrochemically active and which are electrically connected to the current collector. The rather high R_p value for the electrostatically sprayed anode could be related to the Au current collector (cf. subsection 4.3.4) or to the fact that the spray pyrolysis parameters are not yet optimized for the deposition of Ni-YSZ anodes. One should be aware that the anode is severely damaged after the electrochemical measurements (Fig. 4.1f).

The relaxation frequencies are characterized in Tab. 4.3 in form of their absolute values at $\eta = 0$ mV and in form of the slopes determined from the ω vs. η diagrams. For the high frequency relaxation process (ω_1), the absolute values for the relaxation frequencies are found to scatter strongly between 14 Hz and 6 kHz. The slopes show similar tendencies. However, compared to the low frequency relaxation process, the absolute values as well as the slopes are definitely higher for the high frequency relaxation process. Hence, there exist two relaxation processes having clearly different relaxation frequencies. The high frequency process depends strongly on the overpotential, whereas the low frequency process is nearly independent of the overpotential.

Concerning diffusion effects, very close relations between the appearance of a 45° tangent to the high frequency data and the microstructure are found: for the Ni pattern anode as well as for the sputtered Ni-YSZ anode, no 45° tangents to the high frequency data were observed. The anodes have both a two dimensional microstructure (note the coagulated Ni islands at the surface of the sputtered Ni-YSZ anode (Fig. 4.1e)). The Ni gauze anode most probably owes the Warburg-like behavior to the diffusion barrier in form of the YSZ cover on the anode which is necessary to ensure a good contact of the Ni gauze onto the electrolyte. The Ni paste and the screen-printed Ni-YSZ anodes have both a porous microstructure. The fuel gas seems to be hindered in reaching the reaction zone. The electrostatically sprayed Ni-YSZ anode is found to have a dense microstructure in the as-prepared state. The total electrode impedance is rather high (70Ω) and the anode is severely damaged after the electrochemical measurement. Hence, the system cannot be driven into diffusion limitations.

Tab. 4.3: Comparison of the different anode designs concerning the results obtained in subsection 4.4.

Anode design	# arcs _{0 mV}	# arcs _{200 mV}	R _{p,0 mV} [Ω]	ω _{1,0 mV} [Hz]	ω ₁ slope	ω _{2,0 mV} [Hz]	ω ₂ slope	Warburg diffusion	Inductive behavior
Ni pattern	1	1 [†]	400	14	0.5	-	-	no	no
Ni gauze	2	2	> 1 k	-	-	-	-	yes	-
Ni paste	1	2	7	5750	170	< 10	-0.01	yes	yes
screen-printed Ni-YSZ	1-2	1-2	5	6350	135	-	-	possible	yes
sputtered Ni-YSZ	2	2	5	400	2	20	-0.003	no	yes
sprayed Ni-YSZ	1-2	2	70	350	7 + 24	3	0.01	no	yes

[†] at 400 mV: 2 arcs

With regard to the inductive behavior which was found for several anodes, it should be noted that an inductive behavior was never found for a Ni pattern anode (cf. the impedance measurements in chapter 3), whereas it is always found for anodes with low impedance. In the literature, low frequency inductive loops were also found for different types of SOFC electrodes [23-27]. However, so far, the nature of these inductivities is not well understood and only some rough explanations exist. For instance, in [24], the inductive behavior is attributed to intermediate adsorbates. In [25], the adsorption of several species at the same site seems to be responsible for the inductive loops. It is also suggested that electronic defects in the electrolyte or partial reduction of the electrolyte or the electrode at the counter electrode interface contribute to inductivities in the low frequency region [26]. According to [27], the inductive behavior is caused by a bad cathode performance. This would imply that the degradation of the Ni paste anode might lower the effect due to a bad cathode and, hence, reduce the inductive behavior (compare the curve for $\eta = 0$ mV in Fig. 4.6 with the curve for $T = 973$ K in Fig. 4.8). This hypothesis might, in fact, explain the inductive loops found in this study, since inductive loops were always found in case of an anode with high performance. However, an explicit explanation for the inductive loops is not possible yet.

4.3.5.1 Polarization Resistance

The polarization resistance is defined as the low frequency intercept of the impedance data in the Nyquist plot with the real axis less the high frequency intercept which is due to a certain contribution of the electrolyte. The polarization resistances of the different anodes are summarized as a function of the overpotential in Fig. 4.19. Only the curve for the Ni gauze anode is missing, since the low frequency intercept of the impedance data of the gauze anode could not be analyzed because the semicircles in the Nyquist plot were not closed (Fig. 4.5).

It is found that the polarization resistances of the different anodes vary by almost three orders of magnitude, i.e. $1 \Omega - 10^3 \Omega$. The polarization resistances decrease with increasing overpotential and they are all exponentially dependent on the overpotential with slopes between -0.9 and -5. According to the Nyquist plots, most anodes show two distinct semicircles, in particular, at high overpotential. This effect is accounted for with the closed and the open symbols in Fig. 4.19: the main impedance arc, i.e. the high frequency one, is represented by the closed

symbols. The exponential decrease of the polarization resistance is attributed to this arc. The open symbols signify the total anode impedance with low and high frequency impedance arc. Due to the increase of the low frequency arc at high overpotentials, the total anode impedance increases towards higher overpotentials. This effect is found for all anodes except the screen-printed YSZ anode which shows already at low overpotentials only little sensitivity to the applied overpotential. In the case of the Ni pattern anode, the second impedance arc appears only at extremely high overpotentials of $\eta = 400$ mV.

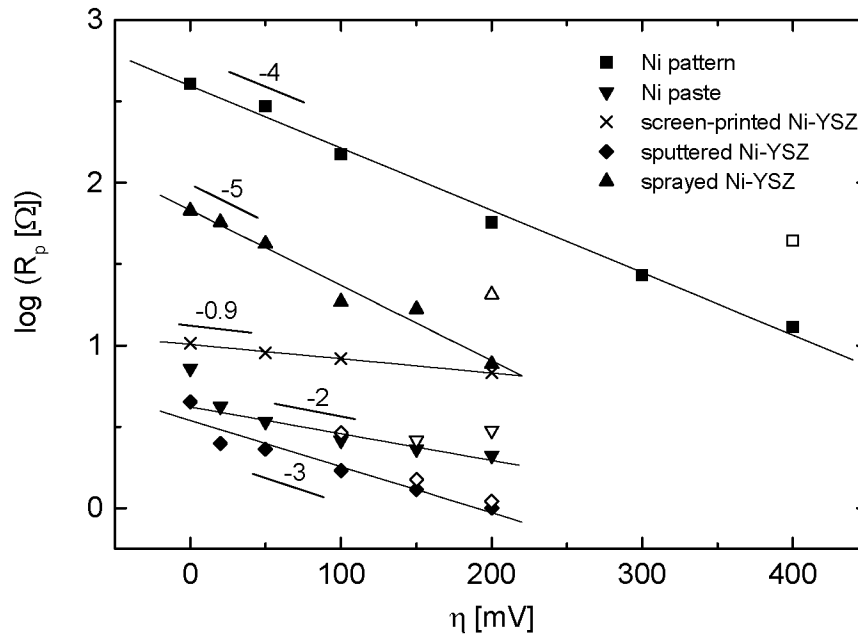


Fig. 4.19: Polarization resistance, R_p , as a function of the overpotential, η , for the different anodes. Closed symbols: high frequency impedance arc; open symbols: total anode impedance (for the experimental conditions see Tab. 4.2).

4.3.5.2 Current Density

The current density is a measure of the performance of the anode. According to the relatively low current densities found for the anodes measured in this study, the anodes are all rather bad. In particular, the Ni gauze, the Ni pattern, and the electrostatically sprayed Ni-YSZ anodes have only a very low current density (< 10 mA/cm² at $\eta = 200$ mV). The Ni paste, the screen-printed, and the

sputtered Ni-YSZ anode have a higher and very similar performance (Fig. 4.20). These results are closely related to the microstructure of the anodes: anodes with a long TPB and a large surface area have a higher performance than anodes with a smaller TPB length. The current densities vary by about three orders of magnitude, as do also the polarization resistances. The shapes of the curves are all very similar. Note that it is not necessary to correct the current densities in Fig. 4.20 for the small current flowing through the electrolyte, since the electrolyte resistances are much smaller than the polarization resistances in the anodes. The current loss through the electrolyte is therefore negligible.

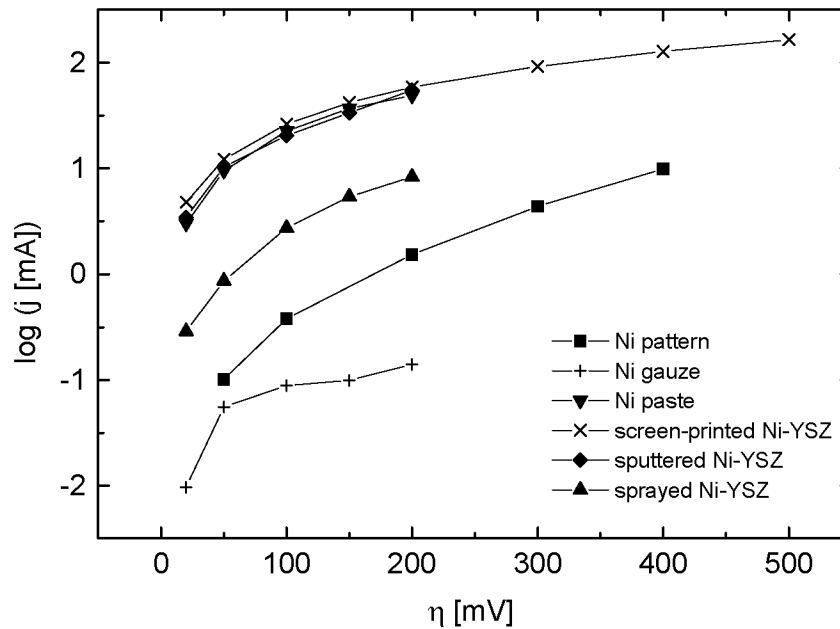


Fig. 4.20: Current density, j , as a function of the overpotential, η , for the different anodes (for the experimental conditions see Tab. 4.2). The lines are drawn to guide the eye.

4.3.5.3 Temperature

The temperature dependence is analyzed in terms of the shape of the impedance spectra as well as in terms of the activation energies of the relaxation processes derived from the impedance data.

Concerning the shape of the impedance spectra, two distinct arcs are found at low temperature ($T = 773$ K) in the case of the porous anodes, i.e. the Ni paste and

the screen-printed Ni-YSZ anodes. With increasing temperature the high frequency arc vanishes and a diffusion effect is observed ($T = 973$ K). This effect disappears at very high temperatures ($T = 1173$ K). In the case of the non-porous Ni pattern anode, the impedance spectra consist always of one main impedance arc which becomes depressed at higher temperature. For all anodes, the relaxation frequency of the main impedance arc increases with increasing temperature signifying that the main electrode process becomes faster at higher temperature.

The activation energies were determined with regard to the total electrode polarization, R_p , as well as concerning the electrolyte contribution, R_e (Tab. 4.4). Data from three different Ni pattern anodes, from one Ni paste anode and from two different screen-printed Ni-YSZ cermet anodes, are compared. Standard deviations were determined separately for the activation energies of R_p and of R_e of the different anode designs. Moreover, the deviations between $E_A(R_p)$ and $E_A(R_e)$ within one sample were calculated (last column in Tab. 4.4). The following results are found (Tab. 4.4):

- The activation energies for R_p as well as for R_e vary strongly within one anode design: compare the activation energies for the Ni pattern anodes 1, 2, and 3 among each other as well as those for the screen-printed anodes 1 and 2.
- The average activation energies for R_p are very similar for the three different anode designs, i.e. 0.94 eV for the pattern, 0.96 eV for the paste, and 0.91 eV for the screen-printed Ni-YSZ anode.
- The average activation energies for R_e are very different for the different anode designs, i.e. 1.15 eV for the pattern, and 0.57 eV for the screen-printed Ni-YSZ anode.
- The activation energies for R_p and for R_e are very different within one sample (refer to the last column).
- The standard deviation concerning all activation energies of R_p and for R_e is rather narrow: (0.925 +/- 0.251) eV.

These results suggest two main conclusions:

- (1) The activation energy of the electrolyte resistance, R_e , depends on the anode design (e.g. pattern, screen-printed anode) and varies from anode to anode. Hence, the contribution from the electrolyte

to the anode impedance depends strongly on the anode itself and seems to be related to the microstructure of the anode.

- (2) Even though the standard deviation of all activation energies is very small ((0.925 ± 0.251) eV), the activation energies for R_p and for R_e do most probably not refer to the same electrode process, since $E_A(R_p)$ and $E_A(R_e)$ deviate considerably within one specific anode (last column in Tab. 4.4).

In [11], the activation energy for a point contact as well as for coarse Ni-YSZ cermet anodes are found to be large ($E_A > 1$ eV), whereas for anodes consisting of a fine structure small activation energies were observed ($E_A < 1$ eV). This would mean that the screen-printed Ni-YSZ anode 1 in Tab. 4.4 has a much coarser microstructure than the screen-printed Ni-YSZ anode 2.

For the Ni paste anode, the activation energy of the low frequency arc was determined to be about 0.5 eV. This is considerably lower than the activation energies calculated for R_p and R_e in Tab. 4.4.

Tab. 4.4: Temperature dependence of the different anodes (for the experimental conditions see Tab. 4.2).

Sample	$E_A(R_p)$ [eV]	$E_A(R_e)$ [eV]	deviation between $E_A(R_p) + E_A(R_e)$
Ni pattern 1	1.04	1.35	30%
Ni pattern 2	0.97	0.91	-6%
Ni pattern 3	0.82	1.18	44%
	0.94 ± 0.11	1.15 ± 0.22	
Ni paste	0.96	-	-
screen-printed Ni-YSZ 1	1.15	0.71	-38%
screen-printed Ni-YSZ 2	0.67	0.42	-37%
	0.91 ± 0.34	0.57 ± 0.21	

standard deviation concerning all $E_A(R_p)$ and $E_A(R_e)$: (0.925 ± 0.251) eV

4.3.5.4 Equivalent Circuit Fitting

The anodes were all fitted to an equivalent circuit of the form $R_e(C_{dl}(R_t(R_1Q_1)(R_2Q_2)))$ where R_i represent resistances, C_i capacitances, and Q_i constant phase elements (CPE) (Fig. 4.21). The code for the description of the equivalent circuit has been adopted from [28]. The impedance of a CPE is given by $Z_{CPE} = 1/Q(i\omega)^n$ where i denotes the imaginary unit, ω the angular frequency, and n the deviation of the impedance of a CPE from an ideal capacitive behavior ($n = 1$ for an ideal capacitor and $n = 0$ for an ideal resistor). A CPE was used for the fitting of the impedance data, as due to the broadening of the bell-shaped curve of the phase angle a distribution of relaxation times is expected which can best be fitted by a CPE [21]. More information about equivalent circuit fitting is given in chapter 1 (subsection 1.2) and in chapter 3 (subsection 3.3.2.1) as well as in the references [21] and [28].

The anodes in this study were fitted to an equivalent circuit model with two RQ elements in series (Fig. 4.21). Remember that a model with only one RQ element was used to fit the Ni pattern anodes measured in chapter 3. The reason for the two RQ elements in this study is due to the two separate arcs which were observed in most impedance diagrams, in particular at high overpotentials. A summary of the fitting data is given in Tab. 4.5. The negative R and Q values in Tab. 4.5 account for inductive loops found in the impedance spectra.

The equivalent circuit fitting yields an electrolyte resistance, R_e , which is very low for most anodes ($< 3 \Omega$). Only for the Ni gauze anode a considerably higher value is found ($R_e = 14 \Omega$). The high value for the electrolyte resistance might be attributed to a bad contact of the Ni gauze onto the YSZ electrolyte. For all anodes, R_e is nearly constant as a function of the overpotential.

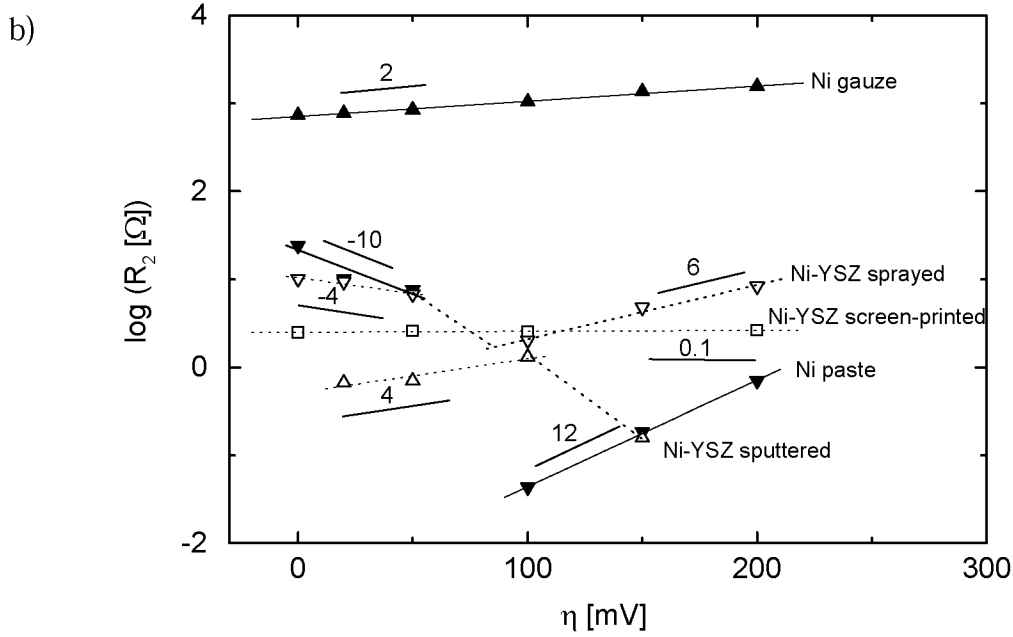
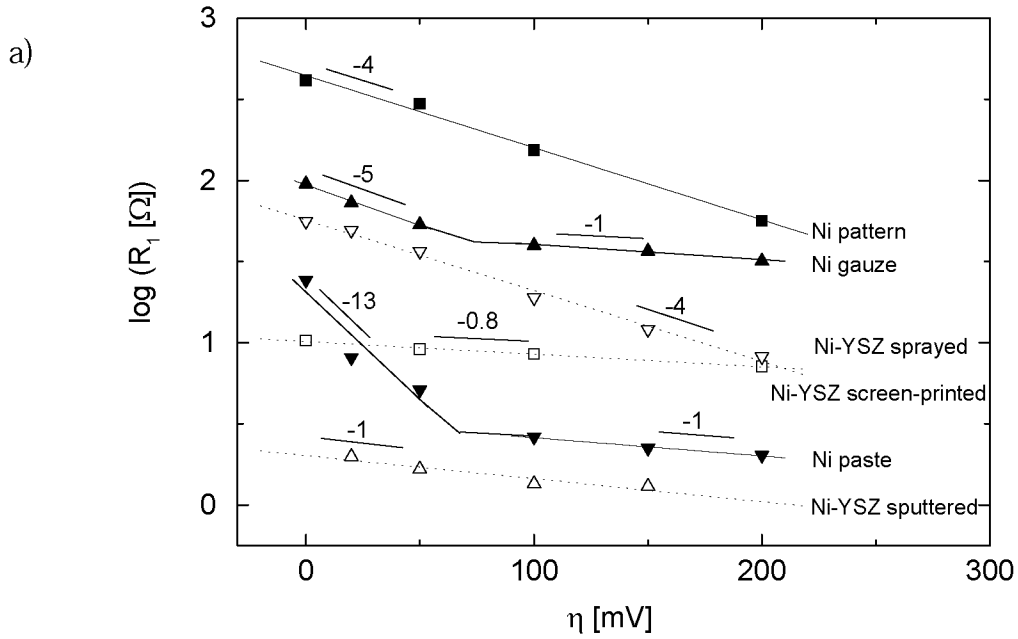
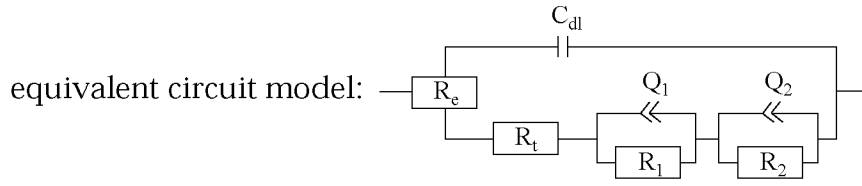
The so-called charge transfer resistance, R_t , is also found to be very small and decreases with an applied overpotential. Due to the small absolute values for R_t ($< 4 \Omega$) as well as due to the fact that considerable errors are associated with these values, this equivalent circuit element seems not to be of importance according to the fitting result.

The double layer capacitances, C_{dl} , are found in a range between 10^{-7} F and 10^{-4} F. They mainly increase with increasing overpotential. This means according to Eq. 3.1 in chapter 3 that either the thickness of the double layer decreases or the area of the electrode increases when a higher overpotential is applied between the working and the reference anode. Both explanations are in principle possible.

The capacitive elements Q_1 and Q_2 are attributed to the RQ elements. The capacitive element Q_1 is, except for the Ni paste anode at low overpotentials as well as for the sputtered Ni-YSZ anode, found in an extremely narrow range of capacitive values around 10^{-5} F. The absolute values are nearly constant as a function of the overpotential. Q_2 scatters intensely for the different anodes and reaches absolute values between 10^{-6} F and 10^{-1} F.

The resistive elements R_1 and R_2 as well as the corresponding relaxation frequencies ω_1 and ω_2 are illustrated in Fig. 4.21. R_1 and R_2 reach absolute values between $10^0 \Omega$ to $10^3 \Omega$ and $10^{-1} \Omega$ to $10^1 \Omega$, respectively. The relaxation frequencies lie between 10 Hz and 10^5 Hz for ω_1 and between 1 Hz and 100 Hz for ω_2 .

The R_1Q_1 element denotes the high frequency impedance arc, whereas the R_2Q_2 element signifies the low frequency arc which is sometimes related to an inductive behavior. Then, the resistive and the capacitive elements adopt negative values. It is found that the main impedance arc of the Ni pattern anode fits well to the high frequency data of the other anodes. Hence, it can be concluded that the main impedance arc of the Ni pattern anode is the same arc which is found in more complex anode designs at high frequencies. The development of the low frequency impedance arc at high overpotentials can be well followed by the equivalent circuit fits. In Fig. 4.21a and Fig. 4.21c, the minima and the maxima in the data at an overpotential of about 100 mV illustrate this.



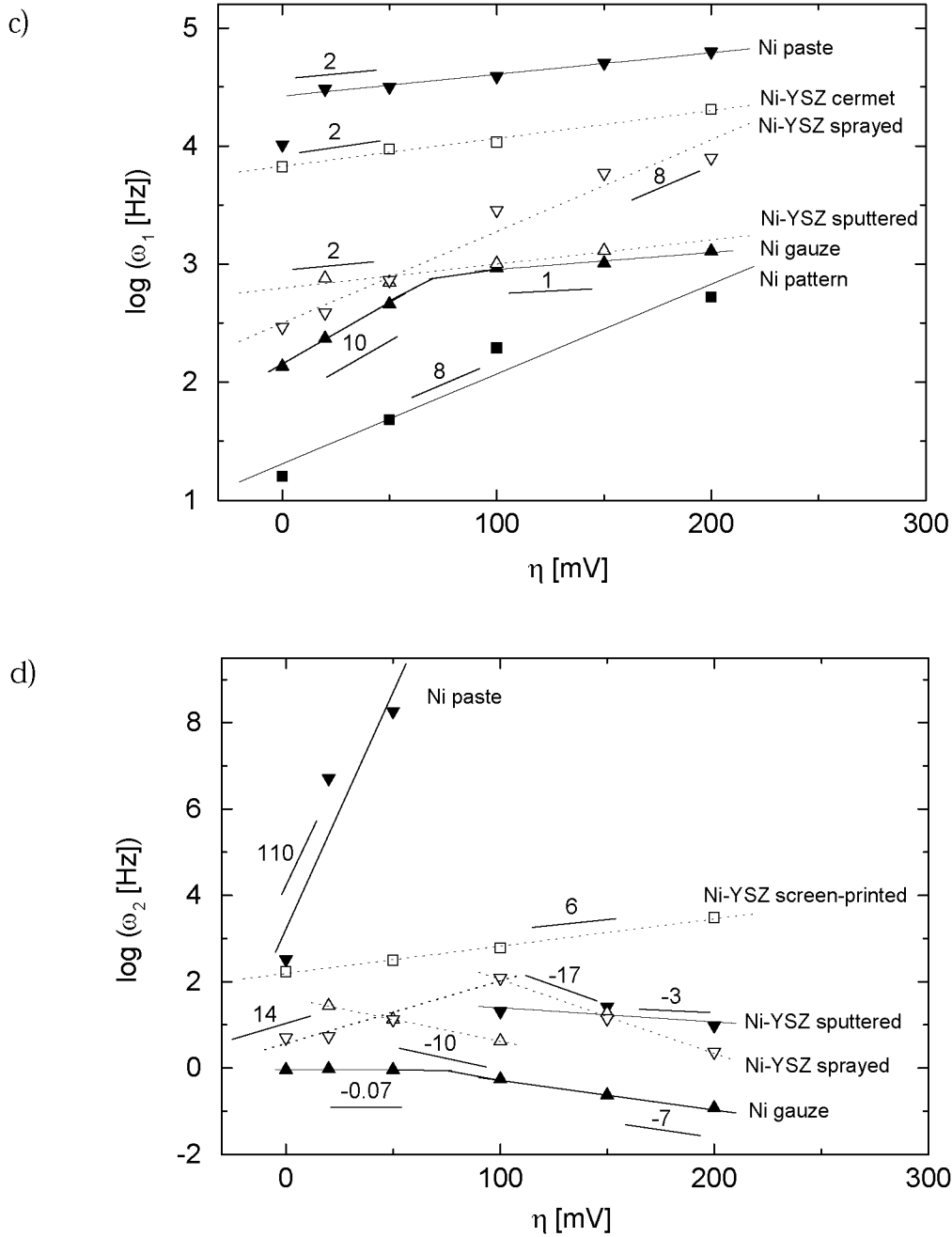


Fig. 4.21: Equivalent circuit fitting data of the different anodes as a function of the overpotential, η , using the model $R_e(C_{d1}(R_t(R_1Q_1)(R_2Q_2)))$: a) resistance R_1 , b) resistance R_2 , c) relaxation frequency ω_1 , d) relaxation frequency ω_2 (for the experimental conditions see Tab. 4.2).

Tab. 4.5: Equivalent circuit ($R_e(C_{dl}(R_t(R_1Q_1)(R_2Q_2)))$) fitting data for the different anodes as a function of the overpotential, η .

Ni pattern	R_e [Ω]	C_{dl} [F]	R_t [Ω]	R_1 [Ω]	Q_1 [F]	R_2 [Ω]	Q_2 [F]
0 mV	0.58	$6.1 \cdot 10^{-5}$	1.9	413.7	$7.3 \cdot 10^{-6}$	-	-
50 mV	0.59	$7.1 \cdot 10^{-5}$	1.4	296.8	$5.9 \cdot 10^{-6}$	-	-
100 mV	0.59	$9.6 \cdot 10^{-5}$	0.7	154.1	$5.7 \cdot 10^{-6}$	-	-
200 mV	0.59	$1.8 \cdot 10^{-4}$	0.2	56.5	$9.5 \cdot 10^{-6}$	-	-

$$n_1 = 0.492$$

Ni gauze	R_e [Ω]	C_{dl} [F]	R_t [Ω]	R_1 [Ω]	Q_1 [F]	R_2 [Ω]	Q_2 [F]
0 mV	14.0	$2.2 \cdot 10^{-7}$	-	95.3	$9.5 \cdot 10^{-6}$	732	$4.0 \cdot 10^{-5}$
20 mV	13.6	$2.7 \cdot 10^{-7}$	-	72.8	$9.7 \cdot 10^{-6}$	772	$3.7 \cdot 10^{-5}$
50 mV	14.2	$7.5 \cdot 10^{-7}$	-	53.5	$9.8 \cdot 10^{-6}$	847	$3.5 \cdot 10^{-5}$
100 mV	14.0	$9.7 \cdot 10^{-7}$	-	39.6	$9.6 \cdot 10^{-6}$	1040	$3.8 \cdot 10^{-5}$
150 mV	13.7	$8.0 \cdot 10^{-7}$	-	36.6	$9.9 \cdot 10^{-6}$	1360	$4.7 \cdot 10^{-5}$
200 mV	14.3	$1.7 \cdot 10^{-6}$	-	31.8	$1.0 \cdot 10^{-5}$	732	$4.0 \cdot 10^{-5}$

$$n_1 = 0.454, n_2 = 0.589$$

Ni paste	R_e [Ω]	C_{dl} [F]	R_t [Ω]	R_1 [Ω]	Q_1 [F]	R_2 [Ω]	Q_2 [F]
0 mV	1.9	$1.2 \cdot 10^{-6}$	1.9	24.3	$4.9 \cdot 10^{-6}$	-23.9	$-1.2 \cdot 10^{-5}$
20 mV	2.1	$1.0 \cdot 10^{-6}$	4.3	8.1	$7.7 \cdot 10^{-6}$	-10.1	$-4.1 \cdot 10^{-6}$
50 mV	2.0	$8.3 \cdot 10^{-7}$	4.3	5.1	$1.2 \cdot 10^{-5}$	-7.5	$-2.7 \cdot 10^{-6}$
100 mV	0.9	$1.5 \cdot 10^{-11}$	1.0	2.6	$2.0 \cdot 10^{-5}$	0.04	$2.5 \cdot 10^{-1}$
150 mV	1.0	$8.0 \cdot 10^{-12}$	0.001	2.2	$1.2 \cdot 10^{-5}$	0.2	$4.8 \cdot 10^{-2}$
200 mV	1.0	$5.8 \cdot 10^{-12}$	0.001	2.0	$1.9 \cdot 10^{-5}$	0.7	$2.6 \cdot 10^{-2}$

$$n_1 = 0.6, n_{2(0 \text{ mV}-50 \text{ mV})} = 0.2, n_{2(100 \text{ mV}-200 \text{ mV})} = 0.733$$

screen-printed Ni-YSZ	R_e [Ω]	C_{dl} [F]	R_t [Ω]	R_1 [Ω]	Q_1 [F]	R_2 [Ω]	Q_2 [F]
0 mV	1.9	$9.1 \cdot 10^{-8}$	0.6	10.3	$1.5 \cdot 10^{-5}$	-2.5	$-4.9 \cdot 10^{-4}$
50 mV	1.8	$5.2 \cdot 10^{-8}$	0.5	9.1	$1.4 \cdot 10^{-5}$	-2.6	$-3.3 \cdot 10^{-4}$
100 mV	1.8	$3.8 \cdot 10^{-8}$	0.5	8.5	$1.4 \cdot 10^{-5}$	-2.5	$-2.3 \cdot 10^{-4}$
200 mV	1.8	$2.3 \cdot 10^{-8}$	0.5	7.2	$1.2 \cdot 10^{-5}$	-2.6	$-9.1 \cdot 10^{-5}$

$$n_1 = 0.539, n_2 = 0.559$$

(Tab. 4.5 continued).

sputtered Ni-YSZ	R_e [Ω]	C_{dl} [F]	R_t [Ω]	R_1 [Ω]	Q_1 [F]	R_2 [Ω]	Q_2 [F]
0 mV	-	-	-	-	-	-	-
20 mV	2.3	$5.0 \cdot 10^{-5}$	0.003	2.0	$3.1 \cdot 10^{-4}$	0.7	$1.6 \cdot 10^{-2}$
50 mV	2.4	$9.4 \cdot 10^{-5}$	0.002	1.7	$3.8 \cdot 10^{-4}$	0.7	$2.7 \cdot 10^{-2}$
100 mV	2.5	$1.6 \cdot 10^{-4}$	0.002	1.3	$3.7 \cdot 10^{-4}$	1.3	$3.6 \cdot 10^{-2}$
150 mV	2.3	$1.5 \cdot 10^{-4}$	0.002	1.3	$3.3 \cdot 10^{-4}$	0.2	$9.2 \cdot 10^{-2}$

$$n_1 = 0.63, n_2 = 0.77$$

sprayed Ni-YSZ	R_e [Ω]	C_{dl} [F]	R_t [Ω]	R_1 [Ω]	Q_1 [F]	R_2 [Ω]	Q_2 [F]
0 mV	2.7	$9.4 \cdot 10^{-6}$	0.03	56.0	$1.7 \cdot 10^{-5}$	10.1	$3.2 \cdot 10^{-3}$
20 mV	2.7	$9.4 \cdot 10^{-6}$	0.03	49.2	$1.7 \cdot 10^{-5}$	9.3	$3.2 \cdot 10^{-3}$
50 mV	2.7	$1.0 \cdot 10^{-5}$	0.02	36.4	$1.5 \cdot 10^{-5}$	6.7	$2.3 \cdot 10^{-3}$
100 mV	2.6	$1.1 \cdot 10^{-5}$	0.02	18.9	$1.3 \cdot 10^{-5}$	2.0	$1.5 \cdot 10^{-3}$
150 mV	2.7	$1.3 \cdot 10^{-5}$	0.01	12.0	$1.4 \cdot 10^{-5}$	4.8	$3.2 \cdot 10^{-3}$
200 mV	2.7	$1.4 \cdot 10^{-5}$	0.02	8.2	$1.7 \cdot 10^{-5}$	8.3	$6.8 \cdot 10^{-2}$

$$n_1 = 0.586, n_2 = 0.742$$

4.4 Conclusions

The relation between the microstructure and the electrochemical behavior of different types of Ni-based SOFC anodes are the main focus of this chapter. The detailed kinetic studies carried out in chapter 3 are the basis for the interpretation of the results. It is found that the kinetics of the SOFC anodes under consideration are dominated by two main relaxation processes:

The high frequency relaxation processes - a very fast process with relaxation times between 0.07 s and 0.2 ms - is strongly dependent on the applied overpotential as well as on the temperature (activation energy around 1 eV). The relaxation frequency is linearly dependent on the overpotential. In chapter 3, this process was assigned to either the adsorption of hydrogen including charge transfer or to the electronation of oxygen at the interface of the anode and the

electrolyte. With regard to the different anodes characterized in this chapter, many arguments affirm the hypothesis that the high frequency relaxation process can be attributed to the adsorption process:

- (1) The activation energy for the adsorption of hydrogen on Ni is determined to be around 1 eV [9,29]. No value is published for the activation energy of the removal of oxygen from the electrolyte in reducing atmosphere. However, a considerably higher value was determined for the Pt, O₂ | YSZ system (1.3 eV - 1.4 eV) [31].
- (2) The activation energies for R_p and R_e are very different within one sample (Tab. 4.4). Hence, both of these activation energies should not be assigned to the same electrode process.
- (3) The main electrode process is rather fast (0.07 s - 0.2 ms). This would not be expected for a bulk process, such as the removal of oxygen from the YSZ.
- (4) The impedance of the main electrode process decreases when an overpotential is applied between the working and the reference anode. This suggests that the adsorption of hydrogen is facilitated in the case that the anode surface is more negatively charged due to the larger amount of oxygen because of the applied overpotential.

The low frequency relaxation process is much slower compared to the high frequency process (relaxation times between 0.3 s and 0.05 s). It appears only under polarization of the anode and increases the higher the polarization of the anode. This results in an increase of the total electrode impedance. Analyses as a function of the temperature yielded in an activation energy of 0.5 eV in the case of the Ni paste anode. The development of this impedance arc is more pronounced the higher the current that can be drawn from the SOFC. Since the water which is produced in the anodic reactions, is directly proportional to the current which can be drawn from the cell, the process seems to be closely related to the water reactions. This hypothesis is enhanced when the thermal activation of this electrode process is considered. The activation energy of the low frequency electrode process was around 0.5 eV. This value is very similar to the one mentioned in the literature for the desorption of water [30]. Note that the activation energy for the removal of oxygen from the YSZ, for example, is presumed to be much higher (1.3 eV - 1.4 eV) [31]. Hence, we assign the low frequency relaxation process to

the desorption of water.

In summary, it should be recognized that the comparison of different types of anodes is, in fact, a very promising approach in order to identify the main limitations of SOFC anodes.

4.5 References

- [1] N.Q. Minh, T. Takahashi, "Science and Technology of Ceramic Fuel Cells", Elsevier, Amsterdam, The Netherlands (1995).
- [2] H. Itho, T. Yamamoto, M. Mori, T. Watanabe, T. Abe, *Denki Kagaku* **64** (1996) 549.
- [3] H. Itho, T. Yamamoto, M. Mori, T. Horita, N. Sakai, H. Yokokawa, M. Dokiya, *J. Electrochem. Soc.* **144** (1997) 641.
- [4] M. Suzuki, H. Sasaki, S. Ootoshi, A. Kajimura, M. Ippommatsu, *Solid State Ionics* **62** (1993) 125.
- [5] T. Iwata, *J. Electrochem. Soc.* **143** (1996) 1521.
- [6] P. Ekanayake, M. Gödickemeier, L.J. Gauckler, Proc. of the 5th Asian Conf. on Solid State Ionics: New Developments, Eds.: B.V.R. Chowdari, M.A.K.L. Dissanayake, M.A. Careem, World Scientific Publishing, Singapore (1996) 535.
- [7] M. Mogensen, S. Skaarup, *Solid State Ionics* **86-88** (1996) 1151.
- [8] T. Tsai, S.A. Barnett, *J. Electrochem. Soc.* **145** (1998) 1696.
- [9] S. Skaarup, B. Zachau-Christiansen, T. Jacobsen, Proc. of the 17th Risø Intern. Symp. on Mat. Sci.: High Temperature Electrochemistry: Ceramics and Metals, Eds.: F.W. Poulsen, N. Bonanos, S. Linderoth, M. Mogensen, B. Zachau-Christiansen, Risø National Laboratory, Roskilde, Denmark (1996) 423.
- [10] S. Sunde, *Electrochimica Acta* **42** (1997) 2637.
- [11] S. Primdahl, PhD Thesis, University of Twente, Twente, The Netherlands (1999).
- [12] S.P. Jiang, S.P.S. Badwal, *Solid State Ionics* **123** (1999) 209.
- [13] P. Holtappels, L.G.J. de Haart, U. Stimming, *J. Electrochem. Soc.* **146** (1999) 2976.
- [14] B. de Boer, PhD Thesis, University of Twente, Twente, The Netherlands (1998).
- [15] T. Kawada, N. Sakai, H. Yokokawa, M. Dokiya, M. Mori, T. Iwata, *Solid State Ionics* **40/41**(1990) 402.
- [16] J. Mizusaki, H. Tagawa, T. Saito, K. Kamitani, T. Yamamura, K. Hirano, S. Ehara, T. Takagi, T. Hikita, M. Ippomatsu, S. Nakagawa, K. Hashimoto, *J. Electrochem. Soc.* **141** (1994) 2129.
- [17] N. Nakagawa, H. Sakurai, K. Kondo, T. Morimoto, K. Hatanaka, K. Kato, *J. Electrochem. Soc.* **142** (1995) 3474.
- [18] M. Brown, S. Primdahl, M. Mogensen, *J. Electrochem. Soc.* **147** (2000) 475.
- [19] B. de Boer, M. Gonzalez, H.J.M. Bouwmeester, H. Verweij, *Solid State Ionics* **127** (2000) 269.

-
- [20] A. Bieberle, L.J. Gauckler, *Solid State Ionics* **135** (2000) 337.
- [21] J.R. Macdonald, "Impedance Spectroscopy", John Wiley & Sons, Inc., New York, NY, USA (1987) 89.
- [22] M. Guillodo, P. Vernoux, J. Fouletier, *Solid State Ionics* **127** (2000) 99.
- [23] M.J. Jørgensen, M. Mogensen, *J. Electrochem. Soc.* (2000) submitted.
- [24] B.A. van Hassel, B.A. Boukamp, A.J. Burggraaf, *Solid State Ionics* **53-54** (1992) 890.
- [25] A. Hammouche, PhD Thesis, Institute National Polytechnique de Grenoble, Grenoble, France (1989).
- [26] H. Narita, J. Mizusaki, H. Tagawa, *Denki Kagaku* **61** (1993) 756.
- [27] J. Mizusaki, private communication (2000).
- [28] B.A. Boukamp, *Solid State Ionics* **20** (1986) 31.
- [29] G.A. Somorjai, "Introduction to Surface Chemistry and Catalysis", John Wiley & Sons, Inc., New York, NY, USA (1994) 347.
- [30] P.A. Thiel, T.E. Madey, *Surf. Sci. Rep.* **7** (1987) 211.
- [31] A. Mitterdorfer, PhD Thesis No. 12380, ETH Zürich, Zürich, Switzerland (1997).

Acknowledgments

Dr. S. Primdahl and Dr. M. Mogensen, Risø National Laboratory, Risø, Denmark, are gratefully acknowledged for very fruitful discussions as well as for providing the Ni paste.

Dr. K. Honegger and C. Sprecher, Sulzer Innotec, Winterthur, Switzerland, are thanked for the sputtering of Ni and of Ni-YSZ layers.

M. Jörger, ETH Zürich, Switzerland, is highly thanked for his efforts concerning screen-printing and spray pyrolysis.

Chapter 5 ^{*)}

Modeling and Simulations of the Ni, H₂ - H₂O | YSZ System

Abstract

The simplified anodic SOFC system, Ni, H₂ - H₂O | YSZ, is investigated using state-space modeling. An electrochemical model is established and the kinetic constants necessary for the simulations are estimated on the basis of literature data first and then by optimization with an experiment under standard conditions. A suitable coincidence of the theoretical and the experimental impedance spectra is found under standard operating conditions. After the optimization procedure, the simulations are carried out as a function of the triple phase boundary (TPB) length, of the partial pressure of hydrogen and of water, and of the overpotential. The simulation results are compared to experiments carried out under the same conditions. For all parameters, the same tendencies are found in the simulations and in the experiments. However, the deviations between the simulated and the experimental results indicate that either the electrochemical model or the kinetic constants determined in the simulations do not represent the system perfectly. The a priori unknown fraction of the surface coverage of oxygen is recognized to have a key influence on the anode kinetics.

^{*)} This chapter has been submitted in two parts as A. Bieberle, L.J. Gauckler, "Modeling and Simulations of the Anodic SOFC System Ni, H₂ - H₂O | YSZ", Solid State Ionics (2000).

5.1 Introduction

The Ni, H₂ - H₂O | YSZ system is the standard electrochemical system at the anode side of a solid oxide fuel cell (SOFC). At the interface of the three phases - metallic Ni, gaseous H₂ - H₂O, and ceramic YSZ - hydrogen is oxidized, oxygen is removed from the electrolyte, and water is produced. The kinetics of these processes were so far mainly studied experimentally using either Ni-YSZ cermet anodes [1-8] or metallic Ni anodes, such as Ni pattern [9-11], Ni point [12,13,14,15], or porous Ni anodes [11,16-20]. The electrochemical information about the system is usually obtained from electrochemical impedance spectroscopy (EIS) measurements and from fitting this data to equivalent circuits [21]. However, the interpretation of the measured data and of the fitting results is not straightforward. Equivalent circuit fitting does not allow a physical and chemical interpretation of the equivalent circuit elements and, thus, of the kinetics of the system.

Despite the difficulties concerning the interpretation of the EIS data, various reaction mechanisms are proposed for the Ni, H₂ - H₂O | YSZ system in the literature. Comprehensive summaries are given in [20,22] as well as in chapter 1 of this study. It should be noticed that no consensus exists so far concerning the kind of the rate determining reaction step. It is assumed to be either the dissociative adsorption of hydrogen, the formation of hydroxyl, a charge transfer reaction, or the desorption of water [1,9,10,11,12,20]. In addition, it is not even evident whether the chemical and the electrochemical reactions take only place on the surfaces of Ni and of YSZ, or whether the bulk material is also active, including, for instance, the formation of interstitial hydrogen and hydroxyl in the YSZ [11].

In contrast to the numerous experimental studies summarized in [20,22], theoretical work in the field of SOFCs is rare. Most theoretical studies focus on structural investigations considering the complex microstructure of composite electrodes [23-27] or on the simulations of the electrochemical reactor [28] and of the gas and mass flows in a SOFC stack [29,30]. Kinetic aspects of the underlying electrochemical processes under SOFC operating conditions have only recently been considered: first simulations on reaction mechanisms devoted to SOFCs focused on the Au, O₂ | YSZ system [31,32]. Electrochemical impedance spectra were simulated from an electrochemical model. A similar approach with the use of tools from control theory was successfully used in our lab for the identification of the reaction mechanisms of the Pt, O₂ | YSZ system [33-36]. This so-called state-space modeling approach is described in detail in [33,34,37,38]. Another

modeling approach is used in [39]: impedance spectra are deconvoluted so that the different relaxation processes can be distinguished. In contrast to the other two approaches, no electrochemical model has to be assumed. However, the physical interpretation of the deconvoluted spectra with the numerous relaxation processes is questionable. A last study based on simulations is described in [12]: an impedance model was established in which an equivalent circuit was derived from electrochemical equations assuming two adsorbed surface species. Experimental data on Ni and Pt point electrodes is discussed by means of these simulations.

A close view to all of the above mentioned studies suggests that simulations of SOFC electrode systems are at the beginning and that the interpretation of the underlying reaction mechanisms is still problematic. In particular, for the anode side of the SOFC, no study exists so far in which the kinetics is modeled and/or simulated.

With regard to surface science and catalysis, the Ni, H₂ - H₂O system is extensively studied due to the high catalytic activity of Ni for the dissociation of hydrogen [40,41]. However, the investigations are usually carried out at low temperatures (about 300 K). As the kinetics are strongly dependent on the temperature, the results for low temperature systems might not be valid for the operation under SOFC conditions (973 K - 1273 K). High temperature data on the Ni, H₂ - H₂O system does not exist.

The system, the most similar to the anodic SOFC conditions which was studied at high temperatures (900 K - 1300 K), is the Pt, H₂-H₂O system [42,43]. It must be noted that the partly experimental and partly theoretical study was carried out at very low partial pressures of hydrogen (1 mTorr - 1000 mTorr = 10⁻⁶ bar - 10⁻³ bar) and that the interface to the YSZ was not considered. The investigations yielded that from the two possible decomposition pathways of water (H₂O → OH + H and H₂O + O → 2 OH), the decomposition into OH and H is the primary one at high temperatures on a Pt surface. Oxygen, on the other side, promotes the decomposition of water due to the fact that oxygen traps H on the surface as OH and thereby promotes the hydroxyl coverage on the surface [43].

It can be summarized that only little is known about the kinetics of SOFC anodes. An improvement of the state-of-the-art anodes demands, however, a better understanding of the anode kinetics. We will therefore focus in this paper on a new and very promising approach for the identification of reaction mechanisms. The so-called state-space modeling (SSM) approach was developed and already

successfully used for the cathode side of the SOFC, i.e. the Pt, O₂ | YSZ system [33-36]. The anode side, Ni, H₂ - H₂O | YSZ, is much more complex and less investigated in the literature so far. Hence, it is first necessary to show the feasibility of the approach for the simulations of the anodic system. For this purpose, an electrochemical model will be established. Several assumptions are mandatory in order to simplify the system. The kinetic constants of the chemical and the electrochemical reactions will be estimated by means of different methods. Electrochemical impedance spectra will then be simulated directly from the established electrochemical model. In order to validate the approach and the electrochemical model, the simulations will be carried out as a function of the TPB (triple phase boundary) length, of the partial pressure of hydrogen and of water, and of the overpotential. The simulations will be compared to experimental EIS data.

5.2 The State-Space Modeling Approach

A summary of the approach for the identification of reaction mechanisms at SOFC electrodes using state-space modeling is shown in Fig. 5.1. It consists of a combination of modeling, simulations, and experiments. The approach is discussed in detail in [33,34,37,38] as well as in chapter 2 of this study.

The optimization procedure for the determination of the kinetic parameters is a very essential part in the simulation process. It is completed when the following criteria are fulfilled:

- The simulated and the experimental impedance spectra are identical. In order to verify this, both the Nyquist as well as the Bode representation have to be considered (requirements: positive Z' , negative Z'' , semicircle-like Nyquist plot, s-shaped $|Z|$ vs. ω plot, negative bell-shaped curve for ϕ vs. ω).
- The system is stable and not sensitive to the starting values, i.e. the estimated reaction rate constants and the surface coverage values.
- The fractions of surface coverages of the different surface species are defined as

$$\theta_x = \frac{[X_{ad}]}{N_0} \quad (5.1)$$

where $[X_{\text{ad}}]$ is the surface concentration of the species X adsorbed on the surface and N_0 is the number of free surface sites. The fraction of surface coverage of each species must adopt values between 0 and 1. The total surface coverage which is the sum of the fractions of all surface coverages, must be smaller than 1.

- The reaction rate constants should be comparable to the literature and to the estimations in subsection 5.4.3.

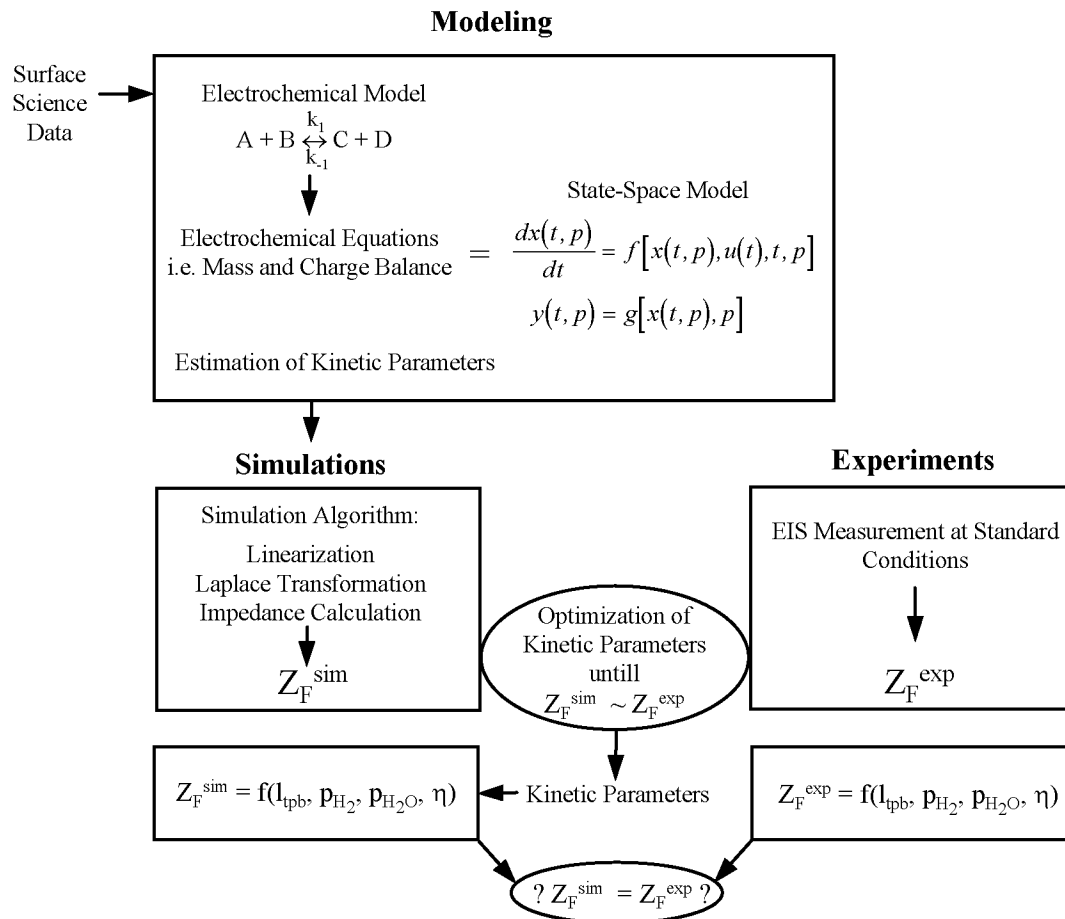


Fig. 5.1: State-space modeling approach for the identification of reaction mechanisms at SOFC electrodes.

5.3 Experimental

The experimental EIS data were obtained from a Ni pattern anode with equidistant lines of Ni and of YSZ of 20 μm width and a TPB length $l_{\text{TPB}} = 3.7 \text{ m/cm}^2$. The Ni pattern anode is deposited on top of a single crystalline YSZ (yttria stabilized zirconia) electrolyte. The preparation of the SOFC with the Ni pattern anode is described in detail in chapter 3 (subsection 3.2.1) and in [44].

The electrochemical measurements were carried out in a single gas chamber measurement set-up at $T = 973 \text{ K}$, $p(\text{H}_2) = 2.5 \cdot 10^4 \text{ Pa}$, total gas flow ($\text{H}_2 + \text{N}_2$) = 40 ml/min, $100 \text{ mHz} < \omega/2\pi < 100 \text{ kHz}$, $V_{\text{exc}} = 10 \text{ mV}$ using an IM6 Zahner impedance analyzer, Kronach, D, in a three electrode, four lead configuration. The gas flows (purity of the gases > 99.5 %) were adjusted with manual mass flow controls (Vögtlin Instruments AG, Aesch, CH). A detailed description of the measurement set-up and of the experimental conditions are given in chapter 3 (subsection 3.2.2) and in appendix 2.

Prior to the optimization procedure, the experimental impedance data were checked for contributions of the electrolyte resistance, R_e , and of the double layer capacitance, C_{dl} , to the entire impedance response (cf. chapter 2, subsection 2.2.4). The approach of Berthier *et al.* described in [45] was used. It is found that the electrolyte resistance is very small ($< 0.5 \Omega$) and that the double layer capacitance is about $1.6 \cdot 10^{-5} \text{ F}$. Both elements have no significant influence on the impedance spectrum. It is therefore feasible to directly use the as-measured impedance data for the optimization procedure and for the determination of the kinetic constants.

The simulations were run under MATLAB[®] Version 5.2 with the graphical programming extension SIMULINK[™].

5.4 Modeling

5.4.1 Electrochemical Model for the Ni, $\text{H}_2 - \text{H}_2\text{O}$ | YSZ System

The electrochemical model is the basis for the simulation process and must, thus, be established first. The reviews [40] and [41] give the most detailed information about the interaction of hydrogen and of water with solid surfaces, respectively. The references [46] and [47] are also excellent treatise of surface chemistry data. However, it must be noted that the data in the surface science and

catalysis literature is solely determined for low temperature applications. The only information about high temperature systems which are most similar to the anodic system, is discussed in [42,43] for the Pt, H_2 - H_2O system. A detailed model of the reactions taking place on a Pt surface is established and the reaction rate constants for the diverse reactions are calculated in [42,43].

For the removal of oxygen from the TPB, no information exists in the literature to the best of our knowledge. It is neither proven how the oxygen is removed from the YSZ electrolyte nor how it reacts with other species, and how the electrical charge is transferred. Detailed studies in our institute on the cathodic system Pt, O_2 | YSZ resulted in estimates for the reaction rate constants for the incorporation of oxygen in the YSZ electrolyte ($k_{1c} = 1.45 \text{ m}^3/(\text{mol s})$) and for the electronation reaction under oxidizing atmosphere ($k_{1c} = 0.3 \text{ m}^3/(\text{mol s})$) [34]. Due to this knowledge, we incorporate the same electrochemical process in the model for the anode kinetics. Using the other sparse information from the literature as well as the assumptions listed in subsection 5.4.2, we propose the following electrochemical model for the Ni, H_2 - H_2O | YSZ system (Fig. 5.2).

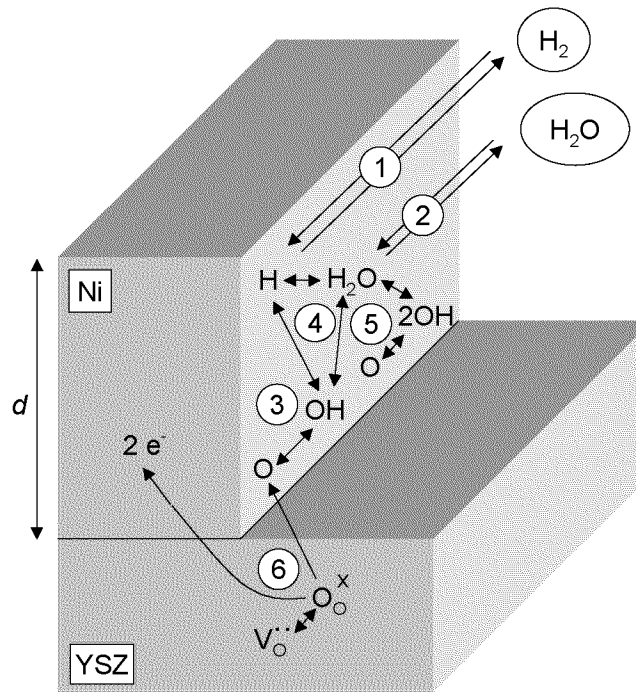


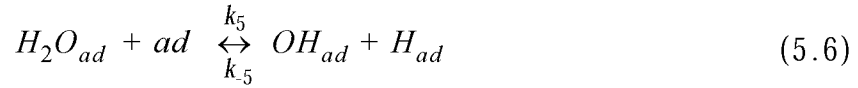
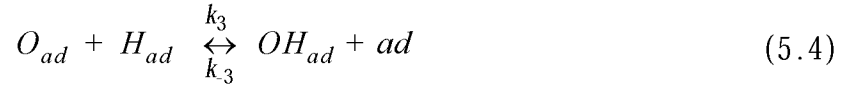
Fig. 5.2: Electrochemical model for the Ni, H_2 - H_2O | YSZ system under SOFC operating conditions.

The system is composed of the following, single reaction steps:

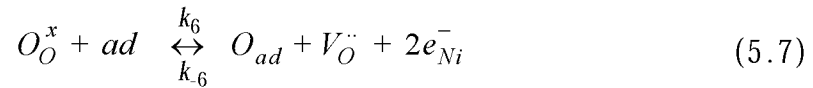
adsorption/desorption:



surface reactions:



interface reaction:



The subscript (*g*) denotes the gas phase and *ad* the adsorbed phase. It is assumed that all surface species are adsorbed on the Ni surface. k_i are the reaction rate constants for the different reaction steps.

The mass balances are calculated as following (for detailed information about the calculation of mass and charge balances refer, for instance, to [48,49]):

$$\begin{aligned} \frac{\partial \theta_H}{\partial t} = & 2k_1' p(H_2) (1-\theta)^2 - 2k_{-1} \theta_H^2 - k_3 \theta_H \theta_O + k_{-3} \theta_{OH} (1-\theta) + \\ & + k_5 \theta_{H_2O} (1-\theta) - k_{-5} \theta_{OH} \theta_H ; \end{aligned} \quad (5.8)$$

$$\begin{aligned} \frac{\partial \theta_{OH}}{\partial t} = & k_3 \theta_O \theta_H - k_{-3} \theta_{OH} (1-\theta) + 2k_4 \theta_{H_2O} \theta_O - 2k_{-4} \theta_{OH}^2 + \\ & + k_5 \theta_{H_2O} (1-\theta) - k_{-5} \theta_{OH} \theta_H ; \end{aligned} \quad (5.9)$$

$$\begin{aligned} \frac{\partial \theta_{H_2O}}{\partial t} = & k_2' p(H_2O) (1 - \theta) - k_{-2} \theta_{H_2O} - k_4 \theta_{H_2O} \theta_O + k_{-4} \theta_{OH}^2 - \\ & - k_5 \theta_{H_2O} (1 - \theta) + k_{-5} \theta_{OH} \theta_H ; \end{aligned} \quad (5.10)$$

$$\begin{aligned} \frac{\partial \theta_O}{\partial t} = & -k_3 \theta_O \theta_H + k_{-3} \theta_{OH} (1 - \theta) - k_4 \theta_{H_2O} \theta_O + k_{-4} \theta_{OH}^2 + \\ & + k_6 [O_O^x] (1 - \theta) - k_{-6} \theta_O [V_O^{\cdot\cdot}] ; \end{aligned} \quad (5.11)$$

where θ_i are the fractions of the surface coverages of the species i , i.e. H_{ad} , OH_{ad} , H_2O_{ad} , O_{ad} , as defined in Eq. 5.1. The total fraction of surface coverage, θ , is $\theta = \theta_H + \theta_{OH} + \theta_{H_2O} + \theta_O$. $k_1' \cdot p(H_2)$ and $k_2' \cdot p(H_2O)$ are in the following replaced by k_1 and k_2 in order to assign the same unit to all reaction rate constants. However, it must be noted that these two reaction rate constants are then not constant, when the partial pressure of hydrogen or the partial pressure of water are modified.

The charge balance gives

$$I_F = 2FA \cdot (k_{-6} \theta_O [V_O^{\cdot\cdot}] - k_6 [O_O^x] (1 - \theta)) \quad (5.12)$$

$$\text{with } k_6 = k_6^0 \cdot \exp\left(-2\beta \frac{F}{RT} \eta\right) \text{ and } k_{-6} = k_{-6}^0 \cdot \exp\left(-2(1-\beta) \frac{F}{RT} \eta\right)$$

where F is the Faraday constant, A the active TPB area, β the charge transfer coefficient, η the overpotential, R the gas constant, and T the temperature.

5.4.2 Assumptions

The electrochemical model implies several assumptions which were used in order to simplify the entire system.

- (1) The chemical and the electrochemical reactions are assumed to take only place on the Ni surface and directly at the TPB. It is also reasonable to assume that the YSZ surface is active for the formation of hydroxyl and the chemisorption of water, in particular, as the adsorption and the diffusion of hydrogen are assumed to be very fast. However, merely due to the complexity of the system, an active YSZ surface is not considered in the electrochemical model so far.
- (2) Hydrogen adsorbs dissociatively on Ni (Eq. 5.2) [41,46,47]. The ad-

sorption of hydrogen on ceramic surfaces, such as YSZ, is very small and is therefore neglected.

- (3) Two different reaction steps are considered for the decomposition and for the formation of water (Eq. 5.5, Eq. 5.6). For the Pt system [43], the unimolecular reaction Eq. 5.6 was found to be the primary water decomposition pathway rather than the bimolecular reaction Eq. 5.5.
- (4) The adsorption of hydrogen and the adsorption of water are both assumed to be non-activated [41,46].
- (5) The reaction rate constants are considered to be independent of the surface coverages.
- (6) All surface species are considered to be uncharged and the charge transfer reaction is assumed to take place in one step (Eq. 5.7). A two step process with negatively charged oxygen adsorbed on Ni or YSZ might also be possible as well as a charge transfer reaction coupled with the adsorption of hydrogen on the Ni surface.
- (7) The concentrations of O_O^x and $V_O^{\cdot\cdot}$ in the YSZ electrolyte as well as the surface sticking coefficients are assumed to be constant.
- (8) Three atom reactions, such as $2H_{ad} + O_{ad} \leftrightarrow H_2O_{ad} + 2ad$, are neglected, since the probability of three atoms hitting each other at the same time seems to be very low.
- (9) Surface diffusion is not implemented into the model so far.
- (10) Gas phase diffusion is not incorporated into the model, as no evidence exists for limitations of the anodic reaction mechanisms due to the gas phase (chapter 3). Also, molecular oxygen (O_2 and O) and hydroxyl should not exist in the gas atmosphere.
- (11) The site where the electrochemical reactions take place is implemented in form of an area owing to the presumption that surface species will not react on a line with an extension of theoretically zero.

5.4.3 Estimation of Kinetic Parameters

The reaction rate constants for the chemical and the electrochemical reactions, k_i , in the equations Eq. 5.2 - Eq. 5.7 are not directly published in the literature, but have to be estimated. For this purpose, three different ways (see column *method* in Tab. 5.1) were used. The methods are described in the following paragraphs and the results are summarized in Tab. 5.1. The estimated reaction rate constants are used as starting values for the optimization procedure.

1. Calculation of the adsorption reaction rate constants (k_1, k_2)

The adsorption of a molecule X_2 from the gas atmosphere on a surface is expressed by the following reaction



where ad is a free adsorption site and k is the reaction rate constant. For a non-activated adsorption process, the rate of adsorption [43,50] is given as

$$\frac{d\theta_x}{dt} = 2k(1-\theta)^2 = 2Zs_\theta \quad (5.14)$$

where θ_x is the fraction of surface coverage of the adsorbed species X on the surface, t the time, $(1-\theta)$ the fraction of free adsorption sites on the surface, \mathfrak{Z} the impingement rate of X_2 on the surface, and s_θ the sticking coefficient for the surface species X . The impingement rate can be calculated from the kinetic gas theory [46]

$$\mathfrak{Z} = \frac{p(X_2)}{\sqrt{2\pi k_B T}} = 2.6 \cdot 10^{24} \cdot \frac{p(X_2)}{\sqrt{M(X_2) T}} \left[\frac{1}{m^2 s} \right] \quad (5.15)$$

where $p(X_2)$ is the partial pressure of X_2 in the gas atmosphere, k_B the Boltzmann constant, T the temperature, and M the molecular mass of the gas species X_2 . The sticking coefficient s_θ is defined as the fraction of particles hitting the surface and becoming temporarily or permanently bound to the surface

$$s_\theta = s_0(1-\theta)^\alpha \quad (5.16)$$

where s_0 is the initial sticking coefficient, $\alpha = 1$ for non-dissociative adsorption and $\alpha = 2$ for dissociative adsorption.

In units of 1/s, the reaction rate constant k is then

$$k = \mathfrak{S} \cdot s_0 \frac{1}{N_A N_0} = 2.6 \cdot 10^{24} \cdot \frac{p(X_2)}{\sqrt{M(X_2) T}} \cdot s_0 \cdot \frac{1}{N_A N_0} \left[\frac{1}{s} \right] \quad (5.17)$$

where N_A is the Avogadro number and N_0 the number of free adsorption sites on the Ni surface ($N_0 = 10^{19} / N_A$ mol/m² [41]).

2. Calculation of reaction rate constants from the activation energies (k_{-1} , k_2 , k_3 - k_5)

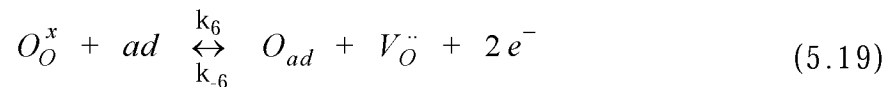
If the activation energy for a process is known, the reaction rate constant is calculated from the Arrhenius expression [46]

$$k = v \cdot N_A N_0 \cdot \exp\left(-\frac{E}{RT}\right) \left[\frac{1}{s} \right] \quad (5.18)$$

where v is the pre-exponential factor, N_A the Avogadro number, N_0 the number of free adsorption sites on the Ni surface ($N_0 = 10^{19} / N_A$ mol/m² [41]), E the activation energy, R and T have their usual meaning.

3. Estimation of reaction rate constants using EIS (k_6 , k_{-6})

The following reaction is assumed to take place at the TPB



where O_O^x denotes an oxygen interstitial and $V_O^{\ddot{}}$ an oxygen vacancy. The resulting Faradaic current I_F is then defined as

$$I_F = FA \cdot (k_6 [O_O^x] (1 - \theta) N_0 - k_{-6} [V_O^{\ddot{}}] \theta N_0) \quad (5.20)$$

with

$$k_6 = k_6^0 \cdot \exp\left(-2\beta \frac{F}{RT} \eta\right) \quad (5.21)$$

$$k_{-6} = k_{-6}^0 \cdot \exp\left(-2(1-\beta) \frac{F}{RT} \eta\right) \quad (5.22)$$

where β is the charge transfer coefficient, η the overpotential, and F , A , R , and T have their usual meaning.

From electrochemical impedance spectroscopy, the charge transfer resistance, R_t , can be determined. Theoretically, it is defined as [51]

$$R_t = \left(\frac{\partial I_F}{\partial \eta}\right)^{-1} \quad (5.23)$$

For $\eta = 0$ mV and using the interim assumption that $\beta = 0.5$ [52], one finds

$$R_t^o = \frac{1}{\frac{F}{RT} (-i_{0c} - i_{0a})} \quad (5.24)$$

with

$$i_{0c} = FA \cdot k_6^0 [O_O^x] (1-\theta) N_0 \quad (5.25)$$

$$i_{0a} = FA \cdot k_{-6}^0 [V_O^{\cdot\cdot}] \theta_O N_0 \quad (5.26)$$

Under equilibrium conditions, no net current is observed at an electrochemical interface and the anodic and the cathodic currents are equal [52]:

$$i_{0a} = i_{0c} = i_0 \quad (5.27)$$

Eq. 5.24 can now be written as

$$i_0 = \frac{-RT}{2FR_t^o} \quad (5.28)$$

R_t^o can be estimated from impedance measurements using equivalent circuit

fitting. According to Eq. 5.21 / Eq. 5.22 and Eq. 5.25 / Eq. 5.26, k_6 and k_{-6} are for $\eta = 0$ mV

$$k_6 = \frac{i_0}{FA [O_O^x] (1 - \theta) N_0} \quad (5.29)$$

$$k_{-6} = \frac{i_0}{FA [V_{\ddot{O}}] \theta_O N_0} \quad (5.30)$$

Tab. 5.1: Reaction rate constants estimated from surface science literature data for $T = 973$ K.

Reaction	k_i	k_i [s^{-1}]	Parameters	Comment	Method	Ref.
$H_2(g) + 2ad \leftrightarrow 2H_{ad}$	k_1	10^7	$s_0(H_2) = 0.2$	$p(H_2) = 10^4$ Pa	1	[53]
	k_{-1}	$2 \cdot 10^8$	$v = 2.5 \cdot 10^{13} s^{-1}; E = 96$ kJ/mol	$v = v^* \cdot N = 2.5 \cdot 10^{-6} m^2/s \cdot 10^{19} m^{-2}$	2	[50]
$H_2O(g) + ad \leftrightarrow H_2O_{ad}$	k_2	$6 \cdot 10^6$	$s_0(H_2O) = 1$	$p(H_2O) = 3 \cdot 10^3$ Pa	1	[40]
	k_2	$2 \cdot 10^{13}$	$v = 10^{16} s^{-1}; E = 52$ kJ/mol	$\theta_{H_2O} < 0.42$ ML	2	[54]
		$8 \cdot 10^{10}$	$v = 10^{13} s^{-1}; E = 39$ kJ/mol	$\theta_{H_2O} > 0.42$ ML	2	[54]
		$2.5 \cdot 10^9$	$v = 10^{13} s^{-1}; E = 67$ kJ/mol	clean Ni surface	2	[55]
10^{11}	$v = 10^{13} s^{-1}; E = 38$ kJ/mol	oxygen-modified Ni surface	2	[55]		
$O_{ad} + H_{ad} \leftrightarrow OH_{ad} + ad$	k_3	$2 \cdot 10^{11}$	$v = 10^{13} s^{-1}; E = 33.7$ kJ/mol	-	2	[42]
	k_{-3}	$4 \cdot 10^2$	$v = 10^{13} s^{-1}; E = 193$ kJ/mol	Pt system, low pressure	2	[42]
		$4 \cdot 10^1$	$v = 10^{13} s^{-1}; E = 212$ kJ/mol	Pt system, low pressure	2	[42]
$H_2O_{ad} + O_{ad} + ad \leftrightarrow 2OH_{ad}$	k_4	10^{12}	$v = 10^{13} s^{-1}; E = 17$ kJ/mol	clean Ni surfac	2	[55]
		$4.5 \cdot 10^6$	$v = 10^{13} s^{-1}; E = 118$ kJ/mol	Pt system, low pressure	2	[43]
	k_{-4}	$2 \cdot 10^2$	$v = 10^{13} s^{-1}; E = 201$ kJ/mol	clean Ni surfac	2	[55]
		$3 \cdot 10^{10}$	$v = 10^{13} s^{-1}; E = 48$ kJ/mol	Pt system, low pressure	2	[43]
$H_2O_{ad} + ad \leftrightarrow OH_{ad} + H_{ad}$	k_5	$6 \cdot 10^5$	$v = 10^{13} s^{-1}; E = 134$ kJ/mol	oxygen-modified Ni surface	2	[55]
		$3 \cdot 10^7$	$v = 10^{13} s^{-1}; E = 102$ kJ/mol	Pt system, low pressure	2	[43]
	k_{-5}	1.5	$v = 10^{13} s^{-1}; E = 239$ kJ/mol	oxygen-modified Ni surface	2	[55]
		10^{12}	$v = 10^{13} s^{-1}; E = 17$ kJ/mol	Pt system, low pressure	2	[43]
$O_x^o + ad \leftrightarrow O_{ad} + V_o^{\cdot\cdot} + 2e^-$	k_6	$5 \cdot 10^2$	$i_0 = 0.042$ A/cm ² ; $R_t = 1 \Omega$	-	3	[34]
		$8 \cdot 10^{-6}$	-	Pt system	-	
	k_{-6}	$3 \cdot 10^4$	$i_0 = 0.042$ A/cm ² ; $R_t = 1 \Omega$	-	3	
		$3 \cdot 10^{-4}$	-	Pt system	-	[34]

5.5 Implementation of the Electrochemical Model

The mass and the charge balances are implemented into the computer using the graphical programming extension SIMULINK™ in MATLAB®. Fig. 5.3 shows as an example the rate equation for the time dependent surface species O_{ad} (Eq. 5.11 and Eq. 5.12). The rate equations for the other time dependent surface species of the system, i.e. H_{ad} , OH_{ad} , and H_2O_{ad} , are implemented similarly, each in one subsystem, such as the one shown in Fig. 5.3. The different subsystems are then connected with each other as illustrated in Fig. 5.4.

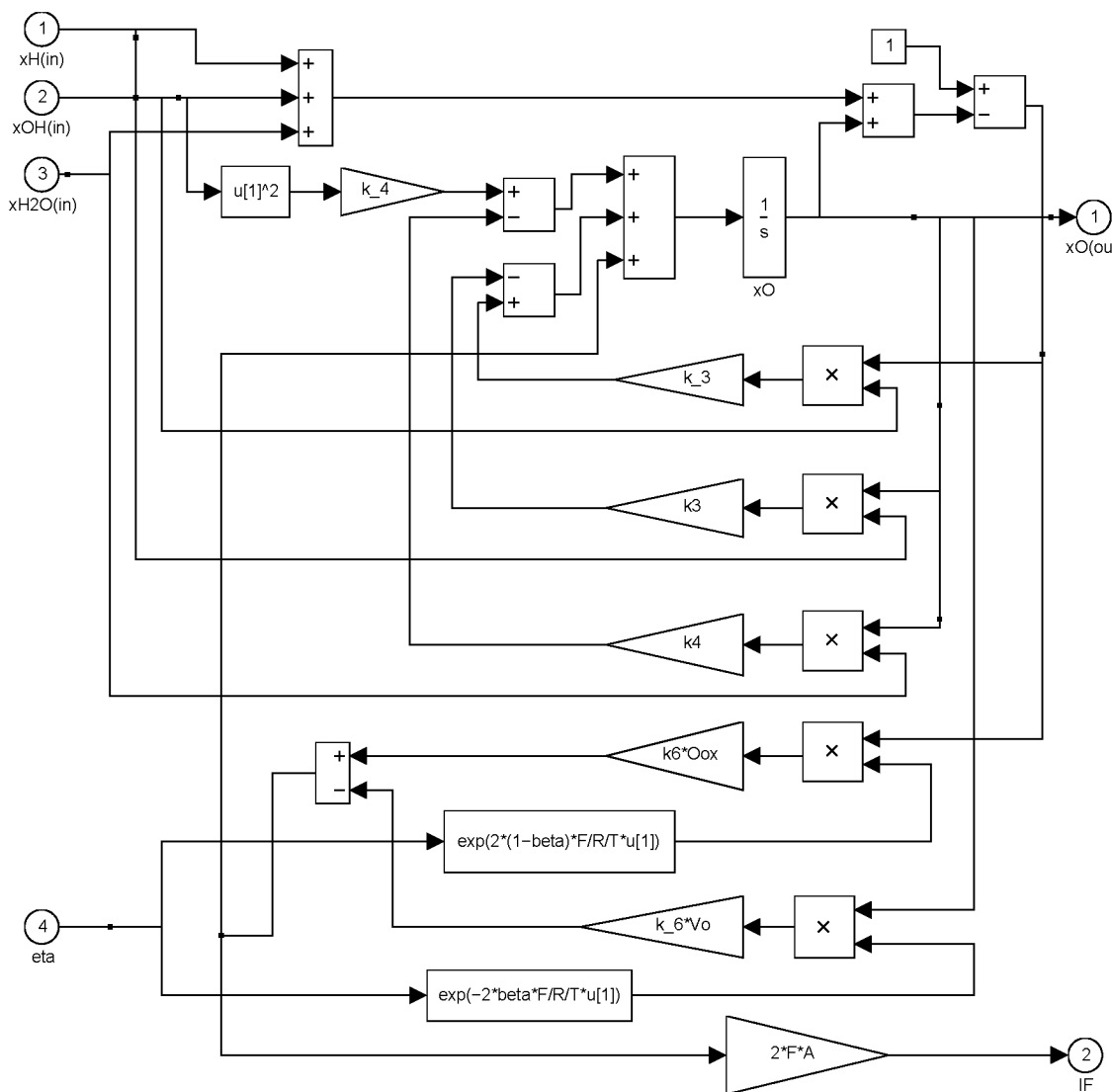


Fig. 5.3: SIMULINK™ block diagram for the rate equation of the time-dependent surface species O_{ad} (Eq. 5.11 and Eq. 5.12).

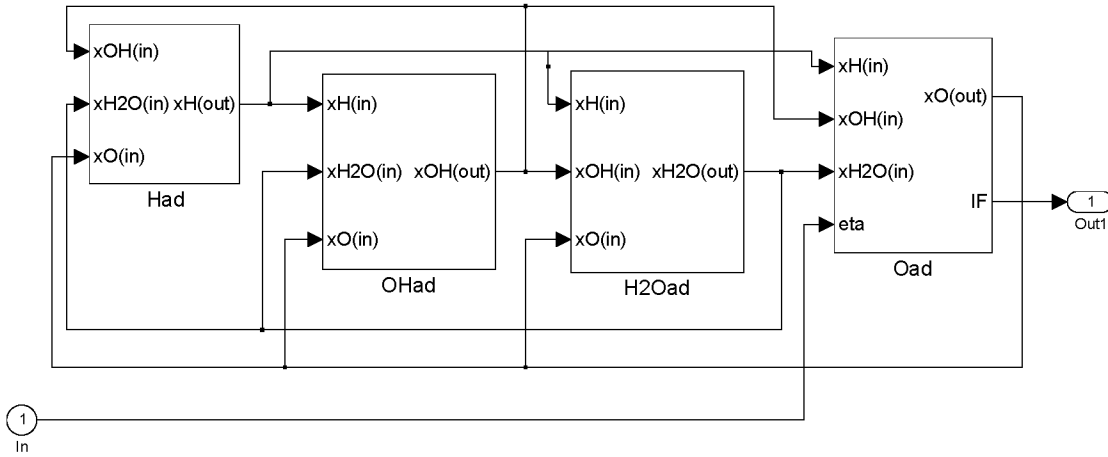


Fig. 5.4: SIMULINK™ block diagram illustrating the connections of the four subsystems which contain the rate equations for H_{ad} , OH_{ad} , H_2O_{ad} and O_{ad} .

For the calculation of the impedance data directly from the electrochemical model, the most important MATLAB® commands are listed in Tab. 5.2. The MATLAB® commands are described in detail in [56]. More detailed information about the simulation algorithm is given in [33,34,37].

Tab. 5.2: MATLAB® commands, descriptions of the commands, as well as the explanations for the calculation of the impedance data directly from the electrochemical model.

Command	Description	Explanation
constr	finds the minimum of a constrained multivariable function (minimize $f(x)$ subject to $G(x) \leq 0$)	used in order to minimize the discrepancy between Z_F^{exp} and Z_F^{sim} by changing the kinetic parameters
trim	finds steady state parameters for a system given a set of conditions	used in order to calculate the surface coverage values
linmod	obtains linear models from systems of ordinary differential equations	calculates the system matrices which describe the linearized state space model
ss2tf	state-space to transfer function conversion	-
nyquist	calculates the nyquist frequency response of a linear time independent model	calculates the real and the imaginary parts of the frequency response

5.6 Simulations

The simulation results can be divided into two groups: simulations under standard conditions and simulations where one parameter, i.e. the TPB length, l_{TPB} , the partial pressure of hydrogen, $p(\text{H}_2)$, the partial pressure of water, $p(\text{H}_2\text{O})$, or the overpotential, η , is varied, while all the other parameters are kept constant. Standard conditions signify those SOFC operating conditions where the majority of the experimental impedance measurements are carried out. The optimization procedure for the determination of the reaction rate constants is carried out under standard conditions. The reaction rate constants are then kept constant, while one or the other experimental parameter (l_{TPB} , $p(\text{H}_2)$, $p(\text{H}_2\text{O})$, η) is varied. It should be noted that the reaction rate constants k_1 and k_2 are dependent on the partial pressure of hydrogen and of water, respectively (see subsection 5.4.1).

5.6.1 Standard Conditions

The constants and variables used for the simulations under standard conditions are listed in Tab. 5.3. Different kinds of constants and variables are used: #1 - #3 are natural constants, #4 - #10 are variables which are set constant for all simulations, and #11 - #14 are variables which are alternated during the simulations.

Using the constants and the variables listed in Tab. 5.3 as well as starting values for the surface coverages and for the reaction rate constants (Tab. 5.1), the electrochemical model is subjected to an optimization procedure with an experimental impedance spectrum recorded under the same conditions. The best and most reasonable fit was obtained with the fractions of the surface coverages, θ_i , listed in Tab. 5.4 and with the reaction rate constants, k_i , listed in Tab. 5.5. The resulting impedance spectrum is shown in comparison to the experimental data in Fig. 5.5.

Tab. 5.3: Constants and variables used for the simulations under standard conditions.

#	Quantity	Symbol	Value	Unit	Ref.
1	gas constant	R	8.3141	J/(mol·K)	[57]
2	Faraday constant	F	96500	C/mol	[57]
3	Avogadro number	N_A	$6 \cdot 10^{23}$	mol ⁻¹	[57]
4	number of free surface sites	N_0	10^{19}	m ⁻²	[41]
5	concentration of oxygen ions in the YSZ	O_O^x	$4.45 \cdot 10^4$	mol/m ³	[34]
6	concentration of oxygen vacancies in the YSZ	$V_O^{\cdot\cdot}$	$4.65 \cdot 10^3$	mol/m ³	[34]
7	active electrode thickness	d	10^{-5}	m	†
8	hydrogen sticking coefficient	$s_0(\text{H})$	0.4	1	[53]
9	water sticking coefficient	$s_0(\text{H}_2\text{O})$	1	1	[40]
10	temperature	T	973	K	*)
11	TPB length	l_{TPB}	3.7	m/cm ²	*)
12	hydrogen partial pressure	$p(\text{H}_2)^{\dagger\dagger}$	$2.5 \cdot 10^4$	Pa	*)
13	water partial pressure	$p(\text{H}_2\text{O})^{**})$	$4 \cdot 10^1$	Pa	*)
14	overpotential	η	0	mV	*)

† assumed data

†† calculated from the gas mixture adjusted at the mass flow controls in the experiments

*) experimental data

***) calculated from the EMF of a YSZ oxygen sensor installed next to the fuel cell in the experimental set-up

The fractions of the surface coverages of the different species, θ_i , are the steady-state solutions of the system of differential equations, i.e. the steady-state solutions of the mass balances described in Eq. 5.8 - Eq. 5.11: $d\theta_i/dt = 0$. Estimates of the surface coverages allow to calculate the reaction rate constants k_6 and k_6 according to Eq. 5.29 and Eq. 5.30, respectively. Hence, the surface coverages were determined for Eq. 5.2 to Eq. 5.7 using the starting values for k_1 and k_5 and ignoring the TPB reaction, i.e. Eq. 5.7, which contains the reaction rate constants

k_6 and k_{-6} . The surface concentrations listed in Tab. 5.4 are, thus, determined for the pure Ni surface. The θ_i values fulfill all the physical condition to be between 0 and 1. It should be noted that all θ_i are very low. In particular, θ_H seems to be rather low with an absolute value of 0.06. In the literature, a fraction of surface coverage of about 0.39 was calculated for hydrogen adsorbed on Ni(110) at 973 K at $p(\text{H}_2) = 2.5 \cdot 10^4$ Pa [50].

Tab. 5.4: Fractions of the surface coverages of the different species adsorbed on Ni determined from the electrochemical model presented in subsection 5.4.1.

θ_H	θ_{OH}	$\theta_{\text{H}_2\text{O}}$	θ_O	$1-\theta$
$6 \cdot 10^{-2}$	$4 \cdot 10^{-4}$	$5 \cdot 10^{-9}$	$3 \cdot 10^{-3}$	0.94

The reaction rate constants in Tab. 5.5 must be compared to the starting values which were derived in subsection 5.4.3 (Tab. 5.1). Maximum deviations of 4 orders of magnitude in the rate constants are found. These deviations are not surprising, as the starting values are only very rough estimates. Note e.g. the considerable differences in the systems which were evaluated as well as the fact that already the literature data scatters strongly (Tab. 5.1). Using the same reaction rate constants for the simulations as suggested in Tab. 5.1, no arc in the impedance spectrum was obtained. While the reaction rate constants k_1 to k_5 are all very high, the reaction rate constants k_6 and k_{-6} are much smaller. This might be due to the fact that the reaction rate constants k_1 to k_5 symbolize surface reactions, whereas k_6 and k_{-6} include a bulk reaction.

Comparing the forward and the backward reaction rate constants in Tab. 5.5, reasonable tendencies are found: for example, the formation of hydroxyl (k_3) is much faster than the decomposition of hydroxyl into hydrogen and oxygen (k_{-3}). Also, the electronation reaction (k_6) is faster than the incorporation of the oxygen into the YSZ (k_{-6}).

Tab. 5.5: Reaction rate constants determined by the optimization of an EIS measurement under standard conditions with the electrochemical model presented in subsection 5.4.1 (for comparison with the starting values see Tab. 5.1).

k	k₁ [s⁻¹]	k₂ [s⁻¹]	k₃ [s⁻¹]	k₄ [s⁻¹]	k₅ [s⁻¹]	k₆ [s⁻¹]
k_i	2·10 ⁷	8·10 ⁷	5·10 ⁷	10 ¹⁰	10 ⁸	6·10 ⁻⁴
k_{-i}	7·10 ⁹	2·10 ¹³	10 ⁴	5·10 ⁹	3·10 ⁴	2·10 ⁰

The simulated impedance spectrum calculated directly from the electrochemical model (Eq. 5.2 - Eq. 5.7) and using the constants and the variables listed in Tab. 5.3, Tab. 5.4, and Tab. 5.5 is shown in comparison to the experimental impedance spectrum in Fig. 5.5. The simulated impedance yields values in the same order of magnitude as the experimental one and the spectrum exhibits one arc, like in the experiment (Fig. 5.5a). Also, in the Bode representation (Fig. 5.5b and c), a rather good agreement of the simulated and the experimental data is found.

Nevertheless, some deviations between the experiment and the simulation appear: first, the simulated Nyquist plot consists of a perfect semicircle, whereas the experimental one is distorted (Fig. 5.5a). The phase angle in the Bode plot deviates more from $\phi = -90^\circ$ in the experiments compared to the simulations (Fig. 5.5c). These two effects suggest that the experimental data is distorted by an effect which is not considered in the electrochemical model. Second, it is found that the relaxation frequency is higher for the simulated data ($\omega^* = 58$ Hz) compared to the experimental data ($\omega^* = 7$ Hz). This means that the electrode process is faster in the simulations than it is found in the experiments.

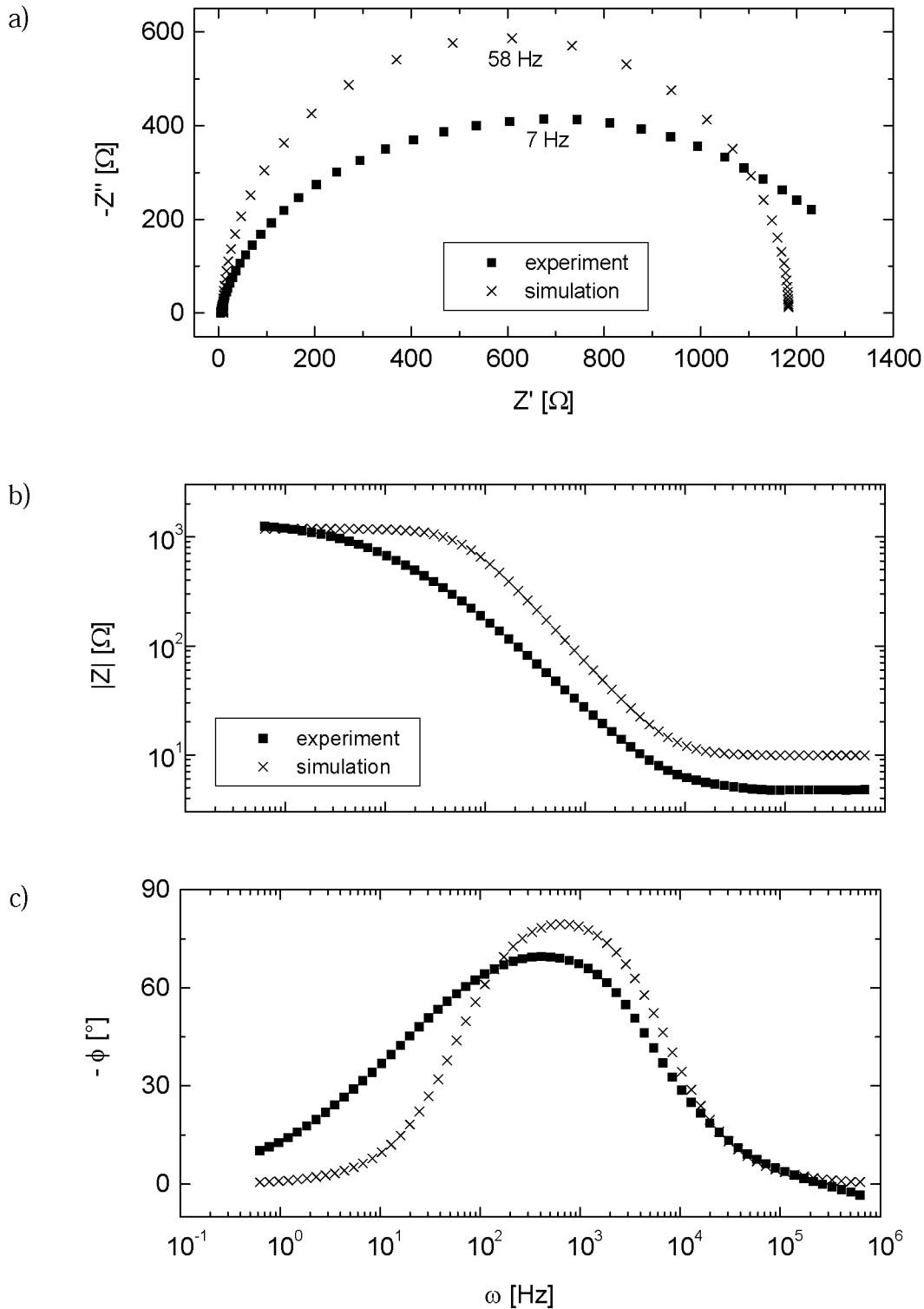


Fig. 5.5: a) Nyquist and b) and c) Bode plots of the experimental and the simulated impedance data (the kinetic parameters used for the simulations are listed in Tab. 5.3, Tab. 5.4, and Tab. 5.5).

With regard to the sensitivity of the system on the starting values, it is found that the surface coverage values can be varied by several orders of magnitude and always the same surface coverages are found (Tab. 5.4). Hence, the system is stable with respect to the starting values for the surface coverages. Concerning the reaction rate constants, it is found that these values can all be varied by one order of magnitude without losing the shape of an arc in the Nyquist plot. The total impedance merely changes. The reaction rate constants k_4 and k_{-4} (Eq. 5.5) are found not to influence the total impedance. Even without Eq. 5.5, the simulated impedance spectrum stays constant. Thus, it can be concluded that the water might react only via Eq. 5.6. However, the elimination of Eq. 5.6 instead of Eq. 5.5 results also in a rather similar impedance spectrum which might be transformed into the spectrum in Fig. 5.5 with some changes in other parameters. Hence, both paths for the formation of water are, in principle, feasible and it is up to now not possible to decide unambiguously which one is favored.

5.6.2 Triple Phase Boundary

The triple phase boundary (TPB) is considered as the region where the three phases of the anode which are mandatory for the anode kinetics, are interconnected: the catalyst Ni, the oxygen supplier YSZ, and the pores which contain the fuel gas. The electrochemistry is assumed to take place at this TPB. In the electrochemical model, the TPB is implemented by means of an area, A , since the surface species will not react on an indefinitely small line. The TPB area is the product of the TPB length, l_{TPB} , and of a certain active anode thickness, d . The TPB length can be varied with the anode design and is rather precisely known for Ni pattern anodes. The standard Ni pattern anode used in the experiments has a TPB length of 3.7 m/cm^2 with an uncertainty of about 10% (cf. chapter 3). The simulations are compared to this anode design.

The active electrode thickness, d , in contrast, is not known from the experiments. Since the electrochemical model considers only the Ni surface, the active anode thickness extends onto the Ni surface (Fig. 5.2) and is kept constant for all simulations. The absolute value for the active electrode thickness specified in Tab. 5.3 seems to be rather high with a value of $10 \text{ }\mu\text{m}$. However, one has to consider that the active electrode thickness is multiplied in the simulations with the TPB length in order to specify the electrochemically active area. Since the TPB length is supposed to be known from the experiments, it is the active electrode

thickness which allows to scale the simulated impedance spectrum in size. Hence, the high value for the active electrode thickness can either be attributed to an under-estimation of the actual TPB length in the experiments or to problems associated with the electrochemical model, most probably with the estimation of the reaction rate constants. In subsection 5.4.2, it is assumed that the chemical and the electrochemical reactions do not take place on the YSZ surface. Hence, an extension of the TPB onto the YSZ surface must not be considered in the discussion of the TPB length.

The influence of the TPB length on the simulated impedance spectra is shown in Fig. 5.6. In the logarithmic plot, the total impedance $|Z|$ seems to be shifted parallel as a function of the TPB length (Fig. 5.6a). This does not signify that the polarization resistance which is $|Z|_{\omega(\min)} - |Z|_{\omega(\max)}$, stays constant. In fact, it decreases exponentially with increasing TPB length (note the logarithmic plotting of $|Z|$). Hence, the highest impedance is found for the shortest TPB length of $l_{\text{TPB}} = 0.04 \text{ m/cm}^2$. This observation is in agreement with the experimental findings in chapter 3 (subsection 3.3.2.5).

The purely ohmic resistance at high frequencies is usually interpreted as the electrolyte resistance, R_e , in the experiments. Due to a very low electrolyte resistance found in the experiments, R_e is not considered in the simulations. Thus, the increase of the high frequency ohmic resistance in Fig. 5.6a does not signify an increase of the electrolyte resistance. It originates from the fact that $|Z|$ is not zero at high frequencies and that the high frequency ohmic resistance scales with the TPB length.

Fig. 5.6b represents the bell-shaped curves of the phase angle vs. the frequency. The data does not change, since the electrochemistry is not altered when the TPB is modified.

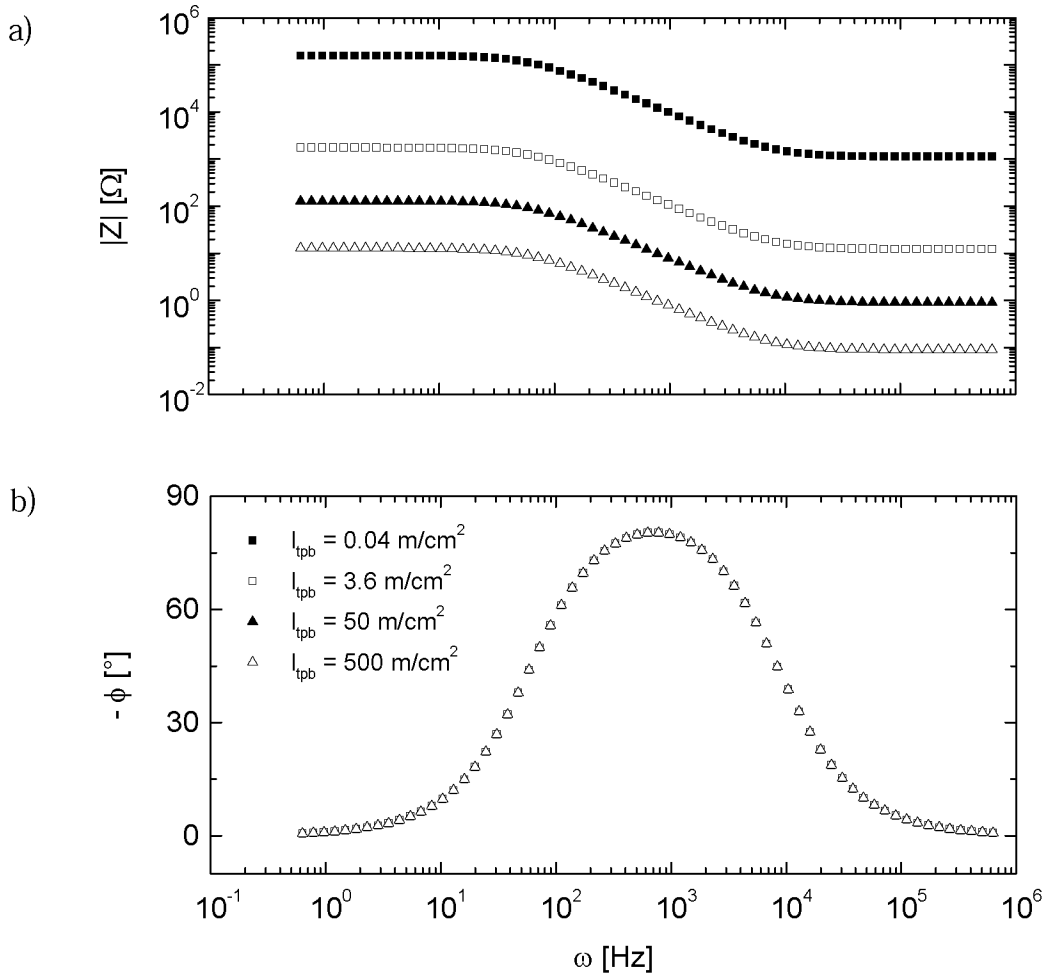


Fig. 5.6: Simulated impedance data as a function of the TPB length, l_{TPB} (the kinetic parameters used for the simulations are listed in Tab. 5.3, Tab. 5.4, and Tab. 5.5).

Fig. 5.7 illustrates the polarization resistance, R_p , as a function of the TPB length. The polarization resistance is the maximum of the real part of the impedance minus the ohmic contribution at high frequency. A power law dependence of the polarization resistance as a function of the TPB length is found with an exponent of -1 (Fig. 5.7). In the experiments of Ni pattern anodes, this behavior is only found for long TPB lengths (Fig. 5.7). The real TPB length seems to be underestimated in the experiments in the case of a very short TPB length of 0.04 m/cm² (cf. chapter 3, subsection 3.3.2.5).

The results obtained in this subsection are rather straight-forward, since the electrochemical model includes the assumption that the chemical and the electro-

chemical reactions are restricted to the TPB. However, in order to validate the proper implementation and the simulations of the electrochemical model, Fig. 5.6 and Fig. 5.7 provide excellent assistance. Furthermore, the experimental results can be judged better.

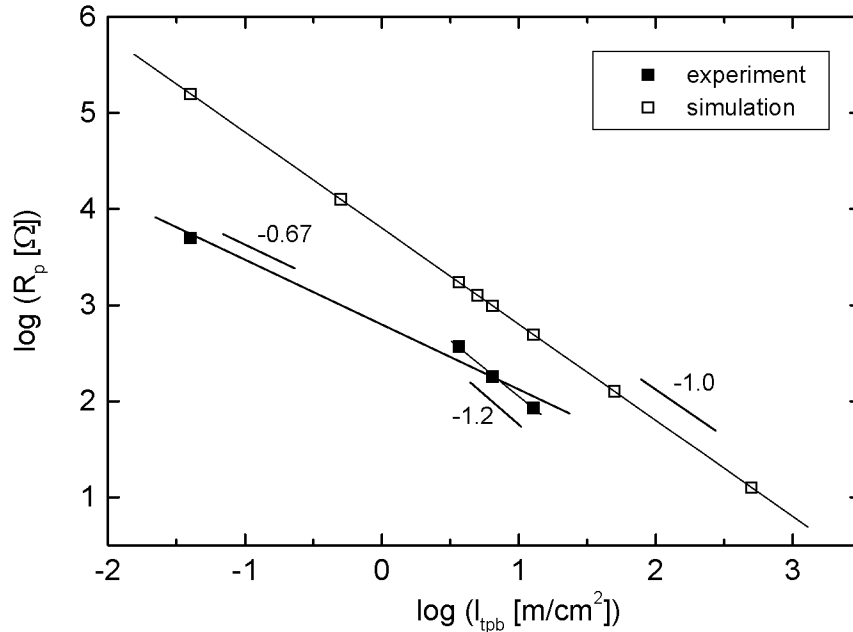


Fig. 5.7: Polarization resistance, R_p , as a function of the TPB length, l_{TPB} : a comparison between simulation and experiment (same simulation conditions as in Fig. 5.5). Note that the data is corrected for R_e .

5.6.3 Partial Pressure of Hydrogen

From the experimental data on Ni pattern anodes, it is known that the partial pressure of hydrogen has no significant influence on the anode behavior, as long as at least some hydrogen is available for the maintenance of the electrode process (chapter 3 and [10,11]). The simulations confirm this hypothesis: the total electrode impedance reaches almost the same value for all partial pressures of hydrogen (Fig. 5.8a). However, also here, a considerable shift of the impedance data in the high frequency region is found as a function of the partial pressure of hydrogen. The phase angle behavior (Fig. 5.8b) indicates that the simulated system is, in contrast to the experimental results (chapter 3), sensitive to changes in the partial pressure of hydrogen.

The variation in the partial pressure of hydrogen comes along with changes in

the fraction of the surface coverages of the different surface species (Fig. 5.9). While θ_{H} decreases slightly for decreasing partial pressure of hydrogen, θ_{O} increases strongly to almost 0.8 for $p(\text{H}_2) = 10 \text{ Pa}$. The oxygen seems to be trapped onto the Ni surface due to a lack of hydrogen.

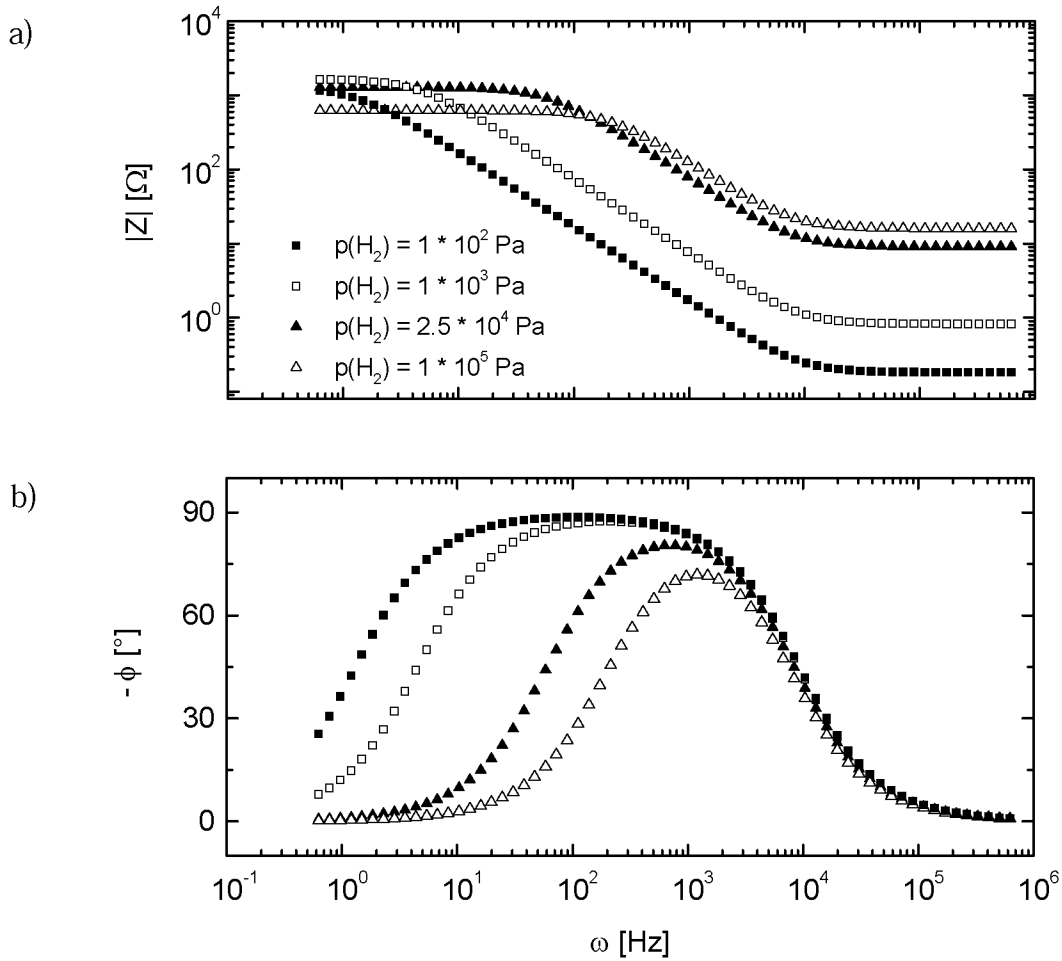


Fig. 5.8: Simulated impedance data as a function of the partial pressure of hydrogen, $p(\text{H}_2)$ (the kinetic parameters used for the simulations are listed in Tab. 5.3, Tab. 5.4, and Tab. 5.5).

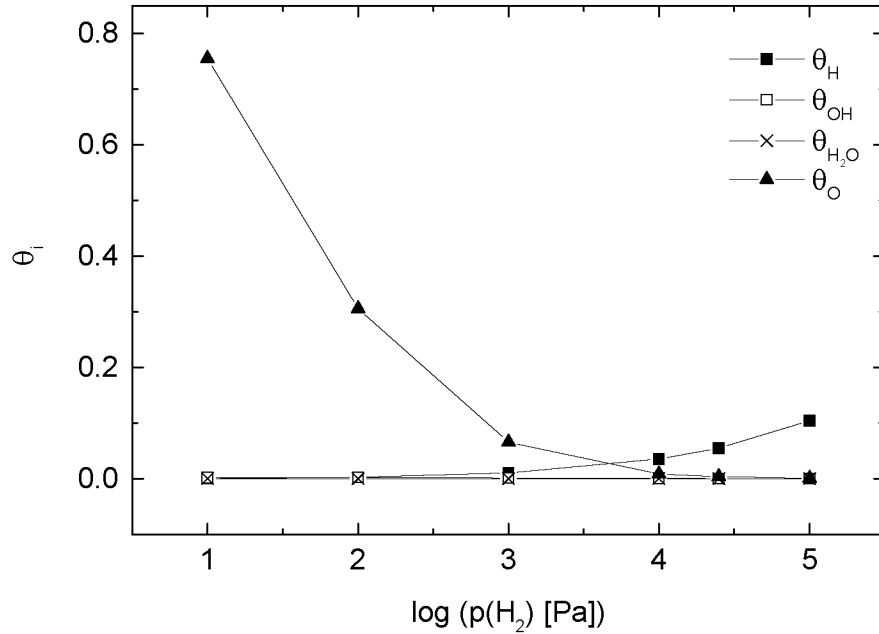


Fig. 5.9: Fractions of the surface coverages of the different surface species, θ_i , as a function of the partial pressure of hydrogen, $p(\text{H}_2)$ (same simulation conditions as in Fig. 5.8). The lines are drawn to guide the eye.

5.6.4 Partial Pressure of Water

Increasing the partial pressure of water in the fuel gas atmosphere is known to decrease the polarization resistance of the anode due to a catalytic effect of the water which is not clearly understood so far (chapter 3 (subsection 3.3.2.3 and subsection 3.4) and [16,17]). A positive effect on the performance of the anode was also confirmed in the simulations. The total electrode impedance decreases strongly (Fig. 5.10). The phase angle, in contrast, does not change considerably.

The polarization resistance and the relaxation frequency are shown as a function of the partial pressure of water in Fig. 5.11 and in Fig. 5.12, respectively. It is found that the polarization resistance shows mainly the same behavior in the simulations and in the experiments (Fig. 5.11). However, the absolute values for the simulated spectra are always slightly lower than for the experimental data. The slopes indicate that the simulated data reacts more intensely to an increase in the partial pressure of water than the experimental data.

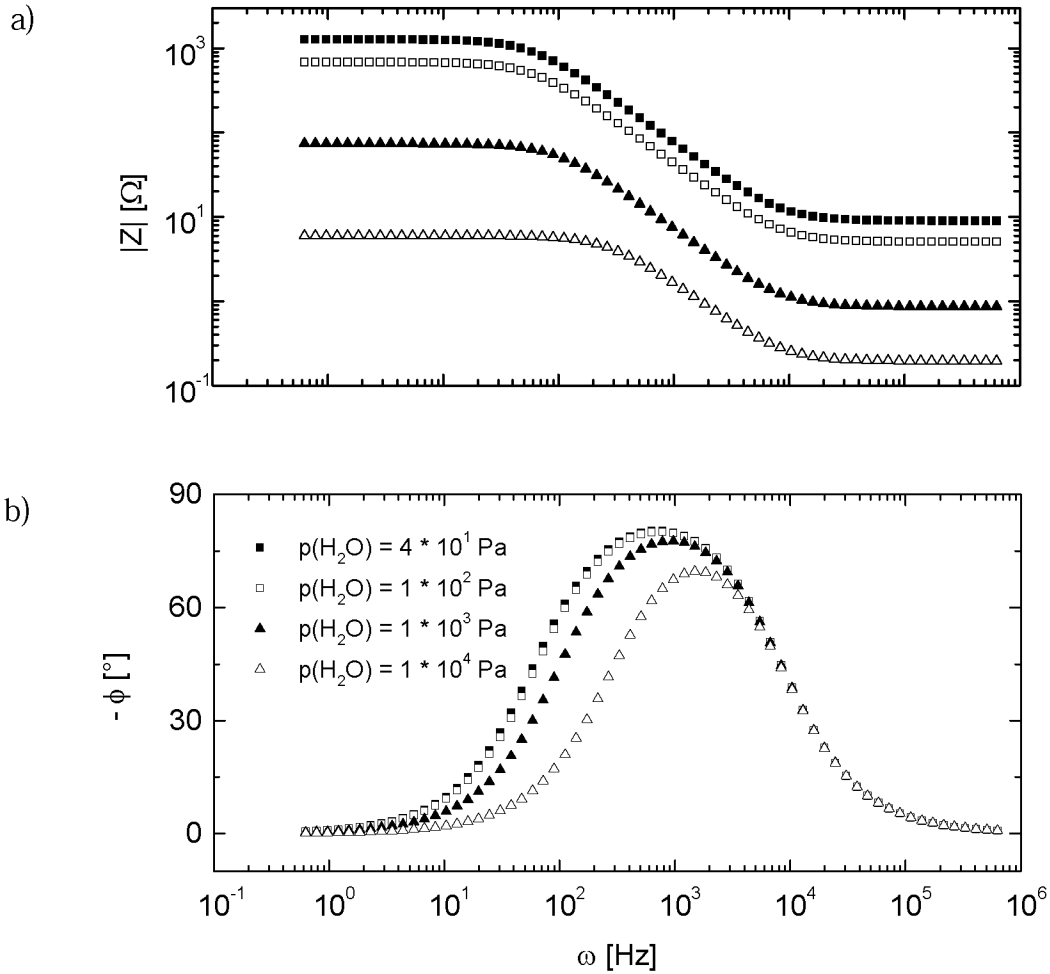


Fig. 5.10: Simulated impedance data as a function of the partial pressure of water, $p(\text{H}_2\text{O})$ (the kinetic parameters used for the simulations are listed in Tab. 5.3, Tab. 5.4, and Tab. 5.5).

In the case of the relaxation frequency, ω^* , a significantly different behavior is found for the simulations and for the experiments (Fig. 5.12): the absolute values for the relaxation frequency agree only for partial pressures of water around 10^3 Pa. The slopes of the curves are different: 0.81 for the experiments and 0.29 for the simulations. However, the overall tendency is the same for both the experiments as well as for the simulations, the electrode process becomes faster with an increasing amount of water in the fuel gas.

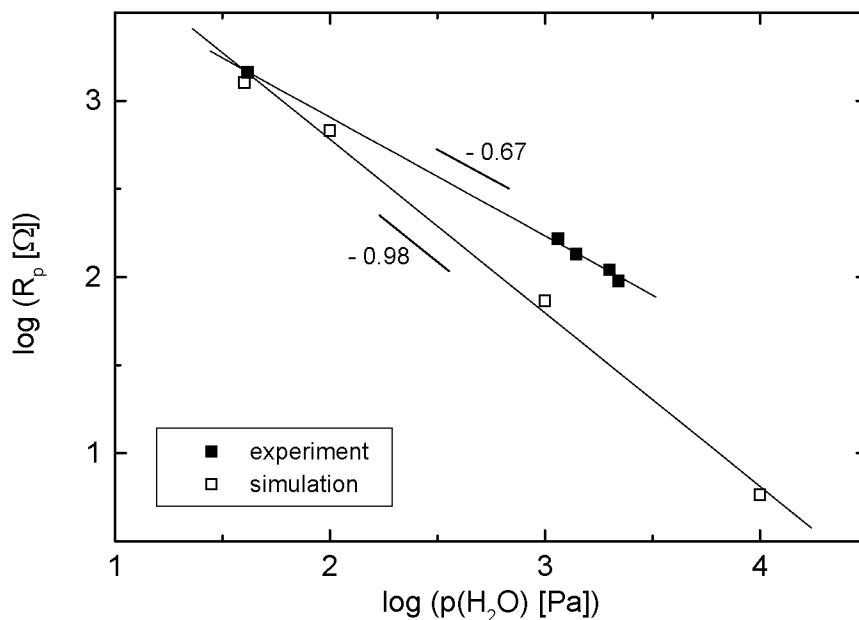


Fig. 5.11: Polarization resistance, R_p , as a function of the partial pressure of water, $p(H_2O)$: a comparison between simulation and experiment (same simulation conditions as in Fig. 5.10).

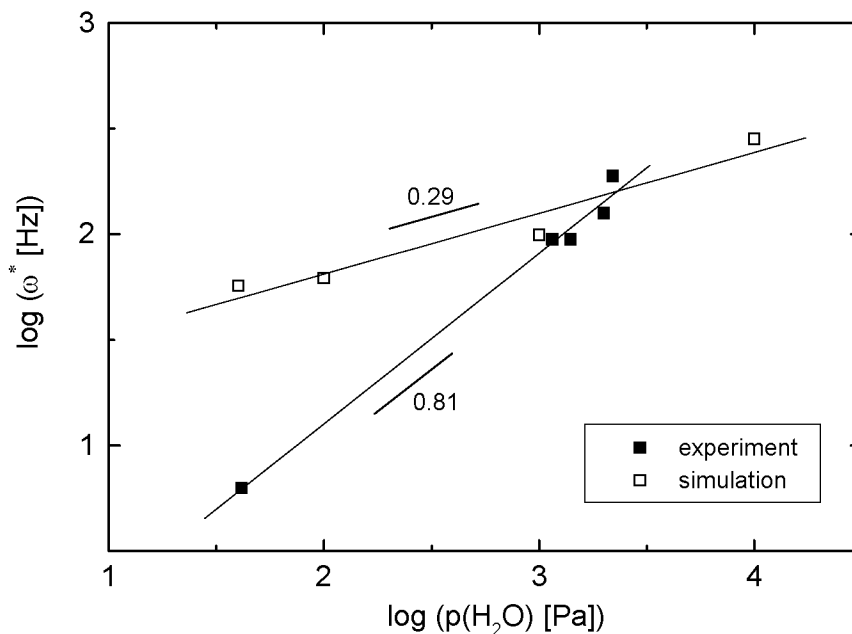


Fig. 5.12: Relaxation frequency, ω^* , as a function of the partial pressure of water, $p(H_2O)$: a comparison between simulation and experiment (same simulation conditions as in Fig. 5.10)

The surface coverage data indicates a strong increase of θ_{O} the higher the amount of water in the fuel gas (Fig. 5.13). The other fractions of the surface coverage change much less. Qualitatively, a similar behavior was found when the partial pressure of hydrogen was varied (Fig. 5.9): θ_{O} is strongly affected by a variation in the partial pressure of hydrogen, whereas the other θ_i stay almost constant.

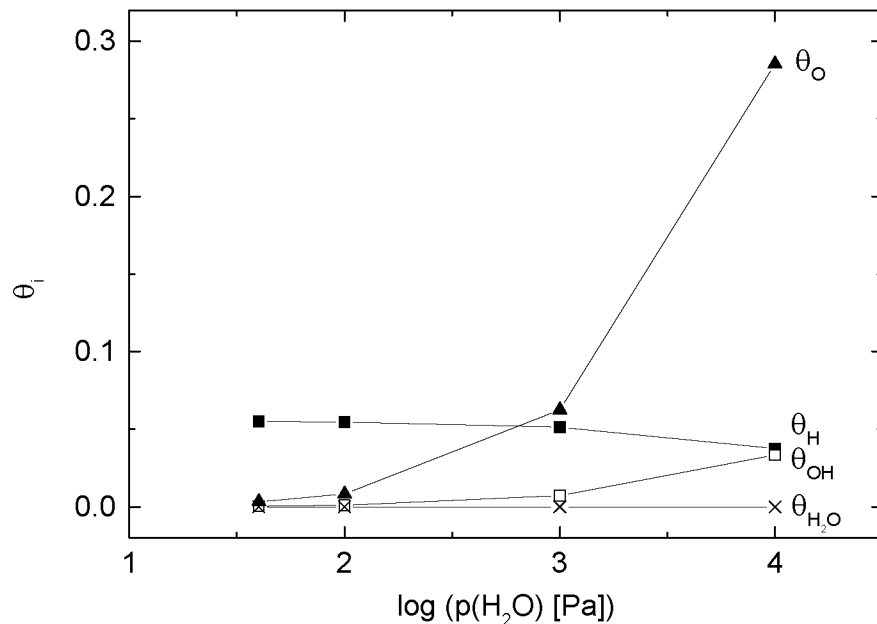


Fig. 5.13: Fractions of the surface coverages of the different surface species, θ_i as a function of the partial pressure of water, $p(\text{H}_2\text{O})$ (same simulation conditions as in Fig. 5.10). The lines are drawn to guide the eye.

5.6.5 Overpotential

The overpotential is the electrical driving force which sets the system to a certain operating point on the characteristic current - voltage curve of a fuel cell. According to the experiments, the electrode impedance decreases the higher the applied overpotential (chapter 3). This result could also be confirmed by the simulations (Fig. 5.14).

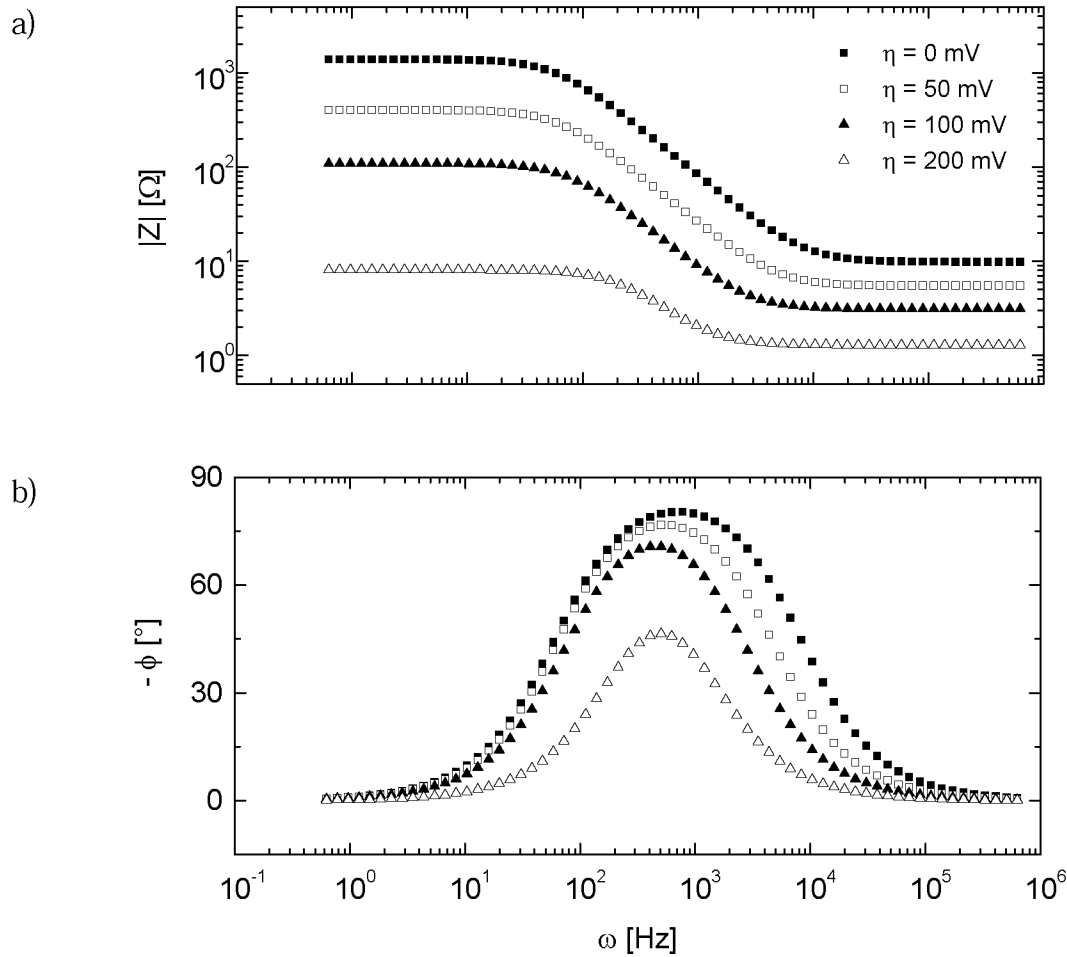


Fig. 5.14: Simulated impedance data as a function of the overpotential, η (the kinetic parameters used for the simulations are listed in Tab. 5.3, Tab. 5.4, and Tab. 5.5).

The effect of the overpotential on the polarization resistance is illustrated in Fig. 5.15. R_p decreases exponentially with increasing overpotential similarly to the experiments. This effect is more pronounced in the simulated data meaning that the simulated impedance spectra are more sensitive to an applied overpotential than the experimental impedance spectra.

The current density, j , as a function of the applied overpotential is shown for the experimental and the simulated data in Fig. 5.16. The shape of the curves is very similar for both data sets. However, the experimental and the simulated current densities vary by several orders of magnitude.

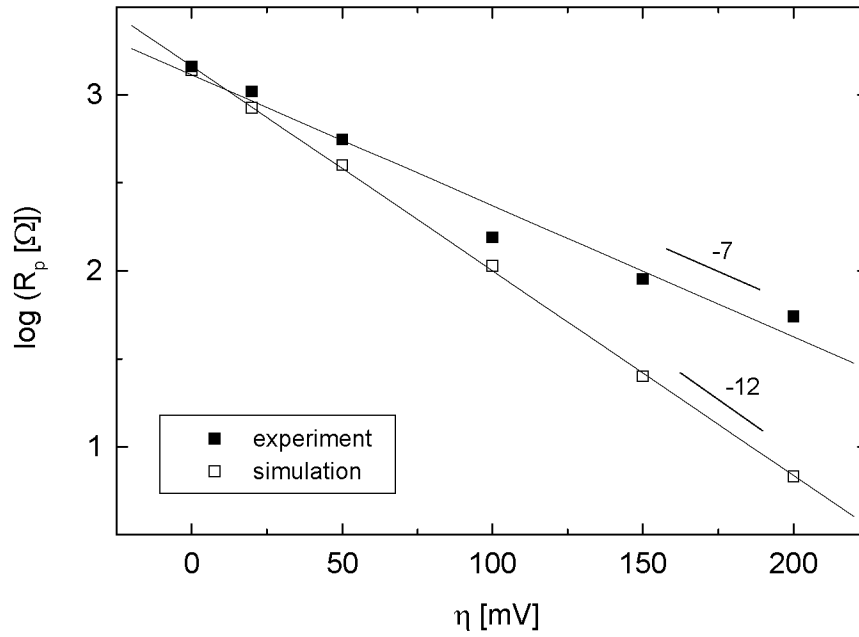


Fig. 5.15: Polarization resistance, R_p , as a function of the overpotential, η : a comparison between simulation and experiment (same simulation conditions as in Fig. 5.14).

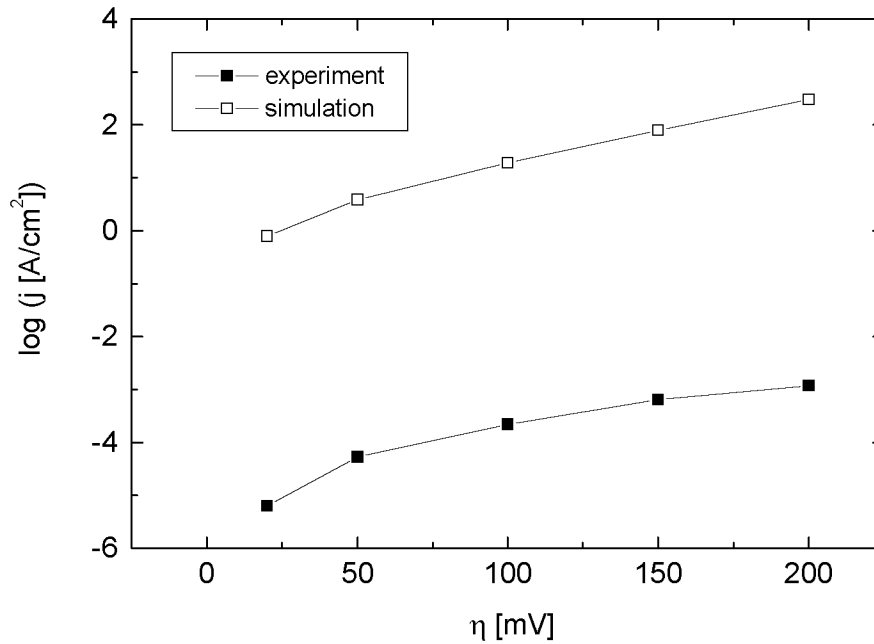


Fig. 5.16: Current density, j , as a function of the overpotential, η : a comparison between simulation and experiment (same simulation conditions as in Fig. 5.14). The lines are drawn to guide the eye.

The fractions of the surface coverages for the different adsorbed species are found to behave nearly in the same way as a function of the applied overpotential (Fig. 5.17) as they were changing as a function of the partial pressure of water (Fig. 5.13): the fraction of oxygen adsorbed on the surface increases drastically the higher the applied overpotential or the more water is added to the fuel gas. Also, the fraction of hydroxyl species increases, whereas the fraction of hydrogen decreases.

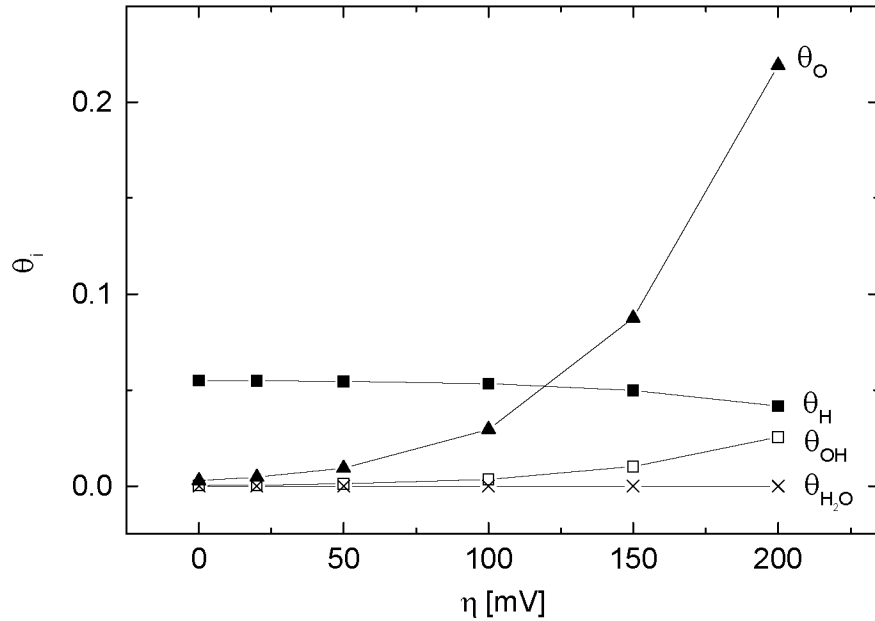


Fig. 5.17: Fractions of the surface coverages of the different surface species, θ_i as a function of the overpotential, η (same simulation conditions as in Fig. 5.14). The lines are drawn to guide the eye.

5.7 Discussion

The simulation results clearly indicate that the state-space modeling approach developed for the Pt, O₂ | YSZ [33,34,37] is also suitable to simulate the anodic reactions of a SOFC. A first electrochemical model established in subsection 5.4.1 allows the simulation of an impedance spectrum which is similar to an experimental impedance spectrum under the same conditions (Fig. 5.6). To use such a complex model for the first simulations of this system is a rather questionable strategy. However, one should keep in mind that an even more simplified system

would not straight-forwardly allow to simulate an impedance spectrum under the specific conditions of interest. In order to find the most relevant parameters, it is reasonable to consider the entire system from the beginning on.

In subsection 5.2, several criteria were stated which have to be fulfilled in order to consider a fit as good. It is found that most of the criteria are fulfilled at least partially:

- The simulated spectra are similar to the experimental ones which includes that a reasonable shape of the impedance spectra is obtained: positive Z' , negative Z'' , semicircle-like Nyquist plot, s-shaped $|Z|$ vs. ω plot, bell-shaped curve for ϕ (Fig. 5.5). This criterion must obviously be fulfilled from the impedance spectroscopy side. However, when simulating an impedance spectrum directly from the chemical and the electrochemical reactions, this criterion is not straight-forwardly fulfilled.
- The system is found to be rather stable, when a set of parameters is found and the parameters are then varied separately. The total impedance changes, but the shape of the curves is more or less constant. However, in the optimization procedure, it was very difficult to find a stable solution. It seems that this problem is inherent to the optimization procedure due to the large number of parameters and, hence, due to the large number of possibly very close local minima. In the future, it is, thus, necessary to ameliorate the optimization procedure in order to find more stable results during the optimization.
- The fractions of the surface coverages of the different surface species are all very low. In the case of θ_{H} , a higher value was expected [50]. No presumptions are given in the literature for θ_{OH} , θ_{O} , and $\theta_{\text{H}_2\text{O}}$. It is just assumed that the surface coverages should be very small at high temperatures.
- The reaction rate constants were found to be in a reasonable range as far as it can be judged by comparison with the literature and with the estimates in subsection 5.4.3. However, it should be noted that these estimates are very rough. Significant deviations are therefore possible and could be quite misleading. A check is not possible and only the comparison with the experimental impedance data allows a conclusive judgment.

Besides the simulations under standard conditions, the simulations were car-

ried out as a function of the same parameters which were varied in the experiments, i.e. the TPB length, the partial pressure of hydrogen and of water, and the overpotential. Rather similar results were found in the simulations and in the experiments. Not only the tendency as a function of a certain parameter was comparable (linear or logarithmic behavior, decrease or increase), but also the slopes of the curves are rather similar (e.g. Fig. 5.11, Fig. 5.15). This overall result is very important. It indicates that the proposed reaction mechanism captures many essential aspects of the real system. However, since no perfect correspondence of the experimental and the simulated data was obtained in all the simulations, it is evident that the electrochemical model is not totally appropriate.

Concerning the determination of the rate limiting reaction step, it should be noted that the reaction rate constants of Eq. 5.2 - Eq. 5.6 are all very similar, whereas the reaction rate constants of Eq. 5.7 are significantly lower (Tab. 5.5). In particular, the reaction rate constant of the electronation processes, k_6 , is very small. This might imply that the electronation process with the smallest reaction rate constant determines the total electrode impedance, as it is the slowest process in the electrochemical model. However, it is found that the total electrode impedance can also be significantly varied when changing one of the other reaction rate constants by one order of magnitude. This is due to the fact that the reaction rate constants themselves are coupled with the stationary solutions of the system, i.e. the surface concentrations. Hence, changes of the reaction rate constants imply changes of the stationary solutions of the system which, then, both change the impedance data. Thus, the relation between the reaction rate constants and the surface coverages is worth studying in the future.

With regard to the surface coverage profiles very similar dependencies were found as a function of the different parameters (Fig. 5.9, Fig. 5.13, Fig. 5.17): θ_{H} , θ_{OH} , and $\theta_{\text{H}_2\text{O}}$ are always very low and are neither strongly dependent on the partial pressure of hydrogen or water nor on the overpotential. However, θ_{O} changes considerably by the variation of a certain parameter. An exponential behavior might underlay the overall process. The increase of θ_{O} always comes along with a decrease in the total electrode impedance. Hence, the surface concentration of oxygen has a key influence on the limitation of the anode kinetics in the simulations.

Besides the electrochemical model and the kinetic parameters, the numerous assumptions which have to be taken into account (subsection 5.4.2), have to be kept in mind. Some aspects of the anode kinetics are simplified or neglected in

order to handle a system of as low a complexity as possible. For instance, the distorted Nyquist diagram of the experimental impedance data was never obtained with any set of parameters for the simulations. The simulated impedance spectra are always more perfectly shaped, i.e. a real semicircle arises in the Nyquist plot. In order to account for this discrepancy, surface diffusion was implemented tentatively using a finite element approach. However, since a considerable improvement of the simulated data was not obtained, surface diffusion was rejected at this stage.

So far, the simulations are all based on the electrochemical model which was established in subsection 5.4. Changes in the electrochemical model were not undertaken, as due to the complexity of the system many parameter variations are necessary until the evaluation of an electrochemical model is finished. However, as it was not possible to find a perfect coincidence of the simulated and the experimental data, it is advisable to modify the electrochemical model in the near future. For example, the charge transfer reaction must not be coupled with the oxygen removal from the electrolyte, i.e. the reverse reaction which takes place at the cathode side of the SOFC. It is more advisable to couple the charge transfer with the adsorption of hydrogen on the Ni surface. In this case, however, no kinetic data is available to the best of our knowledge. Furthermore, an active YSZ surface has to be considered in further simulations. The discussion about the effect of an increase of the partial pressure of water on the anode kinetics in chapter 3 (subsection 3.4) should be the basis for this. Valuable data will also be published in [58].

5.8 Summary

The simulations in this study indicate that the state-space modeling approach for the simulations of impedance spectra on the basis of an electrochemical model is very promising not only for the Pt, O₂ | YSZ system, but also for the anodic SOFC system, Ni, H₂ - H₂O | YSZ. Although an electrochemical model has to be assumed, the approach is superior to equivalent circuit fitting where the physical and the chemical interpretation of the equivalent circuit elements is not possible. With state-space modeling, the rate determining reaction steps can be directly interpreted with the electrochemical reactions and information about the surface coverages is obtained. The electrochemical model allows the estimation of kinetic constants for the anodic SOFC system and to simulate impedance spectra

which are rather similar to the experimental ones under the same conditions, i.e. as a function of the TPB length, of the partial pressure of hydrogen and of water, and of the overpotential. The simulated EIS data is found to react much more sensitively to the variation of the before mentioned parameters than the experimental EIS data. The fraction of the surface coverage of oxygen is recognized as a key parameter which influences the performance of the anode. Due to problems with the determination of the kinetic constants in the optimization procedure, this part of the program should be improved in the future. Also, a refined electrochemical model should be tested in order to find a better coincidence of the simulated and the experimental EIS data.

5.9 References

- [1] T. Kawada, N. Sakai, H. Yokokawa, M. Dokiya, M. Mori, T. Iwata, *Solid State Ionics* **40/41** (1990) 402.
- [2] J. Geyer, H. Kohlmüller, H. Landes, R. Stübner, Proc. of the 5th Intern. Symp. on Solid Oxide Fuel Cells (SOFC-V), Aachen, Germany, Eds.: U. Stimming, S.C. Singhal, H. Tagawa, W. Lehnert, The Electrochemical Society, Inc., Pennington, NJ, USA (1997) 585.
- [3] S. Primdahl, M. Mogensen, *J. Electrochem. Soc.* **144** (1997) 3409.
- [4] M. Mogensen, S. Skaarup, *Solid State Ionics* **86-88** (1996) 1151.
- [5] M. Mogensen, S. Sunde, S. Primdahl, Proc. of the 17th Risø Intern. Symp. on Mat. Sci.: High Temperature Electrochemistry: Ceramics and Metals, Eds.: F.W. Poulsen, N. Bonanos, S. Linderorth, M. Mogensen, B. Zachau-Christiansen, Risø National Laboratory, Roskilde, Denmark (1996) 77.
- [6] P. Holtappels, L.G.J. de Haart, U. Stimming, *J. Electrochem. Soc.* **146** (1999) 1620.
- [7] P. Holtappels, L.G.J. de Haart, U. Stimming, *J. Electrochem. Soc.* **146** (1999) 2976.
- [8] J. Divisek, A. Kornyshev, W. Lehnert, U. Stimming, I.C. Vinke, K. Wippermann, Proc. of the 5th Intern. Symp. on Solid Oxide Fuel Cells (SOFC-V), Aachen, Germany, Eds.: U. Stimming, S.C. Singhal, H. Tagawa, W. Lehnert, The Electrochemical Society, Inc., Pennington, NJ, USA (1997) 606.
- [9] J. Mizusaki, H. Tagawa, T. Saito, T. Yamamura, K. Kamitani, K. Hirano, S. Ehara, T. Takagi, T. Hikita, M. Ippomatsu, S. Nakagawa, K. Hashimoto, *Solid State Ionics* **70/71** (1994) 52.
- [10] J. Mizusaki, H. Tagawa, T. Saito, K. Kamitani, T. Yamamura, K. Hirano, S. Ehara, T. Takagi, T. Hikita, M. Ippomatsu, S. Nakagawa, K. Hashimoto, *J. Electrochem. Soc.* **141** (1994) 2129.
- [11] B. de Boer, PhD Thesis, University of Twente, Twente, The Netherlands (1998).
- [12] R.J. Aaberg, PhD Thesis, NTNU Trondheim, Trondheim, Norway (1998).
- [13] T. Norby, O.J. Velle, H. Leth-Olsen, R. Tundold, Proc. of the 3rd Intern. Symp. on Solid Oxide Fuel Cells (SOFC-III), Honolulu, Hawaii, USA, Eds.: S.C. Singhal, H. Iwahara, The Electrochemical Society, Inc., Pennington, NJ, USA (1993) 473.

-
- [14] T. Norby, P. Kofstad, Proc. of the 17th Risø Intern. Symp. on Mat. Sci.: High Temperature Electrochemistry: Ceramics and Metals, Eds.: F.W. Poulsen, N. Bonanos, S. Linderoth, M. Mogensen, B. Zachau-Christiansen, Risø National Laboratory, Roskilde, Denmark (1996) 381.
- [15] F.Z. Mohamedi-Boulenouar, J. Guindet, A. Hammou, Proc. of the 5th Intern. Symp. on Solid Oxide Fuel Cells (SOFC-V), Aachen, Germany, Eds.: U. Stimming, S.C. Singhal, H. Tagawa, W. Lehnert, The Electrochemical Society, Inc., Pennington, NJ, USA (1997) 441.
- [16] S.P. Jiang, S.P.S. Badwal, *J. Electrochem. Soc.* **144** (1997) 3777.
- [17] S.P. Jiang, S.P.S. Badwal, *Solid State Ionics* **123** (1999) 209.
- [18] S.P. Jiang, S.P.S. Badwal, *Solid State Ionics* **122** (1999) 211.
- [19] N. Nakagawa, H. Sakurai, K. Kondo, T. Morimoto, K. Hatanaka, K. Kato, *J. Electrochem. Soc.* **142** (1995) 3474.
- [20] S. Primdahl, PhD Thesis, University of Twente, Twente, The Netherlands (1999).
- [21] J.R. Macdonald, "Impedance Spectroscopy", John Wiley & Sons, Inc., New York, NY, USA (1987).
- [22] K. Wippermann, Materials and Mechanisms: 12th SOFC Workshop, Wadahl, Norway, Ed.: K. Nisanciogly (1999) 31.
- [23] S. Sunde, *J. Electrochem. Soc.* **143** (1996) 1123.
- [24] S. Sunde, *J. Electrochem. Soc.* **143** (1996) 1930.
- [25] S. Sunde, *Electrochimica Acta.* **42** (1997) 2637.
- [26] A. Isolevich, A.A. Kornyshev, W. Lehnert, *J. Electrochem. Soc.* **144** (1997) 3010.
- [27] J. Abel, A.A. Kornyshev, W. Lehnert, *J. Electrochem. Soc.* **144** (1997) 4253.
- [28] P. Costamagna, E. Arato, P.L. Antonucci, V. Antonucci, *Chem. Engin. Sci.* **51** (1996) 3013.
- [29] J. Yan, M. Rokni, B. Sundén, Proc. of the 6th Intern. Symp. on Solid Oxide Fuel Cells (SOFC-VI), Honolulu, Hawaii, USA, Eds.: S.C. Singhal, M. Dokiya, The Electrochemical Society, Inc., Pennington, NJ, USA (1999) 1009.
- [30] E. Achenbach, U. Reus, Proc. of the 6th Intern. Symp. on Solid Oxide Fuel Cells (SOFC-VI), Honolulu, Hawaii, USA, Eds.: S.C. Singhal, M. Dokiya, The Electrochemical Society, Inc., Pennington, NJ, USA (1999) 1125.
- [31] B.A. van Hassel, B.A. Boukamp, A.J. Burggraaf, *Solid State Ionics* **48** (1991) 139.
- [32] B.A. van Hassel, B.A. Boukamp, A.J. Burggraaf, *Solid State Ionics* **48** (1991) 155.
- [33] A. Mitterdorfer, L.J. Gauckler, *Solid State Ionics* **117** (1999) 187.
- [34] A. Mitterdorfer, L.J. Gauckler, *Solid State Ionics* **117** (1999) 203.
- [35] A. Mitterdorfer, L.J. Gauckler, *Solid State Ionics* **120** (1999) 211.
- [36] A. Mitterdorfer, L.J. Gauckler, *Solid State Ionics* **111** (1998) 185.
- [37] A. Mitterdorfer, PhD Thesis No. 12380, ETH Zürich, Zürich, Switzerland (1997).
- [38] A. Bieberle, A. Mitterdorfer, L.J. Gauckler, IEA Workshop: Materials and Mechanisms, January 10-13, Wadahl, Norway, Ed.: K. Nisancioglu, International Energy Agency (1999) 39.

- [39] H. Schichlein, M. Feuerstein, A. Müller, A. Weber, A. Krügel, E. Ivers-Tiffée, Proc. of the 6th Intern. Symp. on Solid Oxide Fuel Cells (SOFC-VI), Honolulu, Hawaii, USA, Eds.: S.C. Singhal, M. Dokiya, The Electrochemical Society, Inc., Pennington, NJ, USA (1999) 1069.
- [40] P.A. Thiel, T.E. Madey, *Surf. Sci. Rep.* **7** (1987) 211.
- [41] K. Christmann, *Surf. Sci. Rep.* **9** (1988) 1.
- [42] B. Hellsing, B. Kasemo, V.P. Zhdanov, *J. Cat.* **132** (1991) 210.
- [43] E. Fridell, A. Rosen, B. Kasemo, *Langmuir* **10** (1994) 699.
- [44] A. Bieberle, L.J. Gauckler, *Solid State Ionics* **135** (2000) 337.
- [45] F. Berthier, J.-P. Diard, B. le Gorrec, C. Montella, *Corr. Sci.* **51** (1995) 105.
- [46] G.A. Somorjai, "Introduction to Surface Chemistry and Catalysis", John Wiley & Sons, Inc., New York, NY, USA (1994).
- [47] M.A. Morris, M. Bowker, D.A. King, in: Comprehensive Chemical Kinetics, Volume 19: Simple Processes at the Gas-Solid Interface, Eds.: C.H. Bamford, C.F.H. Tipper, R.C. Compton, Elsevier, Amsterdam, The Netherlands (1984) 1.
- [48] G. Wedler, "Lehrbuch der Physikalischen Chemie", VCH Verlagsgesellschaft, Weinheim, Germany (1987) 182.
- [49] M. Quack, "Molekulare Thermodynamik und Kinetik, Teil 1: Chemische Reaktionskinetik", Verlag der Fachvereine an den Schweizerischen Hochschulen und Techniken, Zürich, Switzerland (1986) 12.
- [50] S. Skaarup, B. Zachau-Christiansen, T. Jacobsen, Proc. of the 17th Risø Intern. Symp. on Mat. Sci.: High Temperature Electrochemistry: Ceramics and Metals, Eds.: F.W. Poulsen, N. Bonanos, S. Linderoth, M. Mogensen, B. Zachau-Christiansen, Risø National Laboratory, Roskilde, Denmark (1996) 423.
- [51] P.G. Bruce, "Solid State Electrochemistry", Cambridge University Press, Cambridge, UK (1995) 279.
- [52] P.J. Gellings, H.J.M. Bouwmeester, "The CRC Handbook of Solid State Electrochemistry", CRC Press, Boca Raton, Florida, USA (1997) 43.
- [53] A. Winkler, *Vakuum-Technik* **37** (1988) 204.
- [54] M. Schulze, R. Reissner, K. Bolwin, W. Kuch, *Fres. J. Anal. Chem* **353** (1995) 661.
- [55] V.I. Avdeev, I.I. Zakharov, *J. Struct. Chem.* **33** (1992) 185.
- [56] "MATLAB[®] Reference Guide", The MathWorks, Inc., Natick, MA, USA (1992).
- [57] DMK/DPK, "Formeln und Tafeln", Orell Füssli Verlag Zürich, Zürich, Switzerland (1984) 174.
- [58] S. Raz, K. Sasaki, J. Maier, I. Riess, *Solid State Ionics* (2000) submitted.

Chapter 6

General Conclusions

Abstract

The two main interests of the thesis will be discussed and evaluated in this closing chapter: the state-space modeling (SSM) approach and the kinetics of SOFC anodes. The SSM approach allows the kinetics of SOFC anodes to be studied in detail. The experiments and the simulations give complementary aspects of the investigation of the electrochemistry of the entire system. With regard to the kinetics, it is found that Ni-based SOFC anodes are dominated by two main processes which are ascribed to the adsorption and the desorption of hydrogen including charge transfer and to the desorption of water.

6.1 Introduction

The main part of the thesis is organized in three chapters dealing with experiments on Ni pattern anodes (chapter 3), experiments on different types of Ni-based anodes (chapter 4), and on modeling and simulations of the Ni, H₂ - H₂O | YSZ system (chapter 5). These three chapters aim to investigate the kinetics of SOFC anodes. They are linked by the so-called state-space modeling (SSM) approach which combines the three methods, experiments, modeling, and simulations. Hence, in this general conclusion, we will summarize and evaluate the two main aspects, the state-space modeling approach and the kinetics of SOFC anodes.

6.2 The State-Space Modeling Approach

The state-space modeling (SSM) approach combines experiments, modeling, and simulations and aims to investigate the kinetics of SOFC electrodes. It is an approach which is not only appropriate with regard to SOFC electrodes, but can equally be used for other electrochemical systems. One main advantage compared to other approaches is the fact that it includes experimental and theoretical elements likewise. Hence, all the information which is known about an electrochemical system, is taken into consideration for the kinetic studies. In contrast, mainly experimental data is considered in the studies on the electrochemistry of SOFC anodes so far.

The SSM approach has so far only been used for the cathodic Pt, O₂ | YSZ system [1-3]. With regard to modeling, this system is rather well described in the literature. Some of the missing kinetic parameters could be determined and a rather good coincidence of the experimental and the simulated data was obtained. As far as the anodic system, Ni, H₂ - H₂O | YSZ, is concerned, the situation is rather different: almost no information is available on its kinetics under SOFC operating conditions, i.e. temperatures between 873 K and 1273 K and a total gas pressure of 1 atm. Moreover, the system itself is much more complicated, since several chemical species are involved. One has to consider, for instance, that the oxygen which is incorporated into the electrolyte at the cathode side, is also one of the main species at the anode side. In addition, the gas phase consists of at least two components: hydrogen and water. The water itself originates either from the fuel gas atmosphere or is produced during the fuel cell process. Hence, there exist two

sources for the water. It should also be noted that several parameters cannot easily be studied separately. For instance, a variation in the operating temperature simultaneously changes the partial pressure of water in the fuel gas atmosphere or the increase of the overpotential is accompanied with an increase of water in the fuel gas. Hence, the anodic reaction mechanisms are composed of a multifaceted interaction of many parameters and single reaction steps which are often interdependent on each other. Thus, one of the main aims of this thesis was to demonstrate, whether the SSM approach can be used for the investigation of such rather complex systems as well.

From the experimental point of view, it is recommended to start working with a very simple and reproducible system. A Ni pattern on top of a YSZ single crystal electrolyte emerged as a suitable anode design to start with, in particular, since the geometry of this type of anode is well-known (chapter 3). Many detailed measurements with several parameter variations gave a rather explicit picture of the electrochemistry of Ni pattern anodes. The impedance data is dominated by one main arc signifying one main electrode process. This is valid for all experimental conditions under consideration. The data also served as an excellent source for the interpretation of the impedance data of the more complex anode designs discussed in chapter 4. In contrast to Ni pattern anodes, Ni-YSZ anodes have a more complex microstructure and the extension of the electrochemically active reaction zone is not known exactly. The impedance data is, in consequence, more diversified. Nevertheless, due to the detailed data on the Ni pattern anodes and in combination with several electrochemical measurements of different types of Ni-based anodes, general tendencies could be observed. It is found that the Ni-based SOFC anodes are all dominated by two main impedance arcs which are attributed to the adsorption and desorption of hydrogen and of water. However, more detailed studies are necessary in this field in the future (cf. chapter 7), in particular, since the deposition techniques for the preparation of SOFC anodes (sputtering and electrostatic spraying) are not optimized yet.

The modeling and the simulations carried out in this thesis are insofar unique, as the kinetics of SOFC anodes are to the best of our knowledge simulated for the first time directly from an electrochemical model. It was not sure from the beginning, whether it is possible to simulate an impedance spectrum which can be compared to the experimental data, when an electrochemical model must be assumed and much of the kinetic information is missing. The missing data was estimated from the literature. Since it was found that reasonable impedance spectra

could be simulated and since the spectra behaved rather similarly to the experimental ones under the same operating conditions (chapter 5), it can be claimed that the SSM approach is, in fact, suitable for the investigation of complicated electrochemical systems. However, several assumptions have to be taken into account (chapter 5, subsection 5.4.2) and, for an unambiguous investigation of the kinetics of the system, a complex set of kinetic data is required. Even in this detailed study, it is risky to conclude from the simulated results that a specific reaction mechanism uniquely takes place. More detailed studies are required. This includes, in particular, modeling and simulations of the Ni-YSZ system as well as more fundamental work on the adsorption and the desorption processes. This should then allow to clarify the interaction of surface coverages and reaction rate constants.

Summarizing, it can be concluded that the SSM approach is suitable for the investigation of the kinetics of SOFC anodes. Despite the complexity of the system, very promising simulations were obtained and could be compared to experimental data determined under the same conditions. However, due to some divergence between the experimental and the simulated impedance spectra, further simulations are recommended and modifications of the kinetic constants and of the electrochemical model are suggested (cf. chapter 7).

6.3 The Kinetics of SOFC Anodes

The main focus with regard to the kinetics of SOFC anodes is to find the rate limiting reaction step(s) of the anodic process. This information is important, since the performance of an electrode could be considerably enhanced, if the limiting processes are identified. The electrode could then be specifically designed so that the limitations can be reduced or even avoided.

The electrochemical characterization of the Ni pattern anodes in chapter 3 implies that the adsorption of hydrogen and the removal of oxygen from the electrolyte are both identified as feasible electrochemical processes which might limit the anodic reaction mechanisms. Both processes are assumed to be coupled with a charge transfer reaction. In chapter 4, the hypothesis of the adsorption process of hydrogen as the rate limiting step was confirmed. However, as previously mentioned, more detailed studies are recommended in order to validate this hypothesis. Under polarization of the anode, an additional electrode process can be

distinguished from the main impedance arc. Most probably, this process is related to the formation of water during the fuel cell process. The desorption of water seems to limit the anodic reactions at high currents.

With regard to the simulations, it is at this moment not possible to vote unambiguously for one rate limiting reaction step (chapter 5). This is mainly due to two reasons: first, the interrelation between the surface coverages and the reaction rate constants is not investigated so far. This signifies that the absolute values of the reaction rate constants cannot be directly compared to each other. Hence, the process with the smallest reaction rate constant cannot automatically be assigned to the slowest process which would then limit the kinetics. Second, the experimental and the simulated data do not coincide perfectly for all conditions under investigation. Thus, the reaction rate constants and / or the electrochemical model might need some modifications. In general, however, it was demonstrated that the established electrochemical model describes the experimental system rather well. It was possible to estimate the unknown kinetic parameters and to simulate the system under the same conditions as the experiments were carried out. Conclusively, it is recommended to study the interaction of the surface coverages of the different surface species and the reaction rate constants in the future. Moreover, the electrochemical model should be modified in order to obtain a better coincidence of the experimental and the simulated impedance spectra.

If one now compares the electrochemical model which was established for the simulations in this study, and the hypotheses for the kinetics of SOFC anodes derived from the experimental data, one will notice several differences: first, the chemical and the electrochemical reactions in the electrochemical model are restricted to the Ni surface (cf. chapter 5, Fig. 5.2), as suggested in [4,5]. This hypothesis is, at first glance, rather obvious, since Ni is the catalytic material for the oxidation of hydrogen. However, considering the experimentally observed catalytic effect of the addition of water to the fuel gas atmosphere, it becomes evident that the YSZ surface is most likely involved in the anode kinetics as well. A possible reaction mechanism considering a hydroxylated YSZ surface is proposed in chapter 3 (subsection 3.4, Fig. 3.31). Some fundamental work will be published in [6]. The hypothesis of an activated YSZ surface is further enhanced by the discrepancies between some experimental and simulated data. Hence, since the YSZ surface was not considered to be electrochemically active in the simulations, these discrepancies are expected.

Another main difference between the experimental and the simulated impedance data is related to the number of relaxation processes. While merely one process is found in the simulations, two relaxation processes can be clearly separated in the experiments under polarization of the anode. In principle, different relaxation processes can also be separated in the simulations, even though merely one arc was observed for the conditions under consideration. It should, however, be noted that the simulated phase angle plots often show a broadening which already points towards multiple relaxation times.

Finally, under certain experimental conditions (e.g. high current) as well as for certain anode designs (i.e. porous microstructure), diffusion effects were observed. The electrochemical model used for the simulations does, in contrast, not consider diffusion. It is, however, in principle possible to implement a diffusion limitation, such as described in chapter 2. Further simulations will demonstrate, if diffusion effects are, in fact, responsible for the 45° tangents of the experimental impedance data.

In summary, it should be noted that detailed and rather approved predictions can be stated concerning the kinetics of SOFC anodes. In particular, the electrochemistry of Ni pattern anodes is identified rather well. However, the hypotheses still contain several assumptions, since fundamental data is missing. In consequence, more fundamental data has to be collected, in particular, with regard to Ni-YSZ anodes.

6.4 References

- [1] A. Mitterdorfer, L.J. Gauckler, *Solid State Ionics* **117** (1999) 187.
- [2] A. Mitterdorfer, L.J. Gauckler, *Solid State Ionics* **117** (1999) 203.
- [3] A. Mitterdorfer, PhD Thesis No. 12380, ETH Zürich, Zürich, Switzerland (1997).
- [4] S.P. Jiang, S.P.S. Badwal, *J. Electrochem. Soc.* **144** (1997) 3777.
- [5] S.P. Jiang, S.P.S. Badwal, *Solid State Ionics* **123** (1999) 209.
- [6] S. Raz, K. Sasaki, J. Maier, I. Riess, *Solid State Ionics* (2000) submitted.

*This is not the end.
It is not even the beginning of the end.
But it is, perhaps, the end of the beginning.*
(Winston Churchill, 1874 - 1965)

Chapter 7

Outlook

Abstract

The discussions and the conclusions drawn from the results in chapters 3-5 suggest that there still exist several open questions concerning the investigation of the kinetics of SOFC anodes. Considering experiments, further work is mainly recommended with respect to Ni-YSZ cermet anodes. The microstructure as well as the electrochemistry of these anodes should be studied in more detail. Additionally, Ni pattern anodes should be analyzed on ceria electrolytes as well as with fuel gas atmospheres other than hydrogen. With respect to the simulations, it is recommended to devote some more effort to the Ni, H₂ H₂O | YSZ system. The electrochemical model should be refined and the Ni-YSZ cermet system should be simulated.

7.1 Introduction

The aim of this thesis was to investigate the electrochemistry of SOFC anodes by means of a combination of experiments, modeling, and simulations, i.e. the state-space modeling approach. The studies focused mainly on the model system Ni, H₂ - H₂O | YSZ. In the future, more work is needed concerning the investigation of the state-of-the-art anodic system using Ni-YSZ cermet as anode material. In addition, other anode materials which are anticipated for future SOFC stacks, such as ceria [1,2], as well as fuel gases other than hydrogen have to be considered in the experiments as well as in the simulations [2-6]. Besides this rather broad claim for future work, several recommendations originating directly from this thesis will be given in the following and should be addressed in subsequent studies.

7.2 Experiments

The experimental part of the thesis focused on Ni pattern anodes as well as on Ni-YSZ cermet anodes which were measured in hydrogen atmosphere. In the future, the following aspects should be considered:

- Ni pattern anodes should be deposited on ceria electrolytes. Ceria is a mixed ionic electronic conducting (MIEC) material. We suppose that due to the MIEC the electrochemically active part of the electrode can be enlarged. Hence, smaller polarization losses and a higher performance are expected. So far, a direct comparison of both electrolytes using well-defined electrodes was not carried out in the literature and it was not possible to manifest the promoting effect of a MIEC electrolyte exactly.
- The experiments on model anodes suggest that the main anodic processes take place at the TPB where the Ni, the YSZ, and the gas phase meet each other. For model anodes, such as Ni pattern anodes, the TPB length is well-known due to the simple and two dimensional geometry. A linear relation between the TPB length and the anode conductivity is observed (chapter 3). For Ni-YSZ cermet anodes, the TPB length is not exactly known and also not studied in the literature. It is assumed that the performance of the Ni-YSZ anodes is also strongly affected by the TPB length. However, it is not yet proven, whether the TPB length or whether other ef-

fects dominate the anodic limitations. Hence, it is an urgent demand to know the TPB length and its influence on the kinetics of Ni-YSZ cermet anodes. In order to do so, we suggest to analyze the three phases of the Ni-YSZ anode microstructure separately using the following strategy (some preliminary results are shown in appendix 4): The pores could be analyzed in the as-prepared state of the Ni-YSZ cermet using scanning electron microscopy (SEM). A stereo-microscope could be useful to illustrate the three dimensional microstructure. The YSZ network can be separated by etching the metallic Ni using the knowledge acquired for the preparation of the Ni pattern anodes, i.e. wet chemical etching with nitric acid at elevated temperatures (cf. chapter 3). After etching, the YSZ network should remain and can be analyzed by SEM. Alternatively, the Ni network could be separated by decomposing the YSZ network as described in [11,12]. The main challenge here is to avoid that the Ni network is attacked simultaneously. The preliminary experiments in appendix 4 have shown that it is, in fact, possible to decompose the YSZ in a reduced Ni-YSZ substrate with a fusion process using ammoniumsulfate [12]. Metallic Ni was left over and was identified by EDX. It must now be studied whether Ni-YSZ deposited as SOFC anode can be analyzed using this method without destroying the Ni network. Image analyses of the three phases should then allow the determination of the TPB length of Ni-YSZ cermet anodes. Using different starting powders for the Ni-YSZ screen-printing paste, it is possible to prepare Ni-YSZ anodes with different TPB lengths and to evaluate the impact of the TPB length on the performance of these anodes.

- The diversified impedance spectra of the Ni-YSZ cermet anodes in chapter 4 already allow to identify tendencies which seem to be characteristic for Ni-YSZ cermet anodes. However, more detailed studies are required in order to confirm the results. It is recommended to study as many different Ni-YSZ cermet anodes as possible. The anodes should always be measured in the same experimental set-up, under the same experimental conditions, and should be prepared on the same substrate and with the same counter electrode. Different deposition techniques and raw materials should be used. We also suggest to analyze anodes prepared by different research groups (cf. chapter 1, Tab. 1.1). With these statistics more

defined predictions concerning the reaction mechanisms of Ni-YSZ cermet anodes should be possible.

- In parallel, the influence of the counter electrode on the anode kinetics should be studied in the near future. A bad cathode is assumed to hinder the performance of a good anode. In particular, the inductive loops observed for some anodes discussed in this thesis might be caused by a bad cathode performance (chapter 4). So far, this effect is not clear ([7] and references therein).
- Finally, influences of the fuel gas atmosphere should be studied in the future. SOFC system are not supposed to work under hydrogen / nitrogen atmosphere. Methane, higher hydrocarbons, and natural gas are the most feasible fuels for the application of SOFCs in the future [3-6]. Ni pattern anodes are supposed to be helpful, in particular, since catalytic effects will not overlap with microstructural effects. It is, for instance, expected that the areas of carbon deposition can be localized when using Ni pattern anodes.

7.3 Modeling and Simulations

The modeling and the simulations carried out with regard to the Ni model system turned out to be more complicated than expected. This is mainly due to the fact that much of the electrochemical data which is mandatory for establishing the electrochemical model and for performing the simulations, is not known. Thus, it was a time consuming task to estimate the kinetic parameters and to evaluate the established electrochemical model with regard to several meaningful parameters. Hence, the modeling and the simulation analyses of the Ni, H₂ H₂O | YSZ system are not totally completed yet and the following further investigations are recommended for the future:

- As already mentioned in the discussion in chapter 5, the interrelation of the fractions of the surface coverages of the different surface species i , θ_i , and the reaction rate constants, k_j and k_{-j} , has to be studied in detail (cf. chapter 5, subsection 5.7). This is important in order to make more precise predictions concerning the rate limiting reaction steps.
- The optimization procedure for the determination of the kinetic param-

ters has to be improved. Using an optimization subroutine provided by the MATLAB[®] optimization toolbox, the simulations fail to find a suitable solution: having found a local extremum during the optimization, the absolute extremum can only be localized with difficulty. This problem is most probably due to the numerous parameters which are optimized at the same time. The optimization procedure is supposed to be realized differently and a new subroutine for the optimization procedure has to be programmed in MATLAB[®].

- One suitable set of kinetic parameters is determined in chapter 5. So far, no further set of parameters was found which gives simulation results of a comparable quality as the one discussed in chapter 5. However, the uniqueness of this set of kinetic parameters is not yet proven. Also, no systematic studies with regard to the stability of the solutions were carried out. Hence, some more detailed studies are necessary in this field.
- The surface sticking coefficients of hydrogen and of water were assumed to be constant for all simulations (cf. chapter 5, subsection 5.4.2). This must not necessarily be the case. An exponential dependence of the surface sticking coefficient of oxygen as a function of the surface coverage is, for instance, known for the Pt, O₂ | YSZ system [8-10]. Since a similar behavior might hold for the Ni, H₂ H₂O | YSZ system, the dependence of the surface sticking coefficient of hydrogen and of water from the surface coverages should be studied.
- Concerning the electrochemical model, it has to be mentioned that the model has not been considerably varied yet. However, according to the simulation results, it is advisable to test some fundamental modifications of the electrochemical model with the aim to receive a better agreement of the experimental data and the simulations. A first starting point would be to change the Faraday process with the charge transfer reaction. In the model used in chapter 5, the charge transfer is assumed to be related to the removal of oxygen from the electrolyte. Alternatively, the charge transfer could be linked to the adsorption of hydrogen on the Ni surface.
- In chapter 5 (subsection 5.6.1), it was found that one path for the desorption of water might be sufficient in order to simulate an impedance spectrum which is similar to an experimental one. Hence, it is recommended

to check whether it is possible to simplify the electrochemical model to a model which contains only one pathway for the adsorption and for the desorption of water. This would at the same time considerably reduce the number of parameters to be optimized and the optimization procedure would be simplified. We advice to restart with the simulations using a totally simplified model and to work on adsorption and on desorption kinetics first. Then, a new electrochemical model should be established step by step.

- In the long term, simulations of the electrochemical behavior of the state-of-the-art Ni-YSZ cermet anode have to be carried out as well. Here, the main tasks will be related to the incorporation of diffusion effects which seem to be more relevant in a three dimensional microstructure as it is the case for a Ni-YSZ cermet anode. However, beforehand, it is required from the experimental side that the TPB length can be determined exactly.

In summary, one should recognize that for all parts of the SSM approach, experiments, modeling, and simulations, several questions should be addressed in detail in the future. The prospective experimental work should mainly be concerned with the analyses of Ni-YSZ cermet anodes. In the case of the simulations, some more work on the simplified Ni, H₂ H₂O | YSZ system is required first. Then, the impedance of Ni-YSZ cermet anodes should be modeled and simulated.

7.4 References

- [1] G.M. Christie, P. Nammensma, J.P.P. Huijsmans, Proc. of the 4th Europ. Fuel Cell Forum, Lucerne, Switzerland, Ed.: A.J. McEvoy (2000) 3.
- [2] K. Honegger, J. Krumeich, R. Diethelm, Proc. of the 4th Europ. Fuel Cell Forum, Lucerne, Switzerland, Ed.: A.J. McEvoy (2000) 29.
- [3] K. Ahmed, K. Föger, Proc. of the 4th Europ. Fuel Cell Forum, Lucerne, Switzerland, Ed.: A.J. McEvoy (2000) 69.
- [4] R.H. Cunningham, R.M. Ormerod, Proc. of the 4th Europ. Fuel Cell Forum, Lucerne, Switzerland, Ed.: A.J. McEvoy (2000) 77.
- [5] S.D. Vora, Proc. of the 4th Europ. Fuel Cell Forum, Lucerne, Switzerland, Ed.: A.J. McEvoy (2000) 175.
- [6] R. Diethelm, E. Batawi, K. Honegger, Proc. of the 4th Europ. Fuel Cell Forum, Lucerne,

-
- Switzerland, Ed.: A.J. McEvoy (2000) 183.
- [7] M.J. Jørgensen, M. Mogensen, *J. Electrochem. Soc.* (2000) submitted.
- [8] C.T. Campbell, G. Ertl, H. Kuipers, J. Segner, *Surf. Sci.* **107** (1981) 220.
- [9] H.P. Bonzel, R. Kul, *Surf. Sci.* **40** (1973) 85.
- [10] M. Procop, J. Völter, *Z. Phys. Chem.* **250** (1971) 387.
- [11] B. Ayranci, *Swiss Chem.* **11** (1989) 13.
- [12] G. Bayer, G. Kahr, M. Müller-Vonmoos, *Clay Minerals* **17** (1982) 271.

Appendix 1

Microstructure of Ni Pattern Anodes

A1.1 Ni Pattern Anodes

Typical light microscope (LM) images of Ni pattern anodes are shown in Fig. A1.1. The image on the left side has equidistant lines of Ni and of YSZ with a line width of $20\ \mu\text{m}$ (Fig. A1.1a). The pattern on the right side is much finer with a line width of only $5\ \mu\text{m}$ (Fig. A1.1b). Smaller line widths than $5\ \mu\text{m}$ could not be prepared by wet chemical etching. This is due to two main reasons: first, the etching process does not proceed totally homogeneously. Hence, the edges of the Ni lines are frayed out at both sides. The lines are then easily interrupted in the case of a very fine pattern (cf. subsection A1.3). Second, failures in the sputtered Ni layer caused by contamination during or before sputtering are more pronounced the thinner the lines, since several lines are immediately interrupted at the same time. Fig. A1.1c illustrates the cross section of a sputtered Ni layer. The layer is $1\ \mu\text{m}$ thick and is strongly adherent to the YSZ substrate.

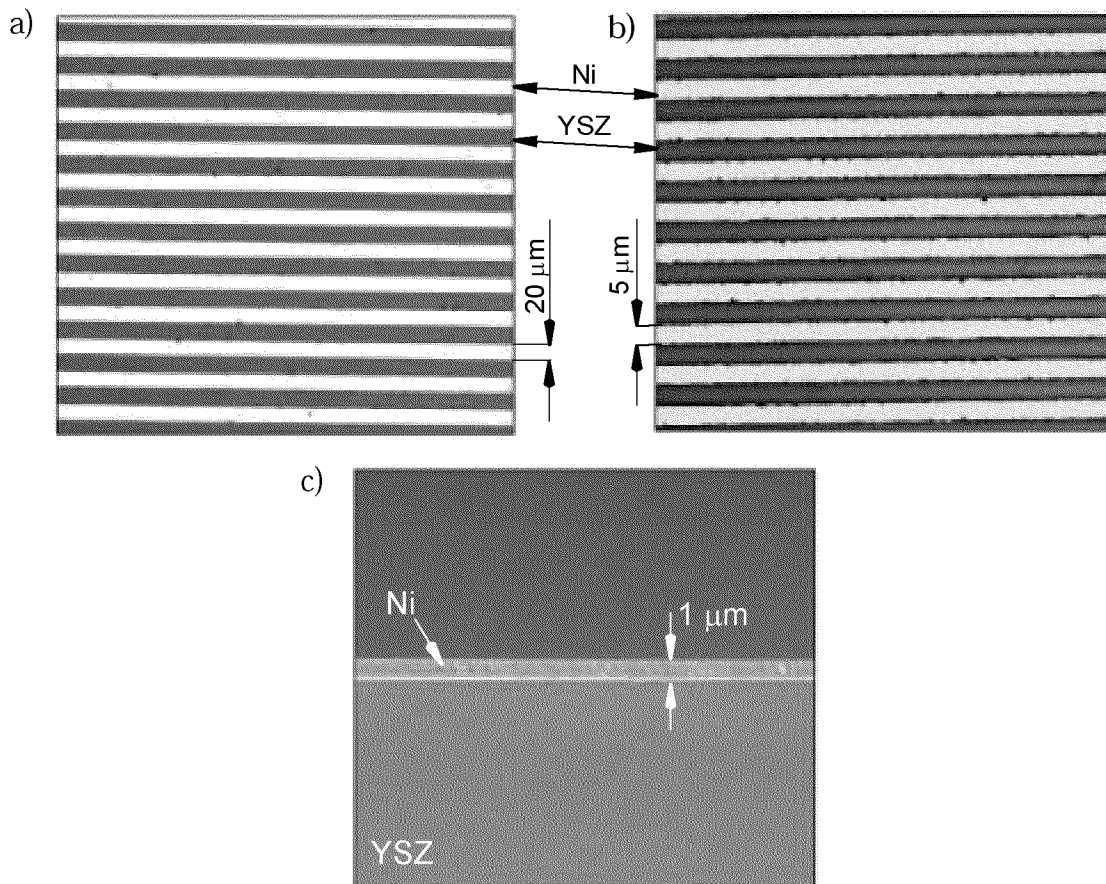


Fig. A1.1: Images of Ni pattern anodes on top of YSZ electrolyte: a) top view of $20\ \mu\text{m}$ line pattern (LM), b) top view of $5\ \mu\text{m}$ line pattern (LM), c) cross section of sputtered Ni layer (SEM).

A1.2 Thermal Treatment

Fig. A1.2 shows SEM images of Ni pattern before and after thermal treatment. The as-prepared Ni pattern has rather frayed out edges (Fig. A1.2a). The line width of the Ni stripe is $18\ \mu\text{m}$ and has, therefore, almost the expected thickness of $20\ \mu\text{m}$. During thermal treatment, the edges of the Ni lines become smoother and small spheres of Ni accumulate near the edge of the Ni line (Fig. A1.2b-d). The width of the Ni lines does not change. However, distinct grains can be distinguished near the Ni line. The grain size increases with increasing dwelling time as well as the higher the temperature for the thermal treatment (compare Fig. A1.2b and Fig. A1.2c as well as Fig. A1.2b and Fig. A1.2d). The small bright spheres on the YSZ are due to underetching of these samples and constitute some residue of Ni on the YSZ surface. This residue was not observed when the samples were etched long enough.

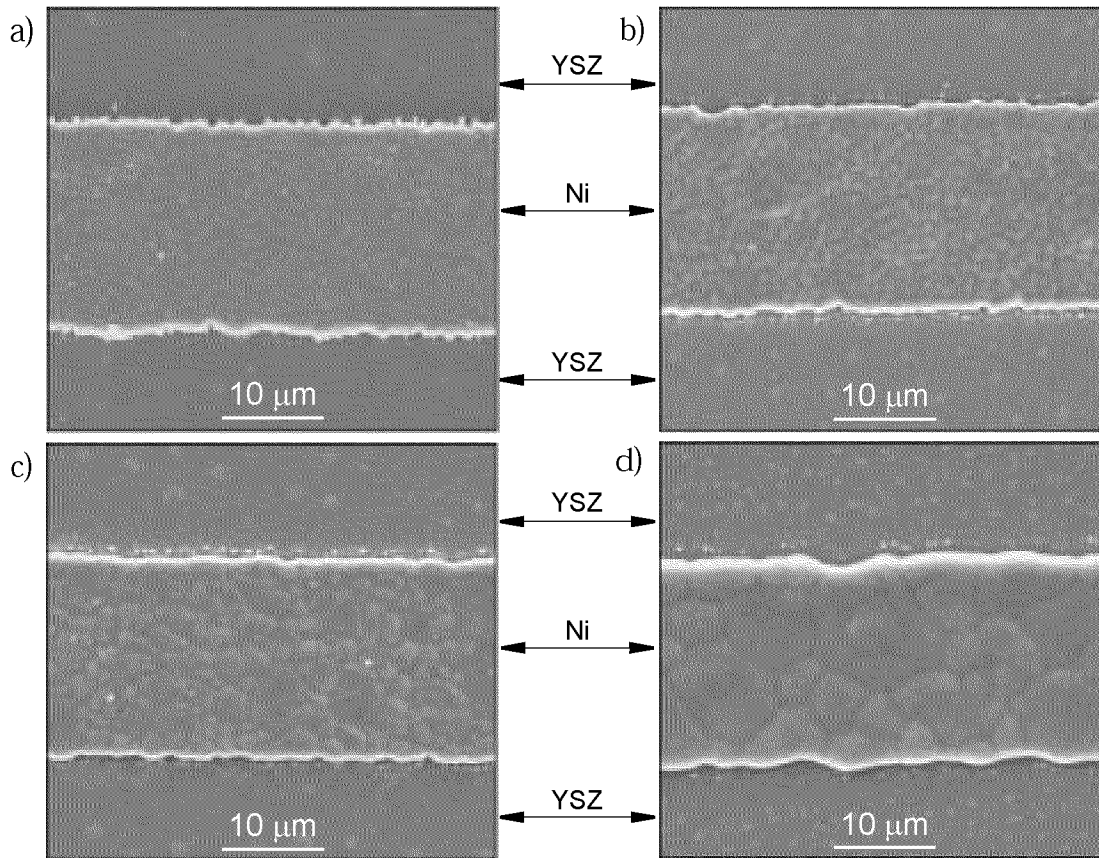


Fig. A1.2: Scanning electron micrographs of Ni pattern with a line width of $20\ \mu\text{m}$: a) without thermal treatment, b) thermal treatment at 973 K for 1 h, c) thermal treatment at 973 K for 24 h, d) thermal treatment at 1373 K for 1 h (heat treatment in $\text{H}_2:\text{N}_2 = 1:3$).

A1.3 Failures in the Ni Pattern

Several examples of typical failures observed at Ni pattern anodes are shown in Fig. A1.3. The interrupted Ni lines in Fig. A1.3a are most probably caused by a large failure in the as-sputtered Ni layer. If the Ni lines are interrupted once per line, the current path is still continuous, since the pattern are designed with a frame of Ni as margin of the electrode. However, two interruptions per line shorten the anode.

Fig. A1.3b illustrates a Ni pattern which is not etched long enough (underetched Ni pattern). The YSZ lines contain much residue of Ni. This residue can, however, be removed in a second photolithography and etching process.

Very fine line pattern with line widths of 5 μm and 2 μm , respectively, are shown in Fig. A1.3c and in Fig. A1.3d. The problem which arises with these thin line widths is associated with the inhomogeneous etching of the Ni. The edges of the Ni lines are always frayed out after etching (Fig. A1.2). In the case of a fine Ni pattern, the Ni lines are already interrupted, as soon as all residue of Ni is removed from the YSZ. A line width of 5 μm with a Ni layer of 1 μm seems to be the lower limit for the wet chemical etching process. The arrows in Fig. A1.3c indicate critical locations where the Ni lines are nearly interrupted. Fig. A1.3d illustrates that it is not possible to prepare a Ni pattern with a line width of 2 μm using the conditions and the method used in this study.

The Ni pattern anodes are all prepared on single crystalline YSZ electrolytes. The reason for this is associated with the surface finishing. Fig. A1.3e shows a Ni pattern prepared on a polycrystalline YSZ electrolyte which was polished in-house. The lines of the Ni pattern are more severely frayed out than in the case of a Ni pattern prepared on a single crystalline electrolyte (Fig. A1.1). This is due to the scratches which could not be removed with the usual polishing procedure. Polishing to a quality which is comparable to the single crystal surfaces would, in principle, be possible, but it is very time consuming. In addition, grain boundaries might disturb the smoothness of the edges. Hence, single crystalline YSZ electrolytes were used throughout this study.

A Ni pattern anode with large areas of Ni and operated under high polarization is illustrated in Fig. A1.3f. Bubbles seemed to form during operation. In consequence, the Ni layer is no longer strongly adherent to the electrolyte.

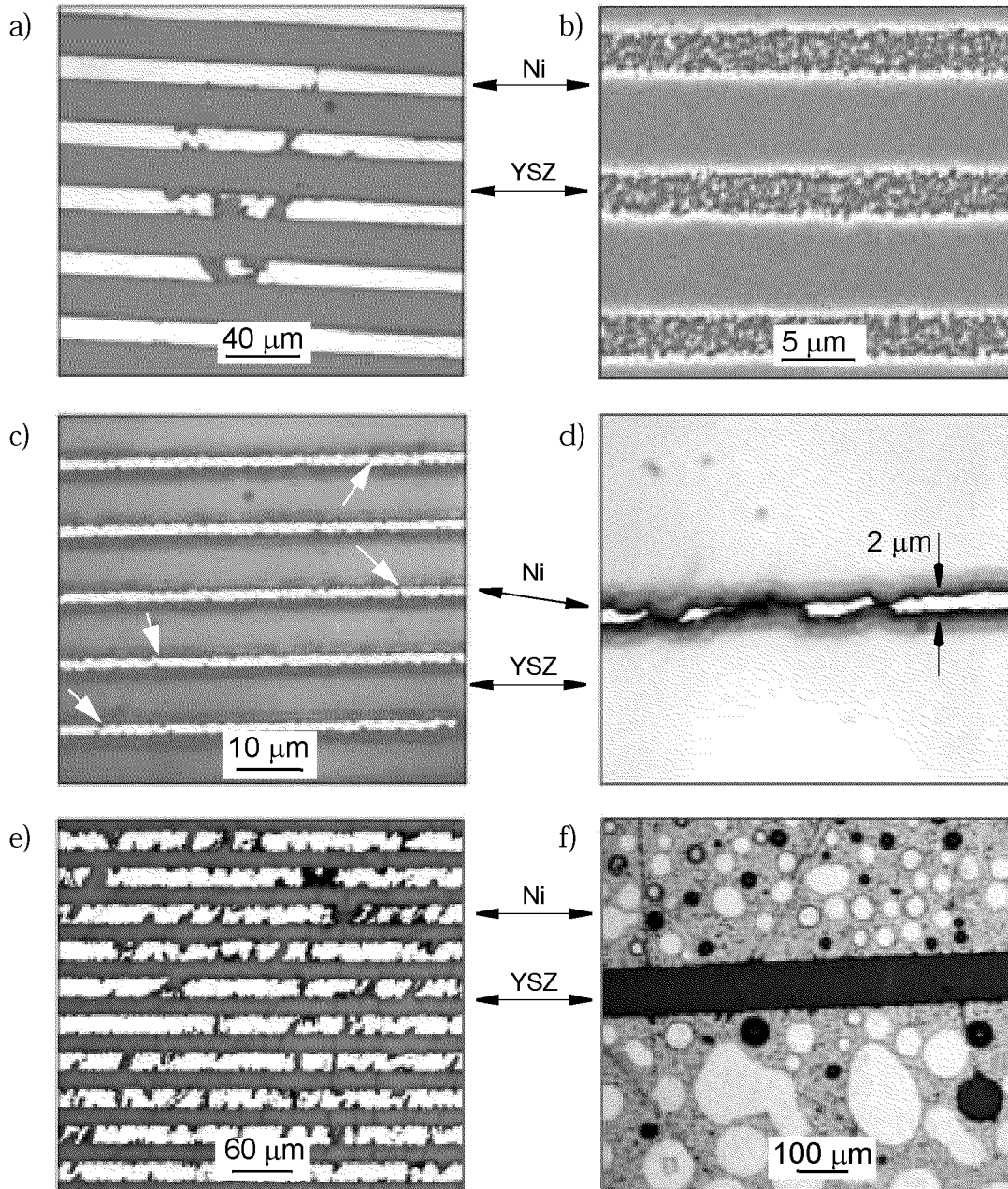


Fig. A1.3: Images of typical failures of Ni pattern anodes: a) 20 μm line pattern with discontinuous lines due to failures in the sputtered Ni layer (SEM), b) underetched Ni pattern (SEM), c) Ni pattern with very thin line width and high possibility of interrupted lines (see arrows) (SEM), d) 2 μm line pattern (LM), e) 20 μm line pattern deposited on a polycrystalline YSZ electrolyte (LM), f) line pattern after high polarization (LM).

Appendix 2

EIS Measurements:

Single vs. Two Gas Chambers

A2.1 The EIS Analyzer

Ni pattern anodes have only a very poor electrochemical performance due to the two dimensional microstructure with the restricted triple phase boundary (TPB) length. The anodes are very sensitive to small deviations from equilibrium conditions, i.e. when applying an external load. In electrochemical impedance spectroscopy (EIS) measurements of electrodes, these currents are obtained by applying an overpotential between the working and the reference electrode (for the wire connections cf. chapter 1), i.e. the electrode is set to a certain working potential compared to the equilibrium state.

Using Ni pattern anodes in a conventional, two gas chamber measurement set-up (the electrical connection of the wires is the same as in a single gas chamber measurement set-up, cf. chapter 1), it was noticed that already the electrical contact with the EIS analyzer of the type ZAHNER[®] IM6, Kronach, D, sets the anode to a certain potential compared to the reference anode. Hence, the electrical contact of the anode to the EIS analyzer is responsible that the entire system is not in equilibrium anymore. This so-called DC potential can reach values of several hundreds of mV in the case of a Ni pattern anode. A DC potential of 260 mV was observed for the anode measured in Fig. A2.1. As a function of an applied overpotential between the working and the reference anode, the total electrode impedance is not strongly affected.

Using the impedance analyzer of the type Solartron SI 1260, Cambridge, UK, the impedances are considerably higher (Fig. A2.2) compared to those measured with the ZAHNER[®] IM6 (Fig. A2.1). No DC potential seems to exist between the working and the reference anode. Note that the measurements were carried out with the same fuel cell, in the same experimental set-up, and under exactly the same experimental conditions. Applying an overpotential between the anode and the reference anode results here in an intense decrease of the anode impedance (Fig. A2.2).

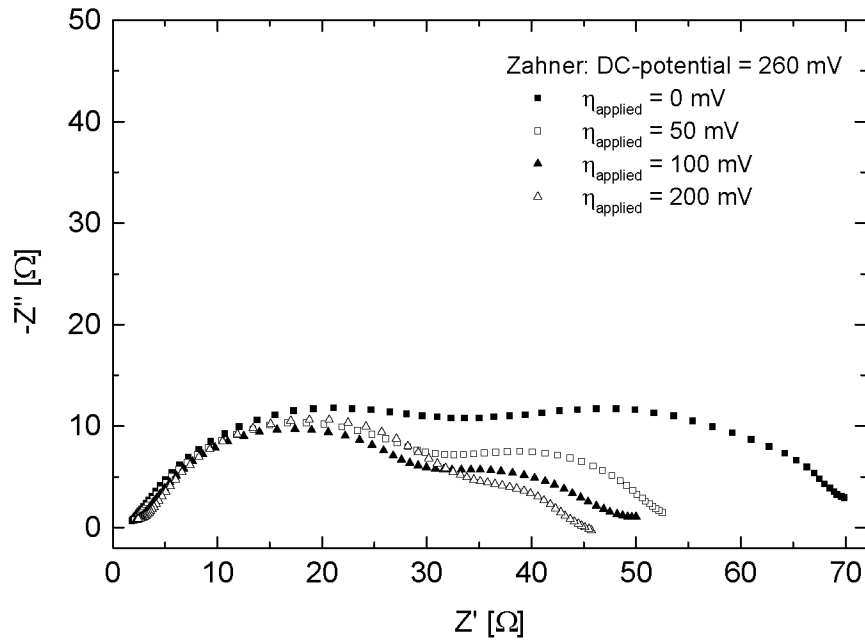


Fig. A2.1: EIS data of a Ni pattern anode as a function of the overpotential, η , measured with a ZAHNER[®] IM6 analyzer in two gas atmospheres. Experimental conditions: $T = 973 \text{ K}$, fuel gas = $\text{H}_2 + \text{N}_2 = 10 \text{ ml/min} + 30 \text{ ml/min}$, air = 40 ml/min .

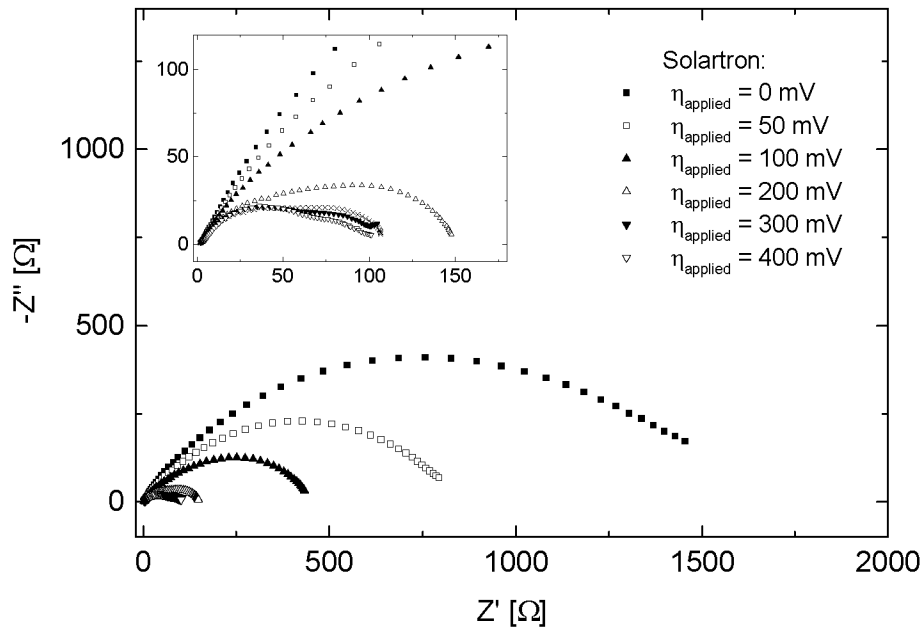


Fig. A2.2: EIS data of a Ni pattern anode as a function of the overpotential, η , measured with a Solartron SI 1260 analyzer in two gas atmospheres (for the experimental conditions see Fig. A2.1).

Comparing the impedance spectra of the ZAHNER[®] IM6 and the Solartron SI 1260 at equilibrium ($\eta = 0$ mV), large differences in the polarization resistances are found: $R_p(\text{ZAHNER}^{\text{®}}) \sim 75 \Omega$ and $R_p(\text{Solartron}) \sim 1700 \Omega$ at $\eta = 0$ mV (Fig. A2.1 and Fig. A2.2, respectively). However, almost identical impedance spectra are found, if an overpotential of $\eta = 250$ mV which is almost the same potential as the DC potential unintentionally applied with the ZAHNER[®] IM6 (DC potential = 260 mV), is applied with the Solartron SI 1260 impedance analyzer (Fig. A2.3). This proves that the ZAHNER[®] IM6 analyzer sets the anode to a certain potential, even though no potential is applied. This so-called DC potential has the same influence as an intentionally applied overpotential.

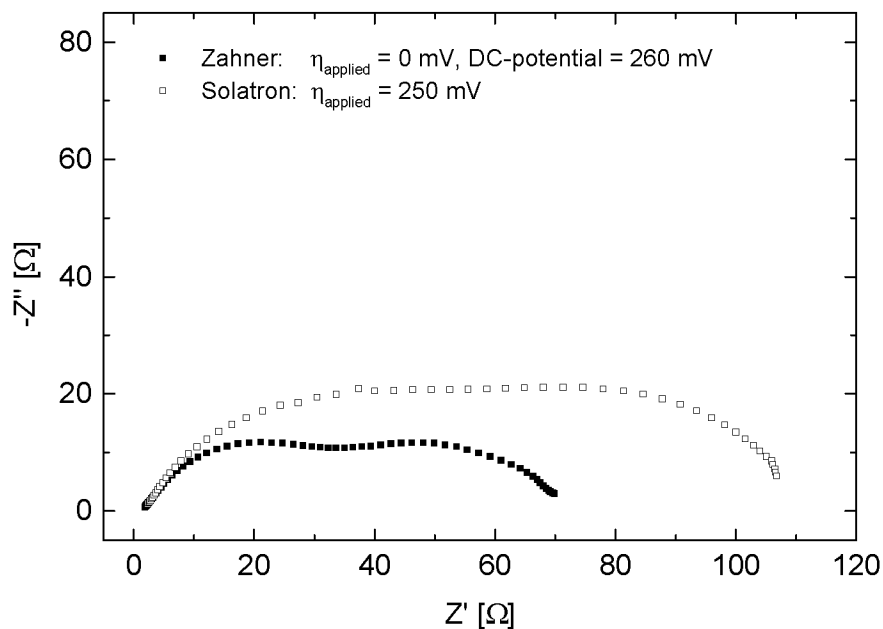


Fig. A2.3: Comparison of the EIS data of a Ni pattern anode measured with a ZAHNER[®] IM6 and a Solartron SI 1260 analyzer, respectively, in two gas atmospheres (for the experimental conditions see Fig. A2.1).

A2.2 The Gas Environment

The effect of an unintentionally applied DC potential between the working and the reference anode was only found when measuring in two gas atmospheres, i.e. fuel gas at the anode side and air at the cathode side of the fuel cell. Impedance measurements of SOFC anodes in a single gas atmosphere resulted in

the same impedance spectra when the ZAHNER[®] IM6 (Fig. A2.4) or the Solartron SI 1260 (Fig. A2.5) EIS analyzer were used. In addition, it is found that no differences in the impedance data (in particular the polarization resistance R_p and the shape of the curves) between the single gas chamber measurements (Fig. A2.4, Fig. A2.5) and the two gas atmosphere measurements with the Solartron SI 1260 (Fig. A2.2) are found. This result affirms us to characterize the anodes in this thesis in a single gas chamber measurement set-up. Not only the experimental set-up is simplified then (no sealing, only one gas supply), but also a better reproducibility of the anode measurements as well as a more facile tuning of the fuel gas atmosphere is possible.

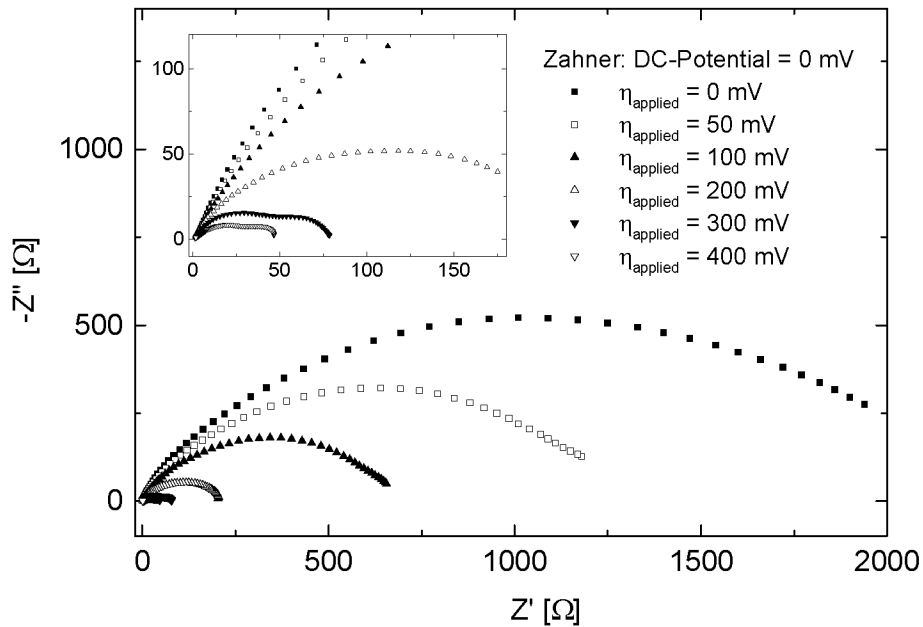


Fig. A2.4: EIS data of a Ni pattern anode as a function of the overpotential, η , measured with a ZAHNER[®] IM6 analyzer in a **single gas atmosphere**. Experimental conditions: $T = 973$ K, fuel gas = $H_2 + N_2 = 10$ ml/min + 30 ml/min.

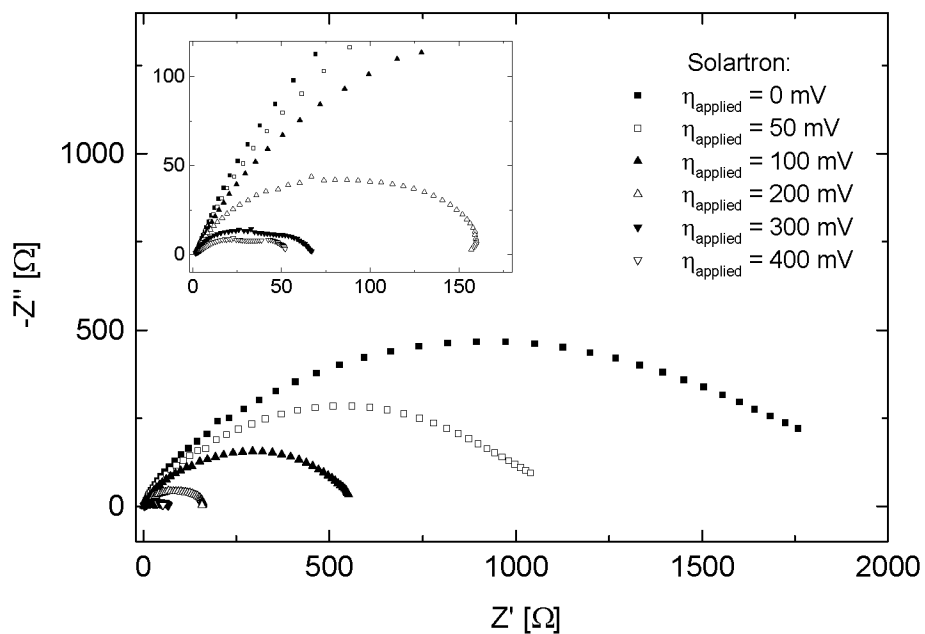


Fig. A2.5: EIS data of a Ni pattern anode as a function of the overpotential, η , measured with a **Solartron SI 1260** analyzer in a **single gas atmosphere** (for experimental conditions see to Fig. A2.4).

Appendix 3

Equivalent Circuit Fitting:

Constant Phase Element (CPE) and Relaxation Frequency

A3.1 Introduction

Electrochemical impedance spectra are usually fitted to equivalent circuits in order to analyze the data [1,2,3]. However, since the physical interpretation of the equivalent circuit elements is not straight-forward, equivalent circuit fitting is only partly used throughout this thesis. Thereby, it was observed that two specific terms, i.e. the Constant Phase Element (CPE) and the relaxation frequency, are not satisfactorily explained in the literature. Since both of these terms were frequently used, it is essential to explain them in the following in some detail.

A3.2 Constant Phase Element (CPE)

A constant phase element (CPE) is used as equivalent circuit element instead of a conventional capacitance. The impedance of a capacitance is given as [1]

$$Z_C = \frac{1}{i\omega C} \quad (\text{A3.1})$$

where i denotes the imaginary unit, ω the frequency, and C the capacitance. Note that an impedance consists in general of a real and of an imaginary part. The real part describes the resistive contribution to the impedance, whereas the imaginary part describes the capacitive contribution. A negative imaginary part describes a capacitive behavior, whereas a positive imaginary part describes an inductive behavior.

The impedance of a CPE is an empirical impedance function which is introduced since anomalous frequency dispersions are often observed in electrochemical systems. It can be identified in the Nyquist plot by means of an angle of tilt [4,5]. Two definitions exist for the impedance of a CPE [6]

$$Z_{CPE}^1 = \frac{1}{Q(i\omega)^n} \quad (\text{A3.2})$$

$$Z_{CPE}^2 = \frac{1}{(Q i\omega)^n} \quad (\text{A3.3})$$

where Q denotes the constant phase element and n is the empirical exponent. According to [6], the definition in Eq. A3.2 is recommended. Q has then the unit

$F/(1/s)^{1-n}$. Note that Q is replaced by $Q \cdot \omega_0^{1-n}$ in the case of the ZAHNER[®] impedance analyzer [7]. Q has then the unit F and Z has the unit Ω .

The exponent n adopts values between 0 and 1. If $n = 1$, then

$$Z_{CPE} = \frac{1}{i\omega Q} . \quad (\text{A3.4})$$

The CPE behaves like an ideal capacitor. An ideal capacitance assumes an ideal continuously and homogeneously charged layer. If $n = 0$, then

$$Z_{CPE} = \frac{1}{Q} . \quad (\text{A3.5})$$

The impedance consists only of a real part signifying that the CPE behaves like a resistor. If n is different from 1 and from 0, a deviation from the ideal behavior exists.

In equivalent circuit fitting, CPEs are mainly used, because they allow a better fitting of the impedance data than a simple capacitance. This is mainly due to the additional parameter n . The appearance of a CPE, i.e. the observation of a frequency dispersion, is often attributed to microscopic material properties which are distributed [1], for instance inhomogeneities in the electrode material or non-uniform diffusion where the electrical analog is an inhomogeneously distributed R - C transmission line [1]. However, besides these rudimentary explanations, no satisfactory chemical or physical explanation for the presence of a CPE in impedance measurements of materials and material interfaces exists at present [8]. The CPE is, thus, considered as an imperfect energy-storage element with the more or less empirical exponent n as a measure of the imperfection.

A3.3 Relaxation Frequency

The relaxation frequency can be determined from the equivalent circuit elements. It gives information about the time constants of single processes. The derivation of the relaxation frequencies of two different equivalent circuit units, a R - C unit and a R - CPE unit, are derived in the following.

A3.3.1 Derivation of the Relaxation Frequency of a R-C Unit

The equivalent circuit model of a R-C unit is shown in Fig. A3.1.

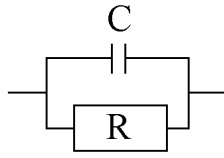


Fig. A3.1: Equivalent circuit model of a R-C unit.

The impedance of the resistive element R is $Z_R = R$ and the impedance of the capacitive element C is $Z_C = \frac{1}{i\omega C}$. According to the parallel connection of R and C , the total impedance is

$$\frac{1}{Z} = \frac{1}{R} + i\omega C . \quad (\text{A3.6})$$

Solving this equation for Z as well as for separated expressions for the real and for the imaginary part, the total impedance becomes

$$Z = \frac{R}{1 + R^2 C^2 \omega^2} - \frac{R^2 C \omega}{1 + R^2 C^2 \omega^2} \cdot i \quad (\text{A3.7})$$

where

$$Z' = \text{real}(Z) = \frac{R}{1 + R^2 C^2 \omega^2} \quad (\text{A3.8})$$

and

$$Z'' = \text{imag}(Z) = \frac{R^2 C \omega}{1 + R^2 C^2 \omega^2} . \quad (\text{A3.9})$$

The relaxation frequency is defined as the maximum frequency of the Z'' vs. Z' curve (Nyquist plot) (cf. chapter 1, subsection 1.2). The maximum is mathe-

matically defined as

$$\frac{dZ''}{dZ'} = 0 . \quad (\text{A3.10})$$

The derivative can be written as

$$\frac{dZ''}{dZ'} = \frac{dZ''}{d\omega} \cdot \frac{d\omega}{dZ'} . \quad (\text{A3.11})$$

A reasonable solution for the relaxation frequency, ω^* , is then

$$\omega^* = \frac{1}{RC} . \quad (\text{A3.12})$$

A3.3.2 Derivation of the Relaxation Frequency of a R-CPE Unit

The capacitance in a *R-C* unit can be replaced by a constant phase element (CPE) which considers the deviation from an ideal capacitive behavior. In the equivalent circuit model in Fig. A3.1 the capacitance is only replaced by a CPE unit. Using Eq. A3.2 as definition for the impedance of a CPE unit, one finds for the impedance of a *R-CPE* unit

$$\frac{1}{Z} = \frac{1}{R} + (i\omega)^n Q . \quad (\text{A3.13})$$

When solving Eq. A3.13 for *Z*, one has to be aware that *i* consists itself of a real and of an imaginary part

$$i^n = \cos\left(\frac{\pi}{2}n\right) + i \cdot \sin\left(\frac{\pi}{2}n\right) . \quad (\text{A3.14})$$

The relaxation frequency can be calculated in the same way as for the *R-C* unit (Eq. A3.7 - Eq. A3.12). For the *R-CPE* unit, it yields

$$\omega^* = \sqrt[n]{\frac{1}{RQ}} . \quad (\text{A3.15})$$

If the resistance, R , is given in units of Ω and the CPE, Q , is given in units of F (this is the case for the ZAHNER[®] impedance analyzer [7]), then the equations for the impedance and for the relaxation frequency have to be normalized with ω_0 where $\omega_0 = 2\pi \cdot 1000 \text{ s}^{-1}$

$$\frac{1}{Z} = \frac{1}{R} + (i\omega)^n Q \omega_0^{1-n} \quad (\text{A3.16})$$

$$\omega^* = \sqrt[n]{\frac{1}{R(Q \cdot \omega_0^{1-n})}} \quad (\text{A3.17})$$

The fitting results for the CPE in the ZAHNER[®] software are then comparable to the fitting results of the Solartron software, i.e. $Q_{\text{Solartron}} = Q_{\text{Zahner}} \cdot \omega_0^{1-n}$.

A3.4 References

- [1] J.R. Macdonald, "Impedance Spectroscopy", John Wiley & Sons, Inc., New York, NY, USA (1987).
- [2] M. Sluyters-Rehbach, J.H. Sluyters, in: Comprehensive Treatise of Electrochemistry, Vol. 9, Ed.: E. Yeager, J. O'M. Bockris, B.E. Conway, S. Saranagapani, Plenum Press, New York, NY, USA (1984) 177.
- [3] M. Sluyters-Rehbach, J.H. Sluyters, in: Electroanalytical Chemistry, A Series of Advances, Vol. 4, Ed.: A.J. Bard, Marcel Dekker, New York, NY, USA (1970) 1.
- [4] P.R. Roberge, V.S. Sastri, *Corr. Sci.* **35** (1993) 1503.
- [5] P.R. Roberge, V.S. Sastri, *Brit. Corr. J.* **29** (1994) 38.
- [6] P. Zoltowski, *J. Electroanalyt. Chem.* **443** (1998) 149.
- [7] ZAHNER[®] Messtechnik - Owner's Manual", Version: Thales IM6, ZAHNER[®] Elektrik, Kronach, Germany (2000) S 6.7.0.
- [8] F.H. van Heuveln *J. Electrochem. Soc.* **141** (1994) 3423.

Appendix 4

Microstructural Characterization of Ni-YSZ Cermet

A4.1 Introduction

The state-of-the-art Ni-YSZ cermet anode consists of three interpenetrating networks of Ni, YSZ, and pores. It is expected that the electrochemically active area is restricted to the zone where the three phases meet each other. This zone is called the triple phase boundary (TPB). If the TPB is, in fact, the electrochemically active area, it is evident that the TPB is closely related to the performance of the anode. So far, this is neither proven nor is it clear, whether other effects might significantly contribute to the performance. Hence, it is of main interest to determine the TPB length of a Ni-YSZ cermet and to investigate the relation between the TPB length and the performance.

In chapter 3, such studies were carried out using Ni pattern anodes. The TPB length can be easily determined for this anode design. In the case of Ni-YSZ cermet anodes, the determination of the TPB length is not straight-forward due to the three 3-dimensionally connected networks of Ni, YSZ, and pores. Hence, this appendix focuses on preliminary experiments which allow to investigate the microstructures of the different networks separately. The experiments are carried out with porous Ni-YSZ substrates which are industrially available.

A4.2 The Ni-YSZ Porous Substrate

Fig. A4.1a and Fig. A4.1b show scanning electron micrographs (SEM) of Ni-YSZ substrates in the oxidized and in the reduced state. The microstructures are rather similar. However, a close view of the images manifests that the reduced substrate has a more porous microstructure (Fig. A4.1b) compared to the oxidized substrate (Fig. A4.1a). This is due to the reduction of NiO to Ni which is associated with a decrease in volume (around 5 % increase in porosity). Energy dispersive X-ray (EDX) analyses did not allow to illustrate the Ni and the YSZ network as single and well distinguished networks. A main problem here is the three dimensional microstructure. A ratio of 57 wt.% Ni : 43 wt.% ZrO₂ was determined by EDX for the reduced substrate (EDX parameters: V = 30 kV, pulse processor = high II, magnification = 160 x, Ni-K, Zr-L).

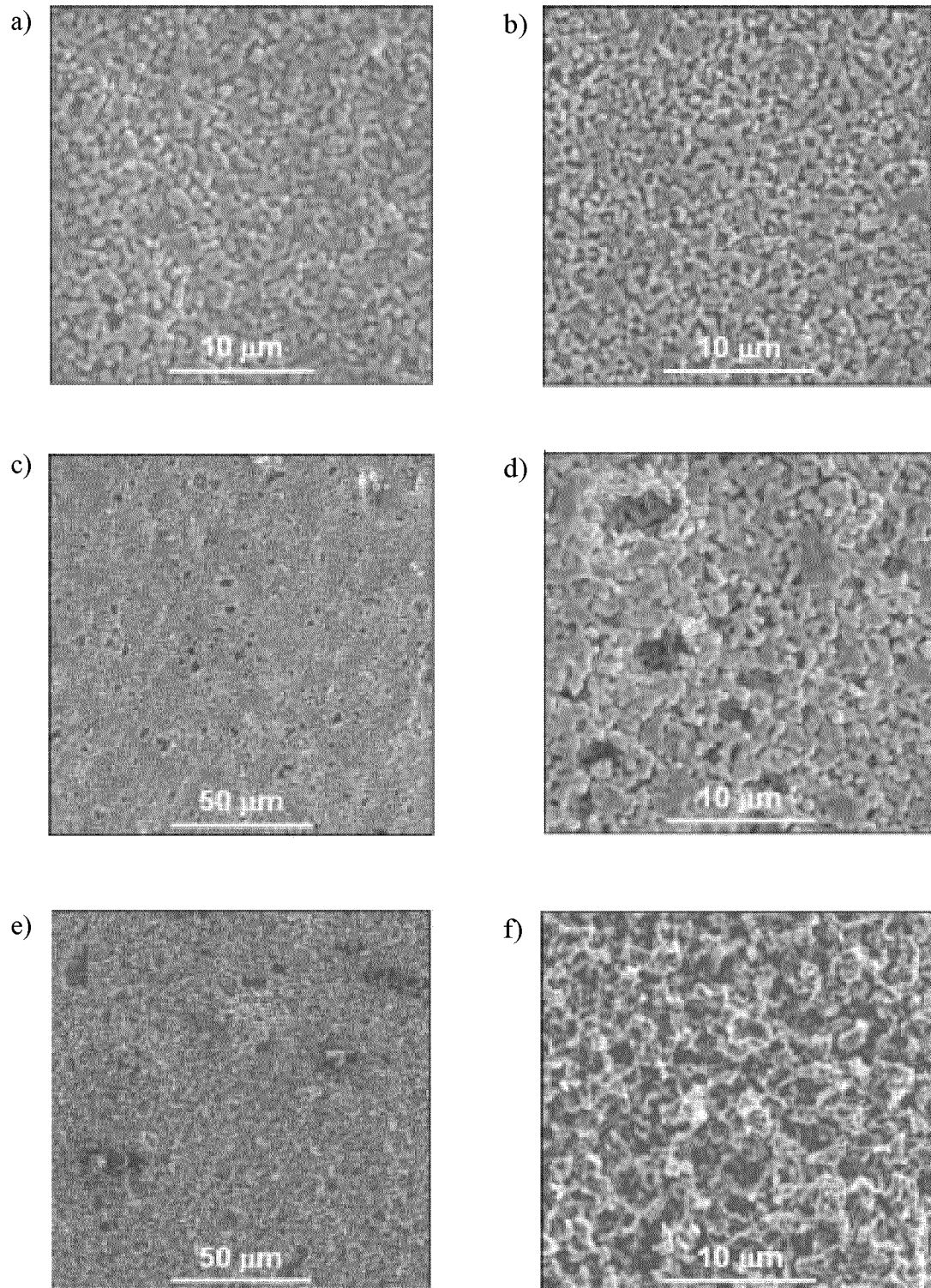


*Fig. A4.1: Scanning electron micrographs of Ni-YSZ substrates (top view):
a) oxidized, b) reduced, c) and d) YSZ network after dissolving
of Ni, e) and f) Ni network after decomposition of YSZ.*

A4.3 The YSZ Network

The etching experiments in chapter 3 demonstrated that metallic Ni deposited onto a YSZ substrate can be dissolved in concentrated nitric acid at elevated temperature (50°C). Hence, the reduced Ni-YSZ substrates were etched under these conditions in order to dissolve the metallic Ni in the cermet microstructure. The YSZ network should be left over.

The SEM images of the substrate after etching are shown in Fig. A4.1c and Fig. A4.1d in two different magnifications. Large holes with diameters of around 5 μm were observed. These large holes after etching originate most probably from coagulated Ni particles. The rest of the microstructure is more porous than the microstructure in the reduced state (Fig. A4.1b). EDX analyses yielded a ratio of 4 wt.% Ni : 96 wt.% ZrO_2 (the same EDX parameters as in subsection A4.2 were used). Thus, it was indeed possible to dissolve and to remove the Ni from the Ni-YSZ cermet by wet chemical etching.

A4.4 The Ni Network

Several methods are discussed in the literature for the decomposition of zirconia [1,2]. Straight-forwardly from these results, the Ni-YSZ substrate in this study was decomposed in the following way: a piece of Ni-YSZ was covered with ammonium-sulfate $(\text{NH}_4)_2\text{SO}_4$ in a Pythagoras crucible. The crucible was heated up to 350°C under atmospheric conditions and was dwelled at this temperature for 3 h. After cooling, the zirconia network should be dissolved by the addition of water.

The SEM images of the substrate after the decomposition procedure are shown in Fig. A4.1e and Fig. A4.1f in two different magnifications. The microstructure becomes very porous and large particles are found at several areas. EDX analyses yielded a ratio of 71 wt.% Ni : 29 wt.% ZrO_2 (the same EDX parameters as in subsection A4.2 were used). This result indicates that the zirconia was not entirely dissolved. This might be due to the fact that the acid easily evaporates at elevated temperatures. The procedure for the decomposition of zirconia should be carried out in a pressure vessel and should be repeated several times.

A4.5 Summary and Outlook

The results have illustrated that it is, in principle, possible to separate the different networks of Ni-YSZ cermet. Whereas almost the entire amount of Ni was dissolved by wet chemical etching, there was still some residue of zirconia remaining after the decomposition procedure. The residue can most probably be removed by repeating the experimental procedure several times. However, it is not necessary to separate all three networks individually. If it is possible to illustrate two of three networks separately, the third network is known as well.

The preliminary experiments are an excellent starting point for the following further investigations:

- (1) A method should be developed which allows to reassemble the different networks in a way that the interfaces between the three networks can be illustrated. Professional image analyses techniques and computer simulations are required.
- (2) Several Ni-YSZ cermet anodes should be prepared as similar as possible. The anodes should be etched in nitric acid so that different ratios of Ni : ZrO₂ can be adjusted. As long as the Ni network is continuous, a direct correlation between the TPB and the performance is expected, when the samples are characterized electrochemically.

A4.6 References

- [1] B. Ayranci, *Swiss Chem.* **11** (1989) 13.
- [2] G. Bayer, G. Kahr, M. Müller-Vonmoos, *Clay Minerals* **17** (1982) 271.

Abbreviations

AC	Alternate Current
CDG	Ceria Doped Gadolinia
CPE	Constant Phase Element
DC	Direct Current
EDX	Energy Dispersive X-Ray
EIS	Electrochemical Impedance Spectroscopy
HEXIS	Heat Exchanger Integrated Stack
LM	Light Microscope
LSM	$\text{La}_{(1-x)}\text{Sr}_x\text{MnO}_3$
MIEC	Mixed Ionic Electronic Conduction / Conductor
ML	Mono-Layer
Ni - YSZ	cermet of Nickel and YSZ
OCV	Open Circuit Voltage
SDC	Samaria Doped Ceria
SEM	Scanning Electron Microscope
SOFC	Solid Oxide Fuel Cell
SSM	State-Space Modeling
TPB	Triple Phase Boundary
YSZ	Yttria Stabilized Zirconia

Symbols

Latin symbols

A, B, C, D	[-]	free definable parameter for a gas phase element, a surface species, an adsorption site, or an electron in a chemical reaction
A	[m ²]	electrode area
ad	[-]	free adsorption site
∇c	[-]	concentration gradient of adsorbed surface species
C_i	[F]	capacitance in equivalent circuit model
C_{dl}	[F]	double layer capacitance
d	[m]	active electrode thickness
D	[m ² /s]	diffusion coefficient
e^-	[C]	elementary electronic charge
E_A	[eV]	activation energy
f	[s ⁻¹ , Hz]	frequency
F	[C/mol]	Faraday constant
I_F	[A]	Faraday current
i	[-]	imaginary part
i_0	[A]	exchange current density
i_{0_a}, i_{0_c}	[A]	anodic and cathodic exchange current density
I_m	[A]	current amplitude
J	[m ² /s]	flux of adsorbate
j	[A]	current density
k_B	[J/K]	Boltzmann constant
k_f	[s ⁻¹]	forward reaction rate constant

k_i	$[s^{-1}]$	backward reaction rate constant
l_{TPB}	$[m/cm^2]$	triple phase boundary length
L_W	$[H]$	Warburg inductance
M	$[g/cm^3]$	molecular weight
n	$[-]$	exponent of the CPE
N_0	$[m^{-2}]$	number of free adsorption sites
N_A	$[1/mol]$	Avogadro number
O^{2-}	$[-]$	oxygen ion
O_O^x	$[mol/m^3]$	oxygen ion in YSZ
\mathbf{p}	$[-]$	vector of unknown parameters
$p(H_2)$	$[Pa]$	partial pressure of hydrogen
$p(H_2O)$	$[Pa]$	partial pressure of water
$p(O_2)$	$[Pa]$	partial pressure of oxygen
Q_i	$[F]$	constant phase element in equivalent circuit model
R	$[J/mol/K]$	gas constant
R_i	$[\Omega]$	resistance in equivalent circuit model
R_e	$[\Omega]$	electrolyte resistance
R_p	$[\Omega]$	polarization resistance
R_t	$[\Omega]$	charge transfer resistance
s_0	$[-]$	initial sticking coefficient
s_θ	$[-]$	sticking coefficient as a function of the fraction of surface coverage
t	$[s]$	time
T	$[K]$	temperature
\mathbf{u}	$[-]$	vector of input variables

U	[V]	voltage
U_m	[V]	voltage amplitude
$V_{\ddot{O}}$	[mol/m ³]	oxygen vacancy in YSZ
V_{exc}	[mV]	excitation voltage
w	[m]	width of lines of Ni pattern
\mathbf{x}	[-]	vector of state variables
[X]	[-]	concentration of species X
\mathbf{y}	[-]	vector of model output, observation function
Z	[Ω]	total electrochemical impedance
$ Z $	[Ω]	absolute impedance
Z'	[Ω]	real part of the impedance
Z''	[Ω]	imaginary part of the impedance
Z_C	[Ω]	impedance of a capacitance
Z_{CPE}	[Ω]	impedance of a constant phase element
Z_F	[Ω]	Faraday impedance
Z_F^{exp}	[Ω]	experimental Faraday impedance
Z_F^{sim}	[Ω]	simulated Faraday impedance

Greek Symbols

α	[-]	exponent of s_0
β	[-]	charge transfer coefficient
ε	[C V ⁻¹ m ⁻¹]	dielectric constant
$\eta, \eta_{\text{applied}}$	[mV]	overpotential applied between the working and the reference electrode

θ_i	[-]	fraction of surface coverage of surface species i
σ	[S/m]	electrical conductivity
τ^*	[s]	relaxation time
ν	[s ⁻¹]	pre-exponential factor
ϕ	[°]	phase shift
ω	[s ⁻¹]	angular frequency
ω^*	[s ⁻¹]	relaxation frequency
ω_0	[s ⁻¹]	normalized angular frequency at $f = 1000$ Hz

Other Symbols

F	[ml/min]	total gas flow
\mathfrak{I}	[m ⁻² s ⁻¹]	impingement rate

Curriculum Vitae

Personal

Name: Anja Bieberle
Date and Place of Birth: October 18, 1971, Erlangen, Germany
Nationality: German

Education

1978 - 1991 Grundschohle and Gymnasium in Erlangen, Germany
1991 - 1996 Student of Materials Science and Engineering, Friedrich-Alexander University Erlangen - Nürnberg, Germany
1996 Diploma in Materials Science and Engineering
1997 - present Research associate and Ph.D. student, Chair of Nonmetallic Inorganic Materials, Department of Materials, ETH Zürich, Switzerland

Study Abroad

08/94 - 05/95 Student at the New York State College of Ceramics, Alfred University, Alfred, NJ, USA (Scholarship of the DAAD (Deutscher Akademischer Auslandsdienst))

List of Publications

Papers

- (1) A. Bieberle, L.J. Gauckler
Reaction Mechanisms of Ni Pattern Anodes for Solid Oxide Fuel Cells
Solid State Ionics, 135 (2000) 337.
- (2) A. Bieberle, L.P. Meier, L.J. Gauckler
The Electrochemistry of Ni Pattern Anodes Used as Solid Oxide Fuel Cell Model Electrodes
Journal of the Electrochemical Society (2000) accepted.
- (3) A. Bieberle, L.J. Gauckler
Modeling and Simulations of the Anodic SOFC System Ni, H₂ - H₂O | YSZ Part I: Electrochemical Model and Simulations Under Standard Conditions
Solid State Ionics (2000) submitted.
- (4) A. Bieberle, L.J. Gauckler
Modeling and Simulations of the Anodic SOFC System Ni, H₂ - H₂O | YSZ Part II: Simulations Under Various Conditions and the Comparison to Experiments
Solid State Ionics (2000) submitted.
- (5) A. Bieberle, L.J. Gauckler
Ni-based SOFC Anodes: Microstructure and Electrochemistry
Zeitschrift für Metallkunde (2001) submitted.

Proceedings

- (1) A. Bieberle, L.J. Gauckler
From Model Anodes to Cermet Anodes
Proc. of the 7th Intern. Symp. on SOFC (SOFC VII), Tsukuba, Japan, The Electrochemical Society, Pennington, NJ, USA (2001) accepted.
- (2) A. Bieberle, L.J. Gauckler
On the Way of Understanding the Electrochemistry of SOFC Anodes

Proc. of the Topical Meeting: Solid Oxide Fuel Cells Materials and Mechanisms, IEA Program of R&D on Advanced Fuel Cells, Ed.: A. Mc Evoy, Les Diablerets, Switzerland (2001) accepted.

- (3) A. Bieberle, L.J. Gauckler
The Effect of the Partial Pressure of Water in the Fuel Gas on the Electrochemical Behavior of SOFC Anodes
Proc. of the 4th Europ. Solid Oxide Fuel Cell Forum, Lucerne, Ed.: A.J. McEvoy, Switzerland (2000) 305.
- (4) A. Bieberle, L.J. Gauckler
Modeling, Simulations, and Experiments in the Ni, H₂ - H₂O / YSZ System
Proc. of the 6th Intern. Symp. on SOFC (SOFC VI), Hawaii, USA, Eds.: S.C. Singhal, M. Dokiya, The Electrochemical Society, Pennington, NJ, USA (1999) 549.
- (5) A. Bieberle, A. Mitterdorfer, L.J. Gauckler
A New Approach for the Identification of Reaction Mechanisms at SOFC Electrodes
Proc. of the 12th SOFC Workshop: Materials and Mechanisms, IEA Program of R&D on Advanced Fuel Cells, Ed.: K. Nisancioglu, Wadahl, Norway (1999) 39.
- (6) A. Bieberle, L.J. Gauckler
Thermal and Isothermal Expansion
Proc. of the Advanced NATO Summer School on Oxygen Ion and Mixed Conductors and Their Technological Applications, Erice, Sicily, July 14-24, 1997, Eds.: H.L. Tuller, J. Schoonman, I. Riess, Kluwer Academic Publishers (2000) 347.
- (7) A. Bieberle, L.J. Gauckler
Metallic Interconnector
Proc. of the Advanced NATO Summer School on Oxygen Ion and Mixed Conductors and Their Technological Applications, Erice, Sicily, July 14-24, 1997, Eds.: H.L. Tuller, J. Schoonman, I. Riess, Kluwer Academic Publishers (2000) 375.

- (8) A. Bieberle, L.J. Gauckler

Glass Seals

Proc. of the Advanced NATO Summer School on Oxygen Ion and Mixed Conductors and Their Technological Applications, Erice, Sicily, July 14-24, 1997, Eds.: H.L. Tuller, J. Schoonman, I. Riess, Kluwer Academic Publishers (2000) 389.

Presentations

- (1) A. Bieberle, L.J. Gauckler

From Model Anodes to Cermet Anodes

7th Intern. Symp. on SOFC (SOFC VII), Tsukuba, Japan, June 3-8, 2001 (talk to be given).

- (2) L.J. Gauckler, A. Bieberle

Solid Oxide Fuel Cells: Materials and Electrochemistry

6th Intern. Symp. Systems with Fast Ionic Transport, Cracow, Poland, May 9-12, 2001 (talk to be given).

- (3) A. Bieberle, L.J. Gauckler

On the Way of Understanding the Electrochemistry of SOFC Anodes

SOFC Workshop, IEA Program of R&D on Advanced Fuel Cells, Les Diablerets, Switzerland, January 16-19, 2000 (talk).

- (4) A. Bieberle, L.J. Gauckler

The Effect of the Partial Pressure of Water in the Fuel Gas on the Electrochemical Behavior of SOFC Anodes

4th European Solid Oxide Fuel Cell Forum, Lucerne, Switzerland, July 10-14, 2000 (talk).

- (5) A. Bieberle, L.J. Gauckler

Reaction Mechanisms at SOFC Anodes

Colloquium of the Department of Materials, ETH Zürich, Switzerland, May 10, 2000 (talk).

-
- (6) A. Bieberle, L.J. Gauckler
Identification of the Anodic Reaction Mechanisms
Jahrestagung des Bundesamtes für Energie, Basel, Switzerland, December 14, 1999 (talk).
- (7) A. Bieberle, L.J. Gauckler
Modeling, Simulations, and Experiments in the Ni, H₂ - H₂O | YSZ System
196th Meeting of the Electrochemical Society (SOFC VI), Hawaii, USA, October 17-22, 1999 (talk).
- (8) A. Bieberle, L.J. Gauckler
Modeling, Simulations, and Experiments in the Ni, H₂ - H₂O | YSZ System
Institute of Materials for Electrical and Electronics Engineering (Prof. E. Ivers-Tiffée), University of Karlsruhe, Germany, October 4, 1999 (talk).
- (9) A. Bieberle, L.J. Gauckler
On the Way of Understanding SOFC Anodes
Risø Materials Research Department, Risø, Denmark, September 5, 1999 (talk).
- (10) A. Bieberle, L.J. Gauckler
Reaction Mechanisms at Solid Oxide Fuel Cell Anodes
12th Intern. Conf. on Solid State Ionics, Halkidiki, Greece, June 6-12, 1999 (invited talk).
- (11) A. Bieberle, L.J. Gauckler
Modeling, Simulations, and Experiments in the Ni, H₂ - H₂O | YSZ System
Institute of Applied Physics - Chemical Physics (Prof. B. Kasemo), Chalmers University, Göteborg, Sweden, January 15, 1999 (talk).
- (12) A. Bieberle, L.J. Gauckler
A New Approach for the Identification of Reaction Mechanisms at SOFC Electrodes
12th SOFC Workshop: Materials and Mechanisms, IEA Program of R&D on Advanced Fuel Cells, Wadahl, Norway, January 10-13, 1999 (talk).
- (13) A. Bieberle, L.J. Gauckler
Identification of the Anodic Reaction Mechanisms

Jahrestagung des Bundesamtes für Energie, Basel, Switzerland, December 17, 1998 (talk).

- (14) A. Bieberle, A. Mitterdorfer, L.J. Gauckler
Electrochemical Behavior of the Ni, H₂ - H₂O / YSZ System: Modeling and Simulations
3rd Europ. Solid Oxide Fuel Cell Forum, Nantes, France, June 2-5, 1998 (poster).

Supervised Student Work

- (1) S. Kurz
Der Einfluss des Wasserdampfpartialdruckes im Brenngas auf die Anoden-Kinetik von Hochtemperatur-Brennstoffzellen
Semesterarbeit, ETH Zürich, Switzerland (2000).
- (2) H. Rudmann
Gasanalyse mit Massenspektrometrie zur Brennstoffzellen-Charakterisierung
Diploma Thesis, ETH Zürich, Switzerland (1998).